

# **BILAYER CHANNEL AND FREE-SURFACE THIN FILM FLOW OVER TOPOGRAPHY**

by

**AYAD A. ABDALLA**

Submitted in accordance with the requirements for the degree of

Doctor of Philosophy



The University of Leeds

School of Mechanical Engineering

September 2014

The candidate confirms that the work submitted is his own and that appropriate credit has been given where reference has been made to the work of others. This copy has been supplied on the understanding that it is copyright material and that no quotation from the thesis may be published without proper acknowledgement.

# ABSTRACT

The work presented in this thesis focuses on gravity driven bilayer flow over a functional surface containing topography, with both liquids taken to be perfectly immiscible. Two such problems are considered and investigated systematically: (i) when the flow is confined between two rigid surfaces ("channel flow"); (ii) for the case of free-surface film flow down an inclined plane ("free-surface flow"). Both problems are underpinned by rigorous and comprehensive mathematical derivations, and the governing equation sets, resulting from application of the long-wave approximation, solved numerically using efficient and accurate finite difference algorithms programmed in C++. Such problems have received scant attention to-date.

The channel flow work begins by revisiting the problem investigated by Lenz and Kumar (2007) and Zhou and Kumar (2012), to explore bilayer flow for the particular case of one Newtonian liquid lying above another and confined by rigid surfaces aligned parallel to each other, the lower one containing a steep-sided topographical feature. The investigation carried out serves a number of important purposes, the first being to establish the validity of the modelling and numerical approaches adopted, with the mesh independent results obtained found to be in excellent agreement with earlier work. In addition, the depth-averaged equation set derived in the thesis enables solutions to be obtained when the Reynolds number is non-zero, in contrast to the work of others which achieved only partial success. Finally, the situation when the upper wall of the channel is allowed to move horizontally with a constant speed, inducing a shear flow, is investigated for the first time.

Bilayer free surface film flow over steep-sided topography, solutions to which have not been reported in the literature hitherto, is similarly investigated; comparisons having to be drawn for consistency and verification purposes with the case of single layer flow, Decré and Baret (2003), Gaskell *et al.* (2004), Veremieiev *et al.* (2010). Both zero and non-zero Reynolds number flow are considered and the governing equation sets and finite difference expressions re-derived to accommodate

non-Newtonian behaviour, for the particular case of power-law liquids; it is found that for the latter case the associated depth-averaged equation set as formulated cannot be solved unless additional simplifications are adopted. In addition, for the case of Newtonian liquids, it is shown that the work can be extended to embody the more practical situation of three-dimensional bilayer film flow over topography. The mathematical model for this same film flow problem is extended to accommodate  $N$  layers, for the case when the Reynolds number is zero, with the derivation provided for completeness.

*To the loving memory of my father.*

*To my mother who gives me unwavering support and prayers.*

*To my wife who supported me in all my endeavours.*

*To my children who makes my life fun.*

## ACKNOWLEDGEMENTS

First and foremost I wish to express my utmost gratitude to my supervisors Prof. Philip H. Gaskell and Dr. Sergii Veremieiev, for introducing me to the subject area of thin film flow and guided my research with vivid interest and great patience. Without their professional advice and expertise, the thesis would not have been possible.

My sincere thanks are also due to Dr. Yeaw Chu Lee for his support and guidance, particularly during my first year, and his continued involvement in my work even after moving away from Leeds. I would also like to acknowledge the help of the I.T. support team within the school and those who maintain and run the high performance computing cluster ARC1.

The financial support from the Libyan Ministry of Higher Education is gratefully acknowledged.

My special thanks go to my mother, who has been a constant source of support and encouragement and to my sisters and brothers for their support. I wish also to acknowledge my late father, Abdulhamid Elfakhri, who have always been a great source of inspiration to me.

Finally, I wish to express my deepest gratitude to my wife; without her support and encouragement this thesis would never have turned into reality; and to my children who have brought great joy to my life.

# Contents

<b>1</b>	<b>Introduction</b>	<b>1</b>
1.1	Motivation . . . . .	2
1.2	Physics of thin film flows . . . . .	4
1.3	Single Layer Flow over Topography . . . . .	6
1.4	Bilayer Systems . . . . .	15
1.5	Thesis outline . . . . .	21
<b>2</b>	<b>Mathematical model</b>	<b>24</b>
2.1	Introduction . . . . .	25
2.2	Governing equations . . . . .	26
2.3	Determination of appropriate velocity scalings . . . . .	36
2.4	Long-wave approximation . . . . .	40
2.5	Depth-averaged formulation . . . . .	42
2.5.1	DAF for free-surface flow . . . . .	42
2.5.2	LUB model for free-surface flow . . . . .	51
2.5.3	DAF for channel flow . . . . .	52
2.5.4	LUB for channel flow . . . . .	54
2.5.5	Compact generic DAF (LUB) equations . . . . .	55
2.6	Topography definition . . . . .	56
<b>3</b>	<b>Methods of solution</b>	<b>58</b>

3.1	Introduction . . . . .	59
3.2	Overall method of solution . . . . .	66
3.2.1	Free-surface flow problem . . . . .	67
3.2.2	Channel problem . . . . .	74
3.3	Methods of solution . . . . .	77
3.3.1	Multigrid solver . . . . .	79
3.3.2	Full weighting restriction and interpolation operators . . . . .	84
3.4	Calculation details . . . . .	87
3.5	Comparison of DAF ( $Re=0$ ) and LUB results . . . . .	89
<b>4</b>	<b>Bilayer film flow in patterned channels</b>	<b>92</b>
4.1	Gravity-driven flow . . . . .	95
4.1.1	Validation . . . . .	95
4.1.2	Effect of the normal gravity term . . . . .	99
4.1.3	Effect of inertia . . . . .	100
4.2	Pressure gradient and shear driven flow . . . . .	121
<b>5</b>	<b>Free-surface bilayer thin film flow over topography</b>	<b>132</b>
5.1	Two-dimensional flow . . . . .	134
5.1.1	Single-layer equivalent . . . . .	134
5.1.2	Exploring parameter space, $Re = 0$ . . . . .	135
5.1.3	Exploring parameter space, $Re \neq 0$ . . . . .	145
5.2	Three-dimensional flow over trench topography . . . . .	155
<b>6</b>	<b>Free-surface non-Newtonian Bilayer thin film flow</b>	<b>163</b>
6.1	Introduction . . . . .	164
6.2	Models for non-Newtonian liquids . . . . .	164
6.3	Depth-averaged formulation for bilayer power-law thin film flow . . . . .	169
6.3.1	Bilayer Non-Newtonian flow with negligible inertia . . . . .	173

6.3.2	Single-layer equivalent non-Newtonian inertial flow . . . . .	175
6.4	Method of solution . . . . .	178
6.4.1	Discretisation of the LUB equations . . . . .	178
6.4.2	Discretisation of the DAF equations . . . . .	180
6.6	Results and discussion . . . . .	182
<b>7</b>	<b>Conclusion and suggestion for future work</b>	<b>189</b>
7.1	Conclusions . . . . .	190
7.2	Suggestions for future work . . . . .	194
<b>A</b>	<b>Derivation of lubrication equations (LUB) for 3D free-surface flow</b>	<b>197</b>
<b>B</b>	<b>Derivation of lubrication equations (LUB) for 2D bilayer channel flow</b>	<b>209</b>
<b>C</b>	<b>Derivation of the depth averaged form (DAF) for channel flow</b>	<b>220</b>
<b>D</b>	<b>Discretisation of the LUB equations</b>	<b>230</b>
D.1	Free-surface bilayer flow . . . . .	230
D.1.1	Spatial discretisation . . . . .	231
D.1.2	Temporal discretisation . . . . .	234
D.2	Channel flow . . . . .	237
D.3	Full weighting restriction and interpolation operators . . . . .	240
<b>E</b>	<b>Lubrication equations for three-dimensional free-surface N-layer thin film flow</b>	<b>242</b>
	<b>Bibliography</b>	<b>249</b>

# List of Figures

1.1	Critical Reynolds number as a function of the mean lower fluid depth $h1$ and viscosity ratio $m$ for two selected values of the density ratio: (a) $\rho = 0.5$ ; (b) $\rho = 0.1$ . Amaouche <i>et al.</i> (2007) . . . . .	18
2.1	Schematic of two-dimensional gravity-driven bilayer flow through a channel (left) and down an inclined substrate (right) inclined at angle $\theta$ to the horizontal, showing the associated geometry and coordinate system for the problem of flow past a trench-like topography.	27
3.1	Staggered mesh arrangement used to solve equation sets based on the DAF. . . . .	67
3.2	Hierarchy of grids showing 3 grid levels ( $\mathcal{G}_0, \mathcal{G}_1$ and $\mathcal{G}_2$ ) with $c = 0$ . . . . .	80
3.3	An illustration os Restriction, R, and Interpolation, I, between grid levels. . . . .	81
3.4	Structure of one multigrid cycle for $\mathcal{K} = 1$ and $\mathcal{K} = 2$ . . . . .	81
3.5	The Full Multigrid, FMG, illustrated for two V-cycles and four grid levels. $u_k^m$ refers to the solution vector on grid level $\mathcal{G}_k$ after performing $m$ FAS V-cycle; $u_0^0$ is the initial solution on the coarsest grid level and $u_k^0$ is the solution on $\mathcal{G}_k$ grid level obtained by FMG interpolation of $u_{k-1}^0$ . . . . .	84

3.6	Mesh dependence of the capillary ridge height for flow over a step-down topography with $h_{10} = 0.5,  s_0  = 0.1, \rho_2 = \mu_2 = 1.0, \theta = 10^\circ$ and $Re = 0$ . . . . .	88
3.7	Convergence history for the problem of Figure 3.6 when the number of grid points on the finest grid level is 1025. . . . .	89
3.8	Comparison of free surface disturbance predicted by LUB and DAF models when $Re = 0$ , for free-surface flow over a trench when $h_0 = 0.4, \rho_2 = \mu_2 = 1,  l_t  = 1.5,  s_0  = 0.1, Ca = 1.167 \times 10^{-4}$ and $\theta = 10^\circ$ . . . . .	90
3.9	Comparison of liquid-liquid interface disturbance predicted by LUB and DAF models when $Re = 0$ for channel flow over a step-down when $h_0=0.4, \rho_2 = \mu_2 = 1.0 \times 10^{-3},  s_0  = 0.1, Ca = 3.33 \times 10^{-4}$ and $\theta = 10^\circ$ . . . . .	91
4.1	Schematic diagram for bilayer flow in a channel containing a step-down (left) and step-up (right) topography. for each problem the flow is from left to right. . . . .	94
4.2	Effect of topography height on the interface profile for flow over a step-down topography when $h_{10} = 0.1, \rho_2 = 0, \mu_2 = 1 \times 10^{-3}$ $Ca = 3.33 \times 10^{-4}; \theta = 90^\circ$ . . . . .	96
4.3	Effect of topography height on the interface profile, for flow over a step-down topography when $h_{10} = 0.1, \rho_2 = 1, \mu_2 = 1, Ca = 3.33 \times 10^{-4}, \theta = 90^\circ$ . . . . .	97
4.4	Effect of topography height on capillary ridge height for flow over a step-down, for $h_{10} = 0.1, Ca = 3.33 \times 10^{-4}, \theta = 90^\circ$ and different combination of upper liquid properties. . . . .	98

4.5	Effect of topography height on capillary ridge height, for flow over a step-down topography when $\rho_2 = \mu_2 = 1$ , $\theta = 90^\circ$ and different values of $h_{10}$ . . . . .	98
4.6	Comparison of current results with those of Lenz and Kumar for flow in channel containing a mound topography given by $ s_0 =0.48$ when $h_{10}=0.5$ , $Ca= 3.33 \times 10^{-4}$ , $\rho_2 = \mu_2 = 1.0$ , $\theta = 90^\circ$ . . . . .	99
4.7	Effect of the normal gravity term on the interface shape for flow through a channel with a step-down of $ s_0  = 0.1$ when $h_{10} = 0.4$ , $Ca= 3.33 \times 10^{-4}$ , $\rho_2 = 1 \times 10^{-3}$ and $\mu_2 = 1.0$ , with: (a) $\theta = 5^\circ$ , (b) $\theta = 10^\circ$ and (c) $\theta = 90^\circ$ ; $Re = 0$ . . . . .	103
4.8	Effect of Reynolds number on the interface shape for flow in a channel with a step-down when $h_{10}=0.4$ , $Ca= 3.33 \times 10^{-4}$ and $\rho_2 = 0$ , $\mu_2 = 1 \times 10^{-3}$ , $\theta = 10^\circ$ , with: (a) $ s_0  = 0.1$ and (b) $ s_0  = 0.4$ . . . . .	104
4.9	Effect of Reynolds number on the interface shape for flow in a channel with a step-down when $h_{10}=0.4$ , $Ca= 3.33 \times 10^{-4}$ and $\rho_2 = \mu_2 = 1.0$ , $\theta = 10^\circ$ , with: (a) $ s_0  = 0.1$ , (b) $ s_0  = 0.4$ and (c) $ s_0  = 0.8$ . . . . .	105
4.10	Lower layer thickness, $h_1$ dependence on $Re$ for flow in a channel with a step-down topography when $h_{10}=0.4$ , $Ca= 3.33 \times 10^{-4}$ , $\rho_2 = \mu_2 = 1.0$ , $ s_0  = 0.1$ , and $\theta = 10^\circ$ . . . . .	106
4.11	The dependence of capillary ridge height on the step height for a step-down when $h_{10} = 0.4$ , $\theta = 10^\circ$ . (a) $\rho_2 = 0$ , $\mu_2 = 1 \times 10^{-3}$ and (b) $\rho_2 = 1$ , $\mu_2 = 1$ . . . . .	107
4.12	The dependence of capillary ridge height on $Re$ for a step-down when when $h_{10}=0.4$ , $Ca= 3.33 \times 10^{-4}$ and $\theta = 10^\circ$ , with: (a) $\rho_2 = 0$ , $\mu_2 = 1 \times 10^{-3}$ and (b) $\rho_2 = 1$ , $\mu_2 = 1$ . . . . .	108

4.13	Pressure gradient profiles for flow in a channel with a step-down of $ s_0  = 0.1$ when $h_{10}=0.4$ , $Ca= 3.33 \times 10^{-4}$ and $\theta = 10^\circ$ ; $\rho_2 = 0$ , $\mu_2 = 1 \times 10^{-3}$ (left), $\rho_2 = \mu_2 = 1$ (right). . . . .	109
4.14	Comparison of interface shape for flow in a channel with a step-down in the absence and presence of inertial effects. $ s_0  = 0.2$ , $Ca= 3.33 \times 10^{-4}$ and $\rho_2 = 1$ , $\mu_2 = 1$ , $\theta = 10^\circ$ and (a) $Re = 0$ and (b) $Re = 150$ . . . . .	110
4.15	Comparison of interface shape for flow in a channel with a step-down in the absence and presence of inertial effects. $ s_0  = 0.2$ , $Ca= 3.33 \times 10^{-4}$ and $\rho_2 = 0$ , $\mu_2 = 1 \times 10^{-3}$ , $\theta = 10^\circ$ and (a) $Re = 0$ and (b) $Re = 150$ . . . . .	112
4.16	Effect of $h_{10}$ on capillary ridge height for flow in a channel with a step-down of $ s_0  = 0.2$ , $Ca= 3.33 \times 10^{-4}$ , $\theta = 10^\circ$ and (a) $\rho_2 = \mu_2 = 1$ and (b) $\rho_2 = 0$ , $\mu_2 = 1 \times 10^{-3}$ . . . . .	113
4.17	Effect of density ratio on the interface shape for flow in a channel with a step-down when $h_{10}=0.4$ , $Ca= 3.33 \times 10^{-4}$ and $\mu_2 = 1.0$ , $\theta = 10^\circ$ with: (a) $Re = 0$ and (b) $Re = 150$ . . . . .	114
4.18	Capillary trough depth for flow situations as in Figure 4.17. . . . .	115
4.19	Effect of Reynolds number on the interface shape for flow in a channel with a step-up when $h_{10}=0.4$ , $Ca= 3.33 \times 10^{-4}$ and $\rho_2 = \mu_2 = 1.0$ , $\theta = 10^\circ$ with: (a) $ s_0  = 0.1$ , (b) $ s_0  = 0.4$ and (c) $ s_0  = 0.8$ . . . . .	116
4.20	Effect of Reynolds number on the interface shape for flow in a channel with a step-up when $h_{10}=0.4$ , $Ca= 3.33 \times 10^{-4}$ and $\rho_2 = 0$ , $\mu_2 = 1 \times 10^{-3}$ , $\theta = 10^\circ$ with: (a) $ s_0  = 0.1$ and (b) $ s_0  = 0.4$ . . . . .	117
4.21	Capillary trough depth of step-up as function of topography height when $h_{10}=0.4$ , $Ca= 3.33 \times 10^{-4}$ , $\theta = 10^\circ$ for two flow configurations: (a) $\rho_2 = 0$ , $\mu_2 = 1 \times 10^{-3}$ and (b) $\rho_2 = 1$ , $\mu_2 = 1$ . . . . .	118

4.22	Capillary trough depth of step-up as function of Reynolds number when $h_{10}=0.4$ , $ s_0  = 0.4$ , $Ca= 3.33 \times 10^{-4}$ , $\theta = 10^\circ$ for two flow configurations: (a) $\rho_2 = 0, \mu_2 = 1 \times 10^{-3}$ and (b) $\rho_2 = 1, \mu_2 = 1$ .	119
4.23	As in Figure 4.6, showing the effect of Reynolds number on interface profile.	120
4.24	Comparison of interface profiles generated by gravity-driven flow, $\theta = 10^\circ$ , and pressure-driven flow in a channel with a step-down given by $ s_0 =0.1$ when $Re = 0$ , $h_{10}=0.4$ , $Ca= 3.33 \times 10^{-4}$ and $\rho_2 = \mu_2 = 1.0$ .	121
4.25	Effect of Reynolds number on the interface shape for pressure-driven flow in a channel with a step-down when $h_{10}=0.4$ , $Ca= 3.33 \times 10^{-4}$ and $\rho_2 = 0.2, \mu_2 = 1, \theta = 0^\circ$ with: (a) $ s_0  = 0.1$ and (b) $ s_0  = 0.8$ .	122
4.26	Effect of Reynolds number on the interface shape for pressure-driven flow in a channel with a step-up when $h_{10}=0.4$ , $Ca= 3.33 \times 10^{-4}$ and $\rho_2 = \mu_2 = 1, \theta = 0^\circ$ with: (a) $ s_0  = 0.1$ and (b) $ s_0  = 0.8$ .	123
4.27	Schematic diagram for bilayer flow in a channel containing a step-down (left) and step-up (right) topography.	124
4.28	Effect of Reynolds number on the interface shape for shear-driven flow in a channel with a step-up when $h_{10}=0.4$ , $Ca= 3.33 \times 10^{-4}$ and $\rho_2 = \mu_2 = 1, \theta = 0^\circ$ with: (a) $ s_0  = 0.1$ and (b) $ s_0  = 0.8$ .	125
4.29	The dependence of capillary ridge height for shear induced flow over a step-down when, $h_{10} = 0.4$ , $Ca= 3.33 \times 10^{-4}$ and $\rho_2 = \mu_2 = 1, \theta = 0^\circ$ with: (a) $ s_0  = 0.1$ and (b) $ s_0  = 0.8$ .	126

4.30	Interface profile for shear-induced flow in a channel with a step-down in the absence and presence of inertial effects. $ s_0  = 0.2$ , $Ca = 3.33 \times 10^{-4}$ , $\rho_2 = \mu_2 = 1$ and several values of $h_{10}$ , $\theta = 0^\circ$ with: (a) $Re = 0$ and (b) $Re = 150$ . . . . .	127
4.31	Capillary ridge as a function of $h_{10}$ for flow situations shown in Figure 4.30 . . . . .	128
4.32	Effect of Reynolds number on the interface shape for shear-driven flow in a channel with a step-up when $h_{10}=0.4$ , $Ca = 3.33 \times 10^{-4}$ and $\rho_2 = \mu_2 = 1$ , $\theta = 0^\circ$ with: (a) $ s_0  = 0.1$ and (b) $ s_0  = 0.8$ . . . .	129
4.33	Capillary ridge depth as a function of step depth $ s_0 $ for flow situations shown in Figure 4.32 . . . . .	130
4.34	Comparison of interface profiles generated by gravity-driven flow and shear-induced flow with $B=12$ in a channel with a step-up given by $ s_0 =0.2$ when $h_{10}=0.4$ and $Ca = 3.33 \times 10^{-4}$ . . . . .	131
5.1	Comparison between DAF predictions of the free surface disturbance when $\rho_2 = \mu_2 = 1$ with the experimental results of Decré and Baret (2003) for flow over a substrate containing topography when $\theta = 30^\circ$ : (a) step-up (height $ s_0  = 0.2$ and $Re = 2.45$ ); (b) step-down (depth $ s_0  = 0.2$ and $Re = 2.45$ ); (c) trench ( $ s_0  = 0.19$ , $l_t = 1.51$ and $Re = 2.84$ ). . . . .	138
5.2	Comparison between DAF predictions of the free surface disturbance when $\rho_2 = \mu_2 = 1$ , $\theta = 30^\circ$ and the numerical results of Veremieiev <i>et al.</i> (2010) for flow over a substrate containing a span-wise (a) step-up and (b) step-down topography when $Re = 15$ and the $ s_0  = 0.2$ . . . . .	139
5.3	As in Figure 5.2 but with $Re = 30$ . . . . .	140

5.4	Influence of density ratio on the free surface shape for different topographical features when $Re = 0$ , $\mu_2 = 1.0$ , $ s_0  = 0.2$ , $h_{10} = 0.5$ and $\theta = 10^\circ$ ; (a) step-up, (b) step-down, (c) trench, $l_t = 1.5$ . . . . .	141
5.5	Influence of density ratio on the liquid-liquid interface for different topographical features when $Re = 0$ , $\mu_2 = 1.0$ , $ s_0  = 0.2$ , $h_{10} = 0.5$ and $\theta = 10^\circ$ ; (a) step-up, (b) step-down, (c) trench, $l_t = 1.5$ . . . . .	142
5.6	Effect of $h_{10}$ on (a) the free surface and (b) the interface disturbance when $Re = 0$ , $\rho_2 = 0.5$ , $\mu_2 = 1.0$ , $ s_0  = 0.2$ and $\theta = 10^\circ$ . . . . .	143
5.7	Influence of viscosity on free surface (top) and interface disturbance (bottom) for step-down (left) and trench (right) topographies when $Re = 0$ , $ s_0  = 0.2$ , $\rho_2 = 1$ , $h_{10} = 0.5$ and $\theta = 10^\circ$ . . . . .	144
5.8	Evolution of the liquid-liquid interface profile when changing the interface height for flow over trench topography when $Re = 0$ , $ s_0  = 0.2$ , $\rho_2 = \mu_2 = 1$ , and $\theta = 10^\circ$ . . . . .	145
5.9	Effect of $Re$ on the (a) free surface and (b) interface profiles for flow over trench topography when $\rho_2 = \mu_2 = 1.0$ , $h_{10} = 0.5$ , $ s_0  = 0.2$ , $l_t = 1.5$ and $\theta = 10^\circ$ . . . . .	147
5.10	Capillary ridge height for flow over trench topography for different combinations of $\rho_2$ and $\mu_2$ when $h_{10} = 0.5$ , $ s_0  = 0.2$ , $l_t = 1.5$ and $\theta = 10^\circ$ . . . . .	148
5.11	Effect of density on free surface shape when $Re = 15$ , $\mu_2 = 1.0$ , $ s_0  = 0.2$ , $h_{10} = 0.5$ and $\theta = 10^\circ$ ; (a) step-up, (b) step-down, (c) trench, $l_t = 1.5$ . . . . .	149
5.12	Effect of density on interface surface shape when when $Re = 15$ , $\mu_2 = 1.0$ , $ s_0  = 0.2$ , $h_{10} = 0.5$ and $\theta = 10^\circ$ ; (a) step-up, (b) step-down, (c) trench, $l_t = 1.5$ . . . . .	150

5.13	Effect of $h_{10}$ on the (a) free surface and (b) interface disturbance for flow over trench topography when $Re = 15$ , $\rho_2 = 0.5$ , $\mu_2 = 1$ , $ s_0  = 0.2$ , $l_t = 1.5$ and $\theta = 10^\circ$ . . . . .	151
5.14	Effect of viscosity on free surface (top) and interface disturbance (bottom) for step-down (left) and trench (right) topographies when $Re = 15$ , $\rho_2 = 1$ , $h_{10} = 0.5$ , $ s_0  = 0.2$ , and $\theta = 10^\circ$ . . . . .	152
5.15	Comparison of free surface and interface disturbance in the presence and absence of inertia for flow over trench topography of $ s_0  = 0.2$ , $l_t = 1.5$ when $\theta = 10^\circ$ for (a) $\mu = 5.0$ and (b) $\mu = 0.5$ . . . . .	153
5.16	Evolution of the liquid-liquid interface profile for flow over trench topography for the single-layer equivalent flow when $\theta = 10^\circ$ and $Re = 15$ . . . . .	154
5.17	Free-surface disturbance for flow over trench topography, $\theta = 30^\circ$ , $l_t = w_t = 1.54$ , $ s_0  = 0.25$ , $Re=0$ . . . . .	157
5.18	Liquid-liquid interface for flow over trench topography, $\theta = 30^\circ$ , $l_t = w_t = 1.54$ , $ s_0  = 0.25$ , $Re=0$ . . . . .	158
5.19	Comparison of predicted streamwise free-surface profile at $y^* = 0$ , $Re = 0$ , with the lubrication approximation result of Gaskell <i>et al.</i> (2004) for flow over a trench of $l_t = w_t = 1.54$ , $ s_0  = 0.25$ when $\theta = 30^\circ$ . . . . .	159
5.20	Free-surface disturbance for flow over trench topography, $Re = 5$ , $\theta = 30^\circ$ , $l_t = w_t = 1.42$ , $ s_0  = 0.197$ , $\rho_2 = \mu_2 = 1$ . . . . .	159
5.21	Liquid-liquid interface disturbance for flow over trench topography, $Re = 5$ , $\theta = 30^\circ$ , $l_t = w_t = 1.42$ , $ s_0  = 0.197$ , $\rho_2 = \mu_2 = 1$ . . . . .	160
5.22	Comparison of predicted streamwise free-surface profile for the flow shown in Figure 5.20 with the results of Veremieiev <i>et al.</i> (2010) at $y^* = 0$ for the. . . . .	160

5.23	Three-dimensional plot for free surface disturbance generated by flow over trench topography, when $\rho_2 = \mu_2 = 0.5$ and $\theta = 10^\circ$ and $l_t = 1.5$ when: (a) $A_t=1$ ; (b) $A_t=5$ ; (c) $A_t=10$ ; (d) $A_t=15$ . . . . .	161
5.24	Effect of topography aspect ratio on (a) streamwise free-surface profiles $y^* = 0$ , and (b) spanwise free-surface profiles along $x^* = 0$ for the flow configurations shown in Figure 5.23 For comparison, the profiles for flow over the corresponding one-dimensional spanwise trench are also given when $\rho_2 = \mu_2 = 0.5$ . . . . .	162
6.1	Types of time-independent non-Newtonian fluid behaviour, Chhabra and Richardson (2011) . . . . .	166
6.2	Comparison of the free-surface disturbance obtained using the LUB model for bilayer non-Newtonian flow, $n_1 = n_2 = 1.0$ , to that of Newtonian fluid over trench topography with $l_t = 1.5$ , $ s_0  = 0.2$ ; $\theta = 10^\circ$ , $Re=0$ . . . . .	183
6.3	Effect of changing the upper liquid layer index, $n_2$ for bilayer flow over trench topography; with $l_t = 1.5$ , $ s_0  = 0.2$ , $\theta = 10^\circ$ , $Re=0$ . . .	184
6.4	Effect of changing the lower liquid layer index, $n_1$ for bilayer flow over trench topography; with $l_t = 1.5$ , $ s_0  = 0.2$ , $\theta = 10^\circ$ , $Re=0$ . . .	184
6.5	Free-surface disturbance generated for different $n_1 - n_2$ combinations for flow over trench topography; with $l_t = 1.5$ , $ s_0  = 0.2$ , $\theta = 10^\circ$ , $Re=0$ . . . . .	185
6.6	Liquid-liquid interface disturbance for different $n_1 - n_2$ combinations for flow over trench topography; with $l_t = 1.5$ , $ s_0  = 0.2$ , $\theta = 10^\circ$ , $Re=0$ . . . . .	185
6.7	Comparison of the free-surface disturbance obtained using the LUB model and the DAF for flow of a power-law fluid, $n = 0.8$ , over trench topography with $l_t = 1.5$ , $ s_0  = 0.2$ ; $\theta = 10^\circ$ , $Re=0$ . . . . .	186

6.8	Comparison of the free-surface disturbance obtained using the LUB model and the DAF for flow of a power-law fluid, $n = 1.2$ , over trench topography with $l_t = 1.5$ , $ s_0  = 0.2$ ; $\theta = 10^\circ$ , $Re=0$ . . . . .	187
6.9	Effect of power-law index on the free-surface disturbance for flow over trench topography with $l_t = 1.5$ , $ s_0  = 0.2$ ; $\theta = 10^\circ$ and $Re = 10$ . . . . .	187
6.10	Effect of Reynolds number on the free-surface disturbance for flow of a power-law fluid, $n = 0.9$ , over trench topography $l_t = 1.5$ , $ s_0  = 0.2$ ; $\theta = 10^\circ$ . . . . .	188
6.11	Effect of Reynolds number on free-surface disturbance for flow of a power-law fluid, $n = 1.1$ , over trench topography with $l_t = 1.5$ , $ s_0  = 0.2$ ; $\theta = 10^\circ$ . . . . .	188
D.1	Collocated mesh arrangement of variables for the LUB model. . . . .	233

# NOMENCLATURE

Below are listed those symbols which have a general meaning. A convention used throughout the thesis is that, unless otherwise stated, quantities in upper case are dimensional while those in lower case are dimensionless. Operators are identified using a mathematical caligraph font, while vectors and tensors are denoted underline and double underline respectively.

## Latin letters

$B$	Dimensionless body force
$Ca$	Capillary number
$C$	Dimensionless constant relating free surface velocity to combined film thickness
$d$	Global defects vector
$F_0, f_0$	Coordinate of substrate / lower channel wall
$F_1, f_1$	Coordinate of interface surface
$F_2, f_2$	Coordinate of free surface / upper channel wall
$f$	Global right-hand-side vector
$\mathcal{F}_i$	Advective operator
$fr_i$	friction term of lower and upper layers $i$ ,
$g$	Standard gravity constant
$\underline{G}$	Acceleration due to gravity
$H_i, h_i$	Thickness of layer $i$
$H_0$	Asymptotic combined film thickness / channel height
$H_{10}, h_{10}$	Asymptotic lower layer thickness
$i$	Subscript denotes the corresponding layer, $i = 1, 2$ for lower and upper layer respectively
$I, J$	Subscript denotes the nodal position of a discrete variable

$\mathbf{I}_{k-1}^k$	Bilinear interpolation operator
$K$	Consistency coefficient for Power-Law liquid
$L_P, W_P, l_p, w_p$	Length and spanwise width of domain
$L_T, W_T, l_t, w_t$	Length and spanwise width of topography
$L_0$	Length scale
$\mathcal{M}^{h_i}, \mathcal{M}^{p_i}, \mathcal{M}^{u_i}, \mathcal{M}^{v_i}$	Operator of averaged mass conservation, pressure, averaged streamwise and spanwise momentum equations
$\mathcal{N}$	Global residual vector
$n$	Power-law index for non-Newtonian Power-Law liquid
$P_i, p_i$	layer $i$ pressure
$P_0, P_A$	Pressure scale and atmospheric pressure
$q_i$	Flow rate of layer $i$
$Q_i, Q_{total}$	Base flow rate of layer $i$ and total rate when interface is flat in the wide part of channel
$\mathbf{R}_k^{k-1}$	Full-weighting restriction operator
$Re$	Reynolds number
$S, s$	Coordinate of topography
$S_0, s_0$	Depth/height of topography
$\underline{\underline{T}}_i$	Viscous stress tensor
$T, t$	Time
$U_i, V_i, W_i, u_i, v_i, w_i$	Components of velocity in Cartesian coordinates
$\underline{U}_i$	Velocity vector
$U_0$	Velocity scale; undisturbed free surface velocity for free-surface flow and average velocity for channel flow
$U_{in}, V_{in}, u_{in}, v_{in}$	Interface velocity
$U_t, u_t$	Velocity of upper of the channel

$\bar{U}_i, \bar{V}_i, \bar{u}_i, \bar{v}_i$	Depth-averaged streamwise and spanwise components of velocity
$\mathbf{v}$	Global corrections vector
$\mathbf{u}$	Global solution vector
$X, Y, Z, x, y, z$	Cartesian coordinates
$X_T, Y_T, x_t, y_t$	Streamwise and spanwise coordinates of centre of topography
$X^*, Y^*, x^*, y^*$	Streamwise and spanwise coordinates shifted to centre of topography

## Greek letters

$\Delta, \delta$	Steepness of topography
$\frac{\Delta P}{\Delta L}, \frac{\Delta p}{\Delta t}$	Imposed pressure gradient in channel flow
$\Delta t$	Time increment
$\Delta x, \Delta y$	Streamwise and spanwise mesh increments
$\varepsilon$	Long-wave ratio
$\theta$	Substrate/channel inclination angle
$\kappa_1, \kappa_2$	Interface and free-surface curvature
$\hat{\mu}_i$	Newtonian dynamic viscosity
$\mu_i$	Ratio of viscosity to lower layer viscosity
$\Pi_{k-1}^k$	Interpolation operator
$\hat{\rho}_i$	Density
$\rho_i$	Ratio of Density to lower layer Density
$\hat{\sigma}_i, \hat{\sigma}_{int}$	Surface tension and interfacial tension
$\sigma_i, \sigma_{int}$	Ratio of Surface tension and interfacial tension to lower layer Surface tension
$\underline{\underline{\tau}}_i$	Dimensionless viscous stress tensor

## **Abbreviations**

DAF	Depth-averaged form
FAS	Full approximation storage
FMG	Full multigrid
HSL	Harwell Subroutine Library
IBL	Integral-boundary-layer approximation
LTE	Local truncation error
LUB	Lubrication equations
N-S	System of Navier-Stokes and continuity equations

# Chapter 1

## Introduction

### Contents

---

<b>1.1</b>	<b>Motivation</b>	<b>2</b>
<b>1.2</b>	<b>Physics of thin film flows</b>	<b>4</b>
<b>1.3</b>	<b>Single Layer Flow over Topography</b>	<b>6</b>
<b>1.4</b>	<b>Bilayer Systems</b>	<b>15</b>
<b>1.5</b>	<b>Thesis outline</b>	<b>21</b>

---

## 1.1 Motivation

Thin liquid film flows appear in many industrial and engineering applications as well as in a variety of natural and biological systems. In industry, numerous manufacturing processes involve the application of thin liquid films on a solid substrate; typical examples are coating operations and the fabrication of electronic components and sensors. In coating processes, several devices have been designed to deposit single or multilayer thin liquid films on a solid - often moving - substrate. These layers are eventually solidified during the drying stage. A successful coating process requires good levelling of the coated layers with minimum disturbance at the free surface itself. This can be achieved by controlling the flow parameters such as the physical properties (density, viscosity and surface tension) of the coating fluid and the coating layer thickness(es). The flow of thin films on flat surfaces has been investigated extensively and the underlying physics is relatively well known, see for example Kistler and Schweizer (1997). A summary of recent relevant research effort in the field is provided by Craster and Matar (2009) in their extensive review.

Thin films flowing on surfaces containing topographic features either desired (man-made) or unwanted (such as scratches or dust particles) are known to feature free surface disturbances, the generation of which can persist over a distance several order of magnitude greater in scale than the topography itself, Stillwagon and Larson (1988); but in general such problems have received far less attention compared to those involving flat substrate. In the coating industry for instance, the need to produce coated layers with a desired thickness, while keeping free surface disturbances to a minimum, highlights the importance of a better understanding of the underlying physics for such flow scenarios. Flow over patterned surfaces occurs, for example, in the manufacture of printed circuits, microdevices, displays etc.,

Decré and Baret (2003), where several thin liquid films are deposited successively, together with the application of photolithography for each layer, Gates *et al.* (2005). Consequently, the thickness and free-surface profile of each layer is influenced by the shape of the previously deposited one. Other applications featuring film flows over surfaces containing topography exist in many technological fields: in particular spanning in chemical engineering, the advantage of thin films being that their thickness is small, which results in large heat- and mass-transfer areas per unit volume, that can be exploited to design efficient process devices such as thin-film heat exchangers, evaporators, condensers, reactors and distillation columns, Focke and Knibbe (1986), Webb (1994) and Helbig *et al.* (2009). Thin film flow is also implemented in: microelectromechanical systems (MEMS) and in the cooling of nanotechnology devices; the fabrication of microfluidic devices, Stone *et al.* (2004) and Squires and Quake (2005); microlithography processes to control film regularity, Ho *et al.* (2004); the fabrication of electrolysis cells, Alekseenko *et al.* (1994), distillation trays, de Santos *et al.* (1991), and liquid-cooled turbine blades, Wilson *et al.* (2001).

Moreover, thin film flow over flat and patterned substrate is important in many biological systems: the corneal liquid film in the eye, Shyy *et al.* (2001); surfactant replacement therapy in preterm newborns as a treatment of respiratory system difficulties, Grotberg (1994, 2001); plant disease control, Walters (2006). On a larger scale thin film flows appear in a range of geophysical phenomena such as glacial, lava, snow avalanche flows and seafloor currents, Ancy (2007), and coastal flows, Helfrich and Melville (2006).

It is clear that the above highlighted importance and range of applications provide strong motivation for continued research in the field of thin film flow and in particular over surfaces containing topographic features.

## 1.2 Physics of thin film flows

Thin liquid films are driven by body forces and/or surface forces in the presence or absence of inertial contributions. Depending on the flow system considered, the degree to which these forces act on a fluid may be promoted or demoted. Inertia is important in cases such as falling films or spin coating, while it can often be neglected in situations where the flow Reynolds number is low, such as in the case of gravity-driven flow down an inclined plane at low speed. Body forces include gravity and centrifugal force; surface forces arise due to surface tension and its variations. The existence of surface tension gradients in a thin liquid film induces shear stresses at the free surface. These stresses can cause the liquid to move from regions of low surface tension to ones of high surface tension and hence produce variations in film thickness. This is called the Marangoni effect and is generated by surface tension variations due to either a thermal gradient (thermocapillarity) or the presence of a surface active agent (surfactant) with nonuniform concentration, Scriven and Sternling (1960).

Surfactants are compounds that accumulate at the surface of a liquid or at the liquid-liquid interface separating liquids in bilayer systems, rather than the bulk liquid, and reduce the surface tension there. Lowering surface tension allows for easier spreading of thin films, Myers (1998). Surfactants are usually used to reduce the occurrence of instabilities related to surface phenomena; however, they may lead to film nonuniformities if not well controlled, Jensen and Grotberg (1993). Disturbances at a free surface due to Marangoni stresses, which may be significant to the extent that they lead to film rupture and dewet, Afsar-Siddiqui *et al.* (2004), are undesirable in situations where uniform thickness is required. On the other hand, these stresses may be exploited in speeding up drying processes, Marra and Huethorst (1991). In

Marangoni drying, alcohol vapour soluble in water is used to generate a concentration gradient across the surface of the wet substrate which gives rise to Marangoni flow and subsequently dries the subjected area, Leenaars *et al.* (1990). This process is used in industry to cleanse integrated circuits and liquid crystal displays, O'Brien (1993).

Curved substrates are also known to affect free surface uniformity: coatings thin at outside corners and thicken at inside ones, Weidner *et al.* (1996). Another cause of free surface nonuniformity is the chemical composition of the substrate. Chemically heterogeneous substrates can cause variation in the wetting pattern depending on the type of heterogeneity, Konnur *et al.* (2000) and Sharma *et al.* (2003).

In addition to thermocapillarity, thermal effect may appear in the variation of physical properties with temperature. Although a temperature gradient across a thin film is generally small enough that physical properties can be evaluated at the average temperature without significant error, the error may be large when liquids of high viscosity are considered as viscosity can vary exponentially with temperature, Oron *et al.* (1997). Reisfeld and Bankoff (1990) found that a heated thin liquid film with a linear dependence of viscosity on temperature has a smaller rupture time compared to the constant viscosity one.

Thin films are also subject to other types of forces such as long-range intermolecular forces (Van der Waals forces) and electrostatic forces. Van der Waals forces are significant in ultrathin films (with thickness  $<100$  nm), Oron *et al.* (1997). This range of thin films is outside the scope of the present work which concentrates on films of several hundreds of microns in height.

Thin film flow is a thriving field of research supported by its increasing importance and applications in science and technology. This has resulted in an enormous amount of literature related to thin films and their behavior. In the following sec-

tions a review of the research effort in the area of thin film flows is presented. The review is limited to articles featuring single-layer film flows over topography and the flow of bilayer films with and without topography.

### **1.3 Single Layer Flow over Topography**

As mentioned above, the flow of thin films over topography has diverse industrial applications. It is also important for the purpose of quality control in coating processes. Among the first attempts to explore the problem of thin film flow over topography theoretically was the work of Pozrikidis and Thoroddsen (1991). They used the boundary element method to solve the governing Stokes equations numerically. Their results showed that the presence of a small particle attached to the surface of an inclined substrate generates variations to the free surface upstream and downstream of the particle. These variations were noticed in the form of a capillary ridge upstream of the topography and a depression downstream of it.

Stillwagon *et al.* (1987) performed a long-wave analysis and experiments to investigate the flow over one-dimensional topography during spin-coating, showing that the levelling of the coating film is driven by capillarity and that levelling depends on viscosity, the thickness of the coated layer and the topography width. The same problem was considered by Stillwagon and Larson (1990) who, conducting a combined experimental and analytical study, succeeded in obtaining a one-dimensional analytical formula for the upstream capillary ridge and its associated downstream exponential decay. For the same spin coating problems, Peurrung and Graves (1991,1993) performed both experimental and numerical studies and found qualitative agreement between the two. Pritchard *et al.* (1992), on the other hand, studied the problem of gravity driven two dimensional thin film flow down an in-

clined plane containing topography, approaching the problem both numerically and experimentally. Their numerical solution was based on a finite element discretisation of the Navier-Stokes equations, using the lubrication approximation, and found to be accurate even in cases of shallow trench topography where lubrication theory is not strictly valid.

Kalliadasis *et al.* (2000) investigated the flow of a thin film down an inclined surface containing a span-wise topographical feature (step-up, step-down, trench and mound). The resulting third-order nonlinear ordinary differential equation for the film thickness was solved as a two-point boundary value problem. Their results showed the flow over a single step-up to be characterised by a depression just upstream of the step while flow over a step-down has two features: a large capillary ridge in advance of the step and a point (the pinch) with a minimum film thickness immediately above the step. They found that for finite topographical features when the width is large enough, the free surface behaves as a combination of two profiles; a step-down followed by a step-up for trenches and the opposite for mounds. For smaller width values the two profiles interact when the exponential tails for the two begin to overlap. The height of the ridge and the pinch are a function of topography depth, width and steepness. It was also found that finite topography width or a significant vertical component of gravity can suppress these effects.

A Green's function formulation was employed to construct analytical solutions for the flow of a thin viscous liquid film over one-dimensional step-up, step-down, trench and mound topographies by Fernandez Parent *et al.* (1998) and Lucea *et al.* (1999). Results were verified via numerical solutions and experimental measurements by the same authors as well as those of Messé and Decré (1997). In a later study Hayes *et al.* (2000) extended this Green's function model to solve the flow over two-dimensional topographies. Different topographies were considered in or-

der to investigate the effects of topography steepness. It was noted that, in general, a rapidly changing topography induces a significant free-surface disturbance while a slowly changing one leads to a more conforming free surface profile. The solutions were verified using the experimental results of Baret and Decré (2000) despite the fact that their analysis is valid for vertically aligned substrate only while in the experiments the substrate was inclined at a fixed angle to the horizontal.

Mazouchi and Homsy (2001) studied the two dimensional viscous flow of thin films over topographic features via Stokes flow solved by boundary element method. Different topographies were considered: trenches and a step-down with different depths and capillary number values. The Stokes equations were written as a set of harmonic and bi-harmonic equations for vorticity and stream function. These equations were converted to integral equations and the boundary integral method used to solve them. Their results showed that, for small capillary number, the free surface developed a ridge and a depression upstream of a step-down and a depression upstream of a step-up, and the amplitudes and locations of these ridges and depressions to be functions of capillary number. Their results are in good agreement with predictions from lubrication theory for small capillary numbers. For the case of large capillary number, they reported discrepancies from the lubrication theory that the free surface conformed to the substrate and the maximum height of the ridge to be exponentially correlated to the capillary number.

Free surface disturbances are not desirable in many industrial applications where a uniform planar surface is required, such as in the coating industry. This has encouraged research into methods of minimizing thin film thickness variations, Stillwagon and Larson (1988 ,1990). The optimal levelling of the capillary ridge which forms during the flow of thin liquid films over a step-down topography, by means of Marangoni stresses was investigated numerically by Gramlich *et al.* (2002). Con-

trolling the Marangoni stresses was achieved by imposing a temperature gradient on the thin film by nonuniform heating of the solid substrate. Two temperature profiles were considered, a rectangular profile and a parabolic one. The governing equation was solved numerically following the method of Kalliadasis *et al.* (2000). Results showed that both rectangular and parabolic temperature profiles were able to reduce the capillary ridge. A reduction in the ridge height by as much as 50% compared with the isothermal case was achieved. It was also found that two- and three-step heaters can reduce the variation in surface height by up to 77%.

It has been shown subsequently that free-surface disturbances can be controlled and if necessary minimised using other means such as appropriate design of the topographical feature, Gaskell *et al.* (2004), Sellier (2008), Heining and Aksel (2009) and Sellier and Panda (2010); employing fluid viscoelasticity, Saprykin *et al.* (2007); using flexible substrate, Matar, Craster and Kumar (2007), Lee *et al.* (2009b); adding surfactants, Pozrikidis (2003); using electrified thin films Tseluiko *et al.* (2008); Veremieiev *et al.* (2012).

Decré and Baret (2003) conducted an experimental study of the flow of thin liquid films over topographies. They studied the flow of water down an inclined surface containing topographical features: a one-dimensional step-up and step-down and two-dimensional square and rectangular trenches. Double-arm phase-stepped interferometry was used in their experiments to measure the free surface profile. Their results, which agree well with previous results for the cases of two-dimensional flow and with the solution of the Green's function problem of Hayes *et al.* (2000) for the three-dimensional case, have emerged to represent a benchmark and valuable data for validating theoretical solutions for the same flow conditions.

Two- and three-dimensional gravity driven thin liquid film flows of Newtonian incompressible fluid with constant density over a non-porous inclined flat surface con-

taining well-defined topography were studied by Gaskell *et al.* (2004). For the two-dimensional flow case, a finite element solution (Bubnov-Galerkin weighted residual) of the Navier-stokes equations was obtained. The nonlinear weighted residual equations were solved using Newtonian iteration coupled to a Frontal solver algorithm. Comparison with the boundary element results of Mazouchi and Homsy (2001) for the case of a full-width trench and with the experimental results of Decré and Baret (2003) for the case of one-dimensional step-up and step-down topographic features showed excellent agreement. For the three-dimensional case, a Full Approximation Storage (FAS), Trottenberg *et al.* (2001) multigrid approach was used to solve the lubrication equations. These were discretised on a square domain using second-order accurate central differences. Results for flow over localized peaks and trenches were generated and compared to the experimental measurements of Decré and Baret (2003) for the case of trenches. Their results were found to agree well with the available experimental data. They also suggested reducing the free surface variations caused by a peak topography by surrounding it with a shallow trench.

Gaskell *et al.* (2006) used the multigrid method to solve the problem of flow of an evaporating gravity-driven thin film over topography in terms of the effects of solvent concentration and topography on the free surface profile by solving the governing of time-dependent lubrication and concentration equations when the viscosity is a function of the concentration change caused by evaporation. They found that localized topography leads to persistent heterogeneities in the composition of the mixture while spanwise topographies have no effect on the composition. The solver has subsequently been refined and improved to solve a variety of flow problem: flow over topography using error controlled automatic mesh refinement, Lee *et al.* (2007); flow past occlusion with automatic mesh refinement and temporal adaptivity, Sellier *et al.* (2009); pesticide droplet spreading, Glass *et al.* (2010);

flow over flexible substrate containing topographical features, Lee *et al.* (2011); rivulet formation, Slade (2013).

The influence of inertia on thin film flow cannot be explored in the framework of lubrication approximation as it is based on the assumption  $Re \approx O(\varepsilon)$ . Among the early attempts to account for inertia in thin film flow was the model developed by Benney (1966). This model, which is often called the long-wave Benney-type-model, is based on perturbation analysis and the expansion of the unknowns in terms of the long-wave parameter,  $\varepsilon$ . The model accounts for inertia in terms of first-order dynamics of the perturbation analysis which imposes the restriction that  $Re = O(1)$ . Several other researchers, for example Lin (1974), Nakaya (1975) and Chang (1986) and more recently Bielarz and Kalliadasis (2003) and Tseluiko *et al.* (2009) have implemented such a model in their work.

To lift the restriction on Reynolds number as it appears in the Benney-type-model, the integral-boundary-layer (IBL) approximation based on the work of Shkadov (1967, 1968) can be employed. This model is derived by averaging the governing equation over the traverse coordinate assuming that the parabolic velocity profile which satisfies the x-momentum equation for zero Reynolds number persist even for non-zero Reynolds numbers. Different versions of the Shkadov IBL model have been proposed by Ruyer-Quil and Manneville (1998, 2000, 2002) and Nguyen and Balakotaiah (2000) based on using higher order polynomials to appropriate the velocity profile and by retaining second order-accurate terms in the long-wave approximation of the Navier-Stokes equations. Amaouche *et al.* (2005) further refined the model proposed by Nguyen and Balakotaiah (2000) by keeping third order-accurate terms in the long-wave approximation and using a polynomial up to eighth order to approximate the velocity profile. Heining *et al.* (2012) used the IBL method, together with Volume Of Fluid (VOF) solutions and complementary experiments,

to investigate the effect of inertia on three-dimensional thin film flow over an undulated surface.

The IBL approximation has also been used to study inertial thin film flow over corrugated surfaces and step topographies by Trifonov (2004) and Saprykin *et al.* (2007), respectively. A depth-averaged form, DAF, of the Navier-Stokes and continuity equations, akin to the IBL method, was proposed by Veremieiev *et al.* (2010) and to investigate three-dimensional gravity-driven inertial thin film flow down an inclined substrate containing topographical features. The DAF, while based on a first-order accurate long-wave approximation, is free from Reynolds number limitations. It is derived by averaging the governing equations across the film and employing the assumption that the parabolic velocity profile occurring when  $Re=0$  persists for non-zero Reynolds number situations. This results in a set of partial differential equations for film thickness, pressure and average velocity which have been solved numerically using an accurate and efficient multigrid solver with automatic time-stepping. The results obtained show that the capillary features are strongly influenced by the presence of inertia. Veremieiev (2011) reported complementary two- and three-dimensional finite element solutions to validate the accuracy of the DAF.

The above mentioned models are based on the long-wave approximation and therefore impose restrictions on the selection of Capillary number, film thickness and topography steepness. These restrictions are avoided if the full Navier-Stokes equations are solved. Analytical solutions to the full Navier-Stokes equations are, more or less, limited to flow over wavy substrate while steep topography problems are treated numerically. Perturbation analyses have been applied successfully to steady two-dimensional thin film flow over wavy substrate by Wang (1981, 1984) and Wierschem *et al.* (2002) and for three-dimensional flows by Wang (2005), Luo and

Pozrikidis (2006, 2007) and Heining (2009). However, they reveal nothing of the eddy structure that occurs within the film itself, as a function of inertia present or the geometry of the substrate undulation, Wierschem *et al.* (2003) and Wierschem and Aksel (2004). The semi-analytical solutions constructed by Scholle *et al.* (2004), Scholle *et al.* (2006) and Scholle and Aksel (2007), however, agree well with the experimental results of Wierschem *et al.* (2003).

For film flow over steep topography, numerical methods such as the boundary element and finite element methods have been used to solve the full Navier-Stokes equations. For example the boundary element method has been used to investigate two-dimensional Stokes flow over topography such as flow over a periodic wall, Pozrikidis (1988) and flow over a spanwise rectangular trench, Mazouchi and Homsy (2001). The flow over a particle adjacent to flat surface investigated by Pozrikidis and Thoroddsen (1991) and Blyth and Pozrikidis (2006) are examples on employing the boundary element method in three-dimensional situations. It has similarly been used to solve three-dimensional gravity-driven flow over a spheroid and around an occlusion Baxter *et al.* (2009) and multiple occlusions Baxter *et al.* (2010).

Finite elements solutions of the full Navier-Stokes equations, on the other hand, have remained restricted almost exclusively to steady two-dimensional problems, due to the high computational requirements. Bontozoglou and Serifi (2008) investigated flow down a vertical wall containing a step topography and found that increasing inertia first amplifies and then suppresses the capillary features. However, the fact that inertial flow over a vertical wall is unstable even for small Reynolds number renders their result unreliable. Other examples involving the use of finite element method for thin film flows are the work of Trifonov (1999), Malamataris and Bontozoglou (1999), Gu *et al.* (2004) and Scholle *et al.* (2008).

Thin films flowing down an inclined flat substrate are prone to inertial instability if the Reynolds number exceeds a certain critical value  $Re_{crit}$ . Benjamin (1957) and Yih (1963) found that the value of  $Re_{crit}$  is a function of the inclination angle according to the relation:

$$Re_{crit} = \frac{5}{4} \cot \theta, \quad (1.1)$$

where  $Re_{crit}$  is defined based on the free surface velocity and  $\theta$  is the inclination angle. This finds support from the experimental investigations of Liu *et al.* (1993) and Liu and Gollub (1993,1994). Numerical investigations of waves at the surface of a flowing film have also been reported, see for example Ramaswamy *et al.* (1996) and Malamataris *et al.* (2002).

When the substrate also exhibits topographical features their influence on stability should be considered together with the effect of inertia. The experimental investigation of Vlachogiannis and Bontozoglou (2002), suggests that the presence of periodic topography broadens the range of  $Re$  values for stable flow which agrees with the finding of the numerical prediction of Trifonov (2007). Argyriadi *et al.* (2006) also demonstrate that the presence of steep corrugation has an stabilising effect on the flow over a step-down topography.

The influence of topography on the stability of thin film flow for the case of steep topography such as a step-down was investigated by Kalliadas and Homsy (2001) and Davis and Troian (2005). They found that the capillary ridge formed downstream of a step topography is surprisingly stable for a wide range of the pertinent parameters due to the pressure gradient induced by the topography at small wavenumbers and by surface tension at high wavenumbers. Recently, D'Alessio *et al.* (2009) employed Floquet–Bloch theory to investigate the influence of substrate topography and surface tension on the stability of gravity-driven isothermal

thin film flow down sinusoidal substrate. The same was used subsequently for non-isothermal film flow, D'Alessio *et al.* (2010). How to extend/apply this work to accommodate the steep topography focussed upon in this thesis is not obvious as it arguably breaks the assumption of smooth topography underpinning their analysis.

Thermocapillary-driven films are subject to Marangoni instability which is caused by variations in the surface tension resulting from temperature changes, Davis (1987). The presence of surfactant, on the other hand, increases  $R_{crit}$  as shown by Blyth and Pozrikidis (2004).

## 1.4 Bilayer Systems

Bilayer thin films occur in a broad class of natural phenomena and are relevant to various fields of engineering, see Stoker (2011) and Han (2012), such as semiconductor devices, the petroleum and plastics industries, chemical reactors, the coating of a colour film which sometimes consists of more than ten different layers. These flows are characterized by the presence of at least one liquid-liquid interface. Bilayer free-surface thin film flow has received much less attention compared to the single-layer case. The majority of published studies on the subject of bilayer thin films deal with stability and dewetting scenarios.

While several studies have been performed to investigate the flow of continuous bilayer free-surface and channel flows, few have considered the presence of surface topography. Dassori *et al.* (1984) performed a perturbation analysis of two-phase flow (three layers) in a channel with sinusoidal periodic walls and found the wavy interface profile to be out of phase with respect to the periodic walls and that instability arises at high viscosity ratios. Two-dimensional steady bilayer flow in a channel containing a topographical feature is investigated in the framework of the

lubrication approximation, by Lenz and Kumar (2007). A single third-order partial differential equation that describes the behaviour of the interface is derived and solved numerically using a finite difference method. They found that density ratio and thickness ratio strongly influence the interface profile while viscosity has a less significant effect. Comparison with equivalent single-layer flow reveals that capillary features can be suppressed under certain flow conditions. More recently, Zhou and Kumar (2012) attempted to extend the work of Lenz and Kumar (2007) by including inertial effects using a diffuse-interface method for transient flow. Their approach was able to simulate flow over step-down but not for step-up topography. They admitted that the reason for this inability is not clear and could be due to the lack of sufficient numerical resolution or due to the choice of initial conditions.

Alba *et al.* (2008) explored the steady gravity-driven bilayer thin film flow emerging out of a channel and flowing down an inclined flat substrate. The density was assumed uniform while viscosity and surface tension were different. The problem was formulated using the model of Shkadov (1967) with an assumed semiparabolic velocity profile. They found that the surface-to-interfacial tension ratio, viscosity ratio and thickness ratio significantly affect the free surface and interface profiles. Khayat and Tian (2009) studied steady bilayer flow in a narrow channel constructed of a moving flat lower wall and stationary, variable height, upper wall. The flow is induced by the translation of the flat wall shearing the lower layer, resembling lubrication flow. The focus of the investigation was on the pressure distribution, as it is the normal force that prevents the two surfaces from coming into contact. The influence of channel topography and viscosity ratio on the pressure distribution is explored showing that for a converging channel and low viscosity ratio the pressure increases everywhere in the channel monotonically with viscosity ratio, reaching a maximum, and decreases afterwards. In contrast, the interface level increases monotonically with viscosity ratio and channel modulation causing considerable

pressure buildup. The work of Alba *et al.* (2008) was revisited by Pandher and Khayat (2011) where a transient version of the problem was solved numerically and a nonlinear stability analysis performed.

In contrast to single-layer films, bilayer films can be unstable even in the absence of inertia. This instability arises due to the existence of an interface and is caused by the discontinuity of fluid properties across it. This type of instability is sometimes called inertialess instability.

The interfacial instability, first identified by Yih (1967), is related to the presence of a solid boundary close to the interface. This was extended to arbitrary densities, viscosities and thickness ratios by Yiantsios and Higgins (1988) who found that viscosity stratification instability can be eliminated by hydrostatic effects. Kao (1965, 1968) first investigated the long-wave stability of gravity-driven bilayer thin films when the two fluids have different viscosity, density and thickness using the long-wave approach used by Yih (1963) for single-layer flow. Two modes of instability were identified: the interface mode and the free-surface mode. It was also found that when the lower layer is less viscous than the upper one the flow becomes unstable even at  $Re = 0$ . The same was concluded by Loewenherz and Lawrence (1989) who further investigated the inertialess instability with their focus being upon the influence of viscosity stratification assuming both fluid are of the same density. Later, Chen (1993) found that this instability can take place at any Reynolds number and surface and interface tensions. Hu *et al.* (2006) found, as expected, that when the heavier fluid is above, the flow is always unstable. Hu *et al.* (2008) extended this finding by considering the nonzero Reynolds number case.

The stability of thin film formed from two immiscible liquids on a horizontal isothermal or heated substrate was considered by Pototsky *et al.* (2005). The problem was solved in the framework of the lubrication approximation. The effects of inter-

molecular interaction on the stability were taken into account. For the purpose of comparison, single layer films were introduced by assuming either the upper or lower layer to be rigid. The results showed that a two-layer thin film is less stable than the corresponding effective single layer film.

Amaouche *et al.* (2007) investigated the stability of two-dimensional gravity-driven flow of two superposed layers of immiscible Newtonian liquids in channels. They extended the weighted residual approach first proposed by Ruyer-Quil and Manneville (2000) for single-layer flows by taking into account second order terms in the long-wave expansion. This allowed them to predict the stability regimes in bilayer channel flow. Their results illustrate the complicated interaction between viscosity ratio and lower layer thickness,  $h_1$ , in determining the stability threshold. Figure 1.1 shows plot for critical Reynolds number,  $R_{crit}$ , for two values of density ratio, 0.5 and 1; it is seen from the figure that  $\cot \theta / R_{crit}$  is always small except when  $h_1$  approaches unity. This indicates that channel flow is more inertially stable than free surface film flow.

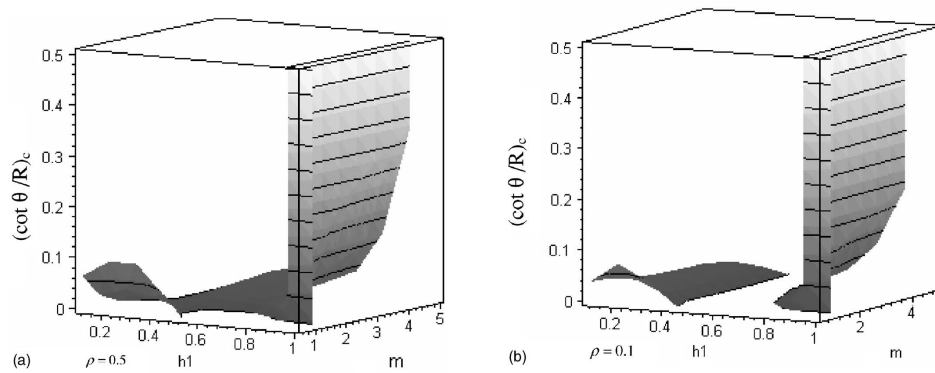


Figure 1.1: Critical Reynolds number as a function of the mean lower fluid depth  $h_1$  and viscosity ratio  $m$  for two selected values of the density ratio: (a)  $\rho = 0.5$ ; (b)  $\rho = 0.1$ . Amaouche *et al.* (2007)

Alba *et al.* (2011) further improved the use of the Shkadov model by implementing the weighted residual approach, first proposed by Amaouche *et al.* (2007), to find

suitable weight functions for depth averaging. They applied this strategy in investigating pressure-gradient-driven transient bilayer flow in a channel. A subsequent perturbation analysis was performed to explore the linear stability of the two-layer system, the main conclusion being that increasing the viscosity of a thicker upper layer destabilises the flow while when the upper layer is more viscous increasing its thickness has a stabilising effect on the flow and that the stability diagram is independent of the Reynolds number.

A large part of the published studies in the context of bilayer thin film flow focusses on issues of dewetting and stability of ultra thin film (thickness  $< 100$  nm). At this scale of layer thickness intermolecular forces become significant and affect the flow dynamics. Ultrathin free surface films on horizontal substrates were first studied via the long-wave approximation by Ruckenstein and Jain (1974). These films may be unstable and dewet due to effective molecular interactions which are introduced into the governing equations in the form of an additional pressure term, the so-called disjoining pressure, which in the simplest case results from the apolar London–van der Waals dispersion forces.

Wang *et al.* (2001) conducted an experimental study for the dewetting of a bilayer thin polymer film and its dependence on film thickness. They concluded that the dewetting time is independent of the thickness for films with a high viscosity lower layer but depends on the thickness of both layers when the viscosity is not high. Kang *et al.* (2003) investigated the dewetting of bilayer thin polymer films. They observed that at first the upper layer dewets the lower one in a way similar to liquid/solid dewetting until dewetting holes merge. This is followed by a partial layer inversion with the upper layer becoming the lower one.

Bandyopadhyay and Sharma (2008) presented a study of the dewetting and morphology of thin liquid bilayer films. They performed a three-dimensional long-wave

nonlinear analysis of the instability caused by Van der Waals forces in ultra thin films. The governing equations were discretised using a finite difference scheme and the resultant set of equations, subject to periodic boundary conditions, solved using Gear's algorithm (NAG library routine D02EJF). They found that thickness, viscosity and surface energy significantly affect the dewetting mode and its final morphology. The same authors, (2010) extended their previous work to account for the instability of thin bilayer films engendered by Van der Waals forces on chemically heterogeneous substrates. Their work showed that thin bilayer films can be used as a means to reproduce or transfer patterns from the lower layer to the free surface and can also be used in the formation of microchannels.

Danov, Paunov, Alleborn, Raszillier and Durst (1998) conducted a stability analysis of horizontal evaporating two-layer thin liquid films based on lubrication theory. A system of equations was derived taking into account the presence of a surfactant soluble in both layers and the evaporation of solvent from the upper layer. A subsequent linear analysis of was performed by Danov, Paunov, Stoyanov, Alleborn, Raszillier and Durst (1998). Marangoni effects, evaporation, surfactant effects, and surface forces effects were studied. The early study was extended by Paunov *et al.* (1998) by performing a non-linear analysis, including the effect of Van der Waals forces. These studies allowed for better understanding of the role of each of the above factors on the stability of thin bilayer films.

The dynamics of a pressure driven bilayer film flow in a channel under high viscosity contrasts was studied by Matar, Lawrence and Sisoiev (2007). They used the lubrication approximation for the high viscosity layer and Karman-Polhausen approximation, Schlichting and Gersten (2000), for the less viscous one. The single equation derived was discretised using a pseudospectral method and the resulting set of nonlinear equations solved using the Newton-Kantorovich method, Argyros

(2007). The results revealed the existence of solution nonuniqueness over certain ranges of the problem parameters.

## 1.5 Thesis outline

The problem of interest in this thesis is the flow of continuous bilayer thin films in the presence of topographical features. The liquid layers are immiscible and two different configurations are considered: free-surface flow down an inclined substrate; confined flow through a channel. As closed form analytical solutions to such problems remain elusive, appropriate mathematical models are developed and the associated governing equation sets solved numerically.

The novelty of the content provided in the thesis focuses in particular on the following aspects:

1. The formulation of a variety of mathematical models based on the long-wave approximation, invoking lubrication theory and deriving depth-averaged forms of the Navier-Stokes and continuity equations.
2. Solution of the governing equation sets resulting from 1., written as appropriate finite difference approximations, using an efficient and accurate multigrid strategy.
3. Exploring, for both flow configurations, the effect of different topography types and flow parameters on the free surface and liquid-liquid interface disturbances that occur when inertia is both neglected and accounted for.
4. A tentative investigation, for the free surface flow configuration, of liquid layers that are non-Newtonian in nature, by deriving governing equation sets

incorporating a Power-law model and solving their discrete finite difference forms using the same multigrid approach.

The thesis has the following structure:

Chapter 2 introduces the flow configurations of interest and provides a rigorous mathematical underpinning to the governing equations used to model them. This involves using the long-wave approximation to reduce the Navier-Stokes and continuity equations to a more numerically tractable form. The dimensionality is reduced by one and two types of equation sets emerge: one encompassing inertia terms, referred to as the depth-averaged form (DAF); the other, valid when inertia effects are neglected, termed the lubrication (LUB) model. Throughout the derivations appropriate scalings are employed. The LUB model follows from the DAF by setting the Reynolds number in the associated equations to zero; alternatively, the LUB model can be derived in its own right from first principles; for completeness a full derivation is provided in Appendix A for both three and two dimensional film flow. The chapter concludes with a generic compact form of the DAF, and attendant boundary conditions, in two-dimensions representing both flow configurations.

Discrete finite difference forms of the governing equation set for the DAF, for the case of three-dimensional film flow, are provided in Chapter 3; the three-dimensional system of equations is purposely considered as it facilitates a more general description of the multigrid strategy adopted and efficient solution methodology employed which requires the use of a staggered grid arrangement of unknowns. The three dimensional equation set for the LUB model is given in Appendix A, while their method of solution, using a collocated grid for the unknowns, is provided in Appendix D. Automatic adaptive time stepping is employed for both equations sets associated with the DAF and LUB model.

A comprehensive set of results for two-dimensional bilayer flow through a chan-

nel containing topography is presented in Chapter 4. The investigation serves two purposes: the first to validate the above mathematical formulations and solution procedures by comparing the results obtained when inertia is neglected with those provided by Lenz and Kumar (2007); the second, to extend the the work of Zhou and Kumar (2012) for such flows with inertia present and to consider other means for driving the flow.

Chapter 5 focuses on solving gravity-driven free-surface film flow down an inclined topographically patterned substrate. The free surface disturbances generated are compared with corresponding experimental data and numerical solutions from the literature where they exist, before moving on to explore the effects of different fluid properties in each layer. In addition, three-dimensional bilayer film flow over localised topography is studied but as a proof of concept only, rather than in a systematic fashion as in the case of its two-dimensional counterpart.

Next it is shown, in Chapter 6, that the problem of free-surface bilayer film flow can be refined to include non-Newtonian liquid behaviour in the form of a Power-law model. For completeness a review is provided of the mathematical models available to describe non-Newtonian fluid behaviour. A governing equation set based on the DAF is derived but it is found that, due to their form, solutions could only be obtained for two limiting cases: (i) bilayer non-Newtonian flow when inertia is neglected; (ii) inertial thin film flow when the two liquids have the same properties (the single-layer-equivalent). The underpinning discrete finite difference equations are provided and results generated for shear-thinning and shear-thickening behaviour.

Finally, conclusions concerning the body of work presented in Chapters 2 to 6 are provided in Chapter 7, together with ideas and suggestions for future work - including, as shown in Appendix E, extension to N-layers for the problem of gravity-driven free surface film flow over topography.

# Chapter 2

## Mathematical model

### Contents

---

<b>2.1</b>	<b>Introduction</b>	<b>25</b>
<b>2.2</b>	<b>Governing equations</b>	<b>26</b>
<b>2.3</b>	<b>Determination of appropriate velocity scalings</b>	<b>36</b>
<b>2.4</b>	<b>Long-wave approximation</b>	<b>40</b>
<b>2.5</b>	<b>Depth-averaged formulation</b>	<b>42</b>
2.5.1	DAF for free-surface flow	42
2.5.2	LUB model for free-surface flow	51
2.5.3	DAF for channel flow	52
2.5.4	LUB for channel flow	54
2.5.5	Compact generic DAF (LUB) equations	55
<b>2.6</b>	<b>Topography definition</b>	<b>56</b>

---

## 2.1 Introduction

Solving thin film fluid flow problems theoretically requires the formulation of an appropriate model followed by the derivation and solution of an accompanying system of governing equations. At present, closed form analytical solutions can be obtained in a small number of cases only and consequently, for the majority of engineering/scientific problems encountered in practice, numerical solution is the only viable alternative. In the case of thin film free-surface and interfacial flows, numerical solutions of the governing full three dimensional Navier-Stokes equations are difficult to obtain as there are several parameters to be considered, and such problems invariably contain one-or-more free boundaries, the location(s) of which is(are) not known *a priori* and has(have) to be obtained as a part of the solution. In addition, high computational memory requirements can prove very challenging and in many cases restrictive. To alleviate these drawbacks, the long wave approximation, Oron *et al.* (1997), can be usefully employed in formulating problems of interest; the main assumption being that the ratio of the undisturbed asymptotic film thickness to that of the characteristic in-plane length scale of the flow is small.

This chapter presents two mathematical formulations for the flow of thin bilayer films, stemming from the long-wave approximation, that are used to model the two flows of interest: a lubrication model (LUB) and a depth-averaged (boundary integral) one (DAF), Veremieiev *et al.* (2010). The LUB model assumes negligible inertia while via the DAF inertia effects can be explored.

## 2.2 Governing equations

The problems of interest in this thesis involve the flow of a bilayer thin liquid film down an inclined substrate and through an enclosed channel, in the presence of surface topography. The two fluids are assumed incompressible, and completely immiscible. Unless stated otherwise, the physical properties of the liquids involved (viscosity, density and surface tension) are assumed constant. Figure 2.1 provides cross-sectional, two-dimensional, schematic diagrams for the two flow configurations investigated. The two-dimensional domain of interest is defined by a Cartesian coordinate system  $(X, Z)$ , with the positive  $X$ -axis in the flow direction and the positive  $Z$ -axis normal to it, as shown. The substrate (or the lower wall in the case of channel flow) contains a topographical feature defined by the function  $Z = S(X)$ , which has a non-zero value at the topography and is zero elsewhere. The length of the topography is  $L_T$  and its depth/height is  $S_0$ . The thickness of the lower layer is  $H_1$  and that of the upper layer is  $H_2$ . The interface separating the two liquids is located at  $H_1 + S$ , while the upper surface (which is either a rigid planer wall, that is stationary or can move with a constant speed  $U_t$ , or a free surface) is located at  $H_2 + H_1 + S$ . The lower layer lies between  $Z = S(X) = F_0(X)$  and the interface  $Z = H_1(X) + S(X) = F_1(X)$ ; the upper layer lies between  $Z = F_1(X)$  and  $Z = H_2(X) + H_1(X) + S(X) = F_2(X)$ . For flow in a channel  $F_2(X) = H_0$ .

The governing equations for the case of Newtonian liquids, in their most general form, for both problems, are the Navier-Stokes and the continuity equations:

$$\hat{\rho}_i \left( \frac{\partial \underline{U}_i}{\partial T} + \underline{U}_i \cdot \nabla \underline{U}_i \right) = -\nabla P_i + \nabla \cdot \underline{\underline{T}}_i + \hat{\rho}_i \underline{\underline{G}}, \quad (2.1)$$

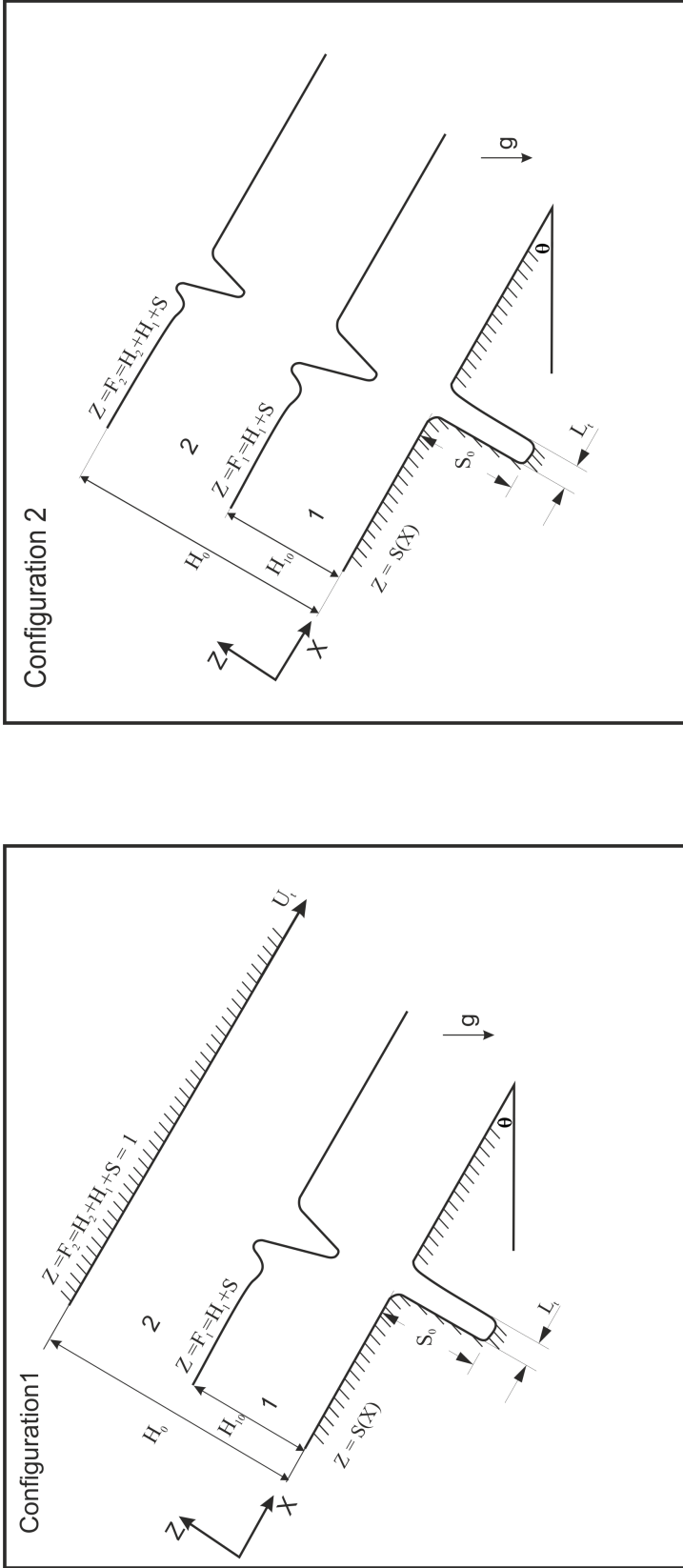


Figure 2.1: Schematic of two-dimensional gravity-driven bilayer flow through a channel (left) and down an inclined substrate (right) inclined at angle  $\theta$  to the horizontal, showing the associated geometry and coordinate system for the problem of flow past a trench-like topography.

$$\nabla \cdot \underline{U}_i = 0. \quad (2.2)$$

The subscript  $i$  denotes the corresponding layer, with  $i = 1$  and  $2$  for the lower and upper layers, respectively. For the case of two dimensional flow:  $\underline{U}_i = (U_i, W_i)$ , where  $U_i, W_i$  are the velocity components in the  $X$  and  $Z$ -direction, respectively;  $P_i$  is the pressure;  $T$  is time;  $\underline{G} = g(\sin\theta, -\cos\theta)$  is the gravitational acceleration, where  $g$  is the standard gravity constant;  $\hat{\rho}_i$  is the density of layer  $i$ . The viscous stress tensor,  $\underline{T}_i = \hat{\mu}_i \left( \nabla \underline{U}_i + (\nabla \underline{U}_i)^T \right)$ , is given by:

$$\underline{T}_i = \hat{\mu}_i \begin{pmatrix} 2\frac{\partial U_i}{\partial X} & \frac{\partial U_i}{\partial Z} + \frac{\partial W_i}{\partial X} \\ \frac{\partial U_i}{\partial Z} + \frac{\partial W_i}{\partial X} & 2\frac{\partial W_i}{\partial Z} \end{pmatrix}, \quad (2.3)$$

where  $\hat{\mu}_i$  is the viscosity of layer  $i$ .

The problem is closed by imposing appropriate initial and boundary conditions. Initially, the interface between the liquid layers and the upper free-surface for film flow down an inclined plate are taken to be flat:

$$H_1|_{T=0} = H_{10} - S, \quad H_2|_{T=0} = H_0 - H_{10}, \quad (2.4)$$

while for channel flow:

$$H_1|_{T=0} = H_{10} - S, \quad (2.5)$$

where  $H_{10}$  is the initial thickness of the lower layer and  $H_0$  is the channel thickness or the undisturbed total asymptotic film thickness for free-surface flow.

The associated boundary conditions are: unidirectional flow at the inlet; no-slip and no-penetration at a liquid-solid interface such that the two velocity components relative to a wall are zero there; at the liquid-liquid interface, kinematic and interface stress boundary conditions apply; at the free surface, kinematic and free-surface stress boundary condition persist. In summary:

At inlet:

$$\begin{aligned} H_1|_{X=0} &= H_{10} && \text{for channel flow,} \\ H_1|_{X=0} &= H_{10}, \quad H_2|_{X=0} = H_0 - H_{10} && \text{for free-surface flow.} \end{aligned} \quad (2.6)$$

At the liquid-solid interface:

$$\begin{aligned} U_1|_{Z=F_0} &= W_1|_{Z=F_0} = 0, \quad U_2|_{Z=F_2} = U_t && \text{for channel flow,} \\ U_1|_{Z=F_0} &= W_1|_{Z=F_0} = 0 && \text{for free-surface flow,} \end{aligned} \quad (2.7)$$

At the liquid-liquid interface and free surface, the kinematic boundary conditions are :

$$\begin{aligned} \frac{\partial F_1}{\partial T} + U_1|_{Z=F_1} \frac{\partial F_1}{\partial X} - W_1|_{Z=F_1} &= 0 && \text{channel and free-surface flow,} \\ \frac{\partial F_2}{\partial T} + U_2|_{Z=F_2} \frac{\partial F_2}{\partial X} - W_2|_{Z=F_2} &= 0 && \text{for free-surface flow.} \end{aligned} \quad (2.8)$$

At the free-surface and liquid-liquid interface the normal and tangential stresses balance and the boundary conditions are thus:

at the liquid-liquid interface for channel and free-surface flow:

$$\begin{aligned} - (P_1 - P_2)|_{Z=F_1} + \left( \underline{T}_1 - \underline{T}_2 \right)|_{Z=F_1} \cdot \underline{n}_1 \cdot \underline{n}_1 &= \hat{\sigma}_{int} k_1 \\ \left( \underline{T}_1 - \underline{T}_2 \right)|_{Z=F_1} \cdot \underline{n}_1 \cdot \underline{t}_1 &= 0, \end{aligned} \quad (2.9)$$

while at the free surface:

$$\begin{aligned} - P_2|_{Z=F_2} + \left( \underline{T}_2 \right)|_{Z=F_2} \cdot \underline{n}_2 \cdot \underline{n}_2 &= \hat{\sigma}_2 k_2 \\ \left( \underline{T}_2 \right)|_{Z=F_2} \cdot \underline{n}_2 \cdot \underline{t}_2 &= 0, \end{aligned}$$

where  $\underline{n}_i = \left( -\frac{\partial F_i}{\partial X}, 1 \right) \cdot \left[ \left( \frac{\partial F_i}{\partial X} \right)^2 + 1 \right]^{-\frac{1}{2}}$  is the unit normal vector pointing outward from surface  $i$ ,  $\underline{t}_i = \left( 1, \frac{\partial F_i}{\partial X} \right) \cdot \left[ \left( \frac{\partial F_i}{\partial X} \right)^2 + 1 \right]^{-\frac{1}{2}}$  is the unit vector tangential to surface  $i$  and  $k_i = -\nabla \cdot \underline{n}_i$  is the curvature of surface  $i$ . The atmospheric pressure is taken as a reference pressure and  $\hat{\sigma}_{int}$  is the interfacial tension at the liquid-liquid interface given, Van Oss *et al.* (1988) and Israelachvili (2011), by:

$$\hat{\sigma}_{int} = \left( \sqrt{\hat{\sigma}_2} - \sqrt{\hat{\sigma}_1} \right)^2, \quad (2.10)$$

where  $\hat{\sigma}_i$  is the coefficient of surface tension of layer  $i$ . The appropriate selection of scaling parameters is important to obtain a set of non-dimensional equations that capture the key feature of the flow problems under consideration.

Following Gaskell *et al.* (2004) and Veremieiev *et al.* (2010), the governing equa-

tions are non-dimensionalised using the following scalings:

$$\begin{aligned} (x, z) &= \left( \frac{X}{L_0}, \frac{Z}{H_0} \right), & (u, w) &= \left( \frac{U}{U_0}, \frac{W}{\varepsilon U_0} \right) \\ t &= \frac{U_0 T}{L_0}, & p &= \frac{P}{P_0}, \quad \text{where } \varepsilon = \frac{H_0}{L_0}. \end{aligned} \quad (2.11)$$

$L_0$  is the in-plane length scale and is proportional to the capillary length, while  $P_0 = \hat{\mu}_1 U_0 L_0 / H_0^2$  is the pressure scale. For the channel flow case,  $H_0$  is the thickness of the channel and  $U_0$  is the average velocity; while in the case of free-surface flow,  $H_0$  is the unperturbed total height and  $U_0$  is the fully developed free surface velocity. In order to find  $U_0$  it is necessary to develop an expression for the fully developed velocity profile of a bilayer flow, this is obtained subsequently in Section 2.3.

Writing equations (2.1) and (2.2) in two dimensions gives:

$$\hat{\rho}_i \left( \frac{\partial U_i}{\partial T} + U_i \frac{\partial U_i}{\partial X} + W_i \frac{\partial U_i}{\partial Z} \right) = -\frac{\partial P_i}{\partial X} + \hat{\mu}_i \left( \frac{\partial^2 U_i}{\partial X^2} + \frac{\partial^2 U_i}{\partial Z^2} \right) + \hat{\rho}_i g \sin \theta, \quad (2.12)$$

$$\hat{\rho}_i \left( \frac{\partial W_i}{\partial T} + U_i \frac{\partial W_i}{\partial X} + W_i \frac{\partial W_i}{\partial Z} \right) = -\frac{\partial P_i}{\partial Z} + \hat{\mu}_i \left( \frac{\partial^2 W_i}{\partial X^2} + \frac{\partial^2 W_i}{\partial Z^2} \right) - \hat{\rho}_i g \cos \theta, \quad (2.13)$$

$$\frac{\partial U_i}{\partial X} + \frac{\partial W_i}{\partial Z} = 0, \quad (2.14)$$

which, on applying the proposed scalings, yields:

$$\begin{aligned} \frac{\varepsilon \hat{\rho}_i U_0^2}{H_0} \left( \frac{\partial u_i}{\partial t} + u_i \frac{\partial u_i}{\partial x} + w_i \frac{\partial u_i}{\partial z} \right) &= -\frac{\varepsilon P_0}{H_0} \frac{\partial p_i}{\partial x} + \\ \frac{\hat{\mu}_i U_0}{H_0^2} \left( \varepsilon^2 \frac{\partial^2 u_i}{\partial x^2} + \frac{\partial^2 u_i}{\partial z^2} \right) &+ \hat{\rho}_i g \sin \theta, \end{aligned} \quad (2.15)$$

$$\begin{aligned} \frac{\varepsilon^3 \hat{\rho}_i U_0^2}{H_0} \left( \frac{\partial w_i}{\partial t} + u_i \frac{\partial w_i}{\partial x} + w_i \frac{\partial w_i}{\partial z} \right) &= -\frac{\varepsilon P_0}{H_0} \frac{\partial p_i}{\partial z} + \\ \frac{\hat{\mu}_i U_0}{H_0^2} \left( \varepsilon^4 \frac{\partial^2 w_i}{\partial x^2} + \varepsilon^2 \frac{\partial^2 w_i}{\partial z^2} \right) &- \hat{\rho}_i g \varepsilon \cos \theta, \end{aligned} \quad (2.16)$$

$$\frac{U_o}{L_o} \frac{\partial u_i}{\partial x} + \frac{\varepsilon U_o}{H_o} \frac{\partial w_i}{\partial z} = 0. \quad (2.17)$$

Dividing both sides of equations (2.15) and (2.16) by  $\frac{\hat{\mu}_1 U_0}{H_0^2}$  results in:

$$\begin{aligned} \varepsilon \rho_i Re \left( \frac{\partial u_i}{\partial t} + u_i \frac{\partial u_i}{\partial x} + w_i \frac{\partial u_i}{\partial z} \right) &= - \left( \frac{P_0}{\frac{\hat{\mu}_1 U_0}{\varepsilon H_0}} \frac{\partial p_i}{\partial x} - \right. \\ \rho_i \frac{\hat{\rho}_1 g H_0^2}{\hat{\mu}_1 U_0} \sin \theta \left. \right) &+ \mu_i \left( \varepsilon^2 \frac{\partial^2 u_i}{\partial x^2} + \frac{\partial^2 u_i}{\partial z^2} \right), \end{aligned} \quad (2.18)$$

$$\begin{aligned} \varepsilon^3 \rho_i Re \left( \frac{\partial w_i}{\partial t} + u_i \frac{\partial w_i}{\partial x} + w_i \frac{\partial w_i}{\partial z} \right) &= - \left( \frac{P_0}{\frac{\hat{\mu}_1 U_0}{\varepsilon H_0}} \frac{\partial p_i}{\partial z} + \right. \\ \rho_i \varepsilon \frac{\hat{\rho}_1 g H_0^2}{\hat{\mu}_1 U_0} \cos \theta \left. \right) &+ \mu_i \left( \varepsilon^4 \frac{\partial^2 w_i}{\partial x^2} + \varepsilon^2 \frac{\partial^2 w_i}{\partial z^2} \right), \end{aligned} \quad (2.19)$$

with,

$$\frac{U_o}{L_o} \left( \frac{\partial u_i}{\partial x} + \frac{\partial w_i}{\partial z} \right) = 0. \quad (2.20)$$

Equations (2.18) to (2.20) can be written in a neater form as:

$$\begin{aligned} \varepsilon \rho_i Re \left( \frac{\partial u_i}{\partial t} + u_i \frac{\partial u_i}{\partial x} + w_i \frac{\partial u_i}{\partial z} \right) = & - \frac{\partial p_i}{\partial x} + \mu_i \varepsilon^2 \frac{\partial^2 u_i}{\partial x^2} \\ & + \mu_i \frac{\partial^2 u_i}{\partial z^2} + \rho_i B \sin \theta, \end{aligned} \quad (2.21)$$

$$\begin{aligned} \varepsilon^3 \rho_i Re \left( \frac{\partial w_i}{\partial t} + u_i \frac{\partial w_i}{\partial x} + w_i \frac{\partial w_i}{\partial z} \right) = & - \frac{\partial p_i}{\partial z} + \mu_i \varepsilon^4 \frac{\partial^2 w_i}{\partial x^2} \\ & + \mu_i \varepsilon^2 \frac{\partial^2 w_i}{\partial z^2} - \rho_i B \varepsilon \cos \theta, \end{aligned} \quad (2.22)$$

$$\frac{\partial u_i}{\partial x} + \frac{\partial w_i}{\partial z} = 0, \quad (2.23)$$

where the Reynolds number  $Re = \frac{\hat{\rho}_1 U_0 H_0}{\hat{\mu}_1}$  with  $B = \frac{2}{C \sin \theta}$  and  $\frac{\hat{\rho}_1 g H_0^2}{\hat{\mu}_1 U_0}$  for free-surface flow and channel flow, respectively, and represents a measure of the gravity force acting in the streamwise direction; C is a constant relating the free-surface velocity to the undisturbed film thickness - as obtained in section 2.3, see equation (2.43). In addition  $\rho_i = \frac{\hat{\rho}_i}{\hat{\rho}_1}$  and  $\mu_i = \frac{\hat{\mu}_i}{\hat{\mu}_1}$ , the ratio of *ith* layer properties to their lower layer counterparts.

The normal vector, tangent vector, surface curvature and dimensionless viscous

stress tensor are given, by:

$$\begin{aligned}
 n_i &= \left( -\varepsilon \frac{\partial f_i}{\partial x}, 1 \right) \cdot \left[ \varepsilon^2 \left( \frac{\partial f_i}{\partial x} \right)^2 + 1 \right]^{-\frac{1}{2}}, \\
 t_i &= \left( 1, \varepsilon \frac{\partial f_i}{\partial x} \right) \cdot \left[ \varepsilon^2 \left( \frac{\partial f_i}{\partial x} \right)^2 + 1 \right]^{-\frac{1}{2}}, \\
 \kappa_i &= \varepsilon^2 \frac{\partial^2 f_1}{\partial x^2} \left[ 1 + \varepsilon^2 \left( \frac{\partial f_1}{\partial x} \right)^2 \right]^{-\frac{3}{2}}, \\
 \underline{\underline{\tau}}_i &= \mu_i \begin{pmatrix} 2\varepsilon \frac{\partial u_i}{\partial x} & \frac{\partial u_i}{\partial z} + \varepsilon^2 \frac{\partial w_i}{\partial x} \\ \frac{\partial u_i}{\partial z} + \varepsilon^2 \frac{\partial w_i}{\partial x} & 2\varepsilon \frac{\partial w_i}{\partial z} \end{pmatrix},
 \end{aligned} \tag{2.24}$$

respectively.

The corresponding boundary conditions are now:

At inlet:

$$\begin{aligned}
 h_1|_{x=0} &= h_{10} && \text{for channel flow,} \\
 h_1|_{x=0} &= h_{10}, \quad h_2|_{x=0} = 1 - h_{10} && \text{for free-surface flow.}
 \end{aligned} \tag{2.25}$$

At the liquid-solid interface:

$$\begin{aligned}
 \mathbf{u}_1|_{z=f_0} &= 0, \quad \mathbf{u}_2|_{z=f_2} = u_t && \text{for channel flow,} \\
 \mathbf{u}_1|_{z=f_0} &= 0 && \text{for free-surface flow.}
 \end{aligned} \tag{2.26}$$

At the liquid-liquid interface and free surfaces, the kinematic boundary conditions are :

$$\begin{aligned}
 \frac{\partial f_1}{\partial t} + u_1|_{z=f_1} \frac{\partial f_1}{\partial x} - w_1|_{z=f_1} &= 0 && \text{channel and free-surface flow,} \\
 \frac{\partial f_2}{\partial t} + u_2|_{z=f_2} \frac{\partial f_2}{\partial x} - w_2|_{z=f_2} &= 0 && \text{for free-surface flow.}
 \end{aligned} \tag{2.27}$$

At the free-surface and liquid-liquid interface the normal and tangential stress boundary conditions are:

$$\begin{aligned}
& - (p_1 - p_2)|_{z=f_1} + 2\varepsilon^2 \mu_1 \left[ \frac{-\frac{\partial u_1}{\partial z} \frac{\partial f_1}{\partial x} + \frac{\partial w_1}{\partial z} + \varepsilon^2 \frac{\partial u_1}{\partial x} \left(\frac{\partial f_1}{\partial x}\right)^2 - \varepsilon^2 \frac{\partial w_1}{\partial x} \frac{\partial f_1}{\partial x}}{1 + \varepsilon^2 \left(\frac{\partial f_1}{\partial x}\right)^2} \right] \Big|_{z=f_1} \\
& - 2\varepsilon^2 \mu_2 \left[ \frac{-\frac{\partial u_2}{\partial z} \frac{\partial f_1}{\partial x} + \frac{\partial w_2}{\partial z} + \varepsilon^2 \frac{\partial u_2}{\partial x} \left(\frac{\partial f_1}{\partial x}\right)^2 - \varepsilon^2 \frac{\partial w_2}{\partial x} \frac{\partial f_1}{\partial x}}{1 + \varepsilon^2 \left(\frac{\partial f_1}{\partial x}\right)^2} \right] \Big|_{z=f_1} = \sigma_{int} \frac{\varepsilon^3}{Ca} \frac{\frac{\partial^2 f_1}{\partial x^2}}{\left(1 + \varepsilon^2 \left(\frac{\partial f_1}{\partial x}\right)^2\right)^{\frac{3}{2}}},
\end{aligned} \tag{2.28}$$

$$\begin{aligned}
& \mu_1 \left\{ \left( \frac{\partial u_1}{\partial z} \right) + \varepsilon^2 \left[ \frac{\partial f_1}{\partial x} \left( -\frac{\partial u_1}{\partial z} \frac{\partial f_1}{\partial x} + 2 \frac{\partial w_1}{\partial z} \right) + \left( -2 \frac{\partial u_1}{\partial x} \frac{\partial f_1}{\partial x} + \frac{\partial w_1}{\partial x} \right) - \varepsilon^2 \frac{\partial w_1}{\partial x} \frac{\partial f_1}{\partial x} \right] \right\} \Big|_{z=f_1} \\
& = \mu_2 \left\{ \left( \frac{\partial u_2}{\partial z} \right) + \varepsilon^2 \left[ \frac{\partial f_1}{\partial x} \left( -\frac{\partial u_2}{\partial z} \frac{\partial f_1}{\partial x} + 2 \frac{\partial w_2}{\partial z} \right) + \left( -2 \frac{\partial u_2}{\partial x} \frac{\partial f_1}{\partial x} + \frac{\partial w_2}{\partial x} \right) - \varepsilon^2 \frac{\partial w_2}{\partial x} \frac{\partial f_1}{\partial x} \right] \right\} \Big|_{z=f_1},
\end{aligned} \tag{2.29}$$

$$\begin{aligned}
& - p_2|_{z=f_2} + 2\varepsilon^2 \mu_2 \left[ \frac{-\frac{\partial u_2}{\partial z} \frac{\partial f_2}{\partial x} + \frac{\partial w_2}{\partial z} + \varepsilon^2 \frac{\partial u_2}{\partial x} \left(\frac{\partial f_2}{\partial x}\right)^2 - \varepsilon^2 \frac{\partial w_2}{\partial x} \frac{\partial f_2}{\partial x}}{1 + \varepsilon^2 \left(\frac{\partial f_2}{\partial x}\right)^2} \right] \Big|_{z=f_2} \\
& = \sigma_2 \frac{\varepsilon^3}{Ca} \frac{\frac{\partial^2 f_2}{\partial x^2}}{\left(1 + \varepsilon^2 \left(\frac{\partial f_2}{\partial x}\right)^2\right)^{\frac{3}{2}}},
\end{aligned} \tag{2.30}$$

$$\mu_2 \left\{ \left( \frac{\partial u_2}{\partial z} \right) + \varepsilon^2 \left[ \frac{\partial f_2}{\partial x} \left( -\frac{\partial u_2}{\partial z} \frac{\partial f_2}{\partial x} + 2 \frac{\partial w_2}{\partial z} \right) + \left( -2 \frac{\partial u_2}{\partial x} \frac{\partial f_2}{\partial x} + \frac{\partial w_2}{\partial x} \right) - \varepsilon^2 \frac{\partial w_2}{\partial x} \frac{\partial f_2}{\partial x} \right] \right\} \Big|_{z=f_2} = 0, \tag{2.31}$$

where  $\sigma_i = \frac{\hat{\sigma}_i}{\hat{\sigma}_1}$ ,  $\sigma_{int} = \frac{\hat{\sigma}_{int}}{\hat{\sigma}_1}$  and  $Ca = \frac{\hat{\mu}_1 U_0}{\hat{\sigma}_1}$  is the capillary number (the ratio of

viscous to surface tension forces).

## 2.3 Determination of appropriate velocity scalings

For steady, fully developed bilayer free-surface film flow, far enough away from a topographical feature, both the interface and the free surface are flat (i.e  $H_1 = H_{10}$  and  $H_2 = H_0 - H_{10}$ ). Noting that pressure is a function of height only,  $\frac{\partial P_i}{\partial X}$  can be eliminated from the Navier-Stokes equation (2.12) which reduces to:

$$\frac{\partial^2 U_i}{\partial Z^2} + \frac{\hat{\rho}_i g \sin \theta}{\hat{\mu}_i} = 0, \quad (2.32)$$

since  $W_i = \frac{\partial W_i}{\partial t} = \frac{\partial W_i}{\partial Z} = 0$  and via the continuity equation, (2.14),  $\frac{\partial U_i}{\partial X} = 0$  and similarly  $\frac{\partial^2 U_i}{\partial X^2}$ . Integrating equation (2.1) twice with respect to  $Z$  for the lower layer yields:

$$U_1 = -\frac{\hat{\rho}_1 g \sin \theta}{\hat{\mu}_1} \frac{Z^2}{2} + C_1 Z + C_2, \quad (2.33)$$

which on applying the no-slip boundary condition at the substrate (at  $Z = 0, U_1 = 0$ ) gives  $C_2 = 0$  and therefore:

$$U_1 = C_1 Z - \frac{\hat{\rho}_1 g \sin \theta}{\hat{\mu}_1} \frac{Z^2}{2}. \quad (2.34)$$

Similarly, for the top layer:

$$\frac{\partial^2 U_2}{\partial Z^2} + \frac{\hat{\rho}_2 g \sin \theta}{\hat{\mu}_2} = 0, \quad (2.35)$$

which on integrating becomes:

$$\frac{\partial U_2}{\partial Z} = -\frac{\hat{\rho}_2 g \sin\theta}{\hat{\mu}_2} Z + C_3; \quad (2.36)$$

applying a zero shear stress condition at the free surface (at  $Z = H_0$ ,  $\frac{\partial U_2}{\partial Z} = 0$ ) gives

$$C_3 = \frac{\hat{\rho}_2 g \sin\theta}{\hat{\mu}_2} H_0 \text{ and thus:}$$

$$\frac{\partial U_2}{\partial Z} = \frac{\hat{\rho}_2 g \sin\theta}{\hat{\mu}_2} (H_0 - Z). \quad (2.37)$$

Integrating equation (2.37) with respect to  $Z$  leads to the following expression for the velocity in the top layer:

$$U_2 = \frac{\hat{\rho}_2 g \sin\theta}{\hat{\mu}_2} \left( H_0 Z - \frac{Z^2}{2} \right) + C_4. \quad (2.38)$$

Continuity of velocity and shear stress at the liquid-liquid interface requires that  $\left( \underline{\underline{T}}_1 - \underline{\underline{T}}_2 \right) \cdot \underline{\underline{n}}_1 = 0$  and  $U_1 = U_2$  at  $Z = H_{10}$ , which when applied to equations (2.34) and (2.38), to find  $C_1$  and  $C_4$ , gives:

$$U_1 = \frac{\hat{\rho}_2 g \sin\theta}{\hat{\mu}_1} (H_0 - H_{10}) Z + \frac{\hat{\rho}_1 g \sin\theta}{\hat{\mu}_1} \left( H_{10} Z - \frac{Z^2}{2} \right), \quad (2.39)$$

and

$$U_2 = \frac{\hat{\rho}_2 g \sin\theta}{\hat{\mu}_2} \left[ H_0 (Z - H_{10}) - \left( \frac{Z^2}{2} - \frac{H_{10}^2}{2} \right) \right] + \frac{\hat{\rho}_2 g \sin\theta}{\hat{\mu}_1} H_{10} (H_0 - H_{10}) + \frac{\hat{\rho}_1 g \sin\theta}{\hat{\mu}_1} \frac{H_{10}^2}{2}. \quad (2.40)$$

The unperturbed free-surface velocity,  $U_0$ , follows from equation (2.40) when  $Z =$

$H_0$ , and is given by :

$$U_0 = \frac{\hat{\rho}_1 g \sin \theta H_0^2}{2\hat{\mu}_1} \left[ \frac{H_{10}^2}{H_0^2} + \frac{\hat{\rho}_2 \hat{\mu}_1}{\hat{\rho}_1 \hat{\mu}_2} \left(1 - \frac{H_{10}}{H_0}\right)^2 + 2 \frac{\hat{\rho}_2}{\hat{\rho}_1} \left(1 - \frac{H_{10}}{H_0}\right) \frac{H_{10}}{H_0} \right], \quad (2.41)$$

which can be expressed as:

$$U_0 = C \frac{\hat{\rho}_1 g \sin \theta H_0^2}{2\hat{\mu}_1}, \quad (2.42)$$

where

$$C = h_{10}^2 + \frac{\rho_2}{\mu_2} (1 - h_{10})^2 + 2\rho_2 h_{10} (1 - h_{10}). \quad (2.43)$$

In the above expression,  $h_{10}$  is the dimensionless version of  $H_{10}$  ( $= \frac{H_{10}}{H_0}$ ). It can be seen from equation (2.43) that when  $\rho_2 = \mu_2 = 1$  the constant  $C$  becomes unity such that equation (2.42) then represents the classic Nusselt solution for the flow of a single layer film down an incline, Spurk and Aksel (2008).

The velocity profiles for both layers, (2.39) and (2.40), can now be written in non-dimensional form, via equation (2.42), namely:

$$u_1 = \frac{U_1}{U_0} = \frac{1}{\mu_1 C} \left( 2\rho_2 (1 - h_{10})z + 2\rho_1 \left( h_{10}z - \frac{z^2}{2} \right) \right), \quad (2.44)$$

$$u_2 = \frac{U_2}{U_0} = \frac{1}{C} \left( \frac{\rho_2}{\mu_2} \left( z - h_{10} - \frac{z^2}{2} + \frac{h_{10}^2}{2} \right) + 2 \frac{\rho_1}{\mu_2} h_{10} (1 - h_{10}) + 2 \frac{\rho_1}{\mu_2} h_{10}^2 \right). \quad (2.45)$$

The average velocities,  $\bar{u}_1$ , and  $\bar{u}_2$ , for the lower and upper layers, respectively, are

derived by averaging the right-hand-sides of expressions (2.44) and (2.45), that is:

$$\bar{U}_i = \frac{1}{H_i} \int_{F_{i-1}}^{F_i} U_i dZ = \frac{1}{h_i} \int_{f_{i-1}}^{f_i} U_i dz. \quad (2.46)$$

So, for the lower layer:

$$\begin{aligned} \bar{u}_1 &= \frac{\bar{U}_1}{U_0} = \frac{1}{\mu_1 h_1 C} \int_0^{h_{10}} \left( 2\rho_2(1-h_{10})z + 2\rho_1(h_{10}z - \frac{z^2}{2}) \right) dz \\ &= \frac{1}{\mu_1 C} \left( \rho_2(1-h_{10})h_{10} + \frac{2}{3}\rho_1 h_{10}^2 \right), \end{aligned} \quad (2.47)$$

while for the upper layer:

$$\begin{aligned} \bar{u}_2 &= \frac{\bar{U}_2}{U_0} = \frac{1}{(1-h_{10})C} \int_{h_{10}}^1 \left( 2\frac{\rho_2}{\mu_2} \left( z - h_{10} - \frac{z^2}{2} + \frac{h_{10}^2}{2} \right) + 2\frac{\rho_2}{\mu_1} (1-h_{10})h_{10} + 2\frac{\rho_1}{\mu_1} \frac{h_{10}^2}{2} \right) dz \\ &= \frac{1}{C} \left( \frac{\rho_1}{\mu_1} h_{10}^2 + \frac{2}{3} \frac{\rho_2}{\mu_2} (1-h_{10})^2 + 2\frac{\rho_2}{\mu_1} (1-h_{10})h_{10} \right). \end{aligned} \quad (2.48)$$

Similar steps and argument lead to the following expression for the average velocity for bilayer film flow through a channel; the details are omitted here but can be found in Appendix B. Accordingly :

$$U_0 = \left( \alpha + \frac{\beta}{\mu_2} \right) \frac{H_0^2}{\hat{\mu}_1} \frac{\Delta P}{\Delta L} - \left( \alpha + \frac{\beta \rho_2}{\mu_2} \right) \frac{\hat{\rho}_1 g \sin \theta H_0^2}{\hat{\mu}_1} + \gamma U_t, \quad (2.49)$$

with

$$\alpha = \frac{\mu_2 h_{10}^2 - (1-h_{10})^2}{4(\mu_2 h_{10} + 1 - h_{10})} h_{10}^2 - \frac{h_{10}^3}{3}, \quad (2.50)$$

$$\beta = \frac{\mu_2 h_{10}^3}{2} - \frac{(h_{10} + 2)(1-h_{10})^2}{6} + \frac{1}{2} \frac{\mu_2 h_{10}^2 - (1-h_{10})^2}{\mu_2 h_{10} + 1 - h_{10}} \left( \frac{h_{10}^2 - 1}{2} - \mu_2 h_{10}^2 \right), \quad (2.51)$$

and

$$\gamma = \frac{\mu_2 h_{10}^2 - (1 - h_{10})^2}{2(\mu_2 h_{10} + 1 - h_{10})} + (1 - h_{10}); \quad (2.52)$$

where  $\frac{\Delta P}{\Delta L}$  is the imposed pressure gradient.

Unlike the case of flow involving a single liquid layer, it is not possible, Lenz and Kumar (2007), to express the capillary length as a function of  $H_0$  and  $Ca$ . For a single layer,  $L_0$  is given by  $\frac{H_0}{(Ca)^{\frac{1}{3}}}$  and  $\frac{H_0}{(6Ca)^{\frac{1}{3}}}$ , for channel and thin film flow configurations, respectively, Decré and Baret (2003) and Gaskell *et al.* (2004). It is assumed therefore that the capillary length for the bilayer problems under investigation can be specified in the same way without loss of generality.

## 2.4 Long-wave approximation

The long-wave approximation, Oron *et al.* (1997), is based on the presence of a disparity between the length scales of the flow in the direction of flow and normal to it, in that there exists a small long-wave ratio  $\varepsilon = H_0/L_0 \ll 1$  such that terms of order  $O(\varepsilon^2)$  can be neglected. This fact is exploited to simplify equations (2.21) to (2.23) and reduce the dimensionality of the problem by one.

Applying the long-wave approximation to equations (2.21) to (2.23), by omitting terms of  $O(\varepsilon^2)$  and higher, leads to:

$$\varepsilon \rho_i Re \left( \frac{\partial u_i}{\partial t} + u_i \frac{\partial u_i}{\partial x} + w_i \frac{\partial u_i}{\partial z} \right) = - \left( \frac{\partial p_i}{\partial x} - \rho_i B \sin \theta \right) + \mu_i \frac{\partial^2 u_i}{\partial z^2}, \quad (2.53)$$

$$\frac{\partial p_i}{\partial z} + \rho_i B \varepsilon \cos \theta = 0, \quad (2.54)$$

$$\frac{\partial u_i}{\partial x} + \frac{\partial w_i}{\partial z} = 0, \quad (2.55)$$

with the associated boundary conditions becoming:

For free-surface flow

$$h_1|_{x=0} = h_{10}, \quad h_2|_{x=0} = h_0, \quad (2.56)$$

$$\mathbf{u}_1|_{z=f_0} = 0, \quad (2.57)$$

$$\frac{\partial f_1}{\partial t} + u_1|_{z=f_1} \frac{\partial f_1}{\partial x} - w_1|_{z=f_1} = 0, \quad (2.58)$$

$$\frac{\partial f_2}{\partial t} + u_2|_{z=f_2} \frac{\partial f_2}{\partial x} + w_2|_{z=f_2} = 0,$$

$$\mu_1 \frac{\partial u_1}{\partial z}|_{z=f_1} = \mu_2 \frac{\partial u_2}{\partial z}|_{z=f_1}, \quad (2.59)$$

$$\mu_2 \frac{\partial u_2}{\partial z}|_{z=f_2} = 0,$$

$$(p_1 - p_2)|_{z=f_1} = -\sigma_{int} \frac{\varepsilon^3}{Ca} \frac{\partial^2 f_1}{\partial x^2}, \quad (2.60)$$

$$p_2|_{z=f_2} - p_A = -\sigma_2 \frac{\varepsilon^3}{Ca} \frac{\partial^2 f_2}{\partial x^2}.$$

For channel flow

$$h_1|_{x=0} = h_{10}, \quad (2.61)$$

$$\mathbf{u}_1|_{z=f_0} = 0, \quad \mathbf{u}_2|_{z=f_2} = \mathbf{u}_t, \quad (2.62)$$

$$\frac{\partial f_1}{\partial t} + u_1|_{z=f_1} \frac{\partial f_1}{\partial x} - w_1|_{z=f_1} = 0, \quad (2.63)$$

$$\mu_1 \frac{\partial u_1}{\partial z}|_{z=f_1} = \mu_2 \frac{\partial u_2}{\partial z}|_{z=f_1}, \quad (2.64)$$

$$(p_1 - p_2)|_{z=f_1} = -\frac{\varepsilon^3}{Ca} \frac{\partial^2 f_1}{\partial x^2}. \quad (2.65)$$

Although the long-wave approximation simplifies the set of governing equations, its range of applicability is restricted :  $Ca \sim O(\varepsilon^3) \ll 1$  ( since  $\varepsilon^3/Ca \sim O(1)$  the capillary pressure terms in equations (2.60) and (2.65) are non-zero); for free-surface flow over peak topography the height of the latter must be much smaller than the undisturbed film thickness, Gaskell *et al.* (2004).

## 2.5 Depth-averaged formulation

### 2.5.1 DAF for free-surface flow

Although the long-wave approximation reduces the complexity of the original governing equations, further simplification is needed in order to solve them. The common approach used to tackle thin film problems is the lubrication approximation which assumes the flow is slow enough that the Reynolds number is  $O(\varepsilon)$  and in such cases the right hand side of equation (2.53) can be set to zero. The lubrication model (LUB) has been shown to yield accurate results in situations where inertial contributions are minimal, Mazouchi and Homsy (2001), Decré and Baret (2003) and Gaskell *et al.* (2004). When this is not the case an alternative approach is needed. One option is the long-wave Benney type model, stemming from the work of Benney (1966). It is based on a perturbation analysis and expansion of the unknowns of the problem in terms of a small long-wave parameter. This model is applicable for flow with  $Re \sim O(1)$ , with inertia taken into account in terms of the first-order dynamics of the perturbation analysis only. An alternative to the Benney-type model which lifts the above limiting restriction on  $Re$ , is the integral-boundary-layer (IBL) approximation characterised by the assumption of a parabolic velocity profile across the liquid layer. The IBL method can be traced back to Shkadov (1967, 1968), who used it to simulate solitary waves in a thin viscous liquid layer on a uniform vertically aligned surface. Since then, various other versions have appeared and been used by Ruyer-Quil and Manneville(1998, 2000, 2002) , Nguyen and Balakotaiah (2000) and Amaouche *et al.* (2005) to tackle different thin film problems.

Depth-averaging the Navier-Stokes and continuity equations, Veremieiev *et al.* (2010),

a method akin to the IBL approximation, is employed in the present work, enabling inertia effects to be accounted for within the long-wave approximation framework. This depth-averaged form (DAF) is free from the zero Reynolds number limitation imposed by the lubrication approximation, but shares the same restriction as the IBL method, in that the velocity across the film is assumed to have a self-similar quadratic profile.

Integrating equation (2.54) with respect to  $z$  for the layer  $i$  from  $z$  to  $f_i$  :

$$\int_z^{f_i} \left( \frac{\partial p_i}{\partial z} + \rho_i B \varepsilon \cos \theta \right) dz = 0, \quad (2.66)$$

yields:

$$p_i = p_{i|z=f_i} + \rho_i B \varepsilon \cos \theta (f_i - z). \quad (2.67)$$

Applying the pressure boundary condition (2.60) to equation (2.67) gives:

$$p_2 = -\frac{\varepsilon^3}{Ca} \sigma_2 \nabla^2 f_2 + \frac{2\rho_2 \varepsilon \cot \theta}{C} (f_2 - z) + p_A, \quad (2.68)$$

and

$$p_1 = p_{1|z=f_1} + \frac{2\rho_1 \varepsilon \cot \theta}{C} (f_1 - z) = p_{2|z=f_1} - \frac{\varepsilon^3}{Ca} \sigma_{int} \nabla^2 f_1 + \frac{2\rho_1 \varepsilon \cot \theta}{C} (f_1 - z) + p_A, \quad (2.69)$$

or

$$p_1 = -\frac{\varepsilon^3}{Ca} \left( \sigma_{int} \nabla^2 f_1 + \sigma_2 \nabla^2 f_2 \right) + \frac{2\varepsilon \cot \theta}{C} [\rho_1 (f_1 - z) + \rho_2 (f_2 - f_1)] + p_A. \quad (2.70)$$

Equation (2.53) depends on the pressure derivative with respect to  $x$  rather than

the pressure itself. This allows z-dependent terms in the pressure equations to be dropped, giving, after setting  $p_A$  to zero:

$$p_1 = -\frac{\varepsilon^3}{Ca} (\sigma_{int} \nabla^2 f_1 + \sigma_2 \nabla^2 f_2) + \frac{2\varepsilon}{C} [\rho_1 f_1 + \rho_2 (f_2 - f_1)] \cot \theta, \quad (2.71)$$

and

$$p_2 = -\frac{\varepsilon^3}{Ca} \sigma_2 \nabla^2 f_2 + \frac{2\rho_2 \varepsilon}{C} f_2 \cot \theta. \quad (2.72)$$

Integrating the continuity equation (2.55) using Leibniz's rule, and applying the boundary conditions (2.57) and (2.58) leads to:

$$\begin{aligned} \int_{f_{i-1}}^{f_i} \left( \frac{\partial u_i}{\partial x} + \frac{\partial w_i}{\partial z} \right) dz &= \frac{\partial}{\partial x} \left( \int_{f_{i-1}}^{f_i} u_i dz \right) - u_i|_{z=f_i} \frac{\partial f_i}{\partial x} + u_i|_{z=f_{i-1}} \frac{\partial f_{i-1}}{\partial x} \\ &+ w_i|_{z=f_i} - w_i|_{z=f_{i-1}} = 0, \end{aligned}$$

and results in the following depth-averaged form of the mass conservation equation:

$$\frac{\partial h_i}{\partial t} + \frac{\partial (h_i \bar{u}_i)}{\partial x} = 0. \quad (2.73)$$

To obtain the depth average form of the u-momentum equation, equation (2.53) is integrated with respect to  $z$  from  $f_{i-1}$  to  $f_i$ , namely:

$$\rho_i \varepsilon Re \int_{f_{i-1}}^{f_i} \left[ \frac{\partial u_i}{\partial t} + u_i \frac{\partial u_i}{\partial x} + w_i \frac{\partial u_i}{\partial z} \right] dz = \int_{f_{i-1}}^{f_i} \left( -\frac{\partial p_i}{\partial x} + \frac{2\rho_i}{C} + \mu_i \frac{\partial^2 u_i}{\partial z^2} \right) dz, \quad (2.74)$$

where the:

$$\text{RHS} = \left( -\frac{\partial p_i}{\partial x} + \frac{2\rho_i}{C} \right) h_i + \mu_i \left( \frac{\partial u_i}{\partial z} \Big|_{z=f_i} - \frac{\partial u_i}{\partial z} \Big|_{z=f_{i-1}} \right), \quad (2.75)$$

and the:

$$\text{LHS} = \rho_i \varepsilon \text{Re} \int_{f_{i-1}}^{f_i} \left[ \frac{\partial u_i}{\partial t} + u_i \frac{\partial u_i}{\partial x} + w_i \frac{\partial u_i}{\partial z} \right] dz = \rho_i \varepsilon \text{Re} \int_{f_{i-1}}^{f_i} \left[ \frac{\partial u_i}{\partial t} + \frac{\partial u_i^2}{\partial x} + \frac{\partial u_i w_i}{\partial z} \right] dz. \quad (2.76)$$

Because  $\frac{\partial u_i}{\partial x} + \frac{\partial w_i}{\partial z} = 0$  and using Leibniz's rule, this gives:

$$\begin{aligned} \text{LHS} &= \rho_i \varepsilon \text{Re} \left[ \frac{\partial}{\partial t} \int_{f_{i-1}}^{f_i} u_i dz + \frac{\partial}{\partial x} \int_{f_{i-1}}^{f_i} u_i^2 dz + \left( \frac{\partial f_{i-1}}{\partial t} u_i \Big|_{z=f_{i-1}} + \right. \right. \\ &\quad \left. \left. \frac{\partial f_{i-1}}{\partial x} u_i^2 \Big|_{z=f_{i-1}} - (u_i w_i) \Big|_{z=f_{i-1}} \right) - \left( \frac{\partial f_i}{\partial t} u_i \Big|_{z=f_i} + \frac{\partial f_i}{\partial x} u_i^2 \Big|_{z=f_i} - (u_i w_i) \Big|_{z=f_i} \right) \right] \\ &= \rho_i \varepsilon \text{Re} \left( \frac{\partial}{\partial t} \int_{f_{i-1}}^{f_i} u_i dz + \frac{\partial}{\partial x} \int_{f_{i-1}}^{f_i} u_i^2 dz \right), \end{aligned} \quad (2.77)$$

where:

$$\frac{\partial f_i}{\partial t} + \frac{\partial f_i}{\partial x} u_i \Big|_{z=f_i} - w_i \Big|_{z=f_i} = 0, \quad (2.78)$$

and finally:

$$\begin{aligned}
LHS &= \rho_i \varepsilon Re \left[ \frac{\partial}{\partial t} (h_i \bar{u}_i) + \frac{\partial}{\partial x} \int_{f_{i-1}}^{f_i} \bar{u}_i^2 dz + \frac{\partial}{\partial x} \int_{f_{i-1}}^{f_i} (\bar{u}_i - u_i)^2 dz \right] \\
&= \rho_i \varepsilon Re \left[ \frac{\partial}{\partial t} (h_i \bar{u}_i) + \frac{\partial}{\partial x} (h_i \bar{u}_i^2) + \frac{\partial}{\partial x} \int_{f_{i-1}}^{f_i} (\bar{u}_i - u_i)^2 dz \right] \\
&= \rho_i \varepsilon Re \left[ h_i \frac{\partial \bar{u}_i}{\partial t} + \bar{u}_i \frac{\partial h_i}{\partial t} + \bar{u}_i \frac{\partial (h_i \bar{u}_i)}{\partial x} + h_i \bar{u}_i \frac{\partial \bar{u}_i}{\partial x} + \frac{\partial}{\partial x} \int_{f_{i-1}}^{f_i} (\bar{u}_i - u_i)^2 dz \right].
\end{aligned} \tag{2.79}$$

Equation (2.79) can be simplified using relation (2.73), to give:

$$LHS = \rho_i \varepsilon Re \left[ h_i \frac{\partial \bar{u}_i}{\partial t} + h_i \bar{u}_i \frac{\partial \bar{u}_i}{\partial x} + \frac{\partial}{\partial x} \int_{f_{i-1}}^{f_i} (\bar{u}_i - u_i)^2 dz \right]. \tag{2.80}$$

Substituting (2.75) and (2.80) into (2.74) gives:

$$\begin{aligned}
&\rho_i \varepsilon Re \left[ h_i \frac{\partial \bar{u}_i}{\partial t} + h_i \bar{u}_i \frac{\partial \bar{u}_i}{\partial x} + \frac{\partial}{\partial x} \int_{f_{i-1}}^{f_i} (\bar{u}_i - u_i)^2 dz \right] \\
&= \left( -\frac{\partial p_i}{\partial x} + \frac{2\rho_i}{C} \right) h_i + \mu_i \left( \frac{\partial u_i}{\partial z} \Big|_{z=f_i} - \frac{\partial u_i}{\partial z} \Big|_{z=f_{i-1}} \right).
\end{aligned} \tag{2.81}$$

Equations (2.71), and (2.72), (2.73) and (2.81) represent the necessary equation set to be solved in order to obtain both the liquid-liquid interface and the free surface location. The problem is closed by specifying the inflow and assuming fully developed flow far upstream and downstream of the topography. The inflow averaged velocities, as given by equations (2.47) and (2.48), are:

$$\begin{aligned}
\bar{u}_1|_{x=0} &= \frac{\rho_2 h_{10}(1 - h_{10}) + \frac{2}{3} \rho_1 h_{10}^2}{\mu_1 C}, \\
\bar{u}_2|_{x=0} &= \frac{2\rho_2 h_{10}(1 - h_{10})}{\mu_1 C} + \frac{\rho_1 h_{10}^2}{\mu_1 C} + \frac{2}{3} \frac{\rho_2(1 - h_{10})^2}{\mu_2 C}, \\
\frac{\partial \bar{u}_i}{\partial x} \Big|_{x=l_s} &= 0,
\end{aligned} \tag{2.82}$$

while the inlet heights are:

$$h_1|_{x=0} = h_{10}, \quad h_2|_{x=0} = 1 - h_{10}, \quad (2.83)$$

and for fully developed flow far downstream:

$$\left. \frac{\partial h_i}{\partial x} \right|_{x=l} = \left. \frac{\partial p_i}{\partial x} \right|_{x=l} = 0, \quad (2.84)$$

where  $l_s$  is the length of the substrate.

Knowledge of velocity profile within the liquid layers is required to determine the dispersion,  $\int_{f_{i-1}}^{f_i} (\bar{u}_i - u_i)^2 dz$ , and the friction,  $\left. \frac{\partial u_i}{\partial z} \right|_{z=f_i}$ , terms in equation (2.81). To overcome this obstacle uni-directional flow based on a self-similar quadratic velocity profile is assumed. For flow over trench and peak topography, provided in the case of the latter the feature is a simple configuration that does not give rise to an enclosed eddy, this assumption has been shown to yield accurate solutions, Veremieiev (2011).

The approach followed is that of Veremieiev *et al.* (2010) as used for single layer free-surface flow and which has been shown able to produce accurate results when compared with experimental and other corresponding numerical results. This assumption results in a velocity profile across the layers of the form:

$$u_1 = 3 (u_{int} - 2\bar{u}_1) \xi_1^2 + 2 (3\bar{u}_1 - u_{int}) \xi_1, \quad (2.85)$$

and

$$u_2 = u_{int} + 3 (u_{int} - \bar{u}_2) \left( \frac{\xi_2^2}{2} - \xi_2 \right), \quad (2.86)$$

where  $\xi_1 = \frac{z-s}{h_1}$  and  $\xi_2 = \frac{z-h_1-s}{h_2}$ ; with the velocity at the liquid-liquid interface,  $u_{int}$ , calculated from:

$$u_{int} = \frac{6\bar{u}_1 h_2 + 3\frac{\mu_2}{\mu_1}\bar{u}_2 h_1}{4h_2 + 3\frac{\mu_2}{\mu_1}h_1}, \quad (2.87)$$

Using the above velocity profiles the friction terms become:

$$\mu_1 \left( \frac{\partial u_1}{\partial z} \Big|_{z=f_1} - \frac{\partial u_1}{\partial z} \Big|_{z=f_0} \right) = 6\mu_1 \frac{u_{int} - 2\bar{u}_1}{h_1}, \quad (2.88)$$

and

$$\mu_2 \left( \frac{\partial u_2}{\partial z} \Big|_{z=f_2} - \frac{\partial u_2}{\partial z} \Big|_{z=f_1} \right) = 3\mu_2 \frac{u_{int} - \bar{u}_2}{h_2}. \quad (2.89)$$

The corresponding dispersion term for the lower layer is given by:

$$\int_{f_0}^{f_1} (\bar{u}_1 - u_1)^2 dz = \int_{f_0}^{f_1} (\bar{u}_1^2 - 2\bar{u}_1 u_1 + u_1^2) dz = \int_{f_0}^{f_1} u_1^2 dz - h_1 \bar{u}_1^2, \quad (2.90)$$

with  $u_1^2$  in equation (2.90) given by:

$$\begin{aligned} u_1^2 &= \left( 3(u_{int} - 2\bar{u}_1) \xi_1^2 + 2(3\bar{u}_1 - u_{int}) \xi_1 \right)^2 = (a_1 \xi_1^2 + b_1 \xi_1)^2 \\ &= a_1^2 \xi_1^4 + b_1^2 \xi_1^2 + 2a_1 b_1 \xi_1^3, \end{aligned} \quad (2.91)$$

which when integrated gives:

$$\begin{aligned} \int_{f_0}^{f_1} u_1^2 dz &= h_1 \int_0^1 u_1^2 d\xi_1 = h_1 \left[ a_1^2 \frac{\xi_1^5}{5} + b_1^2 \frac{\xi_1^3}{3} + 2a_1 b_1 \frac{\xi_1^4}{4} \right]_0^1 \\ &= h_1 \left[ \frac{a_1^2}{5} + \frac{b_1^2}{3} + \frac{2a_1 b_1}{4} \right] \\ &= h_1 \left( \frac{2}{15} u_{int}^2 - \frac{1}{5} \bar{u}_1 u_{int} + \frac{6}{5} \bar{u}_1^2 \right). \end{aligned} \quad (2.92)$$

Substituting (2.92) into (2.90) gives:

$$\int_{f_0}^{f_1} (\bar{u}_1 - u_1)^2 dz = \frac{1}{5} \bar{u}_1^2 h_1 + \frac{2}{15} u_{int}^2 h_1 - \frac{1}{5} u_{int} \bar{u}_1 h_1. \quad (2.93)$$

Differentiating equation (2.93) with respect to x leads to:

$$\frac{\partial}{\partial x} \int_{f_0}^{f_1} (\bar{u}_1 - u_1)^2 dz = \frac{\bar{u}_1}{5} \frac{\partial(\bar{u}_1 h_1)}{\partial x} + \frac{\bar{u}_1 h_1}{5} \frac{\partial \bar{u}_1}{\partial x} + \frac{2}{15} \frac{\partial}{\partial x} (u_{int}^2 h_1) - \frac{1}{5} \frac{\partial}{\partial x} (u_{int} \bar{u}_1 h_1), \quad (2.94)$$

which on substituting for  $\frac{\partial(\bar{u}_1 h_1)}{\partial x}$  from (2.73), yields:

$$\frac{\partial}{\partial x} \int_{f_0}^{f_1} (\bar{u}_1 - u_1)^2 dz = -\frac{\bar{u}_1}{5} \frac{\partial h_1}{\partial t} + \frac{\bar{u}_1 h_1}{5} \frac{\partial \bar{u}_1}{\partial x} + \frac{2}{15} \frac{\partial}{\partial x} (u_{int}^2 h_1) - \frac{1}{5} \frac{\partial}{\partial x} (u_{int} \bar{u}_1 h_1). \quad (2.95)$$

Similarly for the upper layer:

$$\frac{\partial}{\partial x} \int_{f_1}^{f_2} (\bar{u}_2 - u_2)^2 dz = -\frac{\bar{u}_2}{5} \frac{\partial h_2}{\partial t} + \frac{\bar{u}_2 h_2}{5} \frac{\partial \bar{u}_2}{\partial x} + \frac{1}{5} \frac{\partial}{\partial x} (u_{int}^2 h_2) - \frac{2}{5} \frac{\partial}{\partial x} (u_{int} \bar{u}_2 h_2). \quad (2.96)$$

After substituting for the dispersion and friction terms, equations (2.88), (2.89) and (2.95), (2.96), respectively, in the u-momentum equation (2.81), the full set of governing equations are:

$$\rho_1 \varepsilon Re \left[ \frac{\partial \bar{u}_1}{\partial t} - \frac{\bar{u}_1}{5 h_1} \frac{\partial h_1}{\partial t} + \frac{6}{5} \bar{u}_1 \frac{\partial \bar{u}_1}{\partial x} + \frac{2}{15 h_1} \frac{\partial}{\partial x} (u_{int}^2 h_1) - \frac{1}{5 h_1} \frac{\partial}{\partial x} (\bar{u}_1 u_{int} h_1) \right] + \frac{\partial p_1}{\partial x} - \frac{2 \rho_1}{C} - 6 \mu_1 \frac{u_{int} - 2 \bar{u}_1}{h_1^2} = 0, \quad (2.97)$$

$$\begin{aligned} \rho_2 \varepsilon Re \left[ \frac{\partial \bar{u}_2}{\partial t} - \frac{\bar{u}_2}{5h_2} \frac{\partial h_2}{\partial t} + \frac{6}{5} \bar{u}_2 \frac{\partial \bar{u}_2}{\partial x} + \frac{1}{5h_2} \frac{\partial}{\partial x} (u_{int}^2 h_2) \right. \\ \left. - \frac{2}{5h_2} \frac{\partial}{\partial x} (\bar{u}_2 u_{int} h_2) \right] + \frac{\partial p_2}{\partial x} - \frac{2\rho_2}{C} - 3\mu_2 \frac{u_{int} - \bar{u}_2}{h_2^2} = 0, \end{aligned} \quad (2.98)$$

$$\frac{\partial h_1}{\partial t} + \frac{\partial (h_1 \bar{u}_1)}{\partial x} = 0, \quad (2.99)$$

$$\frac{\partial h_2}{\partial t} + \frac{\partial (h_2 \bar{u}_2)}{\partial x} = 0, \quad (2.100)$$

$$p_1 = -\frac{\varepsilon^3}{Ca} (\sigma_{int} \nabla^2 f_1 + \sigma_2 \nabla^2 f_2) + \frac{2\varepsilon}{C} [\rho_1 f_1 + \rho_2 (f_2 - f_1)] \cot \theta, \quad (2.101)$$

$$p_2 = -\frac{\varepsilon^3}{Ca} \sigma_2 \nabla^2 f_2 + \frac{2\rho_2 \varepsilon}{C} f_2 \cot \theta. \quad (2.102)$$

Above, the DAF equations for free-surface bilayer flow have been derived for the two-dimensional flow case; the model can be extended to the more general three-dimensional case by considering the y-momentum equation in a similar manner to the x-momentum equation. The resulting set of equations is given in Chapter 3.

## 2.5.2 LUB model for free-surface flow

Setting the Reynolds number to zero, the above two-dimensional depth-averaged form reduces to the LUB model. Applying this constraint to equations (2.97) and (2.98) yields:

$$\frac{\partial p_1}{\partial x} - \frac{2\rho_1}{C} - 6\mu_1 \frac{u_{int} - 2\bar{u}_1}{h_1^2} = 0, \quad (2.103)$$

$$\frac{\partial p_2}{\partial x} - \frac{2\rho_2}{C} - 3\mu_2 \frac{u_{int} - \bar{u}_2}{h_2^2} = 0, \quad (2.104)$$

Equations (2.103) and (2.104) can be solved in conjunction with equation (2.87) to obtain the following streamwise average velocities across the two layers:

$$\bar{u}_1 = -\frac{h_1^2}{3\mu_1} \left( \frac{\partial p_1}{\partial x} - \frac{2\rho_1}{C} \right) - \frac{h_1 h_2}{2\mu_1} \left( \frac{\partial p_2}{\partial x} - \frac{2\rho_2}{C} \right), \quad (2.105)$$

$$\bar{u}_2 = -\frac{h_1^2}{2\mu_1} \left( \frac{\partial p_1}{\partial x} - \frac{2\rho_1}{C} \right) - \left( \frac{h_1 h_2}{\mu_1} + \frac{h_2^2}{3\mu_2} \right) \left( \frac{\partial p_2}{\partial x} - \frac{2\rho_2}{C} \right), \quad (2.106)$$

Substituting these expressions for  $\bar{u}_1$  and  $\bar{u}_2$  in equations (2.99) and (2.100) yields the following evolution equations:

$$\frac{\partial h_1}{\partial t} - \frac{\partial}{\partial x} \left[ \frac{h_1^3}{3\mu_1} \left( \frac{\partial p_1}{\partial x} - \frac{2\rho_1}{C} \right) + \frac{h_1^2 h_2}{2\mu_1} \left( \frac{\partial p_2}{\partial x} - \frac{2\rho_2}{C} \right) \right] = 0, \quad (2.107)$$

$$\frac{\partial h_2}{\partial t} - \frac{\partial}{\partial x} \left[ \frac{h_1^2 h_2}{2\mu_1} \left( \frac{\partial p_1}{\partial x} - \frac{2\rho_1}{C} \right) + \left( \frac{h_1 h_2^2}{\mu_1} + \frac{h_2^3}{3\mu_2} \right) \left( \frac{\partial p_2}{\partial x} - \frac{2\rho_2}{C} \right) \right] = 0, \quad (2.108)$$

### 2.5.3 DAF for channel flow

A similar procedure is followed to derive a two-dimensional DAF for channel flow; the detailed derivation of which is provided in Appendix C; the resulting set of governing equations is summarised below:

$$\begin{aligned} \varepsilon Re (\rho_2 N_2 - \rho_1 N_1) = -\sigma_{int} \frac{\varepsilon^3}{Ca} \frac{\partial^3 (h_1 + s)}{\partial x^3} + (\rho_2 - \rho_1) B \left( \sin \theta - \varepsilon \cos \theta \frac{\partial (h_1 + s)}{\partial x} \right) \\ + f_{r2} - f_{r1}, \end{aligned} \quad (2.109)$$

where:

$$N_i = \frac{\partial \bar{u}_i}{\partial t} - \frac{\bar{u}_i}{5h_i} \frac{\partial h_i}{\partial t} + \frac{6}{5} \bar{u}_i \frac{\partial \bar{u}_i}{\partial x} + \frac{1}{h_i} \frac{\partial (h_i \phi_i)}{\partial x}, \quad i = 1, 2, \quad (2.109a)$$

$$\phi_1 = \frac{2}{15} u_{int}^2 - \frac{1}{5} \bar{u}_1 u_{int}, \quad \phi_2 = \frac{2}{15} u_{int}^2 - \frac{1}{5} \bar{u}_2 u_{int} + \frac{2}{15} u_t^2 - \frac{1}{5} \bar{u}_2 u_t - \frac{1}{15} u_{int} u_t, \quad (2.109b)$$

$$f_{r1} = 6\mu_1 \frac{u_{int} - 2\bar{u}_1}{h_1^2}, \quad f_{r2} = 6\mu_2 \frac{u_{int} - 2\bar{u}_2 + u_t}{h_2^2}. \quad (2.109c)$$

$$\frac{\partial h_1}{\partial t} + \frac{\partial (h_1 \bar{u}_1)}{\partial x} = 0, \quad (2.110)$$

$$\frac{\partial h_2}{\partial t} + \frac{\partial (h_2 \bar{u}_2)}{\partial x} = 0. \quad (2.111)$$

The above equations embody the generalisation that the upper channel wall has speed  $u_t = U_t/U_0$ ;  $u_t \neq 0$  applies to Configuration 1 shown in Figure 2.1.

For channel flow  $\frac{\partial h_2}{\partial t} = -\frac{\partial h_1}{\partial t}$  because  $h_2 + h_1 + s = 1$ . Replacing  $\frac{\partial h_2}{\partial t}$  by  $-\frac{\partial h_1}{\partial t}$

in equation (2.111) gives:

$$-\frac{\partial h_1}{\partial t} + \frac{\partial(h_2\bar{u}_2)}{\partial x} = 0, \quad (2.112)$$

which when followed by adding equation (2.112) to equation (2.110) yields:

$$\frac{\partial(h_1\bar{u}_1)}{\partial x} + \frac{\partial(h_2\bar{u}_2)}{\partial x} = \frac{\partial}{\partial x} (h_1\bar{u}_1 + h_2\bar{u}_2) = 0, \quad (2.113)$$

showing that the total flow rate in the channel is constant. Integrating equation (2.113) with respect to  $x$ , the global mass balance is:

$$h_1\bar{u}_1 + h_2\bar{u}_2 = Q_1 + Q_2 = Q_{total}, \quad (2.114)$$

where

$$h_2 = 1 - (h_1 + s), \quad (2.115)$$

and the total flow rate is calculated at the disturbance free inlet, such that the flow rates in the undisturbed flow are given by:

$$Q_1 = - \left( \frac{h_{10}^3}{12\mu_1} + \frac{(1-h_{10})h_{10}^2}{4\mu_1(\frac{\mu_2}{\mu_1}h_{10} + 1 - h_{10})} \right) \frac{\Delta p}{\Delta l} + \left( \frac{\rho_1 h_{10}^3}{12\mu_1} + \frac{h_{10}^2(1-h_{10})(\rho_1 h_{10} + \rho_2(1-h_{10}))}{4\mu_1(\frac{\mu_2}{\mu_1}h_{10} + 1 - h_{10})} \right) B \sin \theta + \frac{\mu_2}{\mu_1} \frac{h_{10}^2}{2(\frac{\mu_2}{\mu_1}h_{10} + 1 - h_{10})} u_t, \quad (2.116)$$

and

$$Q_2 = - \left( \frac{(1-h_{10})^3}{12\mu_2} + \frac{(1-h_{10})^2 h_{10}}{4\mu_1 \left( \frac{\mu_2}{\mu_1} h_{10} + 1 - h_{10} \right)} \right) \frac{\Delta p}{\Delta l} + \left( \frac{\rho_2 (1-h_{10})^3}{12\mu_2} + \frac{h_{10} (1-h_{10})^2 (\rho_1 h_{10} + \rho_2 (1-h_{10}))}{4\mu_1 \left( \frac{\mu_2}{\mu_1} h_{10} + 1 - h_{10} \right)} \right) B \sin \theta + \frac{1-h_{10}}{2} \left( 1 + \frac{\frac{\mu_2}{\mu_1} h_{10}}{\frac{\mu_2}{\mu_1} h_{10} + 1 - h_{10}} \right) u_t, \quad (2.117)$$

where  $\frac{\Delta p}{\Delta l}$  is the imposed pressure gradient.

The problem is closed in terms of the following boundary conditions:

$$h_1|_{x=0} = h_{10}, \quad \left. \frac{\partial h_1}{\partial x} \right|_{x=l_s} = 0, \quad (2.118)$$

$$\left. \frac{\partial p_1}{\partial x} \right|_{x=l_s} = \left. \frac{\partial p_2}{\partial x} \right|_{x=l_s} = 0, \quad (2.119)$$

$$\left. \frac{\partial \bar{u}_i}{\partial x} \right|_{x=l_s} = 0, \quad \bar{u}_1|_{x=0} = \frac{Q_1}{h_{10}}, \quad \bar{u}_2|_{x=0} = \frac{Q_2}{1-h_{10}}. \quad (2.120)$$

## 2.5.4 LUB for channel flow

Setting  $Re$  to zero, the above two-dimensional DAF reduce to the following LUB model as derived in full in Appendix C, namely:

$$\begin{aligned} \frac{\partial h_1}{\partial t} - \frac{\partial}{\partial x} \left[ \frac{h_1^3}{12\mu_1} \left( 1 + \frac{3h_2}{\frac{\mu_2}{\mu_1} h_1 + h_2} \right) \left( \frac{\partial p_1}{\partial x} - \rho_1 B \sin \theta \right) \right. \\ \left. + \frac{h_1^2 h_2^2}{4\mu_1 \left( \frac{\mu_2}{\mu_1} h_1 + h_2 \right)} \left( \frac{\partial p_2}{\partial x} - \rho_2 B \sin \theta \right) - \frac{\mu_2}{\mu_1} \frac{h_1^2}{2 \left( \frac{\mu_2}{\mu_1} h_1 + h_2 \right)} u_t \right] = 0, \end{aligned} \quad (2.121)$$

$$p_2 - p_1 = \frac{\varepsilon^3}{Ca} \nabla^2 (h_1 + s) + B \varepsilon \cos \theta (\rho_2 - \rho_1) (h_1 + s), \quad (2.122)$$

$$q_1 + q_2 = Q_1 + Q_2, \quad (2.123)$$

$$h_2 = 1 - h_1 - s, \quad (2.124)$$

where  $Q_1(Q_2)$  is the fully developed flow rate through the lower(upper) layer at the disturbance-free channel inlet and  $q_1(q_2)$  is its developing counterpart - see equation (B.32) and (B.33) in Appendix B. The boundary conditions are:

$$h_1|_{x=0} = h_{10}, \quad (2.125)$$

$$\left. \frac{\partial h_1}{\partial x} \right|_{x=l_s} = 0, \quad (2.126)$$

$$\left. \frac{\partial p_1}{\partial x} \right|_{x=0, l_s} = \left. \frac{\partial p_2}{\partial x} \right|_{x=0, l_s} = 0. \quad (2.127)$$

### 2.5.5 Compact generic DAF (LUB) equations

It is possible to write the equations underpinning the DAF, and by inference the LUB model, for both channel and free-surface bilayer flow in two dimensions, in a general and generic compact form. Namely:

u-momentum equation:

$$\rho_i \varepsilon Re N_i = -\frac{\partial p_i}{\partial x} + \rho_i B \sin \theta + f_{r_i}. \quad (2.128)$$

Continuity equation:

$$\frac{\partial h_i}{\partial t} + \frac{\partial (h_i \bar{u}_i)}{\partial x} = 0. \quad (2.129)$$

Pressure equation:

$$p_1 - p_2 = -\sigma_{int} \frac{\varepsilon^3}{Ca} \frac{\partial^2 f_1}{\partial x^2} + \varepsilon B \cos \theta (\rho_2 - \rho_1) f_1. \quad (2.130)$$

In the case of free-surface flow an additional equation for the pressure in the top layer is required, namely:

$$p_2 = -\sigma_2 \frac{\varepsilon^3}{Ca} \frac{\partial^2 f_2}{\partial x^2} + \rho_2 \varepsilon B \cos \theta f_2, \quad (2.131)$$

while for channel flow a global mass balance is employed:

$$h_1 \bar{u}_1 + h_2 \bar{u}_2 = Q_{total}. \quad (2.132)$$

The functions  $\phi_i$  (via the operator  $N_i$ ) and  $f_{r_i}$  in equation (2.128) depends on which flow problem (Configuration 1 or 2, in Figure 2.1) and which layer is being considered:

For free-surface flow

$$\begin{aligned} \phi_1 &= \frac{2}{15} u_{int}^2 - \frac{1}{5} \bar{u}_1 u_{int}, & \phi_2 &= \frac{1}{5} u_{int}^2 - \frac{2}{5} \bar{u}_2 u_{int}, \\ f_{r1} &= 6\mu_1 \frac{u_{int} - 2\bar{u}_1}{h_1^2}, & f_{r2} &= 3\mu_2 \frac{u_{int} - \bar{u}_2}{h_2^2}. \end{aligned} \quad (2.133)$$

For channel flow

$$\begin{aligned} \phi_1 &= \frac{2}{15} u_{int}^2 - \frac{1}{5} \bar{u}_1 u_{int}, & \phi_2 &= \frac{2}{15} u_{int}^2 - \frac{1}{5} \bar{u}_2 u_{int} + \frac{2}{15} u_t^2 - \frac{1}{5} \bar{u}_2 u_t - \frac{1}{15} u_{int} u_t, \\ f_{r1} &= 6\mu_1 \frac{u_{int} - 2\bar{u}_1}{h_1^2}, & f_{r2} &= 6\mu_2 \frac{u_{int} - 2\bar{u}_2 + u_t}{h_2^2}. \end{aligned} \quad (2.134)$$

## 2.6 Topography definition

Following other authors (e.g. Stillwagon and Larson (1990); Peurrung and Graves (1991); Kalliadasis *et al.* (2000) and Gaskell *et al.* (2004)), since the topography ap-

pears as a function in the governing equations, it is defined via arctangent functions enabling, control of the topography sides steepness.

The current study focuses in the main on two-dimensional topographies such as step-down, step-up and a spanwise trench, although extension to three-dimensional free surface film flow cases is also considered. Accordingly, one-dimensional step-up/-down topographies are defined as:

$$s(x^*) = s_0 \left[ \frac{1}{2} \pm \tan^{-1} \left( \frac{x^*}{\delta} \right) \right] \quad (2.135)$$

while one-dimensional rectangular trench/peak topography is given by:

$$s(x^*) = \frac{s_0}{2 \tan^{-1} \frac{l_t}{2\delta}} \left[ \tan^{-1} \left( \frac{x^* + l_t/2}{\delta} \right) - \tan^{-1} \left( \frac{x^* - l_t/2}{\delta} \right) \right], \quad (2.136)$$

where the coordinate system  $x^*$  has its origin at the centre of the topography,  $x^* = x - x_t$ ,  $\delta$  is an adjustable parameter which controls the steepness of the topography.

# Chapter 3

## Methods of solution

### Contents

---

<b>3.1</b>	<b>Introduction</b>	<b>59</b>
<b>3.2</b>	<b>Overall method of solution</b>	<b>66</b>
3.2.1	Free-surface flow problem	67
3.2.1.1	Spatial discretisation	67
3.2.1.2	Temporal discretisation	71
3.2.2	Channel problem	74
<b>3.3</b>	<b>Methods of solution</b>	<b>77</b>
3.3.1	Multigrid solver	79
3.3.2	Full weighting restriction and interpolation operators	84
<b>3.4</b>	<b>Calculation details</b>	<b>87</b>
<b>3.5</b>	<b>Comparison of DAF (Re=0) and LUB results</b>	<b>89</b>

---

### 3.1 Introduction

The LUB model and DAF derived in Chapter 2 results in equation sets that are simpler to solve than the original full Navier-Stokes and continuity equations, despite the underpinning limiting assumptions made. The main advantages are a reduction of the dimensionality of the problem by one and the explicit presence of a free surface coordinate. Nevertheless, they have to be solved numerically.

When selecting an appropriate numerical method, the most important features to consider and realise are accuracy and efficiency. Fully implicit methods are too computationally expensive while fully explicit ones require a very small time step that is proportional to the square of the spatial increment, which can result in an impractically small and restrictive time step in situations when solutions on finer meshes are required to ensure mesh independence.

Among the attempts made to ease the above restriction concerning the size of time step when solving the LUB equations is to use a time splitting approach, Christov *et al.* (1997). This involves splitting each time-step into, most commonly, two parts and treating different terms implicitly and explicitly. Time-splitting methods are meant to combine some of the stability properties of implicit schemes with the cost efficiency of explicit ones. However, when solutions on fine meshes are required, the choice of time-step becomes severely restrictive. Nevertheless, the approach has been used successfully by Schwartz *et al.* (2001) and co-worker to solve a range of thin film and droplet spreading problems, see for example Schwartz and Eley (1998). Weidner *et al.* (1996) used this method to study the flow over curved substrate and the effect of surface tension gradient. It was also employed by Eres *et al.* (2000) to investigate the stability of gravity-driven and surface tension driven thin coating films.

The limitations associated with time-splitting methods has encouraged the adoption and use of multigrid methods to generate solutions on very fine meshes. Multigrid methods are based on employing a simple classical iterative technique as a smoother on a sequence of grids to reduce high frequency errors, Trottenberg *et al.* (2001). They are more efficient and require less memory than time-splitting ones, as demonstrated recently by Cowling *et al.* (2011).

The three-dimensional predictions obtained by Gaskell *et al.* (2004) for thin film flow over a localised topography, using an accurate and efficient solution strategy based on a full approximated storage (FAS) multigrid algorithm with the use of time step adaptivity based on the local truncation error, were the first of their kind to appear and found to agree extremely well with the benchmark experimental data of Decré and Baret (2003). This methodology has since been used by Gaskell and co-workers to solve a range of thin film flow and droplet spreading problems, see for example Sellier (2003), Sellier *et al.* (2009), Lee *et al.* (2007) Lee *et al.* (2011), Veremieiev *et al.* (2010), Veremieiev (2011), Veremieiev *et al.* (2012).

Lee *et al.* (2007) further developed the solver to embody automatic mesh refinement. They solved the problem of gravity driven thin film flow over a planer surface containing single and grouped topographies. Automatic mesh refinement restricts the use of fine grids to regions of significant changes such as in the vicinity of the topography, the capillary ridge and the downstream wake. Their results revealed corresponding efficient and accurate solutions, obtained using parallel computing, Lee *et al.* (2009a), to be indistinguishable from the ones obtained using automatic mesh refinement, leading to a significant and a considerable saving in CPU time and storage requirements. The approach was subsequently used to great effect by Slade (2013), and Slade *et al.* (2013) to investigate rivulet formation and growth down an inclined plane and on the inner and outer surface of vertically aligned cylinder.

Note that in addition, they implemented a method of grid devolution which resulted in a greater improvement in efficiency.

Veremieiev *et al.* (2010) used a multigrid solver to predict three-dimensional gravity-driven flow over localised topography, with inertia taken into account, using the DAF. The same approach was used subsequently to explore the use of electric field for the purpose of planarising the free-surface disturbance arising, Veremieiev *et al.* (2012).

Of the two problem under investigation in this thesis, the one for bilayer free-surface film flow is arguably of most practical relevance, especially for the case of three-dimensional free-surface film flows. The channel configuration is considered mainly for validation purpose, although in addition previous work involving non-zero Reynolds number conditions is extended; pressure and shear-driven flow is investigated also.

Accordingly, and as mentioned in Chapter 2, the governing DAF set of equations for three-dimensional bilayer film flow are given below, which requires considering the y-momentum equation in a similar fashion to the x-momentum equation:

$$\begin{aligned} & \rho_1 \varepsilon Re \left[ \frac{\partial \bar{u}_1}{\partial t} - \frac{\bar{u}_1}{5h_1} \frac{\partial h_1}{\partial t} + \frac{6}{5} \mathcal{F}_1(\bar{u}_1) + \frac{2}{15h_1} \left[ \frac{\partial}{\partial x} (u_{int}^2 h_1) + \frac{\partial}{\partial y} (u_{int} v_{int} h_1) \right] \right. \\ & \left. - \frac{1}{5h_1} \left[ \frac{\partial}{\partial x} (\bar{u}_1 u_{int} h_1) + \frac{1}{2} \frac{\partial}{\partial y} (\bar{u}_1 v_{int} h_1) + \frac{1}{2} \frac{\partial}{\partial y} (\bar{v}_1 u_{int} h_1) \right] \right] + \frac{\partial p_1}{\partial x} - \frac{2\rho_1}{C} \quad (3.1) \\ & - 6\mu_1 \frac{u_{int} - 2\bar{u}_1}{h_1^2} = 0, \end{aligned}$$

$$\begin{aligned}
\rho_1 \varepsilon Re \left[ \frac{\partial \bar{v}_1}{\partial t} - \frac{\bar{v}_1}{5h_1} \frac{\partial h_1}{\partial t} + \frac{6}{5} \mathcal{F}_1(\bar{v}_1) + \frac{2}{15h_1} \left[ \frac{\partial}{\partial x} (u_{int} v_{int} h_1) + \frac{\partial}{\partial y} (v_{int}^2 h_1) \right] \right. \\
\left. - \frac{1}{5h_1} \left[ \frac{1}{2} \frac{\partial}{\partial x} (\bar{u}_1 v_{int} h_1) + \frac{1}{2} \frac{\partial}{\partial x} (\bar{v}_1 u_{int} h_1) + \frac{\partial}{\partial y} (\bar{v}_1 v_{int} h_1) \right] \right] + \frac{\partial p_1}{\partial y} \quad (3.2) \\
- 6\mu_1 \frac{v_{int} - 2\bar{v}_1}{h_1^2} = 0,
\end{aligned}$$

$$\begin{aligned}
\rho_2 \varepsilon Re \left[ \frac{\partial \bar{u}_2}{\partial t} - \frac{\bar{u}_2}{5h_2} \frac{\partial h_2}{\partial t} + \frac{6}{5} \mathcal{F}_2(\bar{u}_2) + \frac{1}{5h_2} \left[ \frac{\partial}{\partial x} (u_{int}^2 h_2) + \frac{\partial}{\partial y} (u_{int} v_{int} h_2) \right] \right. \\
\left. - \frac{2}{5h_2} \left[ \frac{\partial}{\partial x} (\bar{u}_2 u_{int} h_2) + \frac{1}{2} \frac{\partial}{\partial y} (\bar{u}_2 v_{int} h_2) + \frac{1}{2} \frac{\partial}{\partial y} (\bar{v}_2 u_{int} h_2) \right] \right] + \frac{\partial p_2}{\partial x} - \frac{2\rho_2}{C} \quad (3.3) \\
- 3\mu_2 \frac{u_{int} - \bar{u}_2}{h_2^2} = 0,
\end{aligned}$$

$$\begin{aligned}
\rho_2 \varepsilon Re \left[ \frac{\partial \bar{v}_2}{\partial t} - \frac{\bar{v}_2}{5h_2} \frac{\partial h_2}{\partial t} + \frac{6}{5} \mathcal{F}_2(\bar{v}_2) + \frac{1}{5h_2} \left[ \frac{\partial}{\partial x} (u_{int} v_{int} h_2) + \frac{\partial}{\partial y} (v_{int}^2 h_2) \right] \right. \\
\left. - \frac{2}{5h_2} \left[ \frac{1}{2} \frac{\partial}{\partial x} (\bar{u}_2 v_{int} h_2) + \frac{1}{2} \frac{\partial}{\partial x} (\bar{v}_2 u_{int} h_2) + \frac{\partial}{\partial y} (\bar{v}_2 v_{int} h_2) \right] \right] + \frac{\partial p_2}{\partial y} \quad (3.4) \\
- 3\mu_2 \frac{v_{int} - \bar{v}_2}{h_2^2} = 0,
\end{aligned}$$

$$\frac{\partial h_1}{\partial t} + \frac{\partial (h_1 \bar{u}_1)}{\partial x} + \frac{\partial (h_1 \bar{v}_1)}{\partial y} = 0, \quad (3.5)$$

$$\frac{\partial h_2}{\partial t} + \frac{\partial (h_2 \bar{u}_2)}{\partial x} + \frac{\partial (h_2 \bar{v}_2)}{\partial y} = 0, \quad (3.6)$$

$$p_1 = -\frac{\varepsilon^3}{Ca} (\sigma_2 \nabla^2 f_2 + \sigma_{int} \nabla^2 f_1) + \frac{2\varepsilon}{C} \cot \theta (\rho_1 f_1 + \rho_2 (f_2 - f_1)), \quad (3.7)$$

$$p_2 = -C \frac{\varepsilon^3}{Ca} \nabla^2 f_2 + \frac{2\rho_2 \varepsilon}{C} \cot \theta f_2, \quad (3.8)$$

where the liquid-liquid interface velocities are calculated from:

$$u_{int} = \frac{6\bar{u}_1 + 3\frac{\mu_2}{\mu_1} \frac{h_1}{h_2} \bar{u}_2}{4 + 3\frac{\mu_2}{\mu_1} \frac{h_1}{h_2}}, \quad (3.9)$$

$$v_{int} = \frac{6\bar{v}_1 + 3\frac{\mu_2}{\mu_1} \frac{h_1}{h_2} \bar{v}_2}{4 + 3\frac{\mu_2}{\mu_1} \frac{h_1}{h_2}}, \quad (3.10)$$

and the operator  $\mathcal{F}_i$  is defined as:

$$\mathcal{F}_i(w) = \bar{u}_i \frac{\partial w}{\partial x} + \bar{v}_i \frac{\partial w}{\partial y}. \quad (3.11)$$

The corresponding boundary conditions are:

$$\begin{aligned} \bar{u}_1|_{x=0} &= \frac{\rho_2 h_{10}(1 - h_{10}) + \frac{2}{3}\rho_1 h_{10}^2}{\mu_1 C}, \\ \bar{u}_2|_{x=0} &= \frac{2\rho_2 h_{10}(1 - h_{10})}{\mu_1 C} + \frac{\rho_1 h_{10}^2}{\mu_1 C} + \frac{2}{3} \frac{\rho_2(1 - h_{10})^2}{\mu_2 C}, \\ \bar{v}_i|_{x=0} &= \frac{\partial \bar{u}_i}{\partial x} \Big|_{x=l_s} = \frac{\partial \bar{v}_i}{\partial x} \Big|_{x=l_s} = \frac{\partial \bar{u}_i}{\partial y} \Big|_{y=0, w_s} = \frac{\partial \bar{v}_i}{\partial y} \Big|_{y=0, w_s} = 0, \end{aligned} \quad (3.12)$$

while the inlet heights are:

$$h_1|_{x=0} = h_{10}, \quad h_2|_{x=0} = 1 - h_{10}, \quad (3.13)$$

and for fully developed flow far downstream:

$$\left. \frac{\partial h_i}{\partial x} \right|_{x=l_s} = \left. \frac{\partial h_i}{\partial y} \right|_{y=0, w_s} = \left. \frac{\partial p_i}{\partial x} \right|_{x=l_s} = \left. \frac{\partial p_i}{\partial y} \right|_{y=0, w_s} = 0, \quad (3.14)$$

where  $w_s$  is the width of the substrate. If the Reynolds number is set to zero the above DAF reduces, as shown in Chapter 2, to the LUB model. Namely, applying this constraint to equations (3.1) to (3.4) gives:

$$\frac{\partial p_1}{\partial x} - \frac{2\rho_1}{C} - 6\mu_1 \frac{u_{int} - 2\bar{u}_1}{h_1^2} = 0, \quad (3.15)$$

$$\frac{\partial p_1}{\partial y} - 6\mu_1 \frac{v_{int} - 2\bar{v}_1}{h_1^2} = 0, \quad (3.16)$$

$$\frac{\partial p_2}{\partial x} - \frac{2\rho_2}{C} - 3\mu_2 \frac{u_{int} - \bar{u}_2}{h_2^2} = 0, \quad (3.17)$$

$$\frac{\partial p_2}{\partial y} - 3\mu_2 \frac{v_{int} - \bar{v}_2}{h_2^2} = 0, \quad (3.18)$$

Equations (3.15) and (3.17) can be solved in conjunction with equation (3.9) to obtain the following streamwise average velocities across the two layers:

$$\bar{u}_1 = -\frac{h_1^2}{3\mu_1} \left( \frac{\partial p_1}{\partial x} - \frac{2\rho_1}{C} \right) - \frac{h_1 h_2}{2\mu_1} \left( \frac{\partial p_2}{\partial x} - \frac{2\rho_2}{C} \right), \quad (3.19)$$

$$\bar{u}_2 = -\frac{h_1^2}{2\mu_1} \left( \frac{\partial p_1}{\partial x} - \frac{2\rho_1}{C} \right) - \left( \frac{h_1 h_2}{\mu_1} + \frac{h_2^2}{3\mu_2} \right) \left( \frac{\partial p_2}{\partial x} - \frac{2\rho_2}{C} \right), \quad (3.20)$$

and solving equations (3.16), (3.18) and (3.10) simultaneously yields the spanwise average velocities:

$$\bar{v}_1 = -\frac{h_1^2}{3\mu_1} \frac{\partial p_1}{\partial y} - \frac{h_1 h_2}{2\mu_1} \frac{\partial p_2}{\partial y}, \quad (3.21)$$

$$\bar{v}_2 = -\frac{h_1^2}{2\mu_1} \frac{\partial p_1}{\partial y} - \left( \frac{h_1 h_2}{\mu_1} + \frac{h_2^2}{3\mu_2} \right) \frac{\partial p_2}{\partial y}. \quad (3.22)$$

Substituting these expressions for  $\bar{u}_1$ ,  $\bar{u}_2$ ,  $\bar{v}_1$  and  $\bar{v}_2$  in equations (3.5) and (3.6)

yields the following evolution equations:

$$\begin{aligned} \frac{\partial h_1}{\partial t} - \frac{\partial}{\partial x} \left[ \frac{h_1^3}{3\mu_1} \left( \frac{\partial p_1}{\partial x} - \frac{2\rho_1}{C} \right) + \frac{h_1^2 h_2}{2\mu_1} \left( \frac{\partial p_2}{\partial x} - \frac{2\rho_2}{C} \right) \right] \\ - \frac{\partial}{\partial y} \left[ \frac{h_1^3}{3\mu_1} \left( \frac{\partial p_1}{\partial y} \right) + \frac{h_1^2 h_2}{2\mu_1} \left( \frac{\partial p_2}{\partial y} \right) \right] = 0, \end{aligned} \quad (3.23)$$

$$\begin{aligned} \frac{\partial h_2}{\partial t} - \frac{\partial}{\partial x} \left[ \frac{h_1^2 h_2}{2\mu_1} \left( \frac{\partial p_1}{\partial x} - \frac{2\rho_1}{C} \right) + \left( \frac{h_1 h_2^2}{\mu_1} + \frac{h_2^3}{3\mu_2} \right) \left( \frac{\partial p_2}{\partial x} - \frac{2\rho_2}{C} \right) \right] \\ - \frac{\partial}{\partial y} \left[ \frac{h_1^2 h_2}{2\mu_1} \left( \frac{\partial p_1}{\partial y} \right) + \left( \frac{h_1 h_2^2}{\mu_1} + \frac{h_2^3}{3\mu_2} \right) \left( \frac{\partial p_2}{\partial y} \right) \right] = 0, \end{aligned} \quad (3.24)$$

which are, as can be seen, the same as the lubrication equations for bilayer free-surface flow as derived in full in Appendix A.

The method of solution reported in this chapter is based on the utilisation of multi-grid solution strategies to solve in the main the two-dimensional bilayer flow problem formulated in Chapter 2. However, the three-dimensional equation sets given above provide the opportunity to describe the underpinning multigrid methodology in Section 3.3 for the more general three-dimensional case. Spatial and temporal discretisation of the governing equations for the DAF, for both free-surface and channel bilayer flows, are described together with the associated methods of solution, while their LUB counterparts are presented in Appendix D. A Full Approximation Storage (FAS) variant of the multigrid method for nonlinear equations, Brandt (1982), is also described along with the treatment of boundary conditions.

## 3.2 Overall method of solution

The equation sets governing the DAF, subject to the relevant boundary conditions, are solved on a Cartesian computational domain subdivided using a regular staggered mesh arrangement with increments of  $\Delta x$  and  $\Delta y$  in the x- and the y-directions, respectively, Harlow *et al.* (1965). The pressures and layer thickness are stored at cell centres while the velocities are stored at cell faces. This arrangement is used as a remedy for the well-known checkerboard instability which arises when the first derivative of pressure and the terms in the continuity equation are calculated using central differencing when pressure and velocity are collocated, Trottenberg *et al.* (2001). A staggered grid allows the differencing of the first order derivative of pressure to be calculated using two adjacent nodes rather than two alternate ones if a collocated mesh is used, Patankar (1980). There are several approaches that can be used to circumvent checkerboard instability when solving the Navier-Stokes and continuity equations on collocated grids, Sheu and Lin (2003). Examples include: interpolating cell-face velocities using momentum interpolation methods, Rhie and Chow (1983); the consistent physical interpolation, Schneider and Raw (1987); approximating the pressure gradient using weighted upwinding interpolation, Thiart (1990) and Date (1993). Several studies have conducted comparisons between collocated and staggered grid approaches, see for example Perić *et al.* (1988) and Melaaen (1992).

The continuity and pressure equations are discretised for a control volume centred at  $(I, J)$  while the x-momentum (y-momentum) equation is discretised for a control volume shifted by  $\Delta x/2$  ( $\Delta y/2$ ) in the x-direction (y-direction). Figure 3.1 shows a schematic diagram of the staggered mesh arrangement employed and the different control volumes associated with it.

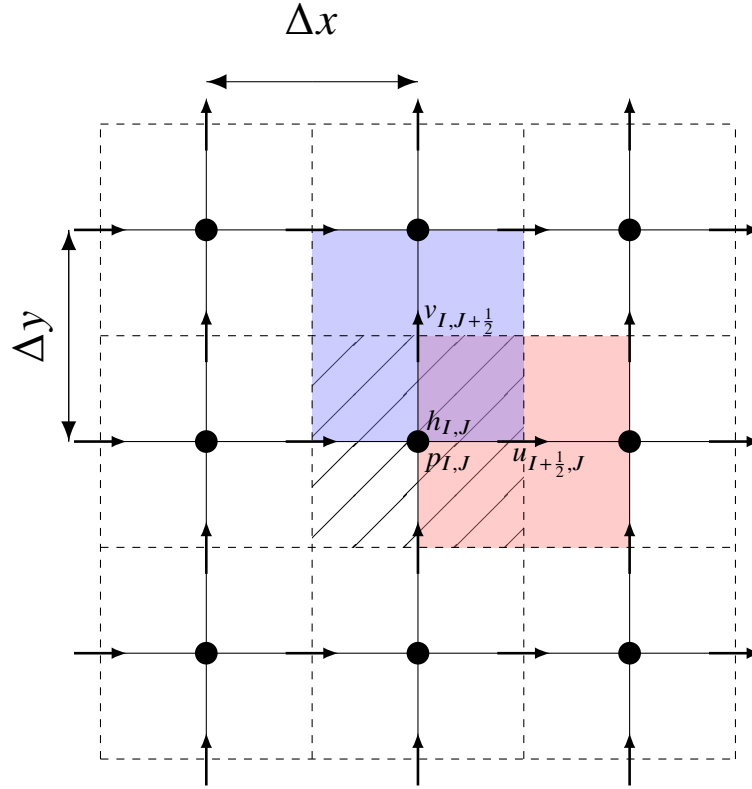


Figure 3.1: Staggered mesh arrangement used to solve equation sets based on the DAF.

## 3.2.1 Free-surface flow problem

### 3.2.1.1 Spatial discretisation

Equations (3.1) to (3.8) are solved, subject to boundary conditions (3.12) to (3.14), on a rectangular computational domain,  $(x, y) \in [0, l] \times [0, w]$  using the multigrid approach described later in Section 3.3.1. Figure 3.1 shows the staggered mesh arrangement and location of the different variables. The unknown scalar variables, lower layer thickness,  $h_1$ , lower layer pressure,  $p_1$ , top layer thickness,  $h_2$ , and top layer pressure,  $p_2$  are located at grid nodes  $(I, J)$  while streamwise average velocities,  $\bar{u}_1$  and  $\bar{u}_2$ , and spanwise average velocities,  $\bar{v}_1$  and  $\bar{v}_2$ , are located at cell faces,  $(I+1/2, J)$  and  $(I, J+1/2)$ , respectively. The corresponding coupled second-

order accurate discretisation scheme for  $h_i$  and  $p_i$  can be written, after grouping convection and time derivative terms together to simplify their numerical treatment and omitting for convenience the overbar denoting velocity averaging, as:

$$\begin{aligned} \varepsilon \rho_i Re \left[ \left( \frac{\partial u_i}{\partial t} - \frac{u_i}{5h_i} \frac{\partial h_i}{\partial t} + \frac{6}{5} \mathcal{F}_i(u_i) \right)_{I+\frac{1}{2},J} + \frac{(h_i \phi_i)_{I+1,J} - (h_i \phi_i)_{I,J}}{0.5 (h_{iI,J} + h_{iI+1,J}) \Delta x} \right. \\ \left. + \frac{(h_i \psi_i)_{I+\frac{1}{2},J+\frac{1}{2}} - (h_i \psi_i)_{I+\frac{1}{2},J-\frac{1}{2}}}{0.5 (h_{iI,J} + h_{iI+1,J}) \Delta y} \right] + \frac{p_{iI+1,J} - p_{iI,J}}{\Delta x} - \frac{2\rho_i}{C} - f_{riI+\frac{1}{2},J} = 0, \end{aligned} \quad (3.25)$$

$$\begin{aligned} \varepsilon \rho_i Re \left[ \left( \frac{\partial v_i}{\partial t} - \frac{v_i}{5h_i} \frac{\partial h_i}{\partial t} + \frac{6}{5} \mathcal{F}_i(v_i) \right)_{I,J+\frac{1}{2}} + \frac{(h_i \psi_i)_{I+\frac{1}{2},J+\frac{1}{2}} - (h_i \psi_i)_{I-\frac{1}{2},J+\frac{1}{2}}}{0.5 (h_{iI,J} + h_{iI,J+1})} \right. \\ \left. + \frac{(h_i \Upsilon_i)_{I,J+1} - (h_i \Upsilon_i)_{I,J}}{0.5 (h_{iI,J} + h_{iI,J+1})} \right] + \frac{p_{iI,J+1} - p_{iI,J}}{\Delta y} - f_{riI,J+\frac{1}{2}} = 0, \end{aligned} \quad (3.26)$$

$$\frac{\partial h_i}{\partial t} \Big|_{I,J} + \frac{h_{iI+\frac{1}{2},J} u_{iI+\frac{1}{2},J} - h_{iI-\frac{1}{2},J} u_{iI-\frac{1}{2},J}}{\Delta x} + \frac{h_{iI,J+\frac{1}{2}} v_{iI,J+\frac{1}{2}} - h_{iI,J-\frac{1}{2}} v_{iI,J-\frac{1}{2}}}{\Delta y} = 0, \quad (3.27)$$

$$\begin{aligned} p_{1I,J} = -\frac{\varepsilon^3}{Ca} \sigma_{int} \left( \frac{f_{1I+1,J} + f_{1I-1,J} - 2f_{1I,J}}{\Delta x^2} + \frac{f_{1I,J+1} + f_{1I,J-1} - 2f_{1I,J}}{\Delta y^2} \right) \\ - \frac{\varepsilon^3}{Ca} \sigma_2 \left( \frac{f_{2I+1,J} + f_{2I-1,J} - 2f_{2I,J}}{\Delta x^2} + \frac{f_{2I,J+1} + f_{2I,J-1} - 2f_{2I,J}}{\Delta y^2} \right) \\ + \frac{2\varepsilon}{C} (\rho_1 f_{1I,J} + \rho_2 (f_{2I,J} - f_{1I,J})) \cot \theta, \end{aligned} \quad (3.28)$$

$$\begin{aligned} p_{2I,J} = -\frac{\varepsilon^3}{Ca} \sigma_2 \left( \frac{f_{2I+1,J} + f_{2I-1,J} - 2f_{2I,J}}{\Delta x^2} + \frac{f_{2I,J+1} + f_{2I,J-1} - 2f_{2I,J}}{\Delta y^2} \right) \\ + \frac{2\rho_2 \varepsilon}{C} f_{2I,J} \cot \theta. \end{aligned} \quad (3.29)$$

The expressions for  $\phi_i$ ,  $\psi_i$  and  $\Upsilon_i$  are :

$$\phi_{1I+\frac{1}{2},J} = \frac{1}{15}u_{intI+\frac{1}{2},J} \left( 2u_{intI+\frac{1}{2},J} - 3u_{1I+\frac{1}{2},J} \right), \quad (3.30)$$

$$\phi_{2I+\frac{1}{2},J} = \frac{1}{5}u_{intI+\frac{1}{2},J} \left( u_{intI+\frac{1}{2},J} - 2u_{2I+\frac{1}{2},J} \right), \quad (3.31)$$

$$\Upsilon_{1I,J+\frac{1}{2}} = \frac{1}{15}v_{inI,J+\frac{1}{2}} \left( 2v_{inI,J+\frac{1}{2}} - 3v_{1I,J+\frac{1}{2}} \right), \quad (3.32)$$

$$\Upsilon_{2I,J+\frac{1}{2}} = \frac{1}{5}v_{inI,J+\frac{1}{2}} \left( v_{inI,J+\frac{1}{2}} - 2v_{2I,J+\frac{1}{2}} \right), \quad (3.33)$$

$$\begin{aligned} \psi_{1I+\frac{1}{2},J} &= -\frac{1}{10} \frac{v_{1I,J+\frac{1}{2}} + v_{1I+1,J+\frac{1}{2}} + v_{1I,J-\frac{1}{2}} + v_{1I+1,J-\frac{1}{2}}}{4} u_{intI+\frac{1}{2},J} \\ &+ \frac{v_{inI,J+\frac{1}{2}} + v_{inI+1,J+\frac{1}{2}} + v_{inI,J-\frac{1}{2}} + v_{inI+1,J-\frac{1}{2}}}{4} \left( \frac{2}{15}u_{intI+\frac{1}{2},J} - \frac{1}{10}u_{1I+\frac{1}{2},J} \right), \end{aligned} \quad (3.34)$$

$$\begin{aligned} \psi_{1I,J+\frac{1}{2}} &= -\frac{1}{10} \frac{u_{1I+\frac{1}{2},J} + u_{1I+\frac{1}{2},J+1} + u_{1I-\frac{1}{2},J} + u_{1I-\frac{1}{2},J+1}}{4} v_{inI,J+\frac{1}{2}} \\ &+ \frac{u_{intI+\frac{1}{2},J} + u_{intI+\frac{1}{2},J+1} + u_{intI-\frac{1}{2},J} + u_{intI-\frac{1}{2},J+1}}{4} \left( \frac{2}{15}v_{inI,J+\frac{1}{2}} - \frac{1}{10}v_{1I,J+\frac{1}{2}} \right), \end{aligned} \quad (3.35)$$

$$\begin{aligned} \psi_{2I+\frac{1}{2},J} &= -\frac{1}{5} \frac{v_{2I,J+\frac{1}{2}} + v_{2I+1,J+\frac{1}{2}} + v_{2I,J-\frac{1}{2}} + v_{2I+1,J-\frac{1}{2}}}{4} u_{intI+\frac{1}{2},J} \\ &+ \frac{v_{inI,J+\frac{1}{2}} + v_{inI+1,J+\frac{1}{2}} + v_{inI,J-\frac{1}{2}} + v_{inI+1,J-\frac{1}{2}}}{4} \left( \frac{1}{5}u_{intI+\frac{1}{2},J} - \frac{1}{5}u_{2I+\frac{1}{2},J} \right), \end{aligned} \quad (3.36)$$

$$\begin{aligned} \psi_{2I,J+\frac{1}{2}} &= -\frac{1}{5} \frac{u_{2I+\frac{1}{2},J} + u_{2I+\frac{1}{2},J+1} + u_{2I-\frac{1}{2},J} + u_{2I-\frac{1}{2},J+1}}{4} v_{inI,J+\frac{1}{2}} \\ &+ \frac{u_{intI+\frac{1}{2},J} + u_{intI+\frac{1}{2},J+1} + u_{intI-\frac{1}{2},J} + u_{intI-\frac{1}{2},J+1}}{4} \left( \frac{1}{5}v_{inI,J+\frac{1}{2}} - \frac{1}{5}v_{2I,J+\frac{1}{2}} \right). \end{aligned} \quad (3.37)$$

with the friction terms calculated as:

$$f_{r1I+\frac{1}{2},J} = 6\mu_1 \frac{u_{intI+\frac{1}{2},J} - 2u_{1I+\frac{1}{2},J}}{h_{1I+\frac{1}{2},J}^2}, \quad (3.38)$$

$$f_{r2I+\frac{1}{2},J} = 3\mu_2 \frac{u_{intI+\frac{1}{2},J} - u_{2I+\frac{1}{2},J}}{h_{2I+\frac{1}{2},J}^2}, \quad (3.39)$$

$$f_{r1I,J+\frac{1}{2}} = 6\mu_1 \frac{v_{inI,J+\frac{1}{2}} - 2v_{1I,J+\frac{1}{2}}}{h_{1I,J+\frac{1}{2}}^2}, \quad (3.40)$$

$$f_{r2I,J+\frac{1}{2}} = 3\mu_2 \frac{v_{inI,J+\frac{1}{2}} - v_{2I,J+\frac{1}{2}}}{h_{2I,J+\frac{1}{2}}^2}, \quad (3.41)$$

and  $h_i$  values at cell faces interpolated from neighbouring nodes as:

$$h_{iI\pm\frac{1}{2},J} = 0.5 (h_{iI\pm 1,J} + h_{iI,J}), \quad (3.42)$$

$$h_{iI,J\pm\frac{1}{2}} = 0.5 (h_{iI,J\pm 1} + h_{iI,J}), \quad (3.43)$$

$$h_{iI+\frac{1}{2},J+\frac{1}{2}} = 0.25 (h_{iI,J} + h_{iI+1,J} + h_{iI,J+1} + h_{iI+1,J+1}), \quad (3.44)$$

The operator  $\mathcal{F}_i$  is discretised using central differencing as:

$$\begin{aligned} \mathcal{F}_i(u_i)|_{I+\frac{1}{2},J} = & u_{iI+\frac{1}{2},J} \left( \frac{u_{iI+\frac{3}{2},J} - u_{iI-\frac{1}{2},J}}{2\Delta x} \right) + \left( \frac{v_{iI,J+\frac{1}{2}} + v_{iI,J-\frac{1}{2}} + v_{iI+1,J+\frac{1}{2}} + v_{iI+1,J-\frac{1}{2}}}{4} \right) \\ & \left( \frac{u_{iI+\frac{1}{2},J+1} - u_{iI+\frac{1}{2},J-1}}{2\Delta y} \right), \end{aligned} \quad (3.45)$$

and

$$\begin{aligned} \mathcal{F}_i(v_i)|_{I+\frac{1}{2},J} = & \left( \frac{u_{iI+\frac{1}{2},J} + u_{iI-\frac{1}{2},J} + u_{iI+\frac{1}{2},J+1} + u_{iI-\frac{1}{2},J+1}}{4} \right) \left( \frac{v_{iI+1,J+\frac{1}{2}} - v_{iI-1,J+\frac{1}{2}}}{2\Delta x} \right) \\ & + v_{iI,J+\frac{1}{2}} \left( \frac{v_{iI,J+\frac{3}{2}} - v_{iI,J-\frac{1}{2}}}{2\Delta y} \right). \end{aligned} \quad (3.46)$$

Dirichlet boundary conditions are assigned as exact values at the boundary points, whereas Neumann boundary conditions are implemented by employing ghost nodes at the edge of the computational domain.

To simplify the description of the calculation procedure presented below, it is con-

venient to separate the leading temporal  $u_i$ ,  $v_i$ ,  $h_i$  and  $p_i$  terms from the discretised u-momentum, v-momentum, continuity and pressure operators and to express them as functions  $\mathcal{M}_{I+\frac{1}{2},J}^{u_i}$ ,  $\mathcal{M}_{I,J+\frac{1}{2}}^{v_i}$ ,  $\mathcal{M}_{I,J}^{h_i}$  and  $\mathcal{M}_{I,J}^{p_i}$ , thus equations (3.25) to (3.29) and can be written as:

$$\rho_i \varepsilon Re \left. \frac{\partial u_i}{\partial t} \right|_{I+\frac{1}{2},J} + \mathcal{M}_{I+\frac{1}{2},J}^{u_i} (u_1, u_2, v_1, v_2, h_1, h_2, p_1, p_2, ) = 0, \quad (3.47)$$

$$\rho_i \varepsilon Re \left. \frac{\partial v_i}{\partial t} \right|_{I,J+\frac{1}{2}} + \mathcal{M}_{I,J+\frac{1}{2}}^{v_i} (u_1, u_2, v_1, v_2, h_1, h_2, p_1, p_2, ) = 0, \quad (3.48)$$

$$\left. \frac{\partial h_i}{\partial t} \right|_{I,J} + \mathcal{M}_{I,J}^{h_i} (u_1, u_2, v_1, v_2, h_1, h_2) = 0, \quad (3.49)$$

$$p_i|_{I,J} + \mathcal{M}_{I,J}^{p_i} (h_1, h_2) = 0. \quad (3.50)$$

The term  $\left. \frac{\partial h_i}{\partial t} \right|_{I,J}$  in the function  $\mathcal{M}^{u_i}$  of equation (3.47) is substituted from equation (3.48) at the appropriate mesh location.

### 3.2.1.2 Temporal discretisation

An automatic adaptive time-stepping scheme is incorporated into the solution strategy to optimise the time step selection in order to reduce the computational resource requirements. The time-stepping procedure adopted uses the local truncation error estimates (LTE) obtained from the difference between a predictor stage and the current solution stage. Fully explicit second order time discretisation of equations (3.47) - (3.50) yields the following expressions for the predicted values of  $u_i$ ,  $v_i$ ,  $h_i$  and  $p_i$ , Veremieiev *et al.* (2010) :

$$\begin{aligned} u_{i\text{pr}}|_{I+1/2,J}^{n+1} &= \gamma^2 u_{i\text{pr}}|_{I+1/2,J}^{n-1} + (1 - \gamma^2) u_{i\text{pr}}|_{I+1/2,J}^n \\ &\quad - \frac{\Delta t^{n+1}}{\rho_i \varepsilon Re} (1 + \gamma) \mathcal{M}_{I+1/2,J}^{u_i} (u_1^n, u_2^n, v_1^n, v_2^n, h_1^n, h_2^n, p_1^n, p_2^n), \end{aligned} \quad (3.51)$$

$$v_{i_{pr}} \Big|_{I,J+1/2}^{n+1} = \gamma^2 v_{i_{pr}}^{n-1} + (1 - \gamma^2) v_{i_{pr}}^n - \frac{\Delta t^{n+1}}{\rho_i \varepsilon Re} (1 + \gamma) \mathcal{M}_{I,J+1/2}^{v_i} (u_1^n, u_2^n, v_1^n, v_2^n, h_1^n, h_2^n, p_1^n, p_2^n), \quad (3.52)$$

$$h_{i_{pr}} \Big|_{I,J}^{n+1} = \gamma^2 h_{i_{pr}}^{n-1} + (1 - \gamma^2) h_{i_{pr}}^n - \Delta t^{n+1} (1 + \gamma) \mathcal{M}_{I,J}^{h_i} (u_1^n, u_2^n, v_1^n, v_2^n, h_1^n, h_2^n), \quad (3.53)$$

$$p_{i_{pr}} \Big|_{I,J}^{n+1} + \mathcal{M}_{I,J}^{p_i} (h_1^n, h_2^n) = 0 \quad (3.54)$$

where  $n$  and  $n + 1$  denote values at the end of the  $n$ th and  $(n + 1)$ st time steps,  $t = t^n$  and  $t = t^{n+1}$ , respectively, and  $\gamma = \Delta t^{n+1} / \Delta t^n$  is the ratio of successive time steps.

Adaptive time-stepping is performed by keeping the LTE for  $u_{i_{pr}}$  within a specified tolerance that in practice automatically restricts the LTE for  $v_{i_{pr}}$ ,  $h_{i_{pr}}$  and  $p_{i_{pr}}$  to provide a means of increasing the time step in a controlled manner. The LTE for  $u_{i_{pr}}$  at the predictor stage can be expressed via a Taylor series expansion of equation (3.51) in the form:

$$(LTE)_{pr} \Big|_{I+1/2,J} = \frac{\Delta t^{n+1} \Delta t^n (1 + \gamma)}{6} \frac{\partial^3 u_2}{\partial t^3} \Big|_{I+1/2,J}^{t_p}, \quad (3.55)$$

with the third-order time derivative term evaluated at time  $t_p \in (t^n, t^{n+1})$ . In the present work, an implicit  $\beta$ -method, see Chung (2002), is used to advance the solution in time:

$$\begin{aligned} u_{i_{pr}}^{n+1} &+ \frac{\beta \Delta t^{n+1}}{\rho_i \varepsilon Re} \mathcal{M}_{I+1/2,J}^{u_i} (u_1^{n+1}, u_2^{n+1}, v_1^{n+1}, v_2^{n+1}, h_1^{n+1}, h_2^{n+1}, p_1^{n+1}, p_2^{n+1}) \\ &= u_{i_{pr}}^n - \frac{(1 - \beta) \Delta t^{n+1}}{\rho_i \varepsilon Re} \mathcal{M}_{I+1/2,J}^{u_i} (u_1^n, u_2^n, v_1^n, v_2^n, h_1^n, h_2^n, p_1^n, p_2^n) \end{aligned} \quad (3.56)$$

$$\begin{aligned}
v_{i,I,J+1/2}^{n+1} + \frac{\beta \Delta t^{n+1}}{\rho_i \varepsilon Re} \mathcal{M}_{I,J+1/2}^{v_i} \left( u_1^{n+1}, u_2^{n+1}, v_1^{n+1}, v_2^{n+1}, h_1^{n+1}, h_2^{n+1}, p_1^{n+1}, p_2^{n+1} \right) \\
= v_{i,I,J+1/2}^n - \frac{(1-\beta) \Delta t^{n+1}}{\rho_i \varepsilon Re} \mathcal{M}_{I,J+1/2}^{v_i} \left( u_1^n, u_2^n, v_1^n, v_2^n, h_1^n, h_2^n, p_1^n, p_2^n \right)
\end{aligned} \tag{3.57}$$

$$\begin{aligned}
h_{i,I,J}^{n+1} + \beta \Delta t^{n+1} \mathcal{M}_{I,J}^{h_i} \left( u_1^{n+1}, u_2^{n+1}, v_1^{n+1}, v_2^{n+1}, h_1^{n+1}, h_2^{n+1} \right) \\
= h_{i,I,J}^n - (1-\beta) \Delta t^{n+1} \mathcal{M}_{I,J}^{h_i} \left( u_1^n, u_2^n, v_1^n, v_2^n, h_1^n, h_2^n \right)
\end{aligned} \tag{3.58}$$

For  $\beta = 1/2$  the method reduces to the second-order accurate in time Crank-Nicolson scheme, whereas  $\beta = 1$  leads to the fully implicit first-order accurate in time unconditionally stable Laasonen method.

The LTE for  $u$  at the solution (sol) stage is similarly given by a Taylor series expansion of equation (3.56):

$$(LTE)_{sol}|_{I+1/2,J} = -\frac{(\Delta t^{n+1})^3}{12} \frac{\partial^3 u_2}{\partial t^3} \Big|_{I+1/2,J}^{t^s}, \quad t^s \in (t^n, t^{n+1}). \tag{3.59}$$

As described in Chapra and Canale (2002), the assumption that the third-order derivative term varies by only a small amount over the time step enables the LTE to be estimated as:

$$(LTE)_{I+1/2,J} = \frac{u_{2I+1/2,J}^{n+1} - u_{2pr I+1/2,J}^{n+1}}{1 + 2(1 + \gamma)/\gamma}. \tag{3.60}$$

which, following Dormand (1996), is used to obtain an estimate of the overall truncation error by finding its Euclidean norm that, in turn, is used to specify the next time step  $\Delta t^{n+2}$  via:

$$\Delta t^{n+2} = 0.9 \Delta t^{n+1} \left( \frac{TOL}{\|LTE\|} \right)^{1/3}, \tag{3.61}$$

if  $\| \text{LTE} \| < \text{TOL}$ . The iteration is restarted with half the current time step if  $\| \text{LTE} \| > \text{TOL}$ , where TOL is a prescribed tolerance.

To simplify the explanation and the steps taken in the multigrid process, presented later in this chapter, based on the system of discrete equations (3.56), (3.57) and (3.58) it is convenient to introduce the following global time-dependent nonlinear operator, right-hand side function (defined by the solution on the previous time step) and solution vectors:

$$\mathcal{N} = \begin{pmatrix} \mathcal{N}_{I+1/2,J}^{u_1} \\ \mathcal{N}_{I+1/2,J}^{u_2} \\ \mathcal{N}_{I,J+1/2}^{v_1} \\ \mathcal{N}_{I,J+1/2}^{v_2} \\ \mathcal{N}_{I,J}^{h_1} \\ \mathcal{N}_{I,J}^{h_2} \\ \mathcal{N}_{I,J}^{p_1} \\ \mathcal{N}_{I,J}^{p_2} \end{pmatrix}, \quad \mathbf{f} = \begin{pmatrix} \mathbf{f}_{I+1/2,J}^{u_1} \\ \mathbf{f}_{I+1/2,J}^{u_2} \\ \mathbf{f}_{I,J+1/2}^{v_1} \\ \mathbf{f}_{I,J+1/2}^{v_2} \\ \mathbf{f}_{I,J}^{h_1} \\ \mathbf{f}_{I,J}^{h_2} \\ 0 \\ 0 \end{pmatrix}, \quad \mathbf{u}^n = \begin{pmatrix} u_{I+1/2,J}^n \\ u_{I+1/2,J}^n \\ v_{I,J+1/2}^n \\ v_{I,J+1/2}^n \\ h_{I,J}^n \\ h_{I,J}^n \\ p_{I,J}^n \\ p_{I,J}^n \end{pmatrix}, \quad (3.62)$$

respectively, where:

$$\mathcal{N}(\mathbf{u}^{n+1}) = \mathbf{f}(\mathbf{u}^n). \quad (3.63)$$

### 3.2.2 Channel problem

The unsteady governing equations (2.109) and (2.110) arising from the DAF for the two-dimensional channel flow are discretised on a staggered mesh as:

$$\begin{aligned}
& \varepsilon \rho_2 Re \left[ \frac{\partial u_{2I+1/2}}{\partial t} - \frac{2u_{2I+1/2}}{5(h_{2I} + h_{2I+1})} \frac{\partial h_{2I+1/2}}{\partial t} + \frac{6}{5} u_{2I+1/2} \frac{u_{2I+3/2} - u_{2I-1/2}}{2\Delta x} \right. \\
& \left. + \frac{1}{h_{2I} + h_{2I+1}} \left( h_{2I+1} \frac{\phi_{2I+1/2} + \phi_{2I+3/2}}{\Delta x} - h_{2I} \frac{\phi_{2I+1/2} + \phi_{2I-1/2}}{\Delta x} \right) \right] - \varepsilon \rho_1 Re \left[ \frac{\partial u_{1I+1/2}}{\partial t} \right. \\
& \left. - \frac{2u_{1I+1/2}}{5(h_{1I} + h_{1I+1})} \frac{\partial h_{1I+1/2}}{\partial t} + \frac{6}{5} u_{1I+1/2} \frac{u_{1I+3/2} - u_{1I-1/2}}{2\Delta x} + \frac{1}{h_{1I} + h_{1I+1}} \left( h_{1I+1} \frac{\phi_{1I+1/2} + \phi_{1I+3/2}}{\Delta x} \right. \right. \\
& \left. \left. - h_{1I} \frac{\phi_{1I+1/2} + \phi_{1I-1/2}}{\Delta x} \right) \right] = (\rho_2 - \rho_1) B \left( \sin \theta - \varepsilon \cos \theta \frac{h_{1I+1} - h_{1I} + s_{I+1} - s_I}{\Delta x} \right) \\
& - \frac{\varepsilon^3 \sigma_{int}}{Ca} \left( \frac{h_{1I+2} - 3h_{1I+1} + 3h_{1I} - h_{1I-1}}{\Delta x^3} + \frac{s_{I+2} - 3s_{I+1} + 3s_I - s_{I-1}}{2\Delta x^3} \right) + f_{r2I+1/2} - f_{r1I+1/2},
\end{aligned} \tag{3.64}$$

$$\left. \frac{\partial h_1}{\partial t} \right|_I + \frac{h_{1I+1/2} u_{1I+1/2} - h_{1I-1/2} u_{1I-1/2}}{\Delta x} = 0. \tag{3.65}$$

These equations are solved, using the multigrid method described in Subsection 3.3.1, for the lower layer thickness and average velocity,  $h_1$  and  $u_1$  only; the upper layer thickness and velocity are obtained from:

$$h_{2I} = 1 - h_{1I} - s_I, \quad u_{2I+1/2} = \frac{Q_{total} - 0.5u_{1I+1/2}(h_{1I} + h_{1I+1})}{0.5(h_{2I} + h_{2I+1})}, \tag{3.66}$$

with the total flow rate calculated via equation (2.114). The associated discretised friction and dispersion terms are:

$$f_{r1I+1/2} = 24\mu_1 \frac{u_{intI+1/2} - 2u_{1I+1/2}}{(h_{1I} + h_{1I+1})^2}, \tag{3.67}$$

$$f_{r2I+1/2} = 24\mu_2 \frac{u_{intI+1/2} - 2u_{2I+1/2} + u_t}{(h_{2I} + h_{2I+1})^2}, \tag{3.68}$$

$$\phi_{1I\pm 1/2} = \frac{1}{15} u_{intI\pm 1/2} (2u_{intI\pm 1/2} - 3u_{1I\pm 1/2}), \tag{3.69}$$

$$\phi_{1I+3/2} = \frac{1}{15} u_{intI+3/2} (2u_{intI+3/2} - 3u_{1I+3/2}), \tag{3.70}$$

$$\begin{aligned}\phi_{2I\pm 1/2} &= \frac{1}{15}u_{intI\pm 1/2} \left( 2u_{intI\pm 1/2} - 3u_{2I\pm 1/2} \right) \\ &\quad - \frac{1}{15}u_t \left( 3u_{2I\pm 1/2} + u_{intI\pm 1/2} - 2u_t \right),\end{aligned}\tag{3.71}$$

$$\begin{aligned}\phi_{2I+3/2} &= \frac{1}{15}u_{intI+3/2} \left( 2u_{intI+3/2} - 3u_{2I+3/2} \right) \\ &\quad - \frac{1}{15}u_t \left( 3u_{2I+3/2} + u_{intI+3/2} - 2u_t \right).\end{aligned}\tag{3.72}$$

The value of  $h_1$  at a cell face is calculated by interpolating between neighbouring nodes:  $h_{1I\pm 1/2} = 0.5 (h_{1I\pm 1} + h_{1I})$ . It is convenient to separate the leading temporal  $u_1$  and  $h_1$  terms from the discretised u-momentum and continuity operators and to express them as functions  $\mathcal{M}_{I+1/2}^{u_1}$  and  $\mathcal{M}_I^{h_1}$ ; thus equations (3.64) and (3.65) can be written as:

$$\left. \frac{\partial u_1}{\partial t} \right|_{I+1/2} + \mathcal{M}_{I+1/2}^{u_1} (u_1, h_1) = 0,\tag{3.73}$$

$$\left. \frac{\partial h_1}{\partial t} \right|_I + \mathcal{M}_I^{h_1} (u_1, h_1) = 0.\tag{3.74}$$

The term  $\left. \frac{\partial h_1}{\partial t} \right|_I$  in the function  $\mathcal{M}^{u_1}$  of equation (3.73), is substituted from equation (3.74) at appropriate mesh locations.

The adaptive time stepping method presented in Section 3.2.1.2 is used and the implicit  $\beta$ -method employed to advance the solution in time:

$$u_{1I+1/2}^{n+1} + \beta \Delta t^{n+1} \mathcal{M}_{I+1/2}^{u_1} (h_1^{n+1}, u_1^{n+1}) = u_{1I+1/2}^n - (1 - \beta) \Delta t^{n+1} \mathcal{M}_{I+1/2}^{u_1} (h_1^n, u_1^n),\tag{3.75}$$

$$h_{1I}^{n+1} + \beta \Delta t^{n+1} \mathcal{M}_I^{h_1} (u_1^{n+1}, h_1^{n+1}) = h_{1I}^n - (1 - \beta) \Delta t^{n+1} \mathcal{M}_I^{h_1} (u_1^n, h_1^n),\tag{3.76}$$

which can be written in the form of equation (3.63) but with:

$$\mathcal{N} = \begin{pmatrix} \mathcal{N}_{I+1/2}^{u_1} \\ \mathcal{N}_I^{h_1} \end{pmatrix}, \quad \mathbf{f} = \begin{pmatrix} \mathbf{f}_{I+1/2}^{u_1} \\ \mathbf{f}_I^{h_1} \end{pmatrix}, \quad \mathbf{u}^n = \begin{pmatrix} u_{I+1/2}^{1n} \\ h_{1I}^n \end{pmatrix}. \quad (3.77)$$

For completeness the corresponding discrete forms of LUB model for three-dimensional free-surface flow and two-dimensional channel flow on a collocated mesh are provided in Appendix D.

### 3.3 Methods of solution

The principal method of solving the above discret equations is the multigrid method; however, in the case of channel flow the problem is also solved using a second methodology akin to the one used by Lenz and Kumar (2007) and Zhou and Kumar (2012) which assumes the flow to be steady. The reason for this is to check whether the failure of the latter authors to solve the problem of flow over a step-up topography with  $Re \neq 0$  was due to the solver they used. In the present work this was achieved using the MA42 subroutine ( a successor of MA32 ) from the Harwell Subroutine Library (HSL) which employs the frontal method variant of Gauss elimination, Scott (2004). The MA42 code solves a set of sparse linear equations by building a LU decomposition of the sparse matrix in order to avoid a large number of operations involving zero terms. The associated equation set is provided below.

For steady flow, the global mass balance changes to a condition where the flow rate in each layer is constant. This can be utilized to write the average velocity in terms of its corresponding layer thickness allowing the problem to be solved for

one variable,  $h_1$ . The discrete equation becomes:

$$\begin{aligned}
& \varepsilon \rho_2 Re \left[ \frac{6}{5} u_{2I+1/2} \frac{u_{2I+3/2} - u_{2I-1/2}}{2\Delta x} + \frac{1}{h_{2I} + h_{2I+1}} \left( h_{2I+1} \frac{\phi_{2I+1/2} + \phi_{2I+3/2}}{\Delta x} \right. \right. \\
& \left. \left. - h_{2I} \frac{\phi_{2I+1/2} + \phi_{2I-1/2}}{\Delta x} \right) \right] - \varepsilon \rho_1 Re \left[ \frac{6}{5} u_{1I+1/2} \frac{u_{1I+3/2} - u_{1I-1/2}}{2\Delta x} + \frac{1}{h_{1I} + h_{1I+1}} \right. \\
& \left. \left( h_{1I+1} \frac{\phi_{1I+1/2} + \phi_{1I+3/2}}{\Delta x} - h_{1I} \frac{\phi_{1I+1/2} + \phi_{1I-1/2}}{\Delta x} \right) \right] = \\
& (\rho_2 - \rho_1) B \left( \sin \theta - \varepsilon \cos \theta \frac{h_{1I+1} - h_{1I} + s_{I+1} - s_I}{\Delta x} \right) \\
& - \frac{\varepsilon^3 \sigma_{int}}{Ca} \left( \frac{h_{1I+2} - 3h_{1I+1} + 3h_{1I} - h_{1I-1}}{\Delta x^3} + \frac{s_{I+2} - 3s_{I+1} + 3s_I - s_{I-1}}{2\Delta x^3} \right) \\
& + f_{r2I+1/2} - f_{r1I+1/2},
\end{aligned} \tag{3.78}$$

where:

$$\begin{aligned}
h_{2I} &= 1 - h_{1I} - s_I, \\
u_{iI+1/2} &= \frac{Q_i}{0.5 (h_{iI} + h_{iI+1})}.
\end{aligned} \tag{3.79}$$

The solution process for the above equation set starts by performing forward elimination which is followed by a back-substitution step. Equation (3.78) is solved for the only unknown  $h_1$ . Results shows that it is possible to solve bilayer channel flow over a step-up topography when  $Re \neq 0$  using the DAF. This indicates that the failure by Zhou and Kumar (2012) to simulate the same flow problem is not due the solver they used. Further investigation of the applicability of the diffuse-interface method they used for this flow situation is required to determine the reason of this failure.

### 3.3.1 Multigrid solver

In this section a discussion is provided of the multigrid methodology used, with particular reference to the problems of interest. The first comprehensive description of the multigrid method is that of Brandt (1977), which was designed to achieve rapid convergence to the solution of a set of nonlinear discretized equations. The method has been described in details for the solution of different types of problems in several comprehensive texts, see for example Briggs *et al.* (2000) and Trottenberg *et al.* (2001). As mentioned in Section 3.1 multigrid solvers have been used successfully to solve several thin film flow problems by Gaskell *et al.* (2004), Lee *et al.* (2007), Gaskell *et al.* (2010), Veremieiev *et al.* (2010) and Slade (2013) and shown to be accurate and efficient in handling such problems. To illustrate the different steps in the multigrid methodology employed, we take equation (3.63) to represent the discretised equation set.

The strategy underpinning the multigrid method is to use iteration, not as a solver but as a smoother, to reduce the high frequency errors in the solution on a particular grid level while the low frequency errors are reduced on a hierarchy of coarser grids. This exploits the fact that iterative methods are efficient as smoothers, rather than solvers, allowing for fast convergence of the solution of a system of equations. This provides multigrid methods with the key feature that the solution of a problem with  $N$  unknowns can be achieved by performing  $O(N)$  operations.

A hierarchy of grids ( $\mathcal{G}_k : k = 0, 1, 2, \dots, K$ ) is employed so that the number of nodes for each grid per unit length in the x-direction is given by  $n_k = 2^{k+c+1} + 1$  where  $c$  is a constant defining the size of the coarsest grid and the mesh size,  $\Delta x = 2^{-(k+c+1)}$ . The same is applied for the number of nodes and mesh size in the y-direction. This means that node spacing is halved from one grid level to the next

fine one which allow for simple inter-grid transformers (interpolation/restriction). Figure 3.2 illustrates a typical grid hierarchy for three grid levels ( $\mathcal{G}_0, \mathcal{G}_1$  and  $\mathcal{G}_2$ ) with  $c = 0$ .

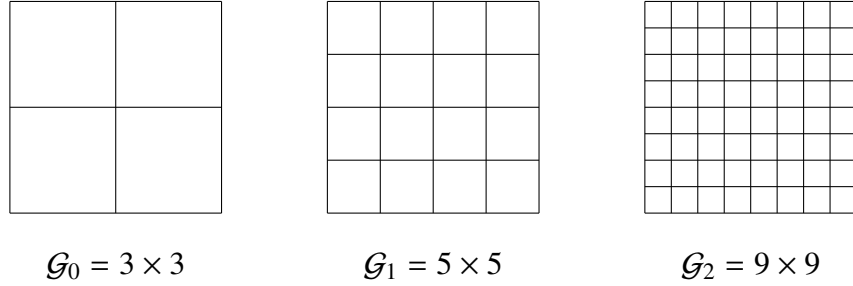


Figure 3.2: Hierarchy of grids showing 3 grid levels ( $\mathcal{G}_0, \mathcal{G}_1$  and  $\mathcal{G}_2$ ) with  $c = 0$ .

A combination of full approximation storage (FAS), described by Brandt (1977), and the full multigrid technique (FMG) is used in the present work. The FAS algorithm is explained below in terms of two grid levels, having coarse grid  $\mathcal{G}_0$  and fine grid  $\mathcal{G}_1$ .

The multigrid process starts by making a number of pre-relaxation sweeps  $\nu_1$  for the initial approximation on the fine grid to produce a relaxed fine grid approximation  $\tilde{\mathbf{u}}_1^m$ , where  $m$  refers to the iteration number and is set to zero at the start of each multigrid cycle. The next step is to restrict  $\tilde{\mathbf{u}}_1^m$  and its residual  $\mathbf{d}_1^m$  onto  $\mathcal{G}_0$  to obtain a coarse grid solution  $\mathbf{w}_0^m$ , which is used to calculate correction terms  $\mathbf{v}_0^m$ . This is known as the coarse grid correction step. An updated fine grid solution is then calculated by interpolating  $\mathbf{v}_0^m$  back onto  $\mathcal{G}_1$ . Restriction and interpolation operation are illustrated in Figure 3.3. The resultant fine grid approximation is then subjected to  $\nu_2$  post-relaxation sweeps to obtain a better approximation for the  $(m + 1)$ th iteration,  $\mathbf{u}_1^m$ . These steps are repeated until a specified convergence criterion is satisfied.

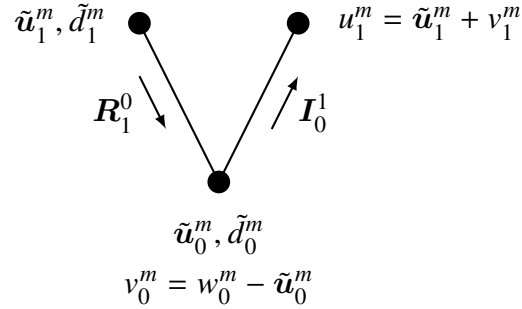


Figure 3.3: An illustration of Restriction,  $R$ , and Interpolation,  $I$ , between grid levels.

The same principles, relaxation and coarse grid correction, are adopted to cater for a larger number of grids in a general multigrid algorithm. This allows longer wavelength errors to be reduced by relaxation on coarser grids. The coarse grid correction is applied repeatedly until the discretised equations can be solved directly or within a few iterations. The number of times a multigrid procedure is applied at the coarse grid level is called the cycle index,  $\mathcal{K}$ , and it specifies the type of coarse grid correction cycle. Since the procedure converges fast  $\mathcal{K} = 1$  and  $\mathcal{K} = 2$ , corresponding to a V-cycle and a W-cycle, respectively, are the typical values used. Figure 3.4 shows the structure of a V-cycle and a W-cycle for a three-level grid; a V-cycle multigrid structure is adopted in the current work.



Figure 3.4: Structure of one multigrid cycle for  $\mathcal{K} = 1$  and  $\mathcal{K} = 2$ .

The full approximation storage (FAS) method employed can be described using the pseudo-code formalism introduced by Trottenberg *et al.* (2001) and employed by

Gaskell *et al.* (2004) and Lee *et al.* (2007) as follows:

$$\mathbf{u}_k^{m+1} = \text{MGFASCYC}(k, \tilde{\mathbf{u}}_1^m, \mathbf{f}_k, \nu_1, \nu_2, \mathcal{K})$$

- Pre-relaxation:

- Perform  $\nu_1$  relaxation sweeps using Gauss-Seidel iteration after linearising using the Newton-Raphson method .

$$\tilde{\mathbf{u}}_1^m = \text{RELAX}(\mathbf{u}_k^m, \mathbf{f}_k)$$

- Coarse grid correction:

- Compute residual on  $\mathcal{G}_k$

$$\tilde{\mathbf{d}}_k^m = \mathbf{f}_k - \mathcal{N}_k(\tilde{\mathbf{u}}_k^m)$$

- Restrict residual to next coarser grid level  $\mathcal{G}_{k-1}$  using full-weighting restriction operator  $\mathbf{R}_k^{k-1}$ :

$$\tilde{\mathbf{d}}_{k-1}^m = \mathbf{R}_k^{k-1} \tilde{\mathbf{d}}_k^m$$

- Restrict fine grid solution to  $\mathcal{G}_{k-1}$

$$\tilde{\mathbf{u}}_{k-1}^m = \mathbf{R}_k^{k-1} \tilde{\mathbf{u}}_k^m$$

- Compute right hand side on  $\mathcal{G}_{k-1}$

$$\mathbf{f}_{k-1} = \tilde{\mathbf{d}}_{k-1}^m + \mathcal{N}_{k-1}(\tilde{\mathbf{u}}_{k-1}^m)$$

- if  $k = 1$ , solve the problem using the coarse grid solver.

$$\mathcal{N}_{k-1}(\mathbf{w}_{k-1}^m) = \mathbf{f}_{k-1}$$

- if  $k > 1$ , perform  $\mathcal{K}$  iterations using  $\tilde{\mathbf{u}}_{k-1}^m$  as the initial approximation

$$\mathbf{w}_{k-1}^m = \text{MGFASCYC}(k-1, \tilde{\mathbf{u}}_{k-1}^m, \mathbf{f}_{k-1}, \nu_1, \nu_2, \mathcal{K})$$

- compute corrections on  $\mathcal{G}_{k-1}$  using

$$\mathbf{v}_{k-1}^m = \mathbf{w}_{k-1}^m - \tilde{\mathbf{u}}_{k-1}^m$$

- Interpolate corrections to  $\mathcal{G}_k$  using bilinear interpolation operator  $\mathbf{I}_{k-1}^k$

$$\mathbf{v}_k^m = \mathbf{I}_{k-1}^k \mathbf{v}_{k-1}^m.$$

- Update approximated solution on  $\mathcal{G}_k$

$$\mathbf{u}_k^m = \tilde{\mathbf{u}}_k^m + \mathbf{v}_k^m$$

- Post-relaxation sweep

- Perform  $\nu_2$  relaxation sweeps using relaxation scheme.

$$\mathbf{u}_k^{m+1} = RELAX(\mathbf{u}_k^m, \mathbf{f}_k)$$

If computations begin by choosing an arbitrary initial guess on the fine grid there is a chance that the solution may diverge. To avoid this problem the full multigrid technique, FMG, is used. An initial guess on each grid is obtained by interpolating the solution from the next coarser one. At the coarsest grid, the solution is calculated by applying a large number of smoothing iterations or by using an exact nonlinear solver, in the present work the Newton-Raphson method is used as a coarse grid solver. The procedure involves performing a small number of FAS V-cycles (1 to 3 cycles) on intermediate grid levels and a sufficient number of V-cycle on the finest grid level. V-cycles are performed on the finest grid level until the residuals become smaller than a predefined tolerance. A schematic representation for FMG is shown in Figure 3.5 for three grid levels. For any number of grid levels,  $K$ , the procedure can be summarized using pseudo-code as:

- For  $k = 0, 1, 2, \dots, K$

- If  $k = 0$  solve  $\mathcal{N}_0(\mathbf{u}_0^{m+1}) = \mathbf{f}_0$  to obtain initial guess  $\mathbf{u}_0^{m+1}$

- If  $k > 0$ , interpolate to finer grid  $\mathcal{G}_k$  from  $\mathcal{G}_{k-1}$

$$\mathbf{u}_0^m = \Pi_{k-1}^k \mathbf{u}_1^m \text{ where } \Pi_{k-1}^k \text{ may or may not be the same as } \mathbf{I}_{k-1}^k.$$

$$\text{Compute } \mathbf{u}_1^{m+1} = MGFASCYC(k, \mathbf{u}_0^m, \mathbf{f}_k, \nu_1, \nu_2, \mathcal{K})$$

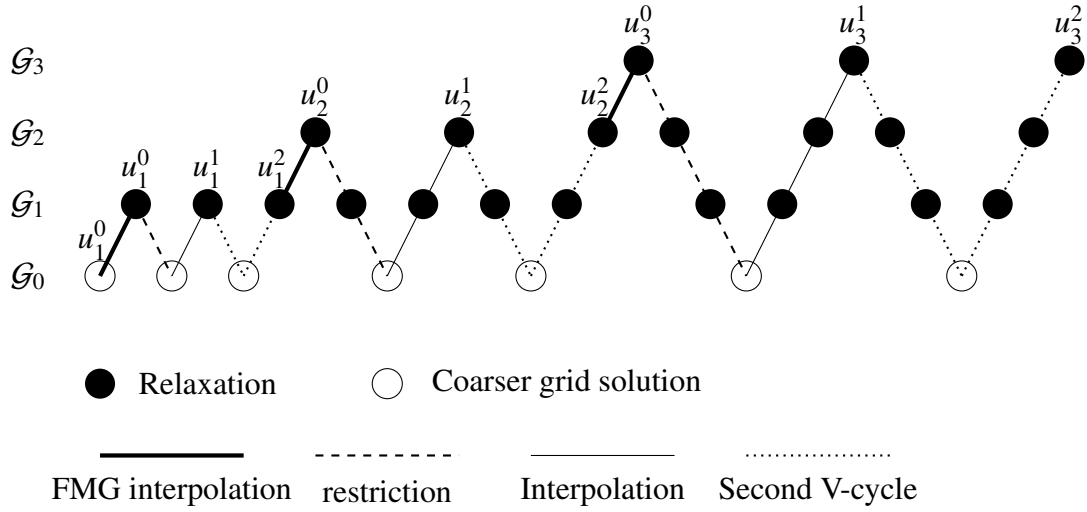


Figure 3.5: The Full Multigrid, FMG, illustrated for two V-cycles and four grid levels.  $u_k^m$  refers to the solution vector on grid level  $\mathcal{G}_k$  after performing  $m$  FAS V-cycle;  $u_0^0$  is the initial solution on the coarsest grid level and  $u_k^0$  is the solution on  $\mathcal{G}_k$  grid level obtained by FMG interpolation of  $u_{k-1}^0$ .

### 3.3.2 Full weighting restriction and interpolation operators

The restriction operator used in the present work to transfer information from one grid level to the next coarser one is a *full weighting* restriction. The operator equations can be written for a one-dimensional staggered grid for  $u$ ,  $h$  and  $p$  as:

$$u_{I+1/2}^{k-1} = \frac{1}{4} \left[ u_{2I-1/2}^k + 2u_{2I+1/2}^k + u_{2I+3/2}^k \right], \quad (3.80)$$

$$h_I^{k-1} = \frac{1}{8} \left[ h_{2I-1}^k + 3h_{2I}^k + 3h_{2I+1}^k + h_{2I+2}^k \right], \quad (3.81)$$

$$p_I^{k-1} = \frac{1}{8} \left[ p_{2I-1}^k + 3p_{2I}^k + 3p_{2I+1}^k + p_{2I+2}^k \right], \quad (3.82)$$

where the subscript denotes the nodal position and the superscript refers to the grid level. For a two-dimensional grid, the restriction operator becomes:

$$\begin{aligned}
u_{I+1/2,J}^{k-1} = & \frac{1}{32} \left[ u_{2I-1/2,2J-1}^k + u_{2I-1/2,2J+2}^k + u_{2I+3/2,2J-1}^k + u_{2I+3/2,2J+2}^k \right. \\
& + 2 \left( u_{2I+1/2,2J-1}^k + u_{2I+1/2,2J+2}^k \right) + 6 \left( u_{2I+1/2,2J}^k + u_{2I+1/2,2J+1}^k \right) \\
& \left. + 3 \left( u_{2I-1/2,2J}^k + u_{2I+3/2,2J}^k + u_{2I-1/2,2J+1}^k + u_{2I+3/2,2J+1}^k \right) \right], \tag{3.83}
\end{aligned}$$

$$\begin{aligned}
v_{I,J+1/2}^{k-1} = & \frac{1}{32} \left[ v_{2I-1,2J-1/2}^k + v_{2I+2,2J-1/2}^k + v_{2I-1,2J+3/2}^k + v_{2I+2,2J+3/2}^k \right. \\
& + 2 \left( v_{2I-1,J+1/2}^k + v_{2I+2,2J+1/2}^k \right) + 6 \left( v_{2I,2J+1/2}^k + v_{2I+1,2J+1/2}^k \right) \\
& \left. + 3 \left( v_{2I,2J-1/2}^k + v_{2I,2J+3/2}^k + v_{2I+1,2J-1/2}^k + v_{2I+1,2J+3/2}^k \right) \right], \tag{3.84}
\end{aligned}$$

$$\begin{aligned}
h_{I,J}^{k-1} = & \frac{1}{64} \left[ h_{2I-1,2J-1}^k + h_{2I-1,2J+2}^k + h_{2I+2,2J-1}^k + h_{2I+2,2J+2}^k + 3 \left( h_{2I,2J-1}^k \right. \right. \\
& + h_{2I,2J+2}^k + h_{2I+1,2J-1}^k + h_{2I+1,2J+2}^k + h_{2I-1,2J}^k + h_{2I-1,2J+1}^k + h_{2I+2,2J}^k \\
& \left. \left. + h_{2I+2,2J+1}^k \right) + 9 \left( h_{2I,2J}^k + h_{2I+1,2J}^k + h_{2I,2J+1}^k + h_{2I+1,2J+1}^k \right) \right], \tag{3.85}
\end{aligned}$$

$$\begin{aligned}
p_{I,J}^{k-1} = & \frac{1}{64} \left[ p_{2I-1,2J-1}^k + p_{2I-1,2J+2}^k + p_{2I+2,2J-1}^k + p_{2I+2,2J+2}^k + 3 \left( p_{2I,2J-1}^k \right. \right. \\
& + p_{2I,2J+2}^k + p_{2I+1,2J-1}^k + p_{2I+1,2J+2}^k + p_{2I-1,2J}^k + p_{2I-1,2J+1}^k + p_{2I+2,2J}^k \\
& \left. \left. + p_{2I+2,2J+1}^k \right) + 9 \left( p_{2I,2J}^k + p_{2I+1,2J}^k + p_{2I,2J+1}^k + p_{2I+1,2J+1}^k \right) \right]. \tag{3.86}
\end{aligned}$$

To transfer information from the coarse grid level to the next fine level, a bilinear interpolation operator is employed which, for a one-dimensional grid, is written as:

$$\begin{aligned}
u_{2I+1/2}^k &= u_{I+1/2}^{k-1}, \\
u_{2I+3/2}^k &= \frac{1}{2} \left[ u_{I+1/2}^{k-1} + u_{I+3/2}^{k-1} \right], \tag{3.87}
\end{aligned}$$

$$h_{2I}^k = \frac{1}{4} [3h_I^{k-1} + h_{I-1}^{k-1}], \quad (3.88)$$

$$h_{2I+1}^k = \frac{1}{4} [3h_I^{k-1} + h_{I+1}^{k-1}],$$

$$p_{2I}^k = \frac{1}{4} [3p_I^{k-1} + p_{I-1}^{k-1}], \quad (3.89)$$

$$p_{2I+1}^k = \frac{1}{4} [3p_I^{k-1} + p_{I+1}^{k-1}],$$

and for two-dimensional grid as:

$$u_{2I+1/2,2J}^k = \frac{1}{4} [3u_{I+1/2,J}^{k-1} + u_{I+1/2,J-1}^{k-1}],$$

$$u_{2I+3/2,2J}^k = \frac{1}{8} [3(u_{I+1/2,J}^{k-1} + u_{I+3/2,J}^{k-1}) + u_{I+1/2,J-1}^{k-1} + u_{I+3/2,J-1}^{k-1}], \quad (3.90)$$

$$u_{2I+1/2,2J+1}^k = \frac{1}{4} [3u_{I+1/2,J}^{k-1} + u_{I+1/2,J+1}^{k-1}],$$

$$v_{2I,2J+1/2}^k = \frac{1}{4} [3v_{I,J+1/2}^{k-1} + v_{I-1,J+1/2}^{k-1}],$$

$$v_{2I+1,2J+1/2}^k = \frac{1}{4} [3v_{I,J+1/2}^{k-1} + v_{I+1,J+1/2}^{k-1}], \quad (3.91)$$

$$v_{2I,2J+3/2}^k = \frac{1}{8} [3(v_{I,J+1/2}^{k-1} + v_{I,J+3/2}^{k-1}) + v_{I-1,J+1/2}^{k-1} + v_{I-1,J+3/2}^{k-1}],$$

$$v_{2I+1,2J+3/2}^k = \frac{1}{8} [3(v_{I,J+1/2}^{k-1} + v_{I,J+3/2}^{k-1}) + v_{I+1,J+1/2}^{k-1} + v_{I+1,J+3/2}^{k-1}],$$

$$h_{2I,2J}^k = \frac{1}{16} [9h_{I,J}^{k-1} + 3(h_{I-1,J}^{k-1} + h_{I,J-1}^{k-1}) + h_{I-1,J-1}^{k-1}],$$

$$h_{2I+1,2J}^k = \frac{1}{16} [9h_{I,J}^{k-1} + 3(h_{I+1,J}^{k-1} + h_{I,J-1}^{k-1}) + h_{I+1,J-1}^{k-1}], \quad (3.92)$$

$$h_{2I,2J+1}^k = \frac{1}{16} [9h_{I,J}^{k-1} + 3(h_{I,J+1}^{k-1} + h_{I-1,J}^{k-1}) + h_{I-1,J+1}^{k-1}],$$

$$h_{2I+1,2J+1}^k = \frac{1}{16} [9h_{I,J}^{k-1} + 3(h_{I+1,J}^{k-1} + h_{I,J+1}^{k-1}) + h_{I+1,J+1}^{k-1}],$$

$$p_{2I,2J}^k = \frac{1}{16} [9p_{I,J}^{k-1} + 3(p_{I-1,J}^{k-1} + p_{I,J-1}^{k-1}) + p_{I-1,J-1}^{k-1}],$$

$$p_{2I+1,2J}^k = \frac{1}{16} [9p_{I,J}^{k-1} + 3(p_{I+1,J}^{k-1} + p_{I,J-1}^{k-1}) + p_{I+1,J-1}^{k-1}], \quad (3.93)$$

$$p_{2I,2J+1}^k = \frac{1}{16} [9p_{I,J}^{k-1} + 3(p_{I,J+1}^{k-1} + p_{I-1,J}^{k-1}) + p_{I-1,J+1}^{k-1}],$$

$$p_{2I+1,2J+1}^k = \frac{1}{16} [9p_{I,J}^{k-1} + 3(p_{I+1,J}^{k-1} + p_{I,J+1}^{k-1}) + p_{I+1,J+1}^{k-1}].$$

### 3.4 Calculation details

Solutions are generated using an implicit  $\beta$ -method, as discussed in Subsection 3.2.1.2, with  $\beta = 3/4$  for the DAF and using an implicit and unconditionally stable Crank-Nicolson scheme for the LUB model. Solution starts with initial conditions of a flat free surface and liquid-liquid interface and a fully developed velocity profile. A typical time step tolerance of  $TOL = 10^{-3}$  was used to adjust the magnitude of the time increment. A computational domain of  $l = 100$  is found to be sufficient to ensure fully developed flow both far upstream and downstream the topography for both flow configurations investigated. However, the figures presented in the subsequent chapters do not necessarily cover the entire solution domain, but focus instead on regions where there is significant free-surface and interface disturbances present to be of interest.

To ensure mesh independence of the results generated several numerical experiments were performed using different numbers of grid points for a reference case of two-dimensional flow over a step-down topography for comparison. For convenience the fluid properties of both layers are taken to be the same and to have the same thickness and  $|s_0|$  taken to be 0.1. The percentage change in the capillary ridge height that forms upstream of the topography for each solution is plotted against the number of mesh points used, Figure 3.6, revealing a solution domain containing 1025 equally spaced grid points on the finest level of a multigrid hierarchy to be more than sufficient to guarantee mesh independent results.

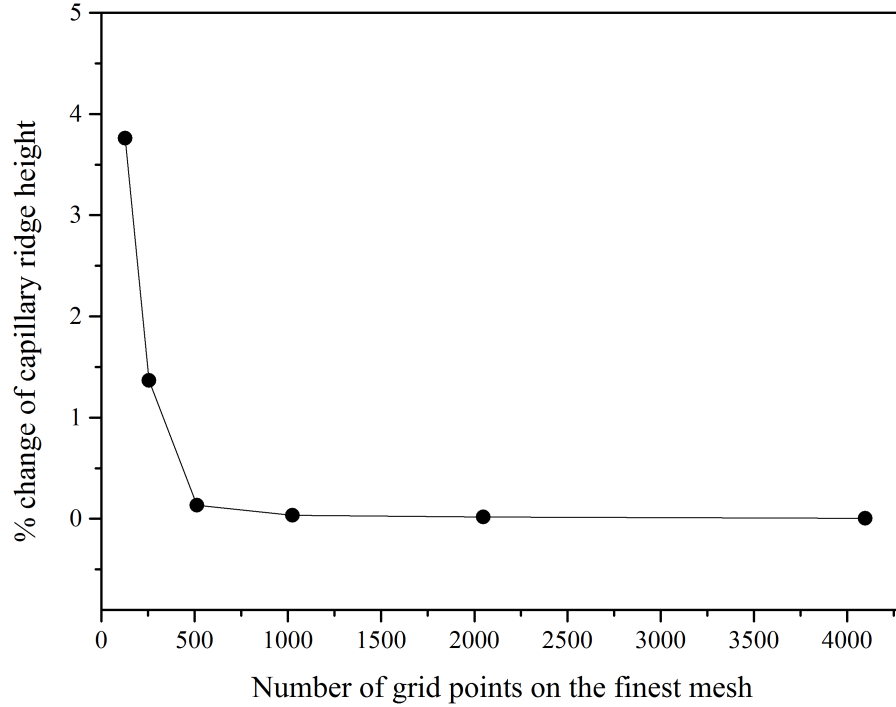


Figure 3.6: Mesh dependence of the capillary ridge height for flow over a step-down topography with  $h_{10} = 0.5$ ,  $|s_0| = 0.1$ ,  $\rho_2 = \mu_2 = 1.0$ ,  $\theta = 10^\circ$  and  $Re = 0$

Therefore for the two-dimensional flow case, five grid levels were used to generate the results with the coarsest level containing 65 and the finest grid level containing 1025 equally spaced grid points in the x-direction. The topography steepness parameter is set to 0.001 which insures the solution is independent of  $\delta$ , Veremieiev *et al.* (2010). Multigrid V-cycles are executed at each time step to reduce residuals below  $10^{-5}$  on the finest grid level. Figure 3.7 shows the convergence history, in terms of the residual, for the problem solved in Figure 3.6 when the number of grid points on the finest grid level is 1025 – note the almost linear reduction achieved.

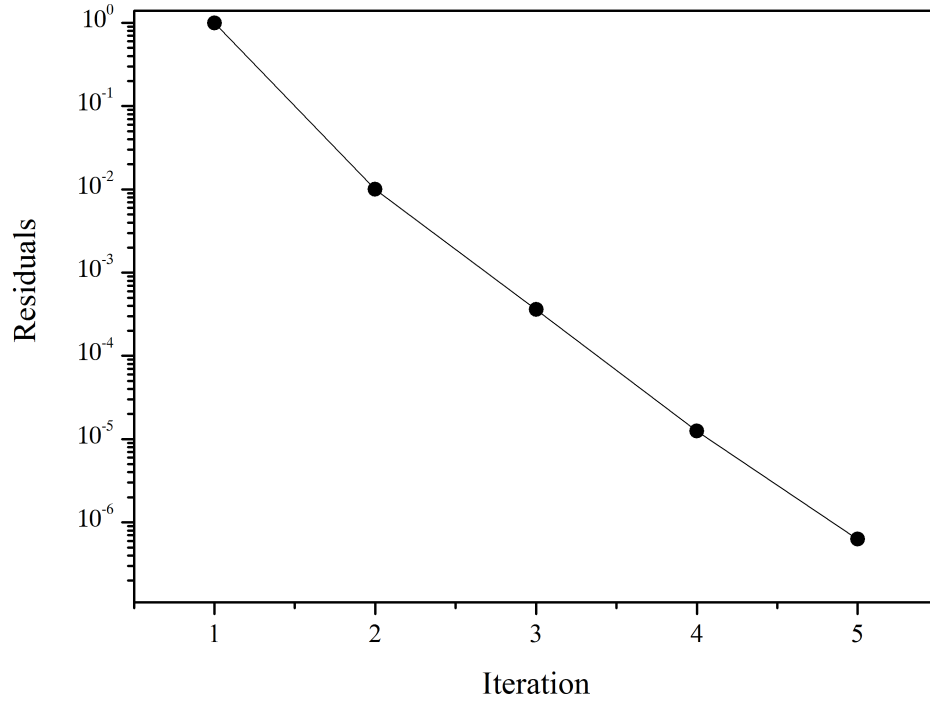


Figure 3.7: Convergence history for the problem of Figure 3.6 when the number of grid points on the finest grid level is 1025.

### 3.5 Comparison of DAF ( $Re=0$ ) and LUB results

Before continuing, in the subsequent chapters, to investigate channel and free-surface bilayer flow in depth, confirmation is established that the DAF and its corresponding discrete equation sets, when  $Re$  is set equal to zero, produce exactly the same set of results as the lubrication equations and their discrete form as given in Appendix D. This is done for two reasons: (i) to confirm the correctness of the bilayer models derived and (ii) that they have been solved consistently; since the mesh structure used in each case is different - the discrete form of the lubrication equations are solved on a collocated grid for the unknowns (see for example Sellier (2003), Gaskell *et al.* (2004), Lee *et al.* (2007)), while the discrete equation set associated with the DAF requires the use of a staggered grid arrangement for the

unknowns.

As shown below, comparison of the numerical solutions produced by both for the two flow configurations shown in Figure 3.8 and Figure 3.9 reveals that exactly the same results are achieved for the same flow parameters.

Figure 3.8 shows the predicted free surface disturbance obtained for film flow over trench topography when  $Re = 0$ ,  $Ca = 1.167 \times 10^{-4}$ ,  $|s_0| = 0.1$ ,  $l_t = 1.5$ ,  $h_0 = 0.4$ ,  $\mu_2 = \rho_2 = 1.0$  and  $\theta = 10^\circ$ ; Figure 3.9 on the other hand shows the predicted disturbance to the liquid-liquid interface for flow in a channel over a step-down topography when  $Re = 0$ ,  $Ca = 3.33 \times 10^{-4}$ ,  $|s_0| = 0.1$ ,  $h_0 = 0.4$ ,  $\mu_2 = \rho_2 = 1.0 \times 10^{-3}$  and  $\theta = 10^\circ$ .

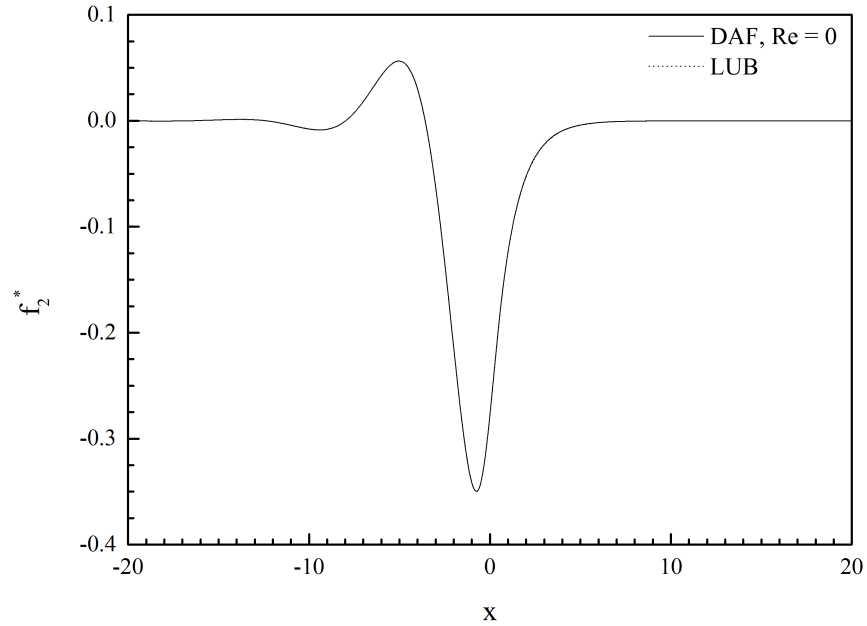


Figure 3.8: Comparison of free surface disturbance predicted by LUB and DAF models when  $Re = 0$ , for free-surface flow over a trench when  $h_0 = 0.4$ ,  $\rho_2 = \mu_2 = 1$ ,  $|l_t| = 1.5$ ,  $|s_0| = 0.1$ ,  $Ca = 1.167 \times 10^{-4}$  and  $\theta = 10^\circ$ .

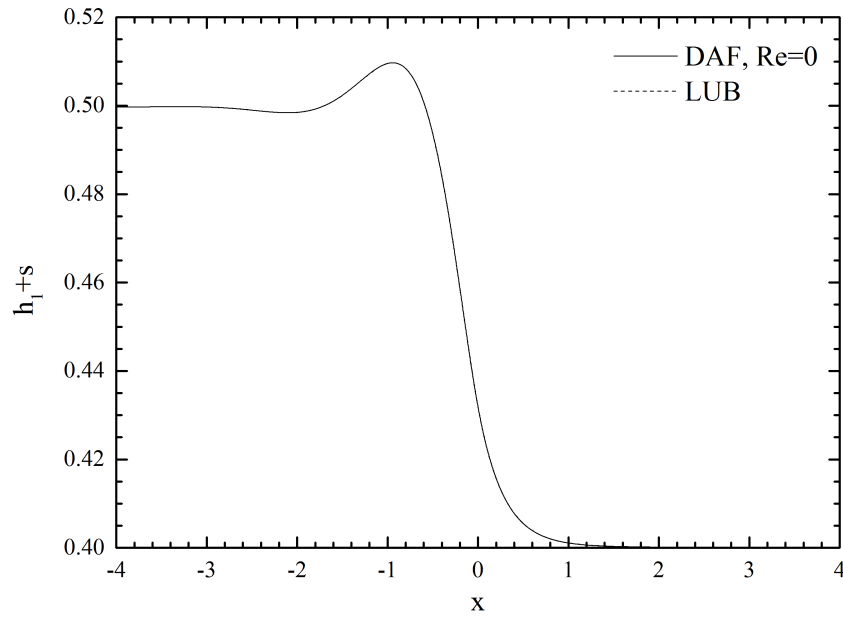


Figure 3.9: Comparison of liquid-liquid interface disturbance predicted by LUB and DAF models when  $Re = 0$  for channel flow over a step-down when  $h_0=0.4$ ,  $\rho_2 = \mu_2 = 1.0 \times 10^{-3}$ ,  $|s_0| = 0.1$ ,  $Ca = 3.33 \times 10^{-4}$  and  $\theta = 10^\circ$ .

For both problems the free-surface/liquid-liquid interface are indistinguishable and the results thus in excellent agreement. Accordingly, all of the results presented in subsequent chapters, unless indicated otherwise, are obtained using the DAF of the associated governing equations.

# Chapter 4

## Bilayer film flow in patterned channels

### Contents

---

<b>4.1 Gravity-driven flow . . . . .</b>	<b>95</b>
4.1.1 Validation . . . . .	95
4.1.2 Effect of the normal gravity term . . . . .	99
4.1.3 Effect of inertia . . . . .	100
<b>4.2 Pressure gradient and shear driven flow . . . . .</b>	<b>121</b>

---

In this chapter the flow of two superimposed immiscible liquids, one above the other, through an inclined channel containing a topographic feature, as shown schematically in Figure 2.1, is explored taking into account inertia effects. The influence of inertia, upper liquid properties as well as the topography type and dimensions are investigated. It extends the work of Lenz and Kumar (2007) who studied the non-inertial flow case only and that of Zhou and Kumar (2012) who considered the same problem including inertia but with limited success.

Figure 4.1 shows a schematic diagram of the interface profile features for flow over step-down and step-up topographies. The interface profile for flow over a step-down topography is characterised by the presence of a capillary ridge upstream of the step while for flow over a step-up the interface profile exhibits an upstream capillary trough. The height(depth) of the capillary ridge(trough),  $h_{ridge}(h_{trough})$ , is defined as the difference between the maximum(minimum) interface height and the inlet height where the interface is flat.

In addition, other means for driving the flow are considered, with the flow (i) due to a pressure difference along the length of the channel and (ii) induced by shearing the upper liquid layer via a translating channel wall, explored.

In their work, Lenz and Kumar (2007) limited their study to situations where inertia is negligible allowing them to construct a lubrication model to tackle the problem. Subsequently, Zhou and Kumar's (2012) attempt to extend this to inertial flows using a diffuse-interface proved problematic. They managed to generate some results for flow over step-down topography but their method was unable to deal with flow past a step-up. Also they simulated flows at arguably unrealistically high Reynolds numbers which may be prone to inertial instability, Amaouche *et al.* (2007).

The set of governing equations, (2.109), (2.110), (2.114) and (2.115), are solved using the the multigrid method described in Chapter 3. A computational domain

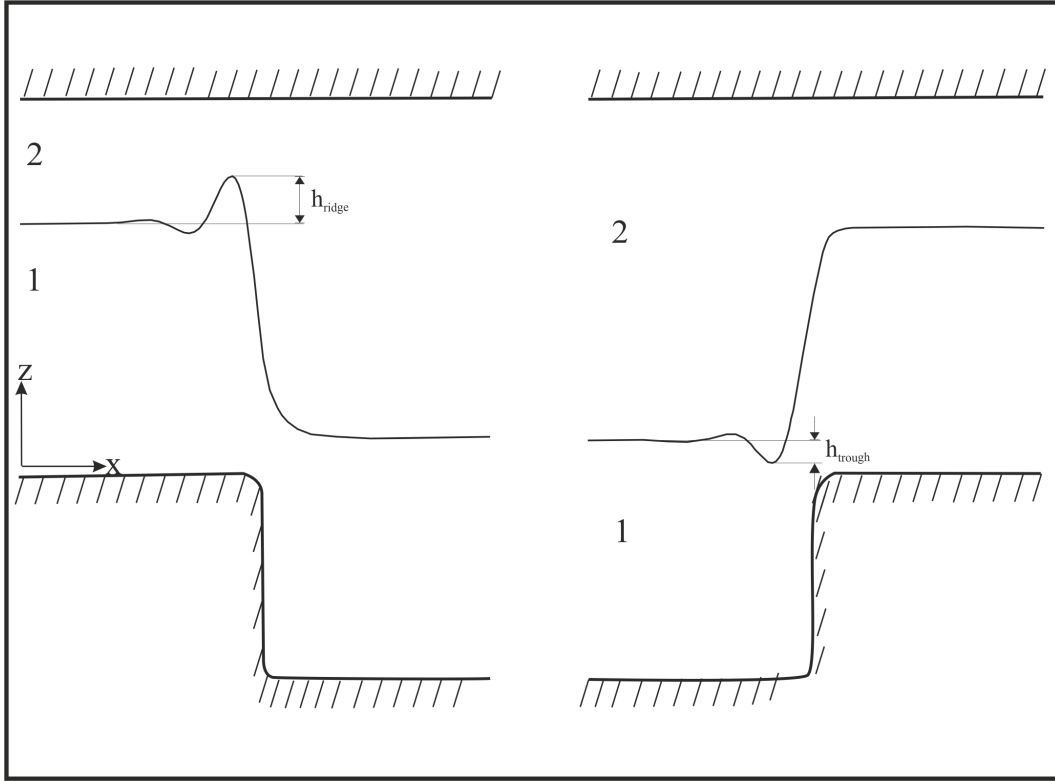


Figure 4.1: Schematic diagram for bilayer flow in a channel containing a step-down (left) and step-up (right) topography. for each problem the flow is from left to right.

of length  $l = 100$  is chosen which is large enough to ensure a flat interface both upstream and downstream of the topography. However, in the subsequent results section only the part of solution domain where there is a significant disturbance to the liquid-liquid interface is shown. It should be remembered, see Chapter 2, that  $h_{10}$  for both step-up and step-down topography is taken as the thickness of the lower layer in the unrestricted part of the channel. Throughout this study the long-wave parameter,  $\varepsilon$  is set to 0.1 and the capillary number  $Ca = 3.33 \times 10^{-4}$  in order to be consistent with the work of Lenz and Kumar (2007) and Zhou and Kumar (2012).

The Reynolds number range investigated is chosen to be in the stable region as proposed by Amaouche *et al.* (2007) so as to avoid the possibility of inertial instabilities. Their analysis requires that  $\left(\frac{\cot \theta}{Re_{crit}}\right)$  is always much smaller than 1.0 except when  $h_{10}$  is close to unity. The inclination angle of the channel is taken to

be  $\theta = 10^\circ$  unless stated otherwise. The stable Reynolds number range based on this value is  $Re \leq 150$ .

## 4.1 Gravity-driven flow

### 4.1.1 Validation

We begin by considering the same channel flow problem solved by Lenz and Kumar (2007). Because they ignored the normal gravity component in the derivation of the lubrication equation describing their model, the results they obtained are only strictly correct when the channel is vertically aligned. For the purpose of comparison the inclination angle is set to  $90^\circ$  throughout this validation section. In subsequent figures the x-axis is shifted so that the origin is located at the centre of the topography.

Figure 4.2 shows the effect of increasing the topography height,  $s_0$ , while keeping  $h_{10} = 0.1$  for flow in a channel containing a step-down topography, when  $\rho_2 = 0$  and  $\mu_2 = 10^{-3}$ , which Lenz and Kumar (2007) called the single-layer limit because the effect of the upper layer is negligible. Each curve in the graph represents a particular value of topography height, starting at  $s_0 = 0.04$  and increasing by intervals of 0.08 to reach the value 0.6. The results obtained show that increasing  $s_0$  leads to a monotonic increase in the capillary ridge height formed upstream of the step-down topography. This behaviour is similar to that experienced by a single layer thin film flowing down an inclined substrate and meeting a step-down feature, Kalliadasis *et al.* (2000), Decré and Baret (2003) and Gaskell *et al.* (2004). The model is unable to generate results for  $|s_0| > 0.6$ .; the reason for this is that the single-layer like behaviour of the flow results in the interface height at the capillary

ridge exceeding 1.0 at step heights larger than 0.6, which violates the model as the upper wall is located at  $z = 1$ .

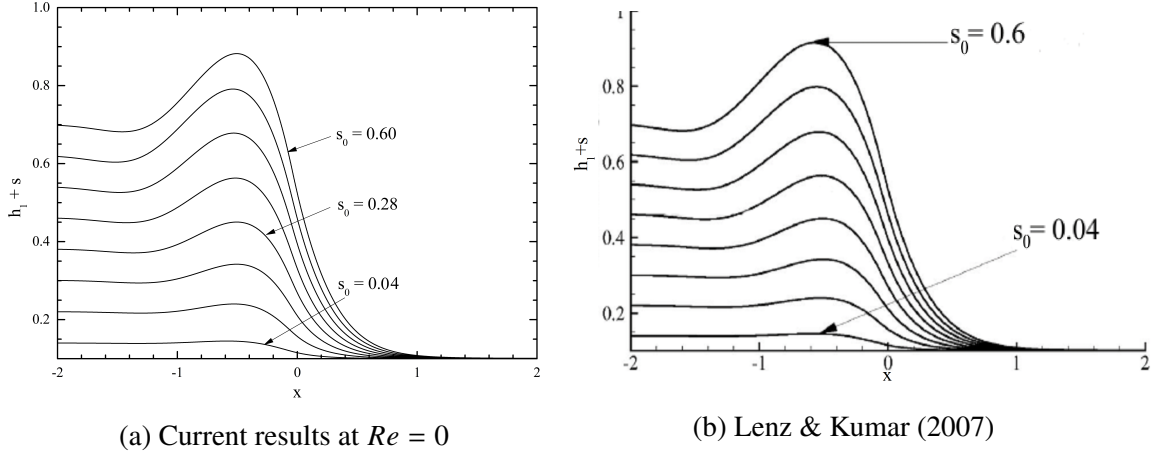


Figure 4.2: Effect of topography height on the interface profile for flow over a step-down topography when  $h_{10} = 0.1$ ,  $\rho_2 = 0$ ,  $\mu_2 = 1 \times 10^{-3}$ ,  $Ca = 3.33 \times 10^{-4}$ ;  $\theta = 90^\circ$ .

Considering instead the case  $\mu_2 = \rho_2 = 1$  leads to an upper layer which destroys the monotonic behaviour described above, in that the capillary ridge height first increases with increasing  $s_0$  before decreasing as the gap between the interface and the upper wall becomes smaller and smaller, as shown in Figure 4.3. This effect can be attributed to the large pressure gradient arising in the upper layer in order to drive the liquid through the narrow gap between the interface and the upper channel wall. Results show that this pressure gradient leads to a decreasing capillary ridge height until it is completely suppressed at large  $s_0$ , as for the case when  $|s_0| = 0.92$ . The presence of a non-negligible upper layer enables the simulation of flows with large  $s_0$ .

Figure 4.4 shows the change of capillary ridge height with topography height for different combinations of  $\rho_2$  and  $\mu_2$ . It is clear that increasing the density or viscosity of the upper layer reduces the capillary ridge and that in all cases, except the single-layer limit, leads to a growth in capillary ridge height with topography height, which reaches a maximum and then decreases subsequently.

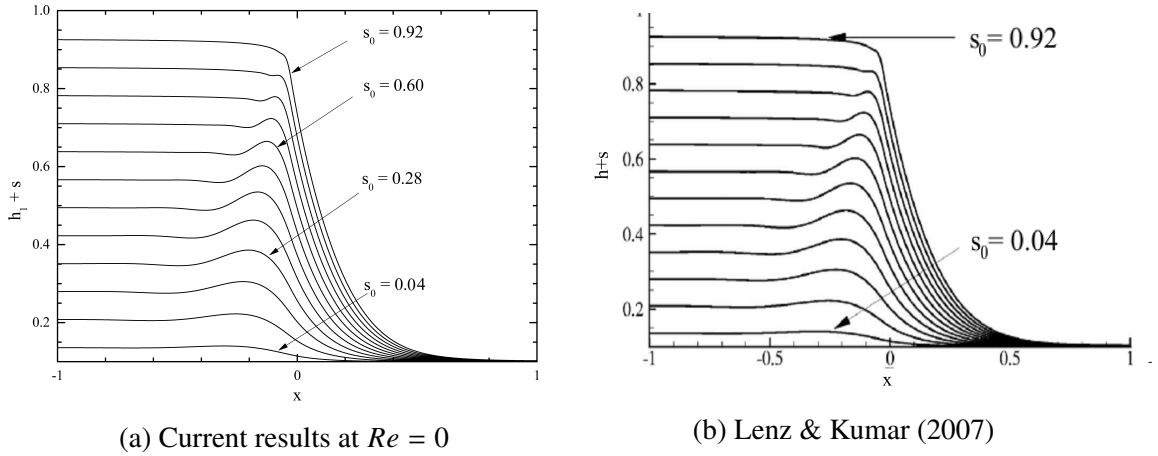
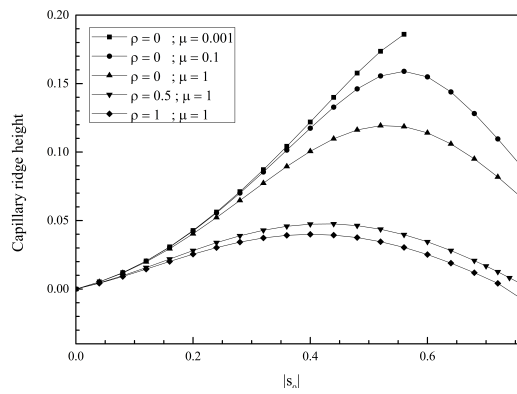


Figure 4.3: Effect of topography height on the interface profile, for flow over a step-down topography when  $h_{10} = 0.1$ ,  $\rho_2 = 1$ ,  $\mu_2 = 1$ ,  $Ca = 3.33 \times 10^{-4}$ ,  $\theta = 90^\circ$ .

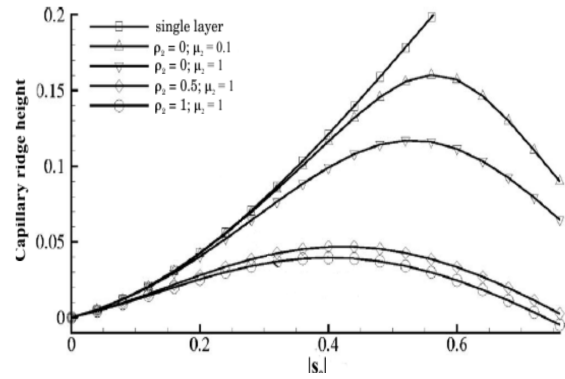
Figure 4.5 reveals the dependence of the capillary ridge on the height of the step-down for several values of  $h_{10}$  when  $\rho_2 = \mu_2 = 1$ . Each curve shows the same trend, that of an increasing capillary ridge height to a maximum value with increasing  $s_0$  followed by a reduction of the ridge height as  $s_0$  is increased further. It can be seen that the ridge height is decreased by increasing the thickness of the lower layer if  $|s_0| < 0.65$ . For a topography height,  $|s_0|$ , above this limit, the curves for different  $h_{10}$  intersect and the capillary ridge height can become negative. A negative ridge height simply means a capillary ridge rather than trough but the interface at the position of the capillary ridge is below the flat interface thickness,  $h_{10}$ , at the channel inlet.

A comparison of results generated here for  $Re = 0$  with those of Lenz and Kumar (2007), is provided in Figure 4.6 for flow in a channel containing a mound with  $s_0 = 0.48$  and a width,  $l_t$  of 2, and 4 when  $\rho_2 = \mu_2 = 1$ . The figure shows that if the topography is wide enough the interface behaves as in the case of flow past two independent topographies; a step-up followed a step-down.

It is clear from each of the above problems that excellent agreement is achieved between the results obtained with the DAF when  $Re = 0$  and the lubrication ap-

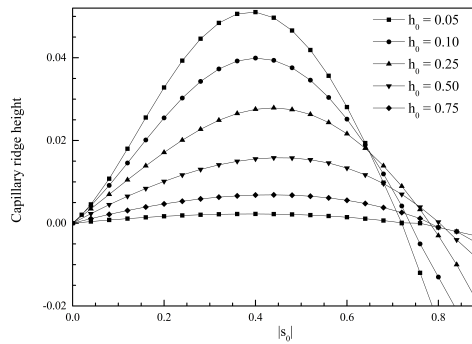


(a) Current results at  $Re = 0$

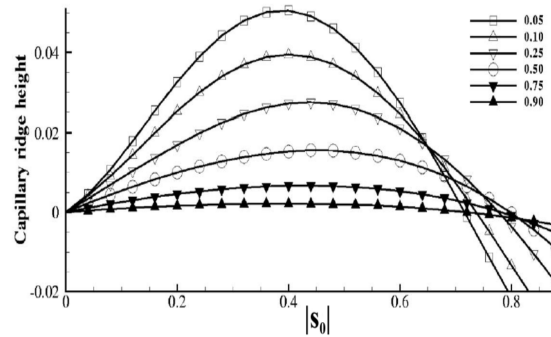


(b) Lenz & Kumar (2007)

Figure 4.4: Effect of topography height on capillary ridge height for flow over a step-down, for  $h_{10} = 0.1$ ,  $Ca = 3.33 \times 10^{-4}$ ,  $\theta = 90^\circ$  and different combination of upper liquid properties.



(a) Current results at  $Re = 0$



(b) Lenz & Kumar (2007)

Figure 4.5: Effect of topography height on capillary ridge height, for flow over a step-down topography when  $\rho_2 = \mu_2 = 1$ ,  $\theta = 90^\circ$  and different values of  $h_{10}$ .

proximation predictions of Lenz and Kumar (2007).

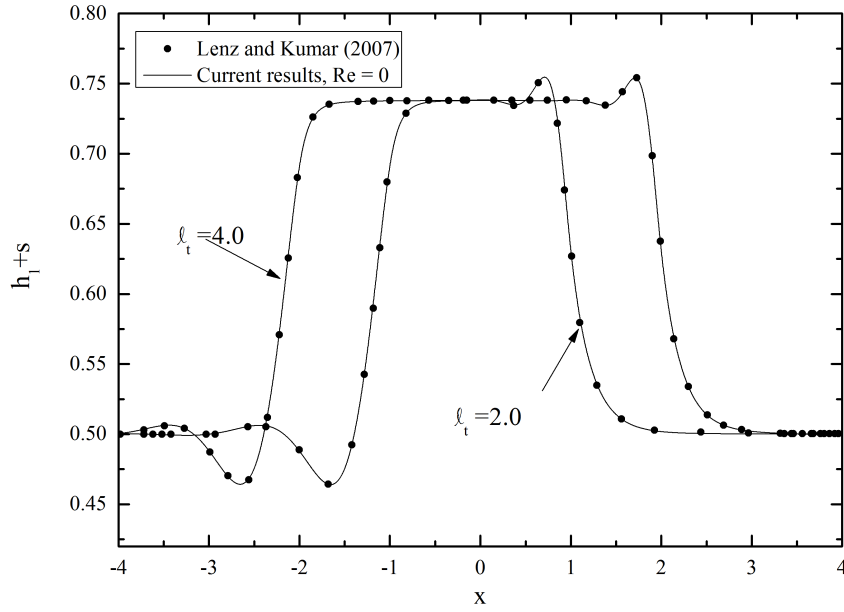


Figure 4.6: Comparison of current results with those of Lenz and Kumar for flow in channel containing a mound topography given by  $|s_0|=0.48$  when  $h_{10}=0.5$ ,  $Ca=3.33 \times 10^{-4}$ ,  $\rho_2 = \mu_2 = 1.0$ ,  $\theta = 90^\circ$ .

#### 4.1.2 Effect of the normal gravity term

As demonstrated above, comparisons with results of Lenz and Kumar (2007) show excellent agreement for the particular case when the angle of inclination,  $\theta = 90^\circ$  and  $Re = 0$ . However, results differ when the channel is not vertical with the deviation between them increasing with decreasing inclination angle. This can be explained in terms of the normal gravity term in the pressure equation. The term  $(\rho_2 - \rho_1)\varepsilon \cos \theta \frac{\partial(h_1 + s)}{\partial x}$  appearing in equation (2.109) represents the gravity component perpendicular to the flow direction. This term does not appear in the Lenz and Kumar (2007) model formulation as they omitted the normal gravity component from their derivation for simplicity. When  $\rho_2 = \rho_1$  or the channel is vertical this term vanishes but the effect of ignoring this term on the result is more pronounced when the inclination angle is small and the two fluids have different densities. This is shown in Figure 4.7 for flow through a channel with a step-down of  $|s_0| = 0.1$ , inclined at angles of  $\theta = 5^\circ, 10^\circ, 90^\circ$ , when  $h_{10} = 0.4$ ,  $\rho_2 = 1 \times 10^{-3}$ ,  $\mu_2 = 1$

and  $B = 12$ . The figure reveals that Lenz and Kumar's results are suitable only for vertical or nearly vertically aligned channels while for small inclination angles the results are quantitatively inaccurate. Bertozzi and Brenner (1997) arrived at the same conclusion when comparing theoretical predictions with experiments for flow down an inclined plane.

### 4.1.3 Effect of inertia

Figure 4.8 shows the interface profile generated for flow through a channel with a step-down of  $|s_0| = 0.1$  and  $0.4$ , when the upper layer effect is negligible ( $\rho_2 = 0, \mu_2 = 1 \times 10^{-3}$ ) and  $h_{10} = 0.4$ . It reveals that far from the step the thickness of the lower layer is the same for both the wide and narrow parts of the channel due to the absence of any effect from the upper layer. The figure also shows that by increasing  $Re$  from 0 to 150 the interface exhibits a wavy profile in the vicinity of the topography and instead of there being a single capillary ridge, as in the case when  $Re = 0$ , there appears a damped capillary effect with a maximum amplitude at the edge of the step-down. This behaviour finds support from the work of Saprykin *et al.* (2007) and Bontozoglou and Serifi (2008) for single layer free surface flow down vertical substrate despite, as it does, their work violating the inertial stability criteria for free-surface flow,  $Re_{crit} = \frac{5}{4} \cot \theta$ , Yih (1963).

When a non-negligible top layer is imposed ( $\rho_2 = \mu_2 = 1$ ) it influences the liquid-liquid interface profile; the capillary ridge height becomes smaller and the far end thickness of the lower layer is no longer the same at inlet and outlet, as shown in Figures 4.9 and 4.10, however the ratio  $\frac{h_2}{h_1} \Big|_{inlet}$  is preserved at the outlet. Compared to the single-layer limit when the ridge height increases monotonically with increasing  $Re$  or  $|s_0|$ , the two-layer case when the upper layer is not negligible shows a different trend, see Figure 4.11. For all  $Re$  values the ridge height increases to a

maximum with increasing  $|s_0|$  and then it drops; the ridge height becomes negative at large topography heights. The same behaviour was noted by Lenz and Kumar (2007) for inertialess flow. Increasing  $Re$  increases the ridge height in a monotonic fashion if  $|s_0| < 0.5$ , while for  $|s_0|$  above this limit the ridge height shows a decrease at high  $Re$ , as shown in Figure 4.12. Inspection of the pressure gradients that develop in both layers, as shown in Figure 4.13, provides some understanding as to the interface behaviour. In the single-layer limit the flow exhibits no pressure gradient in the top layer while in the lower layer a pressure gradient develops in the vicinity of the topography and is zero elsewhere. The magnitude of the pressure variations, including a peak corresponding to the capillary ridge followed by a deep negative minimum, are amplified by increasing  $Re$ . This explains the monotonic growth of the capillary ridge height with  $Re$  and  $|s_0|$  and the constant value of the lower layer thickness when the interface is flat. For the two-layer case the lower layer exhibits similar pressure variations to the single-layer limit but with larger magnitude and a non-zero negative pressure gradient at the narrow part of the channel, while the upper layer now, unlike the single-layer case, exhibits a pressure gradient with the magnitude of its variation increasing with increasing  $Re$ .

Figures 4.14 and 4.15 show the interface profile for flow in a channel with a step-down topography for several values of  $h_{10}$  with negligible and non-negligible upper layer and a  $Re$  value of 0 and 150. The effect of increasing  $h_{10}$  on the interface disturbances is summarised in Figure 4.16. It shows a drop in the capillary ridge height when  $Re = 0$  for both single- and two-layer cases. This may be attributed to the fact that increasing  $h_{10}$ , while keeping  $|s_0|$  constant, is equivalent to reducing the topography height which is known to reduce the capillary ridge height, Lenz and Kumar (2007) and Kalliadasis *et al.* (2000). Furthermore, for the two-layer case this is accompanied by a larger pressure gradient in the top layer due to the increasing resistance to flow caused by reducing the gap between the interface and

the top wall. When  $Re = 150$  the two cases show different trends; the two-layer flow shows almost no change in the capillary ridge height with increasing the interface height until  $h_{10} = 0.5$ , when it then decreases; while in the single-layer limit the ridge height first drops when  $h_{10}$  is increased from 0.1 to 0.2 and then it grows with further increase in  $h_{10}$ . This may be attributed to the fact that the increased inertia of the lower layer in the single-layer limit faces no resistance from the top layer, while for the two-layer case the inertia of the top layer tends to suppress the interface. This might also be connected to the stability of the flow as a single layer flowing at  $Re = 150$  with an angle of inclination of  $10^\circ$  would be considered unstable according to the stability criteria for single layer flow down an inclined substrate as mentioned earlier in this chapter.

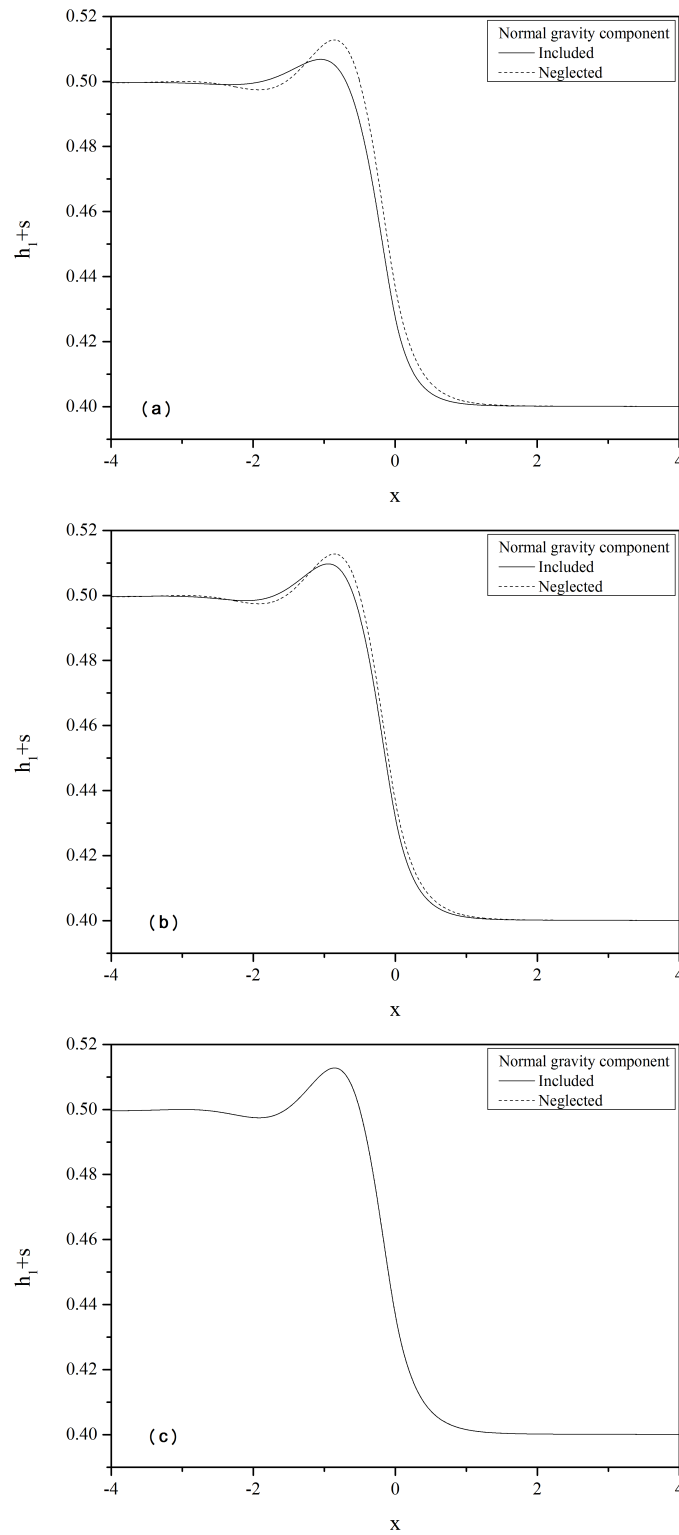


Figure 4.7: Effect of the normal gravity term on the interface shape for flow through a channel with a step-down of  $|s_0| = 0.1$  when  $h_{10} = 0.4$ ,  $Ca = 3.33 \times 10^{-4}$ ,  $\rho_2 = 1 \times 10^{-3}$  and  $\mu_2 = 1.0$ , with: (a)  $\theta = 5^\circ$ , (b)  $\theta = 10^\circ$  and (c)  $\theta = 90^\circ$ ;  $Re = 0$ .

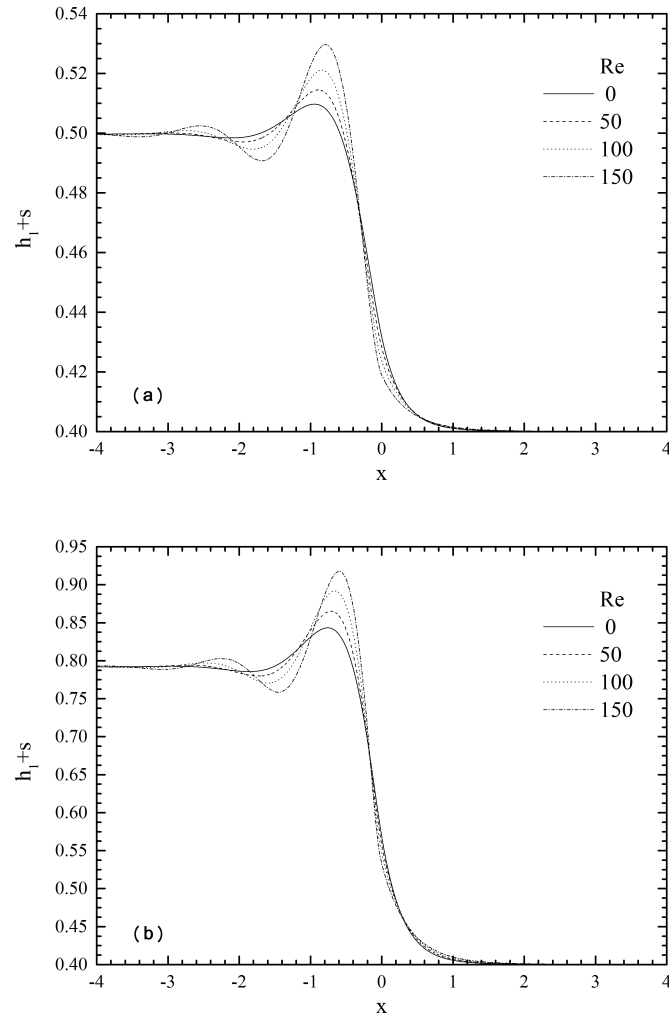


Figure 4.8: Effect of Reynolds number on the interface shape for flow in a channel with a step-down when  $h_{10}=0.4$ ,  $Ca= 3.33 \times 10^{-4}$  and  $\rho_2 = 0, \mu_2 = 1 \times 10^{-3}$ ,  $\theta = 10^\circ$ , with: (a)  $|s_0| = 0.1$  and (b)  $|s_0| = 0.4$ .

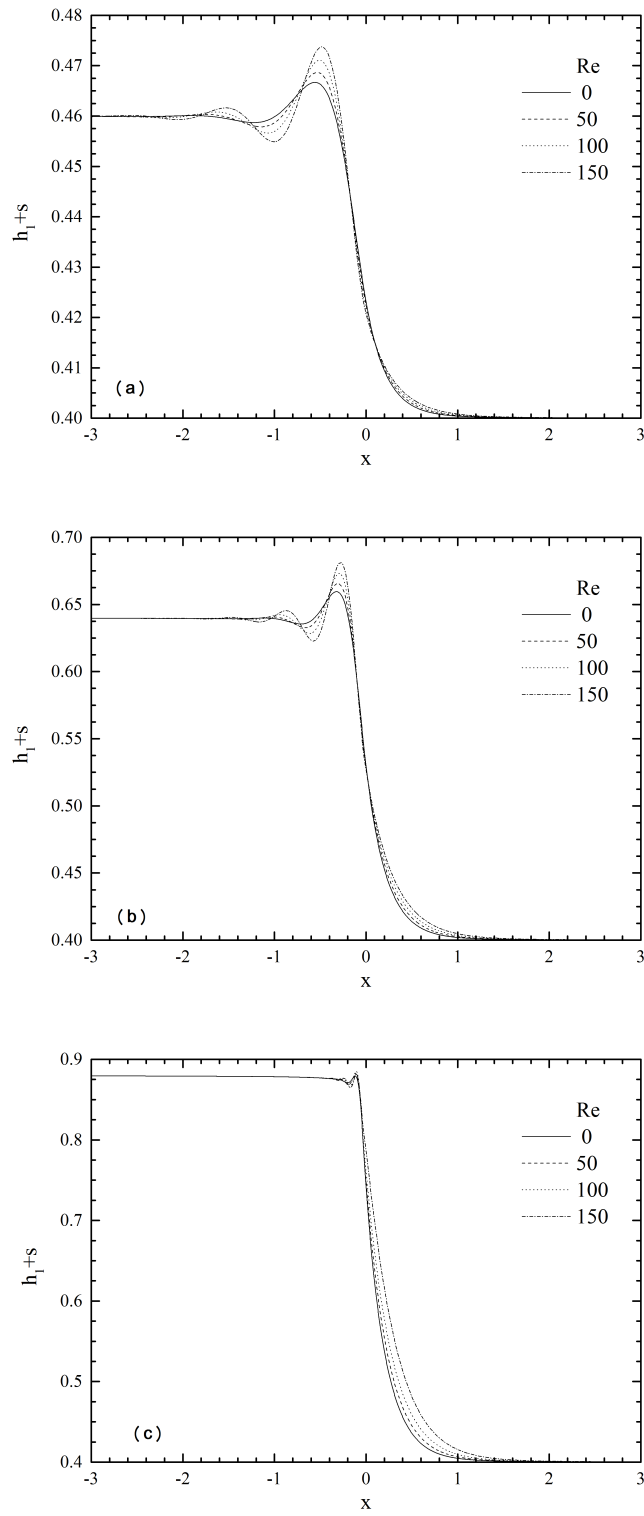


Figure 4.9: Effect of Reynolds number on the interface shape for flow in a channel with a step-down when  $h_{10}=0.4$ ,  $Ca= 3.33 \times 10^{-4}$  and  $\rho_2 = \mu_2 = 1.0$ ,  $\theta = 10^\circ$ , with: (a)  $|s_0| = 0.1$ , (b)  $|s_0| = 0.4$  and (c)  $|s_0| = 0.8$ .

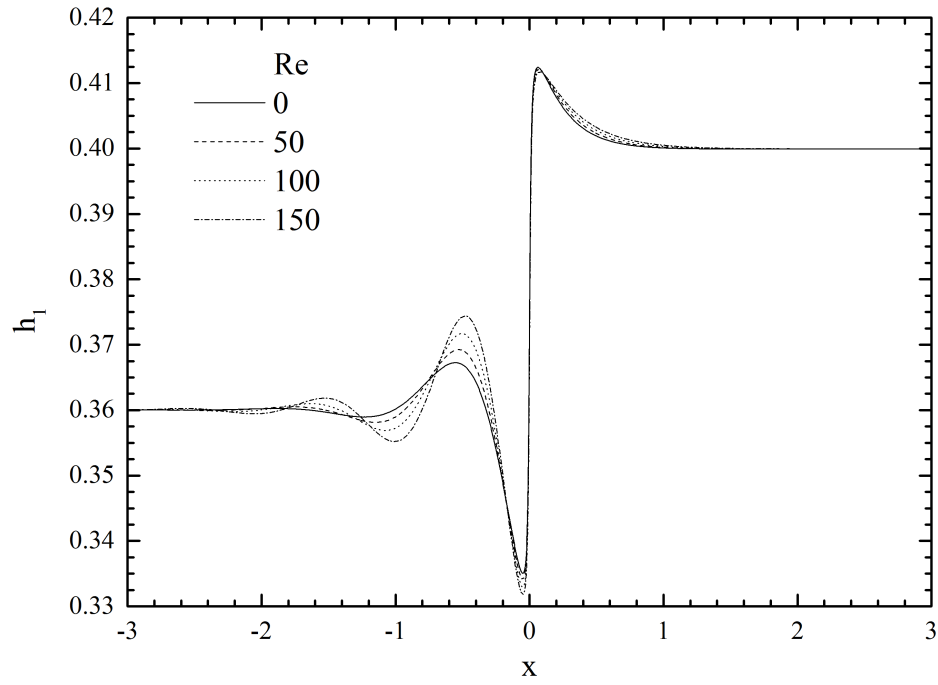


Figure 4.10: Lower layer thickness,  $h_1$  dependence on  $Re$  for flow in a channel with a step-down topography when  $h_{10}=0.4$ ,  $Ca= 3.33 \times 10^{-4}$ ,  $\rho_2 = \mu_2 = 1.0$ ,  $|s_0| = 0.1$ , and  $\theta = 10^\circ$ .

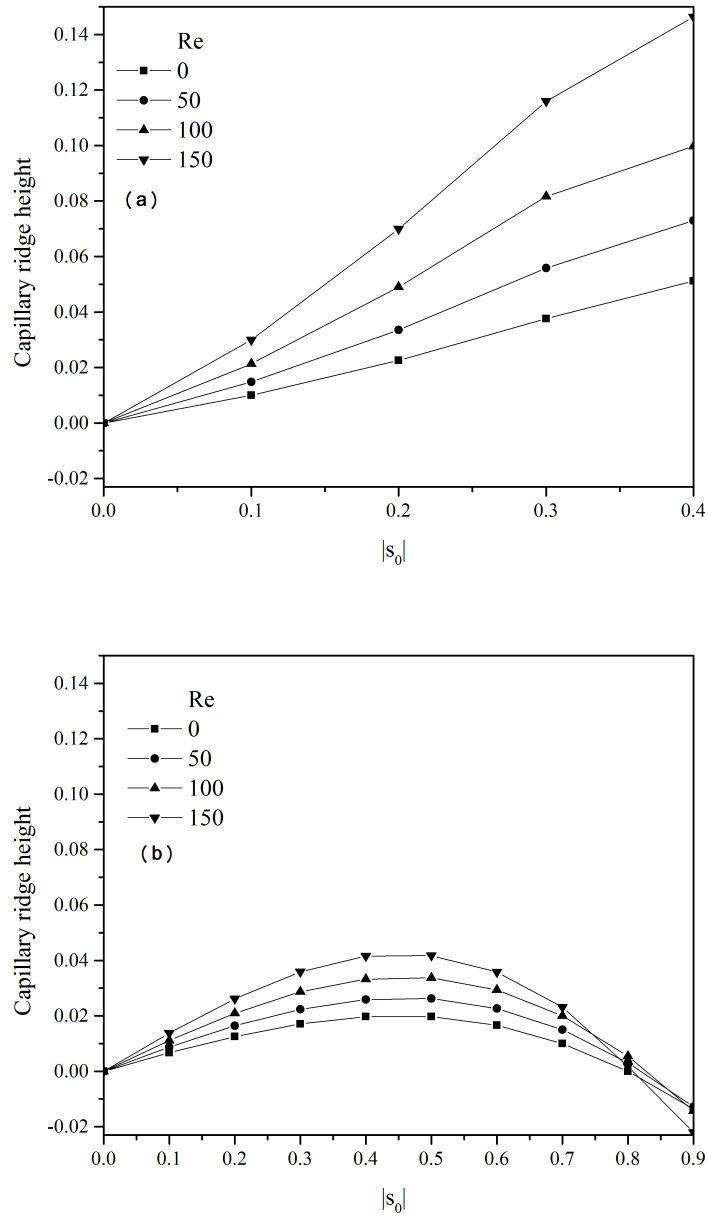


Figure 4.11: The dependence of capillary ridge height on the step height for a step-down when  $h_{10} = 0.4$ ,  $\theta = 10^\circ$ . (a)  $\rho_2 = 0$ ,  $\mu_2 = 1 \times 10^{-3}$  and (b)  $\rho_2 = 1$ ,  $\mu_2 = 1$ .

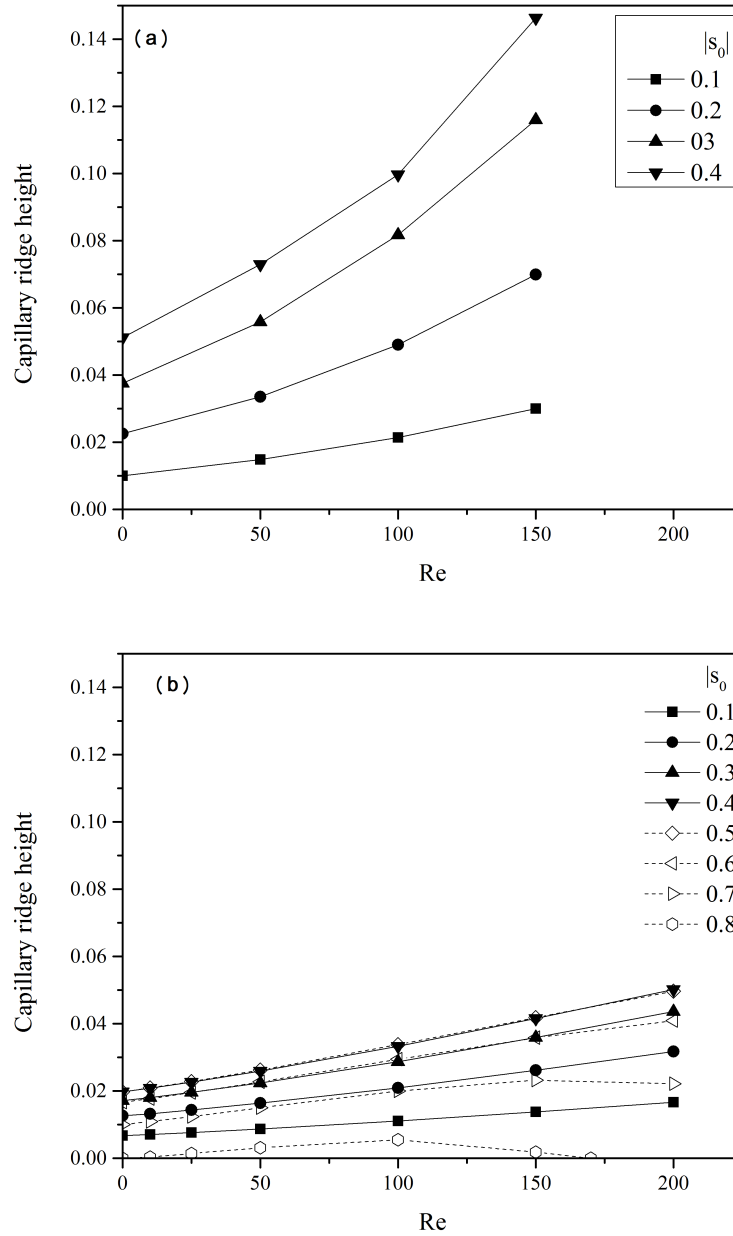


Figure 4.12: The dependence of capillary ridge height on Re for a step-down when  $h_{10}=0.4$ ,  $Ca= 3.33 \times 10^{-4}$  and  $\theta = 10^\circ$ , with: (a)  $\rho_2 = 0$ ,  $\mu_2 = 1 \times 10^{-3}$  and (b)  $\rho_2 = 1$ ,  $\mu_2 = 1$ .

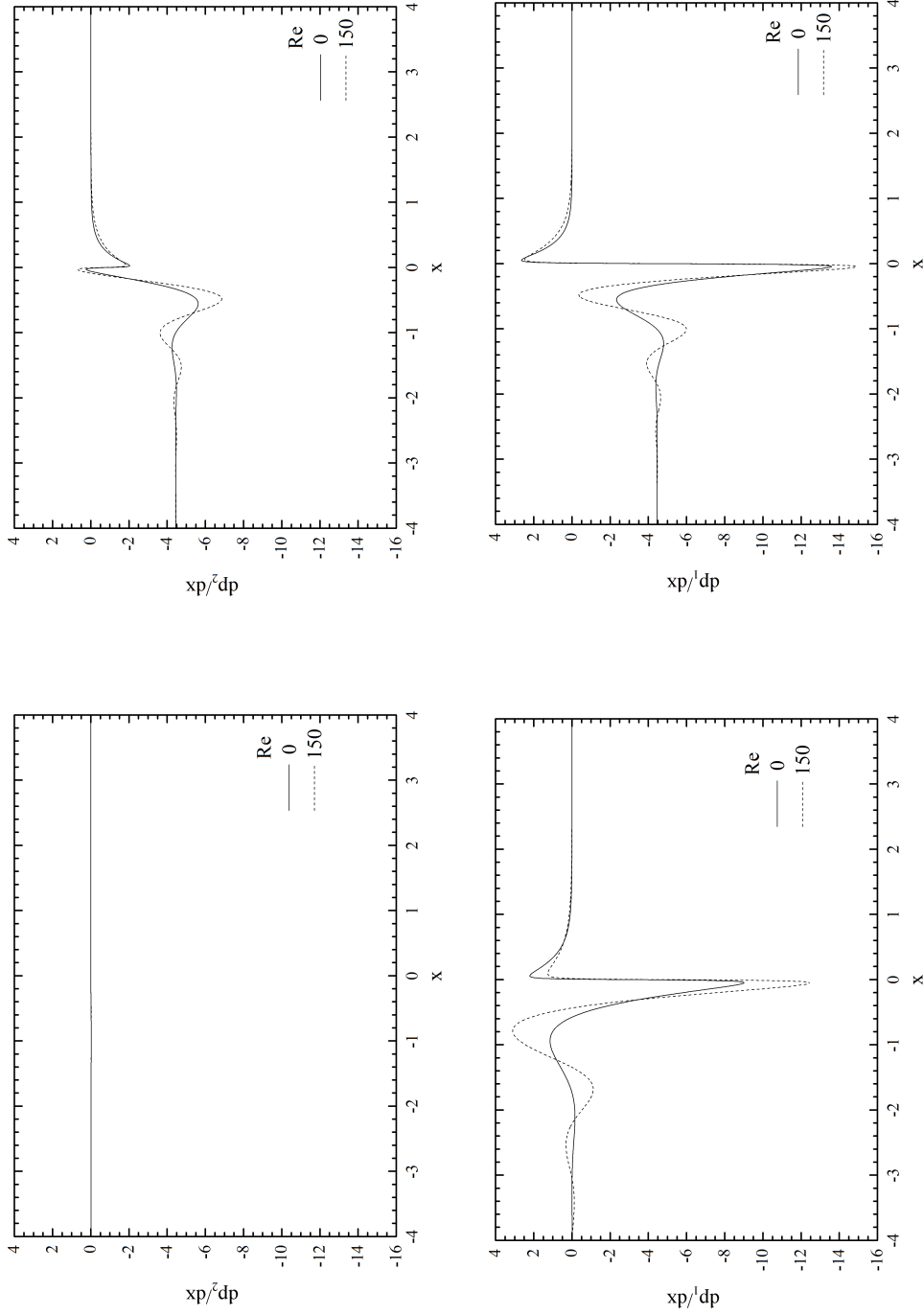


Figure 4.13: Pressure gradient profiles for flow in a channel with a step-down of  $|s_0| = 0.1$  when  $h_{10} = 0.4$ ,  $Ca = 3.33 \times 10^{-4}$  and  $\theta = 10^\circ$ ;  $\rho_2 = 0$ ,  $\mu_2 = 1 \times 10^{-3}$  (left),  $\rho_2 = \mu_2 = 1$  (right).

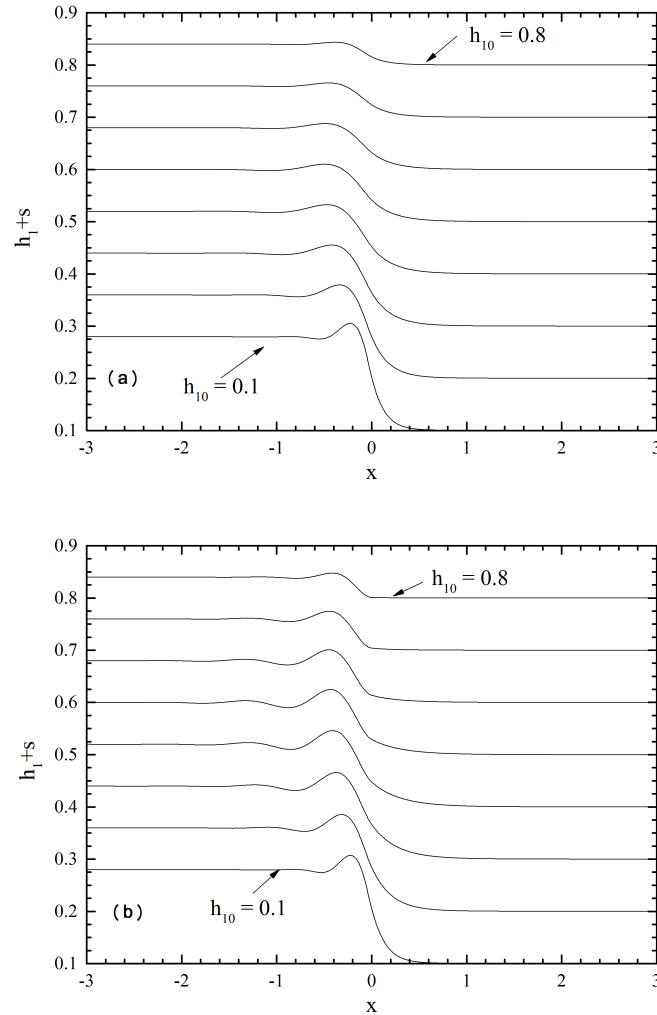


Figure 4.14: Comparison of interface shape for flow in a channel with a step-down in the absence and presence of inertial effects.  $|s_0| = 0.2$ ,  $Ca = 3.33 \times 10^{-4}$  and  $\rho_2 = 1$ ,  $\mu_2 = 1$ ,  $\theta = 10^\circ$  and (a)  $Re = 0$  and (b)  $Re = 150$ .

The effect of varying the density of the upper liquid on the interface profile is shown in Figures 4.17 and 4.18. Increasing the density of the top liquid relative to the lower one reduces the capillary trough depth both in the presence or absence of inertia.

The flow in a channel containing a step-up is also investigated. As in the case of free-surface flow of a single-layer thin film down an inclined substrate featuring a step-up, the interface profile shows a capillary trough upstream the topography. For both situations, a non-negligible top layer shown in Figure 4.19 and a negligible

top layer shown in Figure 4.20, the effect of inertia is the same: widening and amplifying the interface disturbances. Increasing the step height,  $|s_0|$  or Reynolds number,  $Re$ , results in a monotonic increase in the depth of the capillary trough, regardless of the upper layer's properties, as illustrated in Figures 4.21 and 4.22. This behaviour is different from that of the step-down discussed earlier. This may be attributed to the fact that the capillary trough, in contrast to the ridge associated with a step-down, does not obstruct the flow of the upper layer and hence there is no excessive pressure build-up in the top layer in order to satisfy the mass balance.

The effect of increasing Reynolds number on the interface profile for flow in a channel containing a mound of  $s_0 = 0.48$  and a step width,  $l_t$  of 4 when  $\rho_2 = \mu_2 = 1$  is shown in Figure 4.23. An increase in  $Re$  leads to widening of the interface disturbances and also the capillary ridge (trough) is pushed towards the step face by the increased inertia and its height (depth) is noticeably increased.

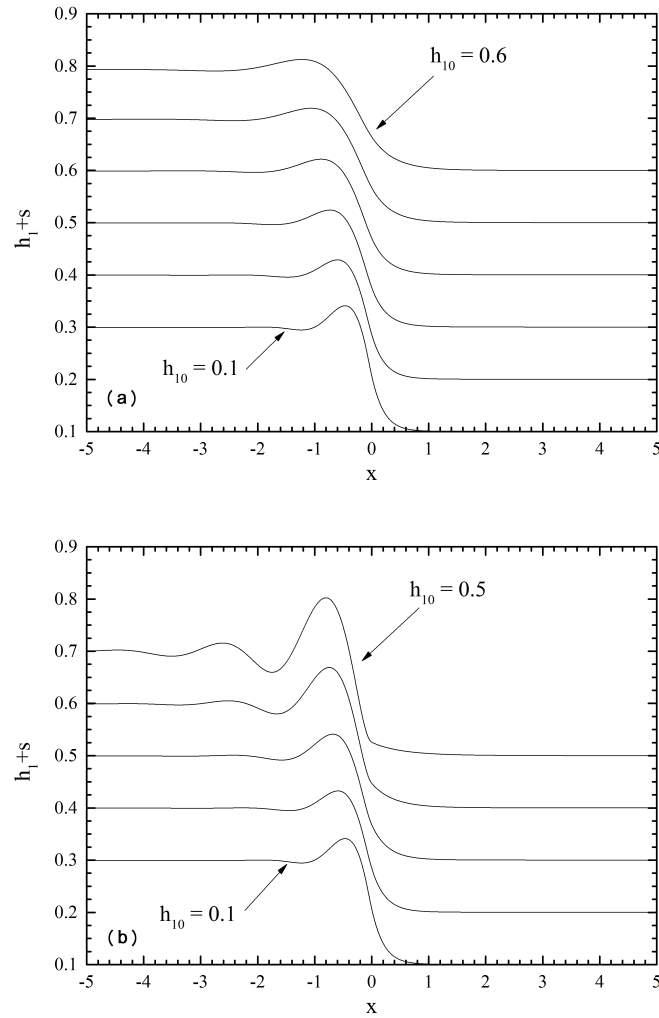


Figure 4.15: Comparison of interface shape for flow in a channel with a step-down in the absence and presence of inertial effects.  $|s_0| = 0.2$ ,  $Ca = 3.33 \times 10^{-4}$  and  $\rho_2 = 0$ ,  $\mu_2 = 1 \times 10^{-3}$ ,  $\theta = 10^\circ$  and (a)  $Re = 0$  and (b)  $Re = 150$ .

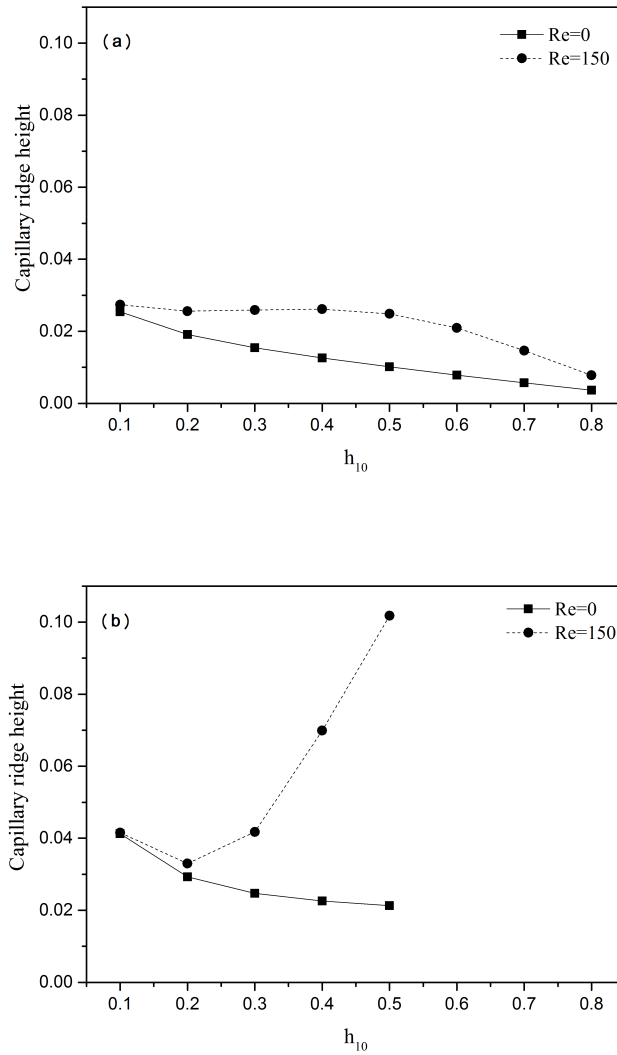


Figure 4.16: Effect of  $h_{10}$  on capillary ridge height for flow in a channel with a step-down of  $|s_0| = 0.2$ ,  $Ca = 3.33 \times 10^{-4}$ ,  $\theta = 10^\circ$  and (a)  $\rho_2 = \mu_2 = 1$  and (b)  $\rho_2 = 0, \mu_2 = 1 \times 10^{-3}$

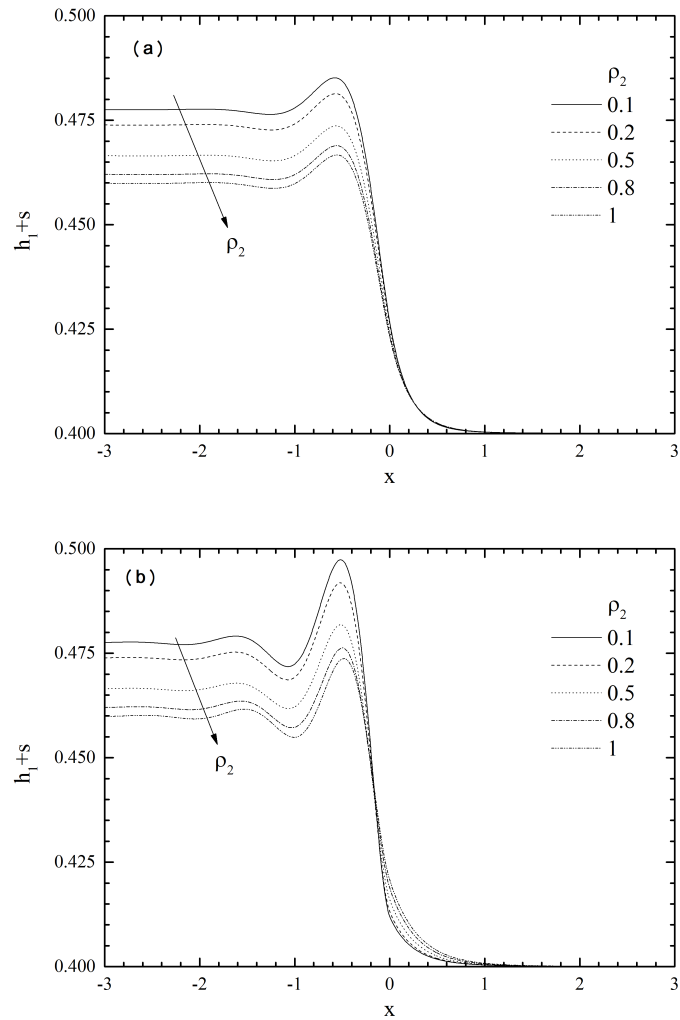


Figure 4.17: Effect of density ratio on the interface shape for flow in a channel with a step-down when  $h_{10}=0.4$ ,  $Ca= 3.33 \times 10^{-4}$  and  $\mu_2 = 1.0$ ,  $\theta = 10^\circ$  with: (a)  $Re = 0$  and (b)  $Re = 150$ .

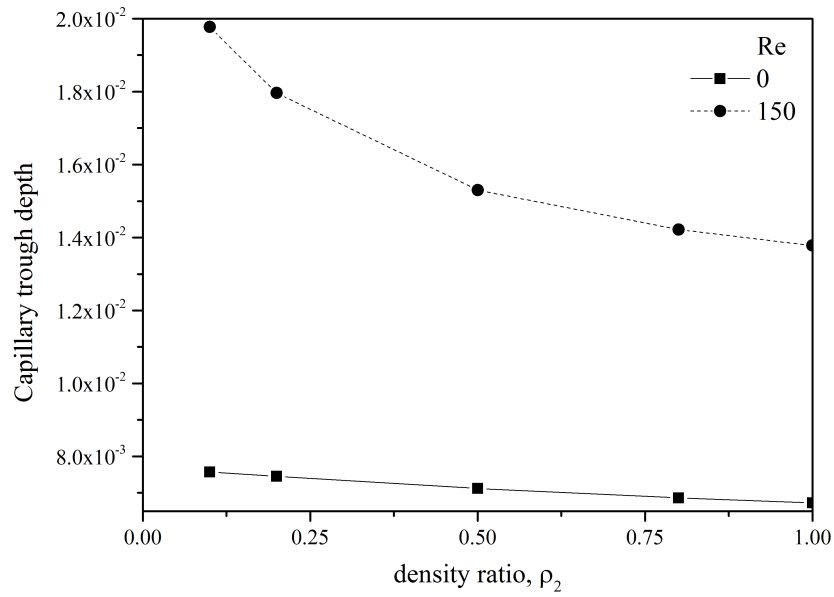


Figure 4.18: Capillary trough depth for flow situations as in Figure 4.17.

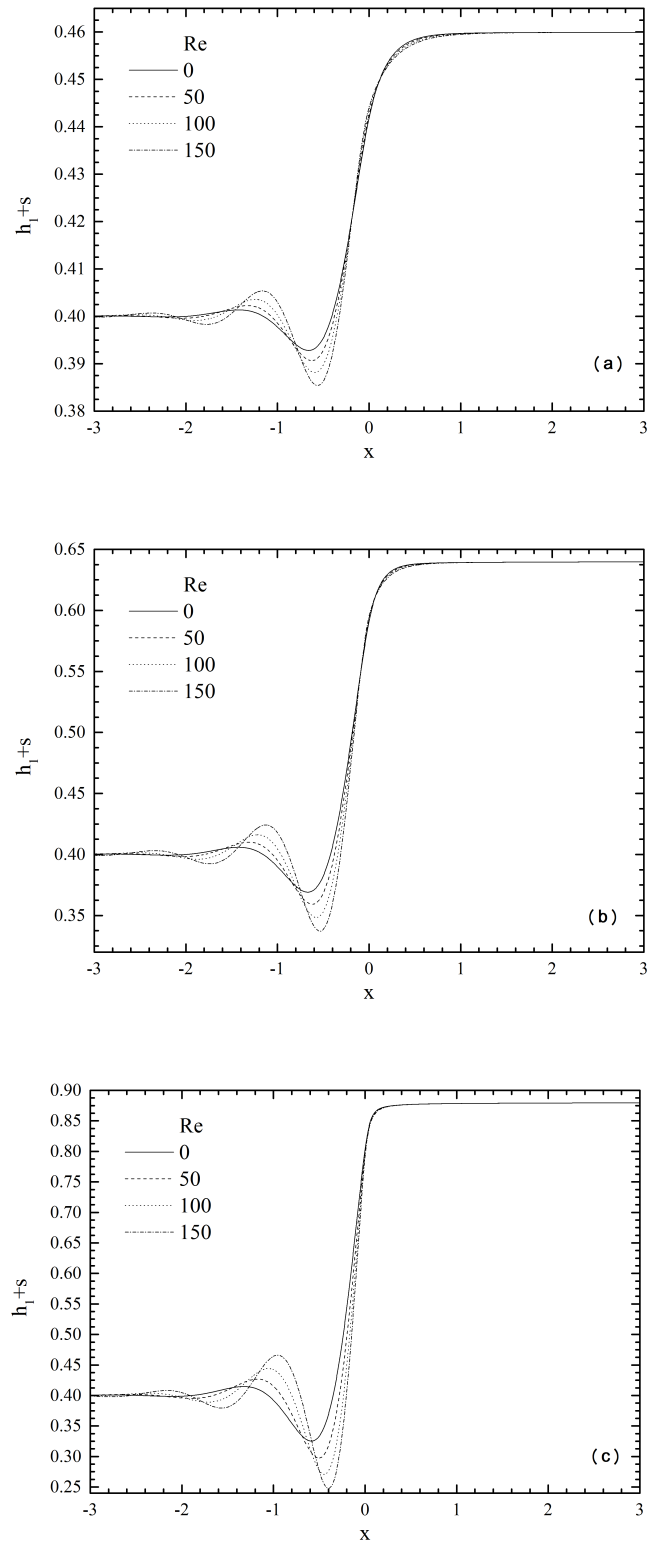


Figure 4.19: Effect of Reynolds number on the interface shape for flow in a channel with a step-up when  $h_{10}=0.4$ ,  $Ca= 3.33 \times 10^{-4}$  and  $\rho_2 = \mu_2 = 1.0$ ,  $\theta = 10^\circ$  with: (a)  $|s_0| = 0.1$ , (b)  $|s_0| = 0.4$  and (c)  $|s_0| = 0.8$ .

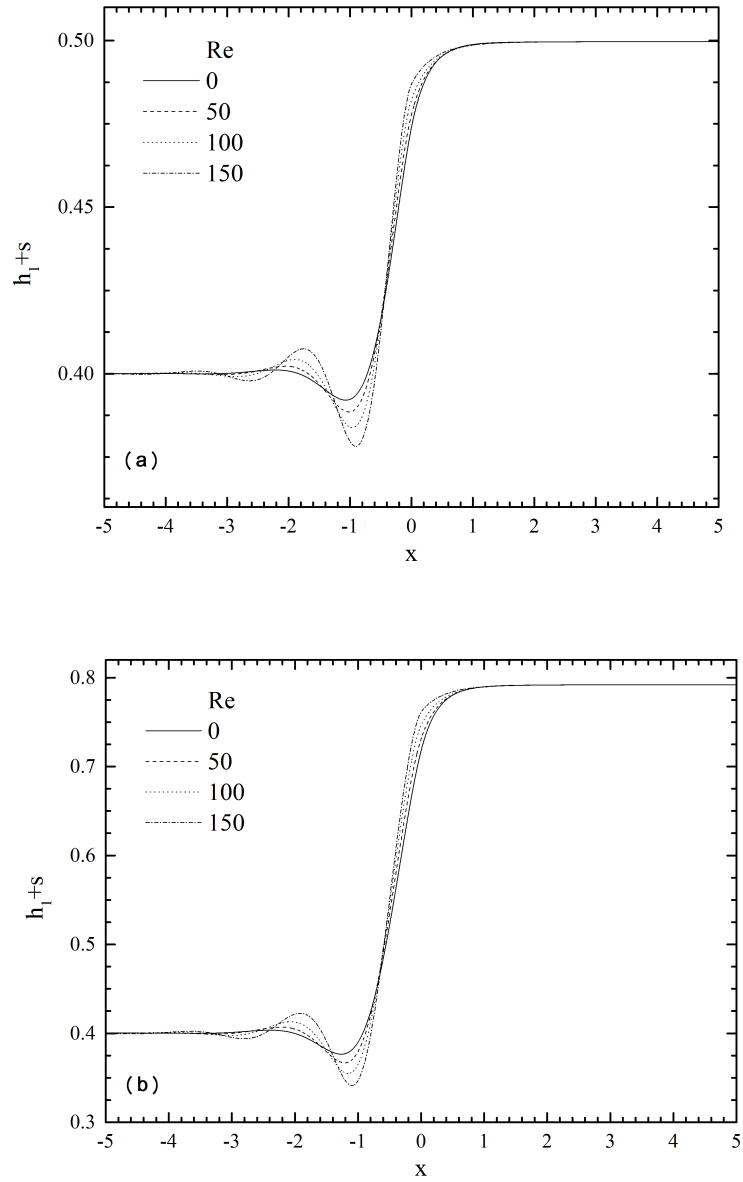


Figure 4.20: Effect of Reynolds number on the interface shape for flow in a channel with a step-up when  $h_{10}=0.4$ ,  $Ca= 3.33 \times 10^{-4}$  and  $\rho_2 = 0$ ,  $\mu_2 = 1 \times 10^{-3}$ ,  $\theta = 10^\circ$  with: (a)  $|s_0| = 0.1$  and (b)  $|s_0| = 0.4$ .

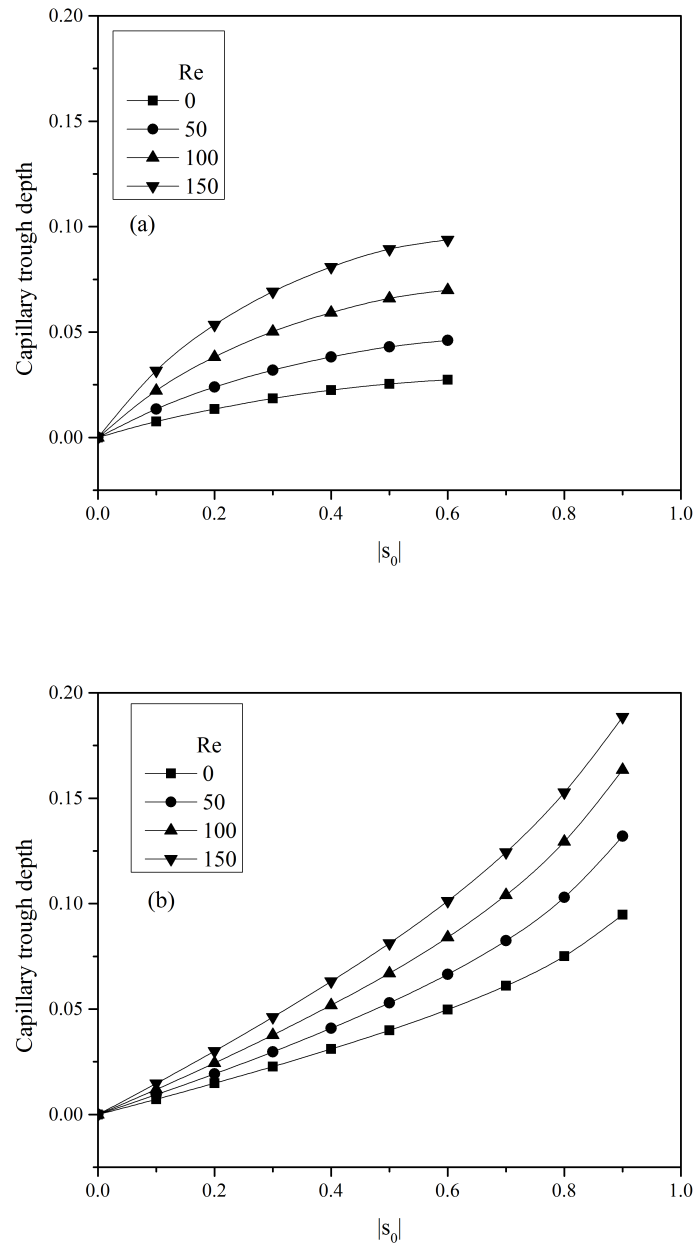


Figure 4.21: Capillary trough depth of step-up as function of topography height when  $h_{10}=0.4$ ,  $Ca= 3.33 \times 10^{-4}$ ,  $\theta = 10^\circ$  for two flow configurations: (a)  $\rho_2 = 0, \mu_2 = 1 \times 10^{-3}$  and (b)  $\rho_2 = 1, \mu_2 = 1$ .

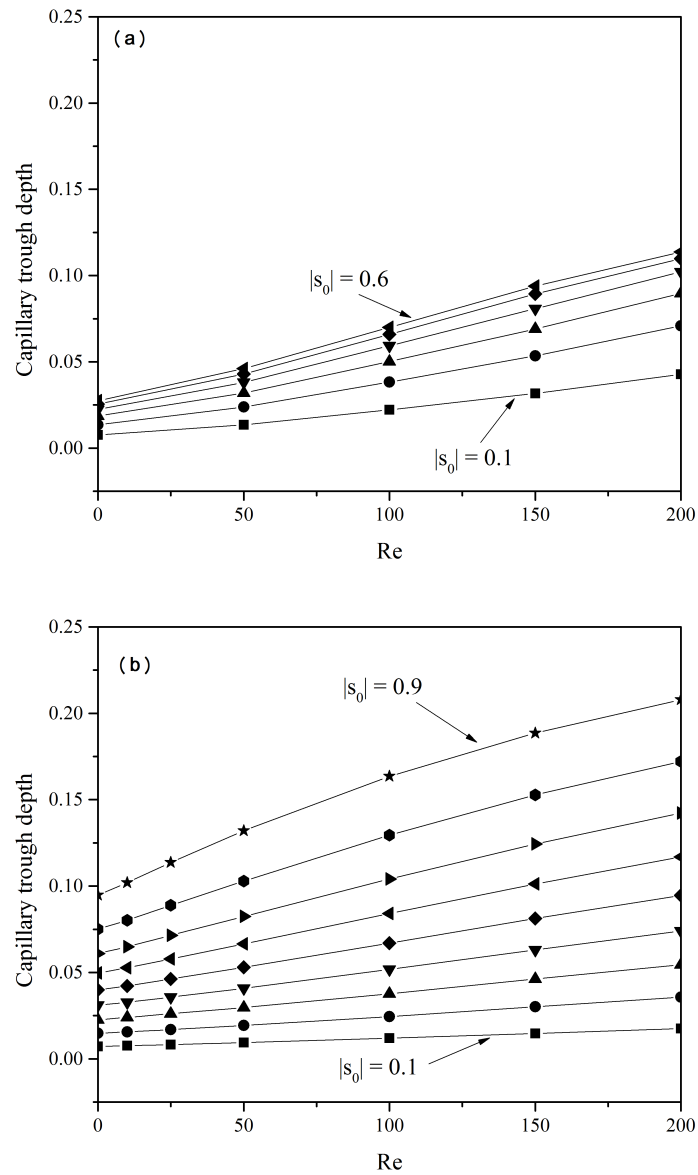


Figure 4.22: Capillary trough depth of step-up as function of Reynolds number when  $h_{10}=0.4$ ,  $|s_0|=0.4$ ,  $Ca=3.33 \times 10^{-4}$ ,  $\theta = 10^\circ$  for two flow configurations: (a)  $\rho_2 = 0, \mu_2 = 1 \times 10^{-3}$  and (b)  $\rho_2 = 1, \mu_2 = 1$ .

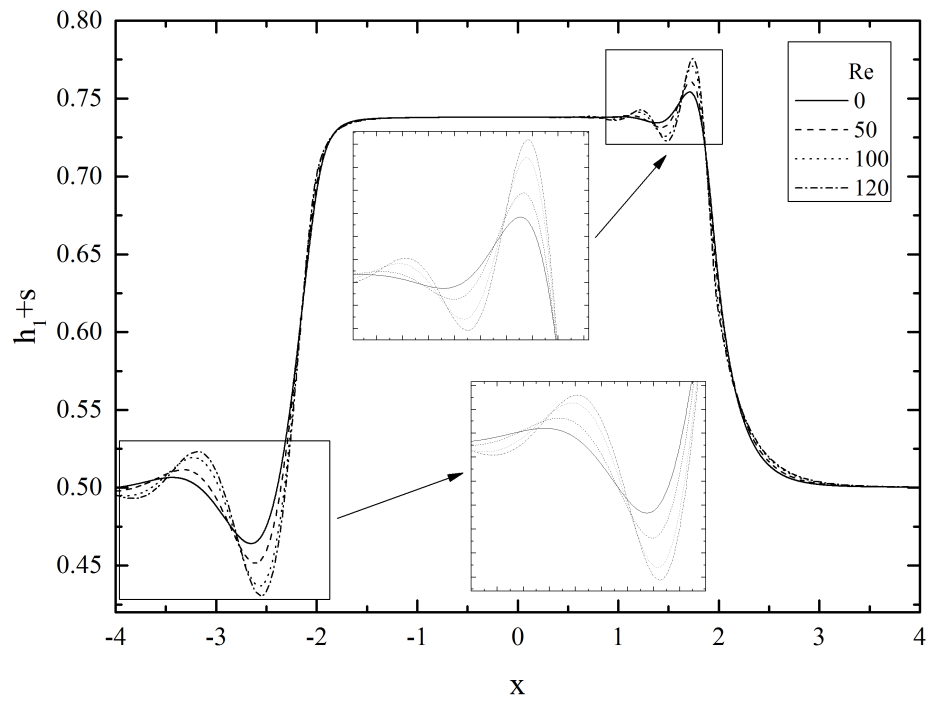


Figure 4.23: As in Figure 4.6, showing the effect of Reynolds number on interface profile.

## 4.2 Pressure gradient and shear driven flow

Flow driven by means other than gravity is also considered. Pressure gradient driven flow shows similar interface behaviour as the gravity ones. In fact, a profile identical to that generated by gravity flow can be obtained for pressure driven flow by choosing the same value of  $B$  and setting  $\rho_2 = 1$  as shown in Figure 4.24 for bilayer channel flow over a step-down given by  $|s_0| = 0.1$  when  $Re = 0$ .

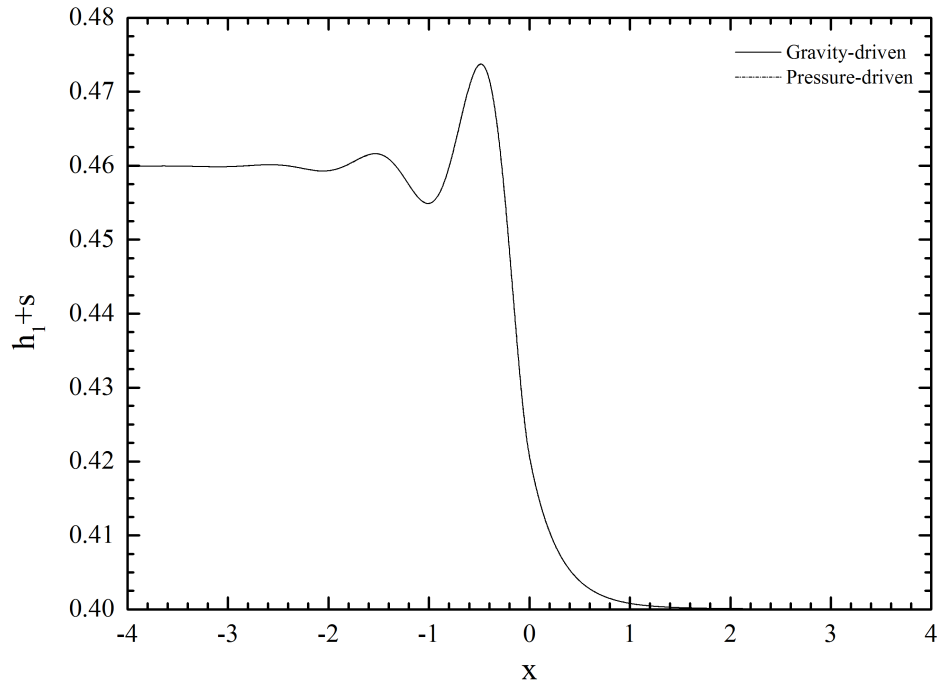


Figure 4.24: Comparison of interface profiles generated by gravity-driven flow,  $\theta = 10^\circ$ , and pressure-driven flow in a channel with a step-down given by  $|s_0|=0.1$  when  $Re = 0$ ,  $h_{10}=0.4$ ,  $Ca= 3.33 \times 10^{-4}$  and  $\rho_2 = \mu_2 = 1.0$ .

The influence of inertia on pressure driven flow is shown in Figure 4.25 for flow over a step-down with  $|s_0| = 0, 0.8$  and in Figure 4.26 for flow over a step-up. The same trend as for gravity flow is noted. In channel flow, it is possible to drive the flow by shearing the upper layer by moving the upper channel wall. Of course, this flow requires a non-negligible upper layer to drag the lower one and

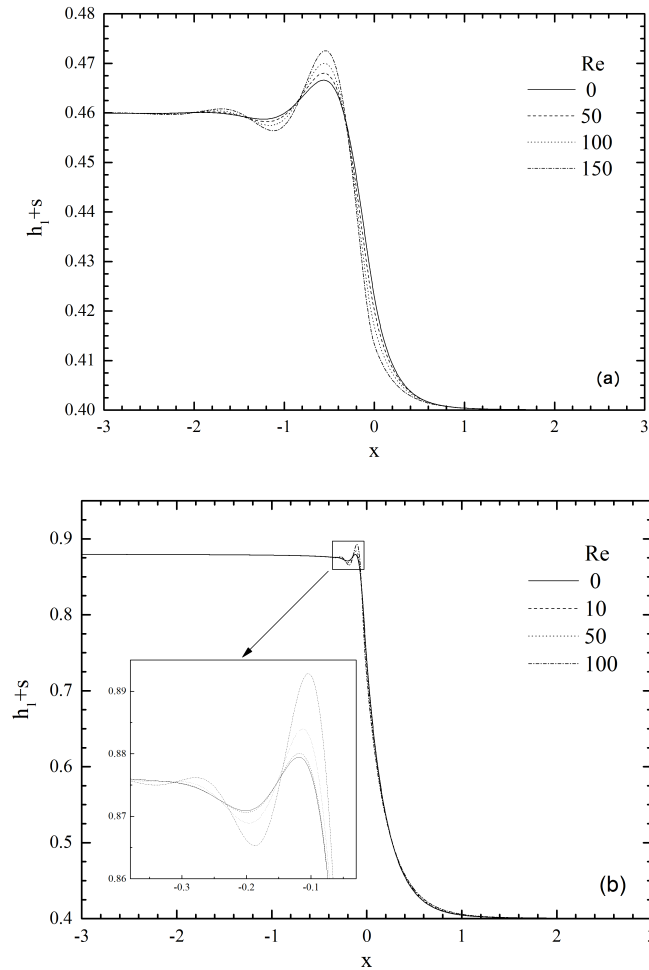


Figure 4.25: Effect of Reynolds number on the interface shape for pressure-driven flow in a channel with a step-down when  $h_{10}=0.4$ ,  $Ca= 3.33 \times 10^{-4}$  and  $\rho_2 = 0.2$ ,  $\mu_2 = 1$ ,  $\theta = 0^\circ$  with: (a)  $|s_0| = 0.1$  and (b)  $|s_0| = 0.8$ .

therefore all the results for shear-driven flow presented in this section is for a non-negligible upper layer,  $\rho_2 = \mu_2 = 1$ . For a horizontal channel and in the absence of an imposed pressure gradient, the upper liquid is dragged in a Couette flow by the upper wall and the lower layer is dragged by the upper layer. When the flow encounter changes in the channel height, due to a topographic feature, a pressure gradient is generated in the narrower part of the channel and hence the flow in this section is the superposition of Couette flow induced by the moving upper wall and Poiseuille flow generated by the pressure gradient as illustrated schematically in

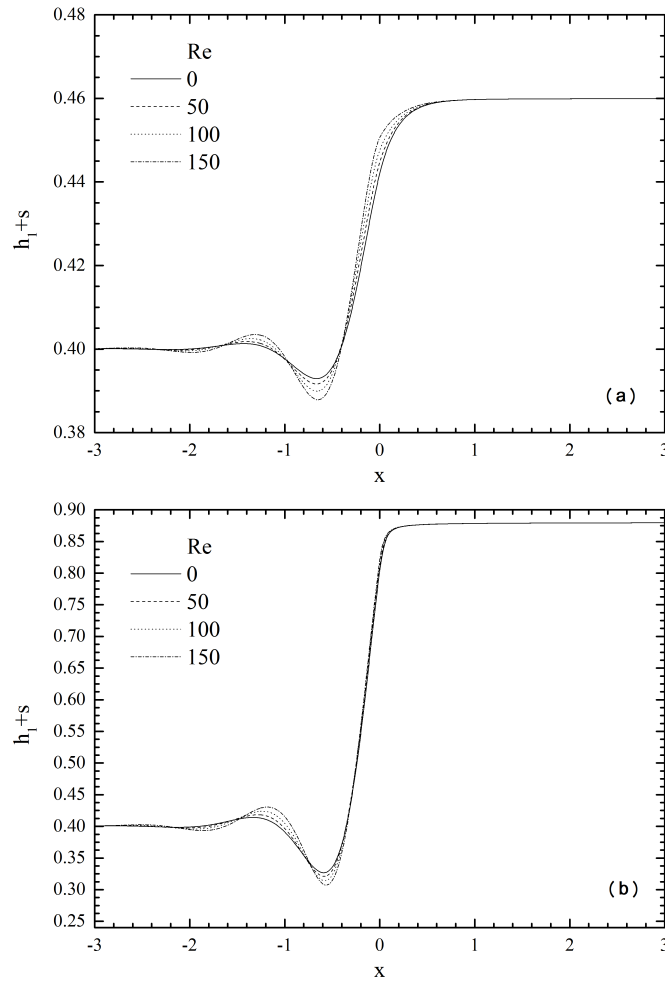


Figure 4.26: Effect of Reynolds number on the interface shape for pressure-driven flow in a channel with a step-up when  $h_{10}=0.4$ ,  $Ca= 3.33 \times 10^{-4}$  and  $\rho_2 = \mu_2 = 1$ ,  $\theta = 0^\circ$  with: (a)  $|s_0| = 0.1$  and (b)  $|s_0| = 0.8$ .

Figure 4.27. Figure 4.28 presents the effect of inertia on shear-driven flow over a step-down of a step depth of 0.1 and 0.8. The effect of increased inertia, amplifying the capillary ridge and widening the disturbance, is more pronounced when  $|s_0| = 0.1$  while at  $|s_0| = 0.8$  the effect is smaller and the capillary ridge is suppressed by increasing inertia. Figure 4.29 shows more details of the dependence of capillary ridge on step depth at  $Re$  values ranging from 0 to 150. The figure shows that for the  $Re$  values considered the capillary ridge first increase to a maximum value with increasing topography height before reaching a maximum after which it decreases.

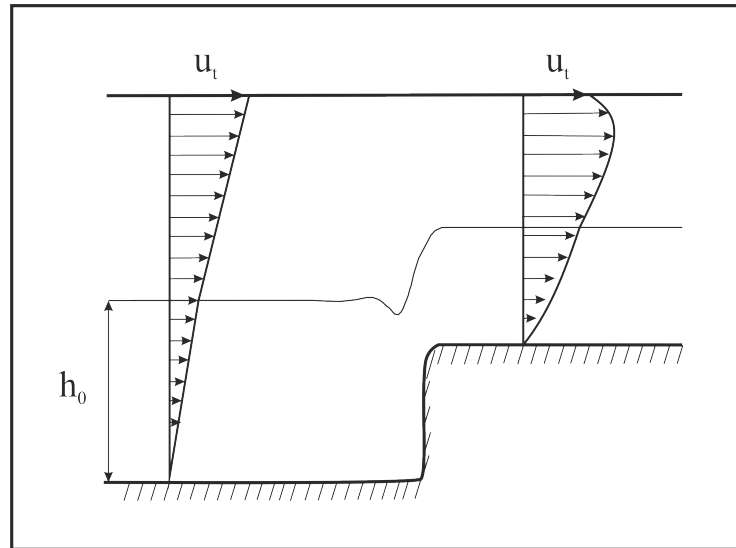


Figure 4.27: Schematic diagram for bilayer flow in a channel containing a step-down (left) and step-up (right) topography.

Comparison of the interface profile for  $h_{10}$  values ranging from 0.1 to 0.8, in the presence and absence of inertia, is shown in Figure 4.30 with the corresponding capillary ridge height results summarised in Figure 4.31. They reveal that for both inertial and non-inertial flows the capillary ridge height is decreased by increasing the interface height at the same step depth due to the pressure build up in the upper layer.

A similar behaviour to that of gravity-driven flow is also noticed for the case of shear-induced flow over a step-up as shown in Figures 4.32 and 4.33, which reveal a monotonic growth in the capillary trough with increasing step height.

Figure 4.34 shows interface profiles for three channel flow situations when  $h_{10}=0.4$  over a step-up topography given by  $|s_0|=0.2$ : flow due to gravity with a negligible upper layer; flow due to gravity with a non-negligible upper with layer  $\rho_2 = \mu_2 = 1$ ; shear flow induced by a moving upper channel wall. For the single layer limit case, the undisturbed lower layer thickness is equal at the two ends of the channel such that the interface height at channel exit is 0.6 (the sum of step height and layer

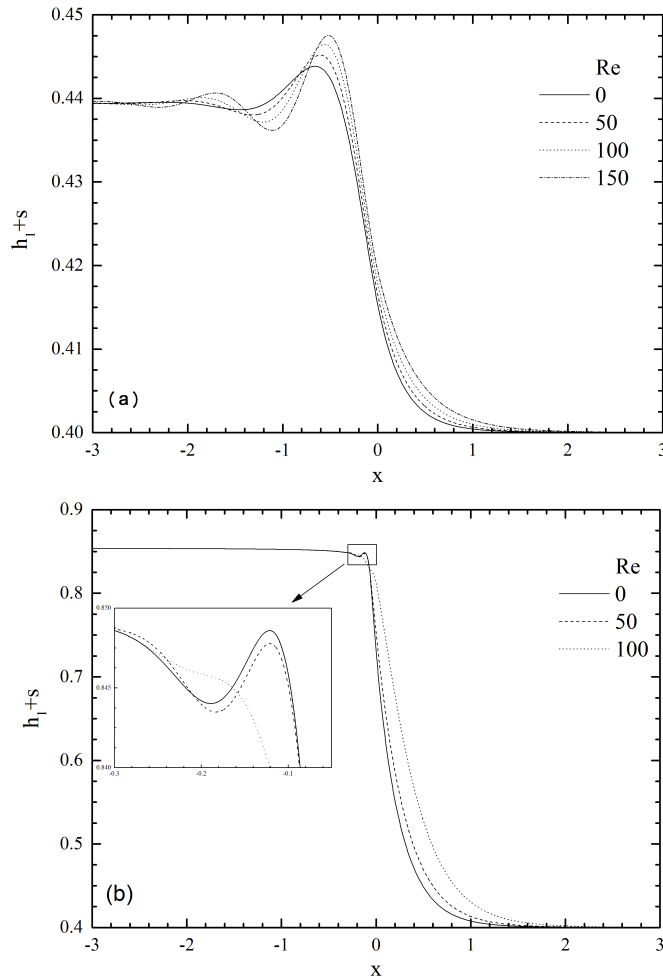


Figure 4.28: Effect of Reynolds number on the interface shape for shear-driven flow in a channel with a step-up when  $h_{10}=0.4$ ,  $Ca= 3.33 \times 10^{-4}$  and  $\rho_2 = \mu_2 = 1$ ,  $\theta = 0^\circ$  with: (a)  $|s_0| = 0.1$  and (b)  $|s_0| = 0.8$ .

thickness,  $0.4+0.2$ ). When the upper layer is non-negligible the contraction of the flow area generates a pressure gradient in the narrower part of the channel. The exit thickness of lower layer is now smaller than the inlet thickness and can be calculated from the mass balance for both layers. For the simple case when the both layers have the same properties it can be calculated by taking into account that the lower layer thickness represents the same fraction of of the channel height in both the wide and narrow parts. For the case shown in Figure 4.34 the step height is 0.2 and therefore the channel thickness in the narrower part is 0.8. The lower layer

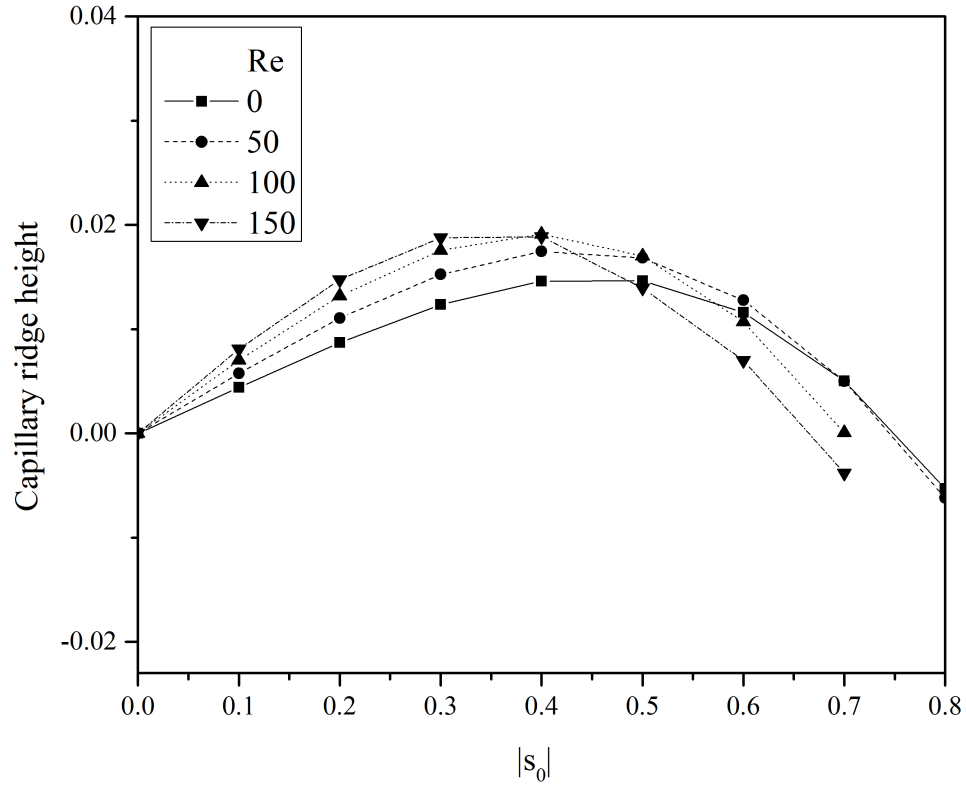


Figure 4.29: The dependence of capillary ridge height for shear induced flow over a step-down when,  $h_{10} = 0.4$ ,  $Ca = 3.33 \times 10^{-4}$  and  $\rho_2 = \mu_2 = 1$ ,  $\theta = 0^\circ$  with: (a)  $|s_0| = 0.1$  and (b)  $|s_0| = 0.8$ .

thickness in the narrower part is 0.32 which represents the same ratio of  $h_{10} = 0.4$  in the wide part making the exit interface height to be 0.52 (0.32+0.2). For the shear-driven flow case the thickness of the lower layer is 0.285 which can be calculated from the mass balance using equations (2.116) and (2.117).

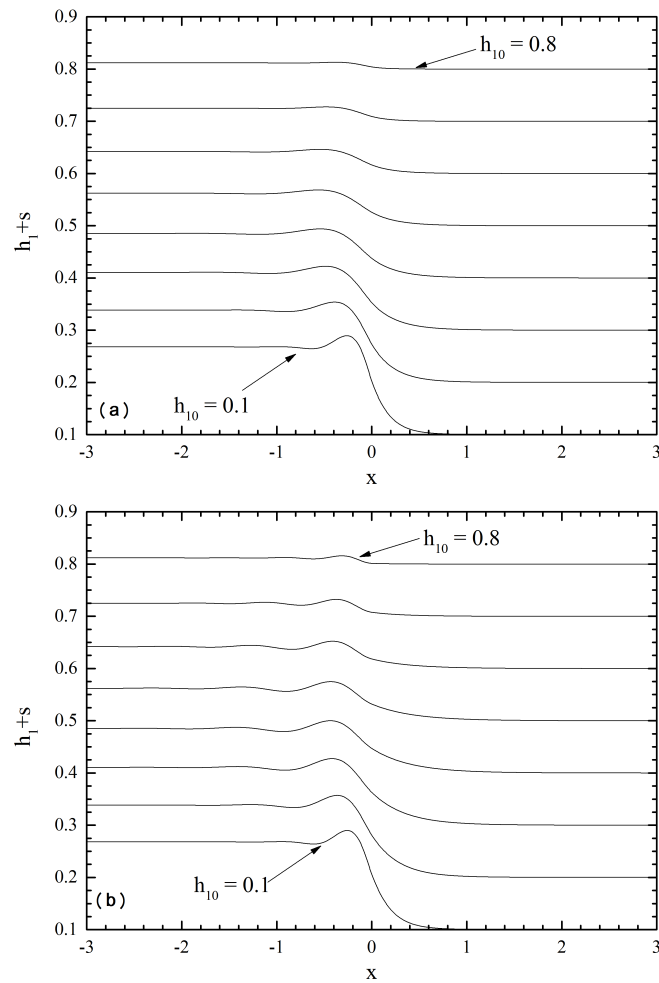


Figure 4.30: Interface profile for shear-induced flow in a channel with a step-down in the absence and presence of inertial effects.  $|s_0| = 0.2$ ,  $Ca = 3.33 \times 10^{-4}$ ,  $\rho_2 = \mu_2 = 1$  and several values of  $h_{10}$ ,  $\theta = 0^\circ$  with: (a)  $Re = 0$  and (b)  $Re = 150$ .

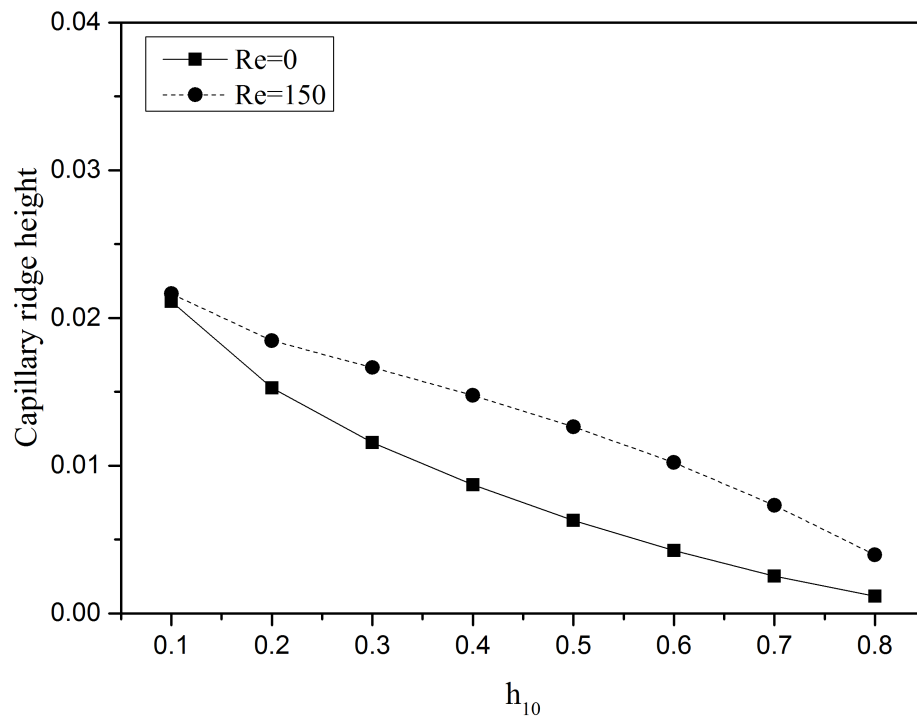


Figure 4.31: Capillary ridge as a function of  $h_{10}$  for flow situations shown in Figure 4.30

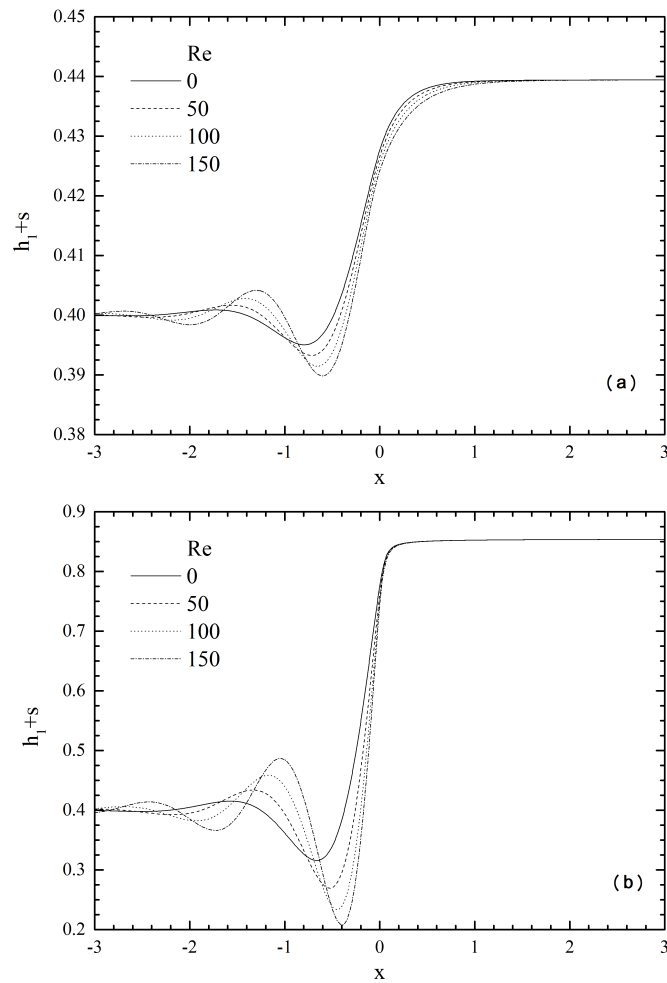


Figure 4.32: Effect of Reynolds number on the interface shape for shear-driven flow in a channel with a step-up when  $h_{10}=0.4$ ,  $Ca= 3.33 \times 10^{-4}$  and  $\rho_2 = \mu_2 = 1$ ,  $\theta = 0^\circ$  with: (a)  $|s_0| = 0.1$  and (b)  $|s_0| = 0.8$ .

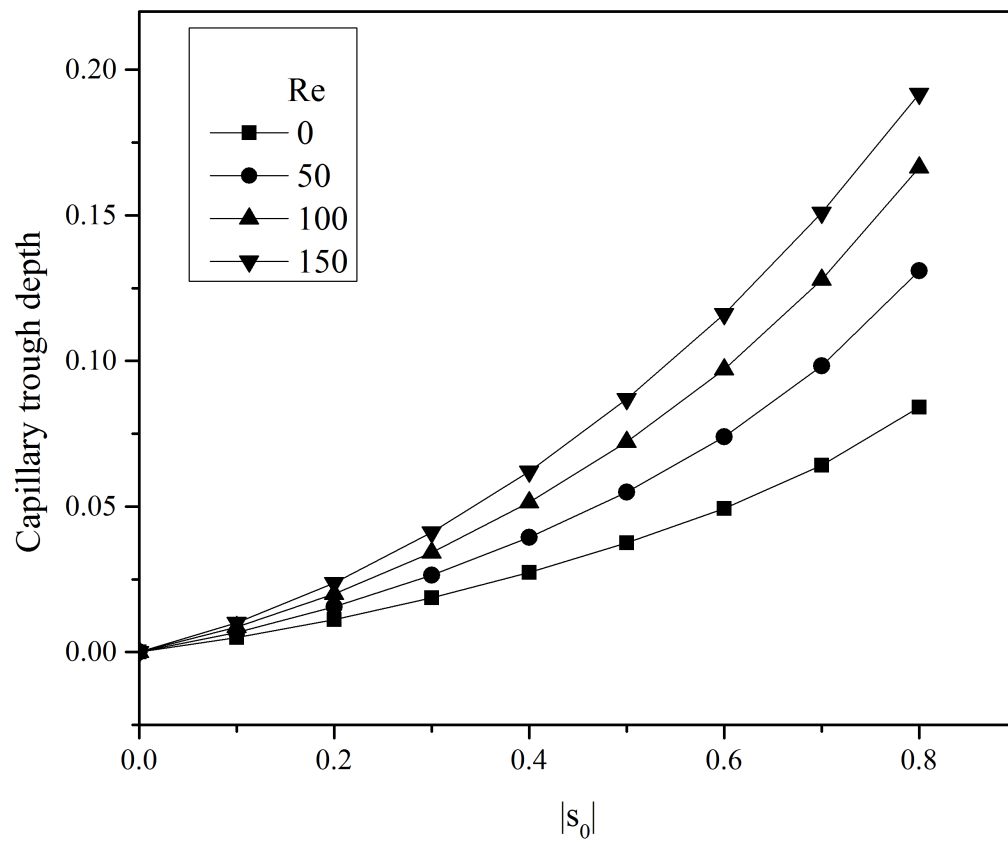


Figure 4.33: Capillary ridge depth as a function of step depth  $|s_0|$  for flow situations shown in Figure 4.32

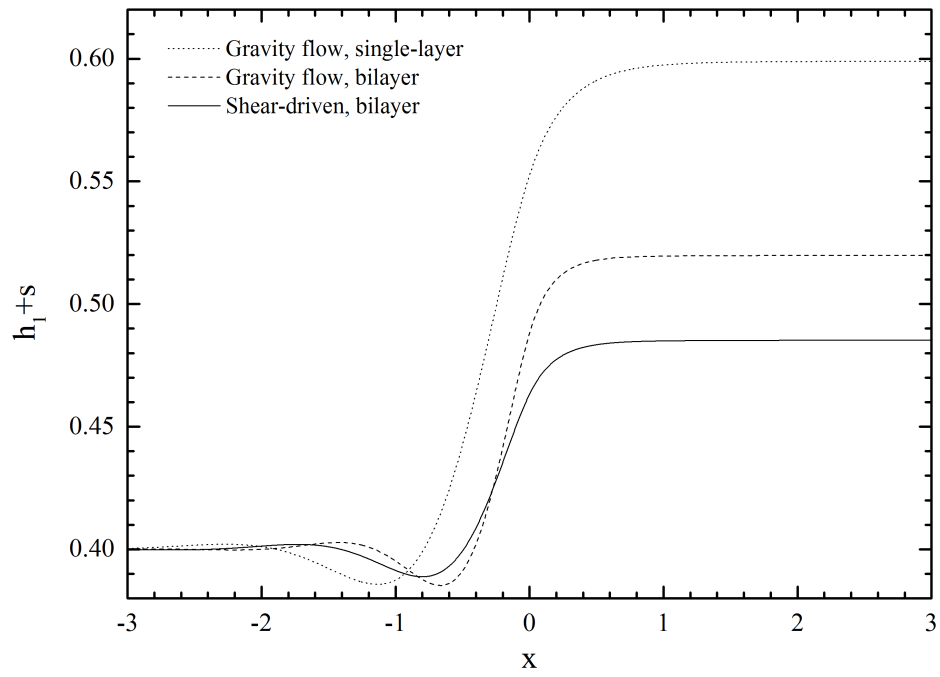


Figure 4.34: Comparison of interface profiles generated by gravity-driven flow and shear-induced flow with  $B=12$  in a channel with a step-up given by  $|s_0|=0.2$  when  $h_{10}=0.4$  and  $Ca= 3.33 \times 10^{-4}$ .

# Chapter 5

## Free-surface bilayer thin film flow over topography

### Contents

---

<b>5.1</b>	<b>Two-dimensional flow . . . . .</b>	<b>134</b>
5.1.1	Single-layer equivalent . . . . .	134
5.1.2	Exploring parameter space, $Re = 0$ . . . . .	135
5.1.3	Exploring parameter space, $Re \neq 0$ . . . . .	145
<b>5.2</b>	<b>Three-dimensional flow over trench topography . . . . .</b>	<b>155</b>

---

In this chapter free-surface bilayer thin film flow down an inclined substrate containing topographical features is investigated. The equation sets for both the LUB model and DAF, derived in Chapter 2, are solved numerically using the multigrid methodology presented in Chapter 3. The effect of inertia and the upper layer properties are explored for different topography geometries and comparisons drawn with complementary experimental results and numerical predictions from the literature. The extension to three-dimensional bilayer flows over localised topography is also addressed.

Due to the absence of an explicit inertial stability criteria for bilayer free-surface flow over topography and to avoid generating results in unstable flow regimes it was decided to use the inertial stability criterion for single-layer flow down flat inclined substrate as a guide when determining the stable Reynolds number range to be explored. The well-known stability criterion for gravity-driven flow down inclined substrate requires the Reynolds number to be smaller than a certain critical value,  $Re_{crit}$ . The value of the critical Reynolds number depends on the inclination angle,  $\theta$ , of the substrate, Benjamin (1957) and Yih (1963), and is given by:

$$Re_{crit} = \frac{5}{4} \cot \theta. \quad (5.1)$$

When the density of the upper layer is smaller than that of the lower one the bilayer flow becomes more stable than the single layer counterpart, while a heavier upper layer has a non-stabilising effect, Kao (1968). Using the above criteria and setting  $\rho_2 \leq 1$  ensures the flow is stable. It is clear from equation (5.1) that if the substrate is vertical the flow is unstable no matter how small  $Re$  is.

## 5.1 Two-dimensional flow

### 5.1.1 Single-layer equivalent

Due to the lack of numerical or experimental results in the literature for continuous bilayer flow over topography, the limiting case where both the lower and the upper liquids have the same properties is used as a test bed enabling comparison with single layer results available in the literature, in particular the experimental data of Decré and Baret (2003). In order to make direct comparison the following fluid properties are used:  $\hat{\rho}_1 = 1000 \text{ kg/m}^3$ ,  $\hat{\mu}_1 = 0.001 \text{ Pa.s}$  and  $\hat{\sigma}_1 = 0.07 \text{ N/m}$  and the inclination angle is set to  $30^\circ$ .

Figure 5.1 shows the comparison for flow over step-up and step-down topographies of  $|s_0| = 0.20$  when  $Re = 2.45$  and a spanwise trench of  $|s_0| = 0.19$  and  $l_t = 1.51$  when  $Re = 2.84$ . The origin is moved such that it is located at the centre of the topography and the free-surface location and topography profile are scaled with respect to the height/depth of the topography, namely  $s^* = s/s_0$  and  $f_2^* = (f_2 - 1)/s_0$ , respectively. For the three cases compared the current DAF is found to capture accurately the main features of the free surface profile. These features are the characteristic free-surface trough and capillary ridge just upstream of the step-up and step-down topographies, respectively, and the free-surface depression characteristic of flow over a trench, Gaskell *et al.* (2004). The height of the capillary ridge or the depth of capillary trough is measured from the flat free surface in the z-direction, as described in Chapter 4. The figure reveals excellent agreement between the current numerical predictions and the experimental measurements for all three topographical features considered. The r.m.s. deviation between the numerical and experimental results obtained for the free-surface profiles for all three spanwise topographies

is within the experimental accuracy of 2% reported by Decré and Baret (2003).

Similarly, comparison can be drawn with associated numerical predictions, in this case those of Veremieiev *et al.* (2010). Figure 5.2 presents just such a comparison when  $\rho_2 = \mu_2 = 1$  for flow over step-up and step-down topographies when  $Re = 15$  and  $|s_0| = 0.2$ ,  $Ca = 1.17 \times 10^{-3}$  and  $\varepsilon = 0.191$ . The profiles reveal excellent agreement between the two sets of the results.

Those for  $Re=30$ ,  $Ca = 1.86 \times 10^{-3}$  and  $\varepsilon = 0.223$ , see Figure 5.3, similarly demonstrate very close agreement between the current results and those of Veremieiev *et al.* (2010). Note that  $\sigma_2 = 1.0$ , result in an over prescription the problem as formulated and consequently oscillatory behaviour of the numerical solution. This is not the case if a value of  $\sigma_2$  close to but less than 1 is used. In generating Figures 5.2 and 5.3  $\sigma_2$  was given a value of 0.95.

### 5.1.2 Exploring parameter space, $Re = 0$

The current bilayer DAF enables exploration of the influence of the upper liquid layer properties as well as the initial interface height on the free surface and interface disturbance generated. The angle of inclination is set to  $\theta = 10^\circ$ , the capillary number to  $Ca = 1.167 \times 10^{-4}$  and  $\varepsilon = 0.1$ . Figure 5.4 illustrates the influence of the upper layer density on the free surface disturbance for flow over topography when  $Re = 0$ . Three topographical features, a step-up, -down and a trench with  $l_t = 1.5$ , are considered when  $\mu_2 = 1$ ,  $|s_0| = 0.2$  and  $h_{10} = 0.5$ . The investigations cover only the flow regimes when the presence of the upper layer has a stabilising effect (i.e  $\rho_2 \leq 1$ ). The effect of decreasing  $\rho_2$  from 1 to 0.1 for step-up/down topography is to slightly increase the depth/height of the capillary feature and to push its peak away from the topography side wall. The effect on the free surface is more pro-

nounced for flow over trench topography where the depth of the depression, formed after the capillary ridge, is reduced by 23%

The corresponding liquid-liquid interface profiles for the flow configurations mentioned above, scaled with respect to the height/depth of the topography as  $f_1^* = (f_1 - h_{10})/s_0$ , are shown in Figure 5.5. For this figure, as in other subsequent plots of Chapter 5 and Chapter 6, insets showing exploded views of the liquid-liquid interface profiles formed are provided. These show that what appear as "kinks" are in fact smooth changes and simply an artefact of the scaling employed. In general, the interface exhibits a profile similar to that of the free surface. However, it also shows features similar to those of the interface profile discussed in Chapter 4 and also reported by Lenz and Kumar (2007). The step-down flow has a capillary ridge with its peak pushed below the inlet flat interface which was noted for bilayer channel flow at high  $|s_0|$  as shown, for example, in Figure 4.3. The effect of changing density on the interface profile is small compared to its effect on the free surface.

Changing the inlet thickness of the lower layer,  $h_{10}$  is also expected to have an impact on the free surface disturbance when the two liquids are not the same. Increasing  $h_{10}$  when  $\rho_2 < 1$  is expected to have the same effect of increasing  $\rho_2$  while  $h_{10}$  is constant because both lead to an increased flow rate. This can be examined by comparing Figure 5.6a, which shows the free surface and interface profile for flow over a trench for different  $h_{10}$  values when  $\rho_2 = 0.5$  and  $\mu_2 = 1$ , with Figure 5.4c for flow over a trench at different  $\rho_2$  values. The two figures show the same trend of increasing the depth of free surface depression when either  $h_{10}$  or  $\rho_2$  increased.

The corresponding interface profile behaviour is shown in Figure 5.6b when  $h_{10} = 0.2, 0.4$  and  $0.8$ . The profile for  $h_{10} = 0.2$  is very similar to the free surface profile characteristic of the flow of a single-layer thin film over a wide trench, as described by Mazouchi and Homsy (2001) who used the boundary element (BE) method to

study the Stokes flow of a thin liquid film over a one-dimensional trench and by Gaskell *et al.* (2004) who used a finite element method and lubrication theory to solve the problem of thin film flow over topography. When  $h_{10} = 0.8$  the interface profile becomes very similar to that of the free surface.

Next the effect of changing the upper layer viscosity is explored while keeping  $h_1 = 0.5$  and  $\rho_2 = 1.0$ . Figure 5.7 shows the influence of  $\mu_2$  on the flow over step-down and trench topographies. It can be seen that for step-down topography decreasing  $\mu_2$  leads to widening of the capillary ridge for both the free surface and interface and the movement of the associated peak upstream of the topography side wall. The flow over a trench shows in addition a considerable decrease in the depth of free surface and interface depression of 14% and 15%, respectively, when  $\mu_2$  is decreased from 5 to 0.5.

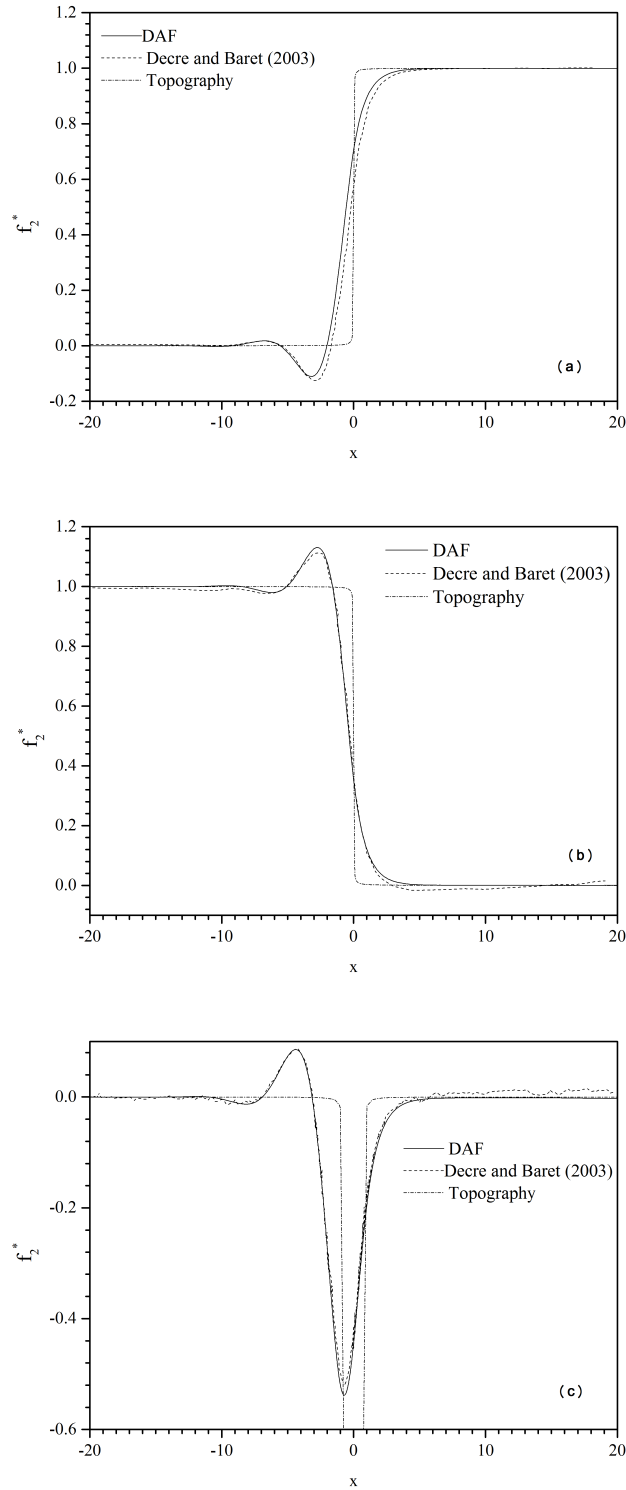


Figure 5.1: Comparison between DAF predictions of the free surface disturbance when  $\rho_2 = \mu_2 = 1$  with the experimental results of Decré and Baret (2003) for flow over a substrate containing topography when  $\theta = 30^\circ$ : (a) step-up (height  $|s_0| = 0.2$  and  $Re = 2.45$ ); (b) step-down (depth  $|s_0| = 0.2$  and  $Re = 2.45$ ); (c) trench ( $|s_0| = 0.19$ ,  $l_t = 1.51$  and  $Re = 2.84$ ).

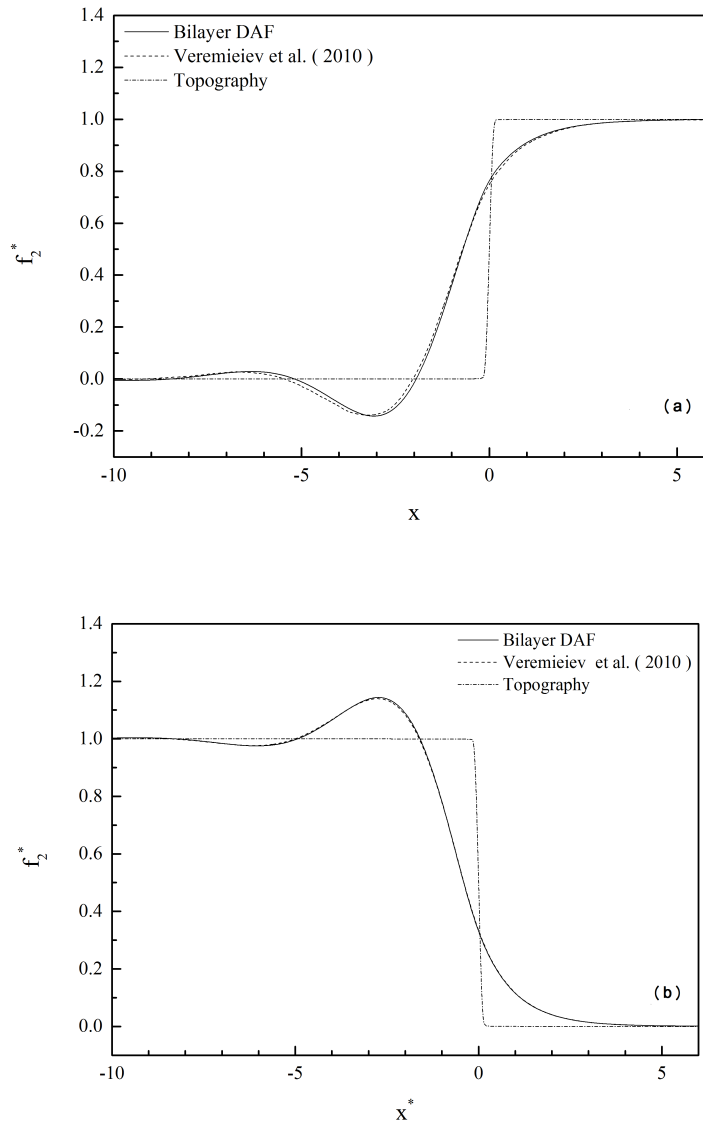
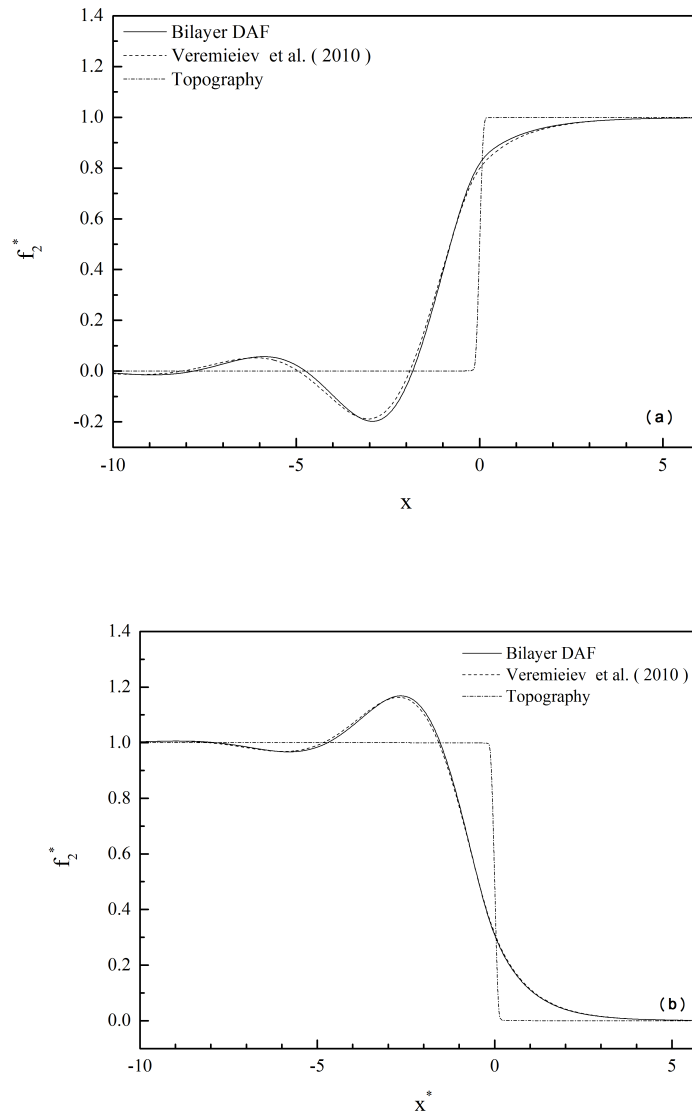


Figure 5.2: Comparison between DAF predictions of the free surface disturbance when  $\rho_2 = \mu_2 = 1$ ,  $\theta = 30^\circ$  and the numerical results of Veremieiev *et al.* (2010) for flow over a substrate containing a spanwise (a) step-up and (b) step-down topography when  $\text{Re} = 15$  and the  $|s_0| = 0.2$ .

Figure 5.3: As in Figure 5.2 but with  $Re=30$ .

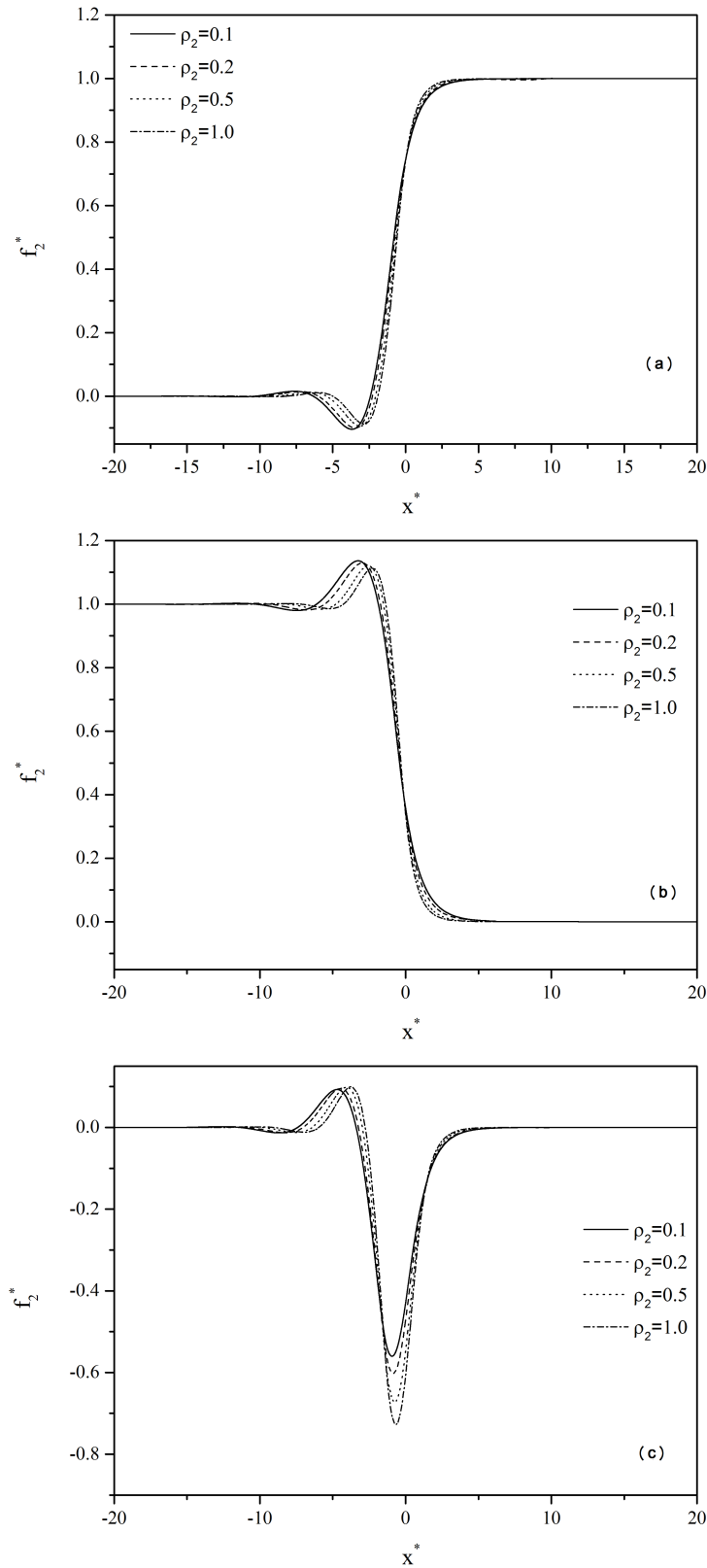


Figure 5.4: Influence of density ratio on the free surface shape for different topographical features when  $Re = 0$ ,  $\mu_2 = 1.0$ ,  $|s_0| = 0.2$ ,  $h_{10} = 0.5$  and  $\theta = 10^\circ$ ; (a) step-up, (b) step-down, (c) trench,  $l_t = 1.5$ .

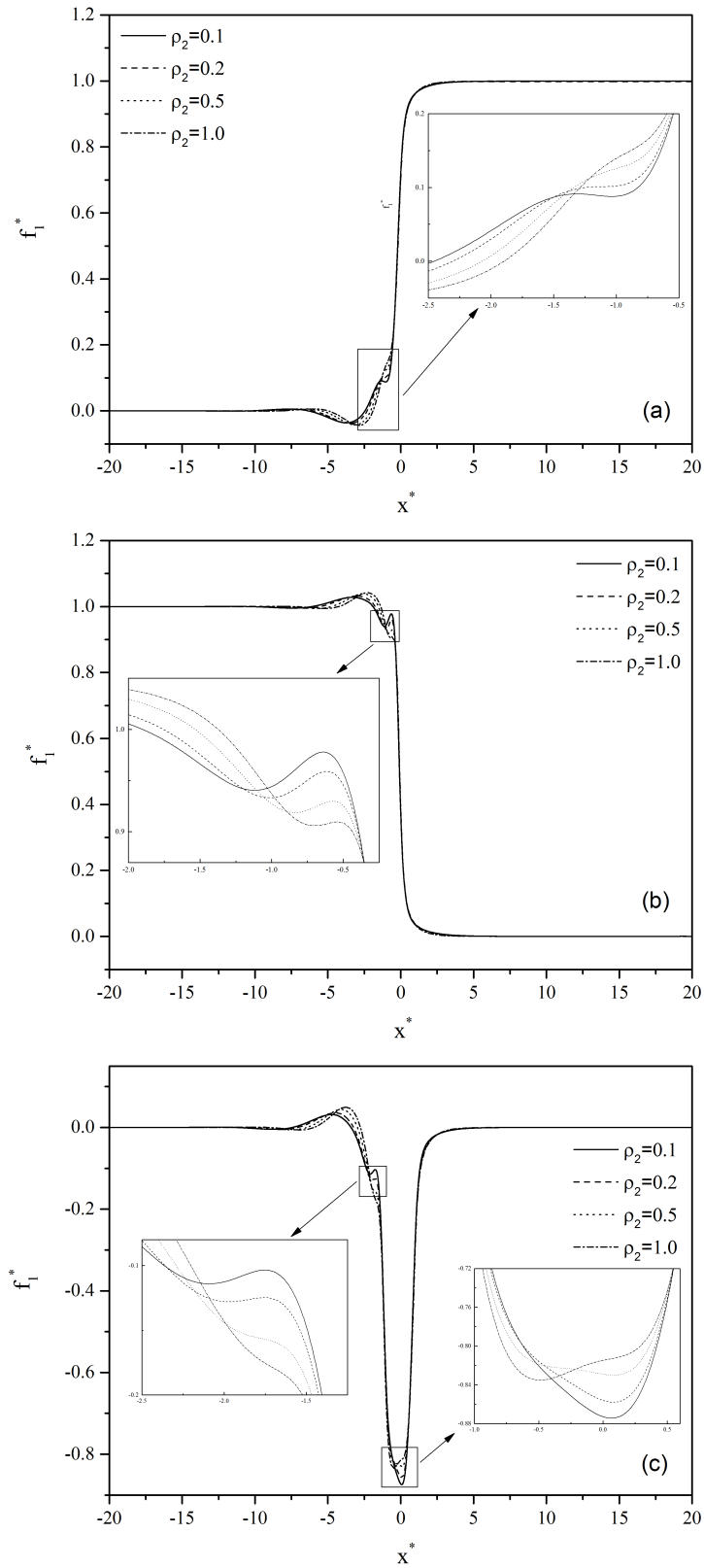


Figure 5.5: Influence of density ratio on the liquid-liquid interface for different topographical features when  $Re = 0$ ,  $\mu_2 = 1.0$ ,  $|s_0| = 0.2$ ,  $h_{10} = 0.5$  and  $\theta = 10^\circ$ ; (a) step-up, (b) step-down, (c) trench,  $l_t = 1.5$ .

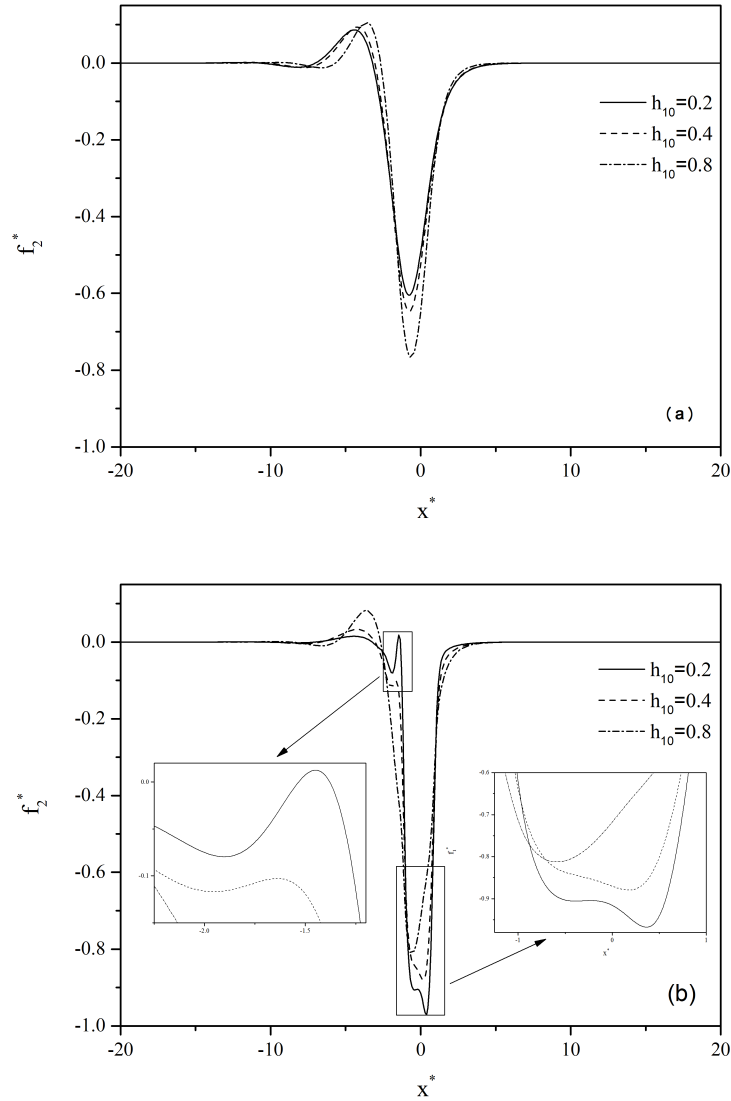


Figure 5.6: Effect of  $h_{10}$  on (a) the free surface and (b) the interface disturbance when  $Re = 0$ ,  $\rho_2 = 0.5$ ,  $\mu_2 = 1.0$ ,  $|s_0| = 0.2$  and  $\theta = 10^\circ$ .

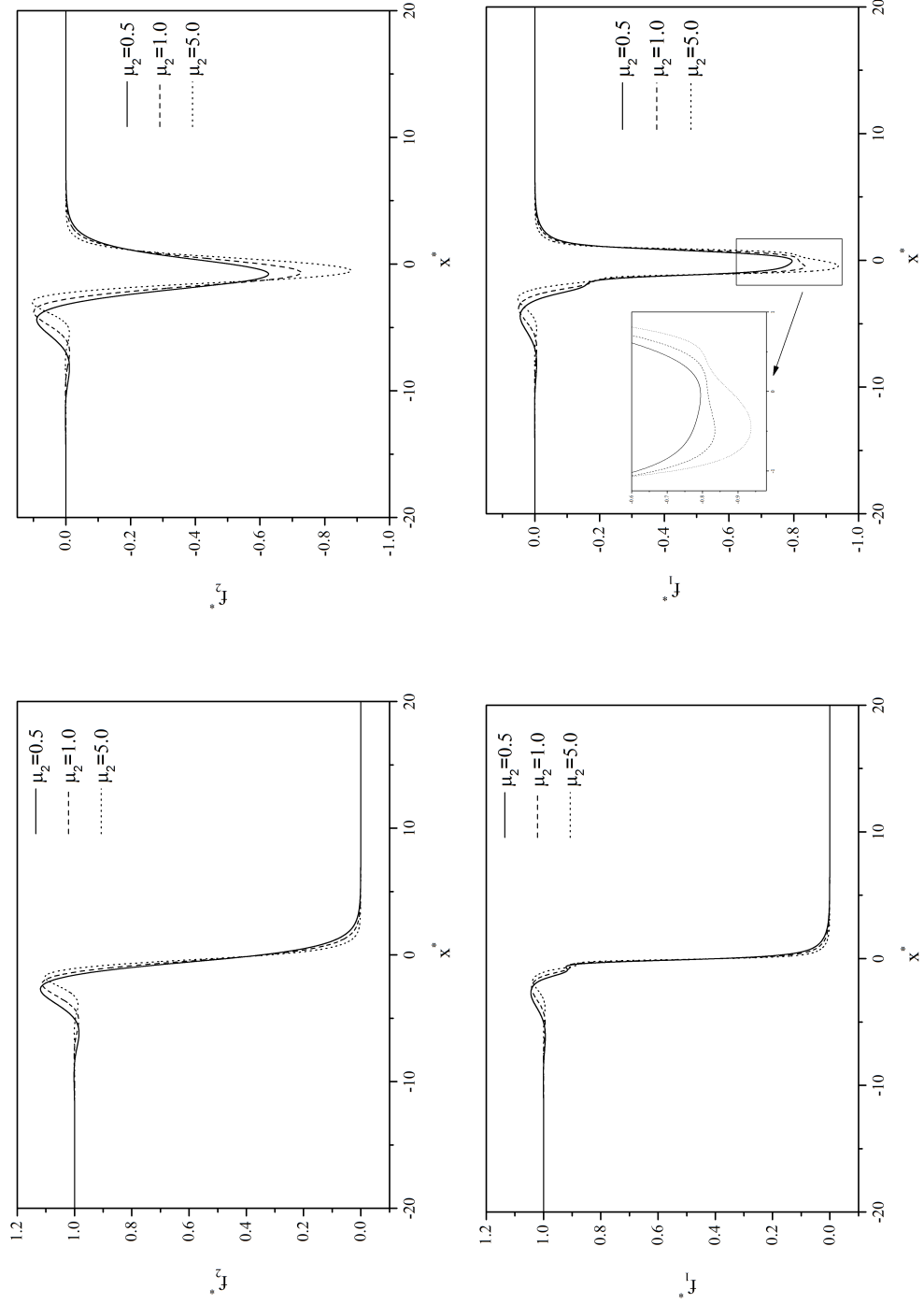


Figure 5.7: Influence of viscosity on free surface (top) and interface disturbance (bottom) for step-down (left) and trench (right) topographies when  $Re = 0$ ,  $|s_0| = 0.2$ ,  $\rho_2 = 1$ ,  $h_{10} = 0.5$  and  $\theta = 10^\circ$ .

The bilayer model can be employed to illustrate the evolution of the interface from close to the topography when the lower layer is infinitely thin up to the full extent of the film by changing  $h_{10}$ . This is demonstrated in Figure 5.8 for flow over a trench topography when  $\mu_2 = \rho_2 = 1$  which essentially represents a single-layer flow;  $h_{10}$  takes values from 0.2 to 0.9 and is increased in increments of 0.1. These interface profiles effectively represents the streamlines of the flow as there is no flow across them.

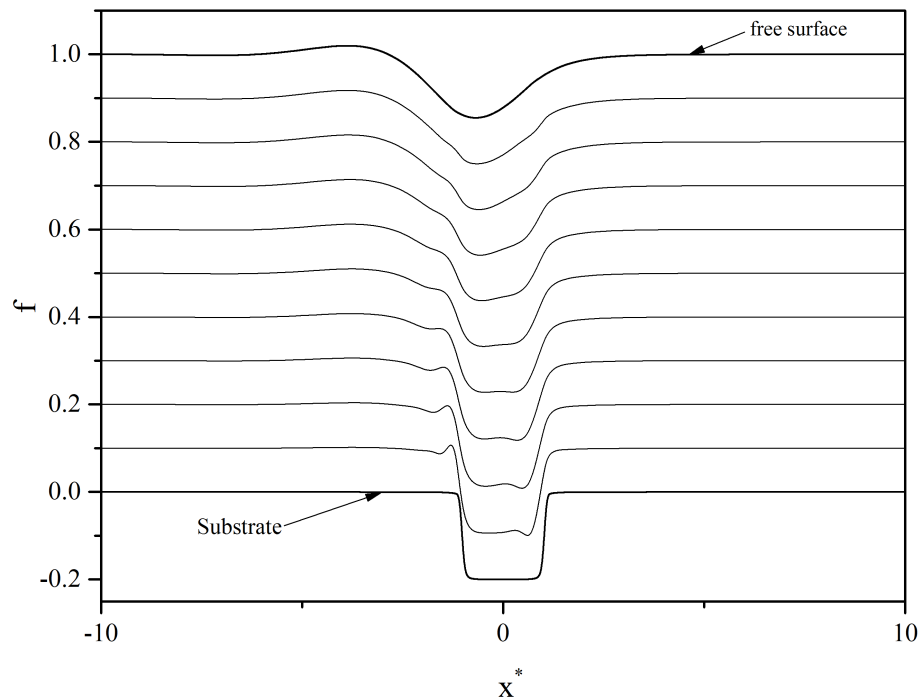


Figure 5.8: Evolution of the liquid-liquid interface profile when changing the interface height for flow over trench topography when  $Re = 0$ ,  $|s_0| = 0.2$ ,  $\rho_2 = \mu_2 = 1$ , and  $\theta = 10^\circ$ .

### 5.1.3 Exploring parameter space, $Re \neq 0$

In this section the effect of inertia on both the free surface and liquid-liquid interface disturbance is investigated together with the influence of flow parameters,  $\rho_2, \mu_2$

and  $h_{10}$ .

Figure 5.9 shows the free surface and interface disturbance generated for flow over trench topography,  $l_t = 1.5$  and  $|s_0| = 0.2$ . Increasing  $Re$  widens and increases the amplitude of the free surface and interface disturbances. The free surface capillary ridge height,  $h_{ridge}$ , increases by 76% and the interface's by 84% when  $Re$  increases from 0 to 30. The same behaviour was noted for the single-layer limit of channel flow as discussed in Chapter 4 and also agrees with the predictions of Veremieiev *et al.* (2010) for single-layer free-surface flow. The change of  $h_{ridge}$  with  $Re$  for different combinations of  $\rho_2$  and  $\mu_2$  is shown in Figure 5.10. For all  $\rho_2$ - $\mu_2$  combinations, increasing  $Re$  increases  $h_{ridge}$  monotonically due to the increased inertia. The wavy interface seen in the case of bilayer channel flow at high  $Re$  is not observed here as the range of  $Re$  is limited due to stability constraints.

The flow regimes presented in Section 5.1.1 are now investigated in the presence of inertia. In the following figures the Reynolds number is set to  $Re = 15$ .

Figure 5.11 shows the effect of density on flow over step-up/down and trench topographies; the corresponding interface disturbance is shown in Figure 5.12. The trend of a widening of the capillary features and deepening of the free surface and interface depressions for flow over a trench is noted when  $\rho_2$  is increased.

The influence of  $h_{10}$  when  $\rho_2 = 0.5$  is demonstrated in Figure 5.13. The figure shows similar behaviour to flow at zero Reynolds number but with magnified capillary features.

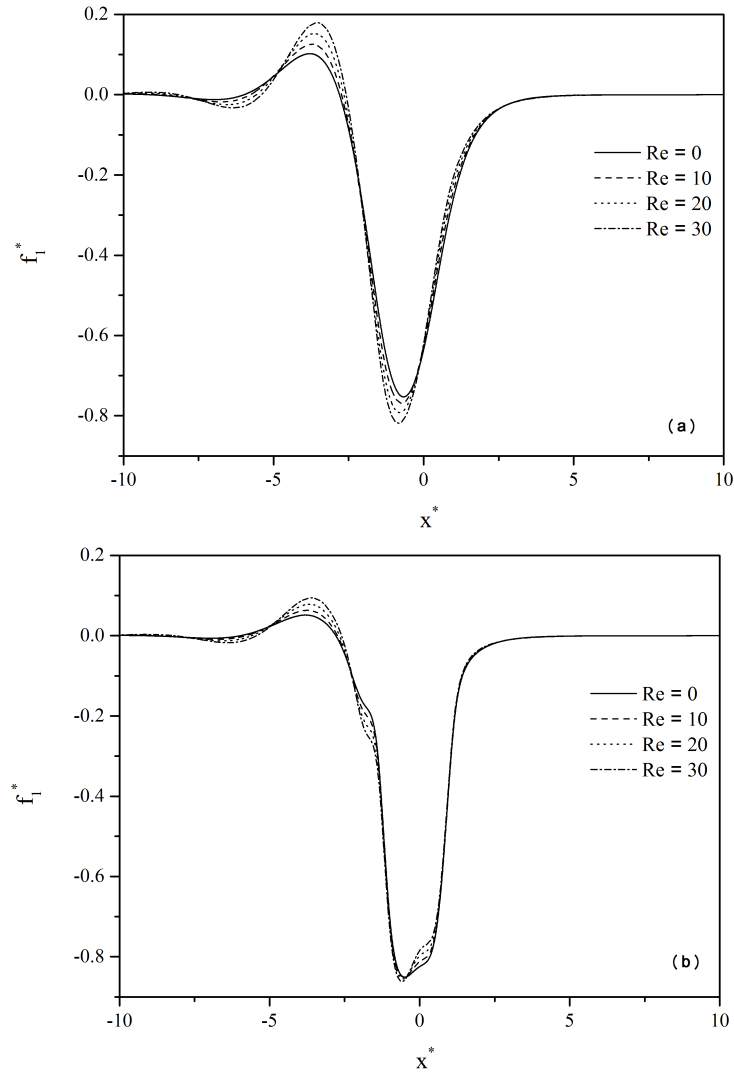


Figure 5.9: Effect of  $Re$  on the (a) free surface and (b) interface profiles for flow over trench topography when  $\rho_2 = \mu_2 = 1.0$ ,  $h_{10} = 0.5$ ,  $|s_0| = 0.2$ ,  $l_t = 1.5$  and  $\theta = 10^\circ$ .

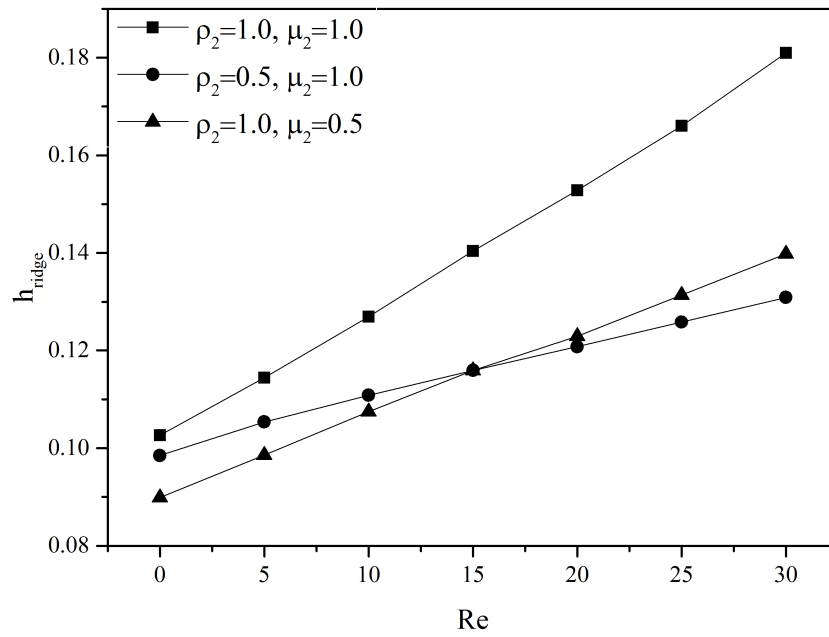


Figure 5.10: Capillary ridge height for flow over trench topography for different combinations of  $\rho_2$  and  $\mu_2$  when  $h_{10} = 0.5$ ,  $|s_0| = 0.2$ ,  $l_t = 1.5$  and  $\theta = 10^\circ$ .

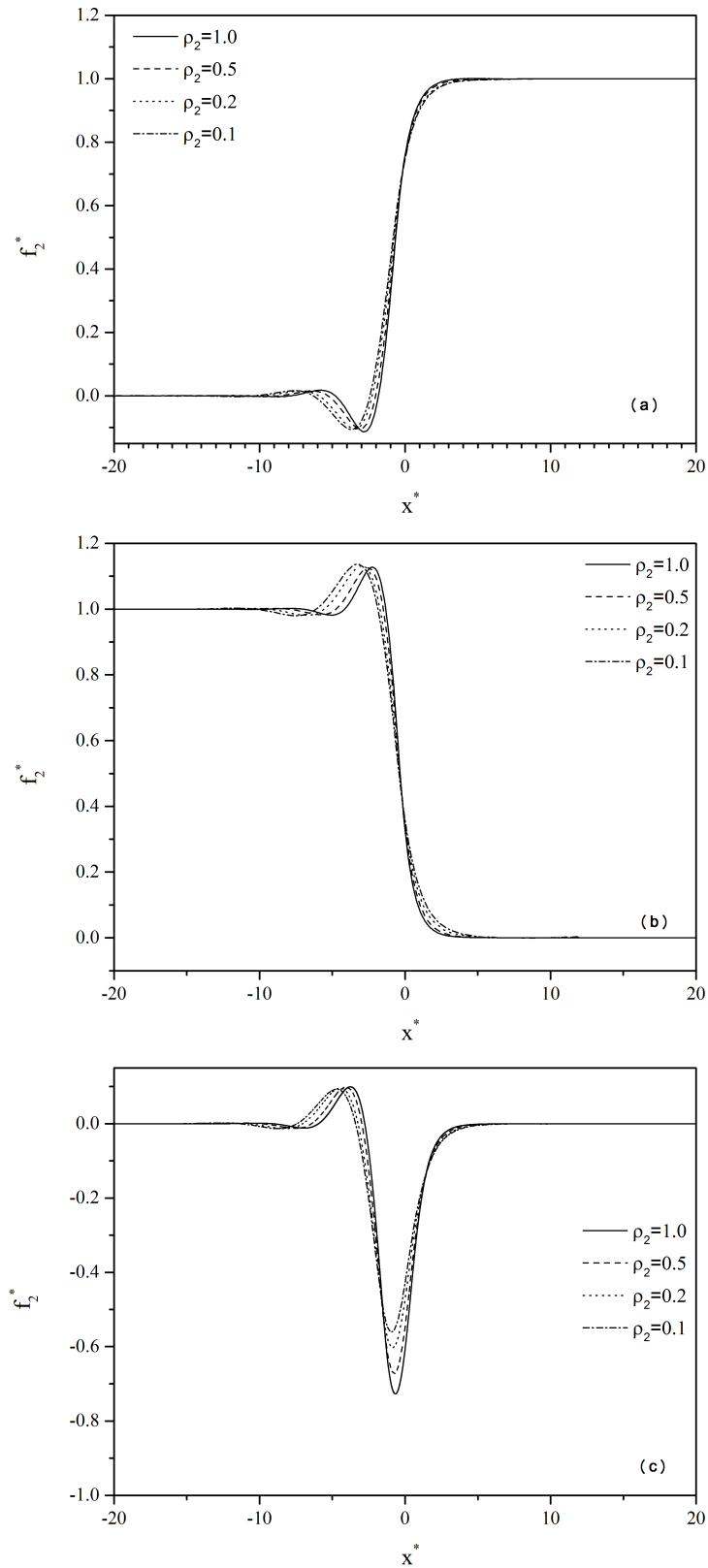


Figure 5.11: Effect of density on free surface shape when  $Re = 15$ ,  $\mu_2 = 1.0$ ,  $|s_0| = 0.2$ ,  $h_{10} = 0.5$  and  $\theta = 10^\circ$ ; (a) step-up, (b) step-down, (c) trench,  $l_t = 1.5$ .

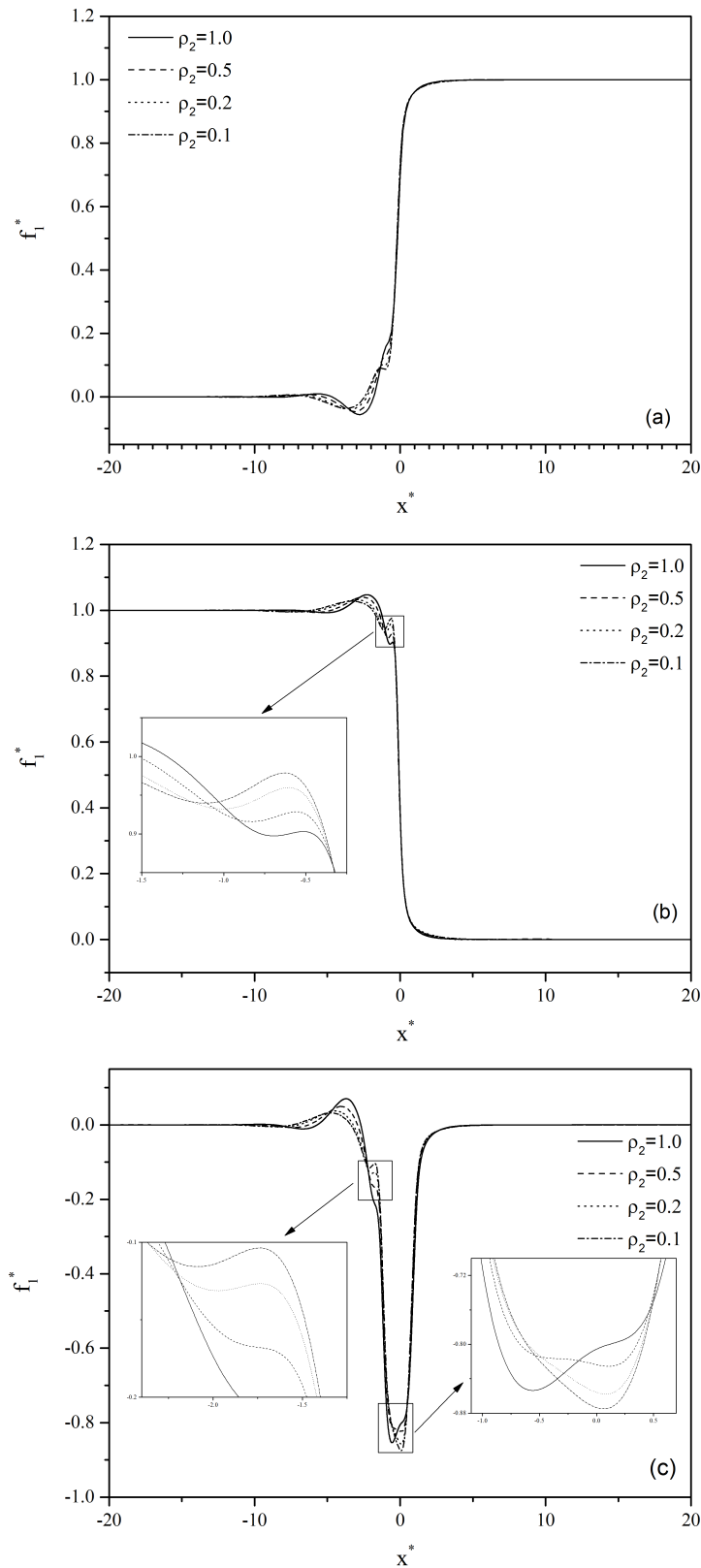


Figure 5.12: Effect of density on interface surface shape when when  $Re = 15$ ,  $\mu_2 = 1.0$ ,  $|s_0| = 0.2$ ,  $h_{10} = 0.5$  and  $\theta = 10^\circ$ ; (a) step-up, (b) step-down, (c) trench,  $l_t = 1.5$ .

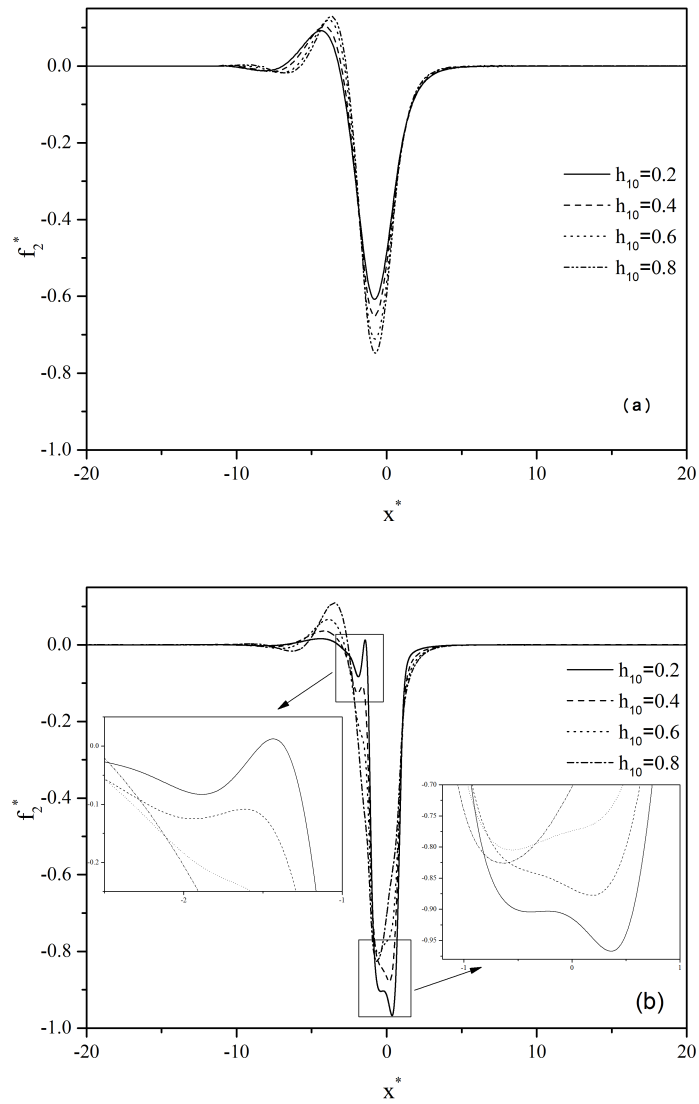


Figure 5.13: Effect of  $h_{10}$  on the (a) free surface and (b) interface disturbance for flow over trench topography when  $Re = 15$ ,  $\rho_2 = 0.5$ ,  $\mu_2 = 1$ ,  $|s_0| = 0.2$ ,  $l_t = 1.5$  and  $\theta = 10^\circ$ .

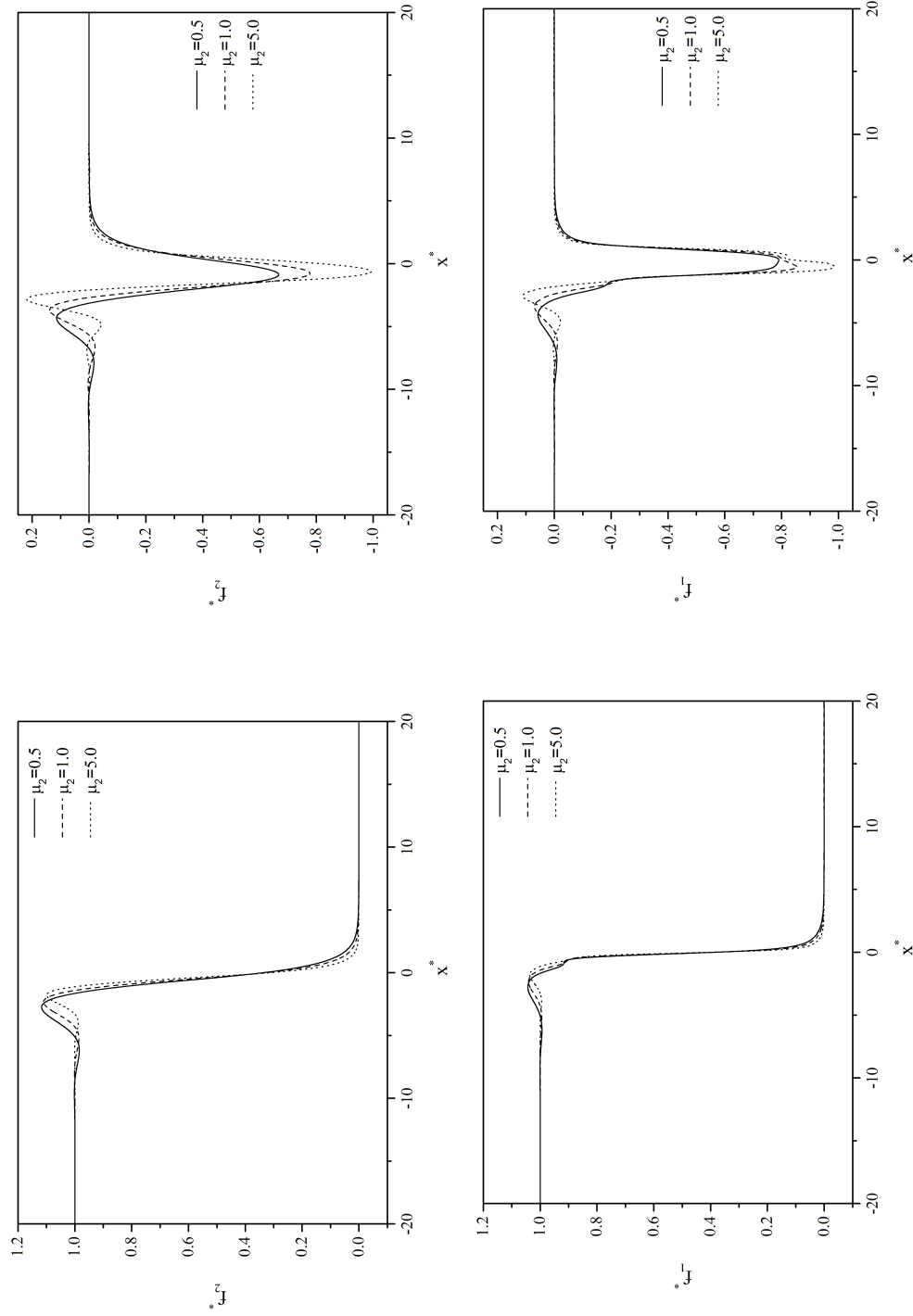


Figure 5.14: Effect of viscosity on free surface (top) and interface disturbance (bottom) for step-down (left) and trench (right) topographies when  $Re = 15$ ,  $\rho_2 = 1$ ,  $h_{10} = 0.5$ ,  $|s_0| = 0.2$ , and  $\theta = 10^\circ$ .

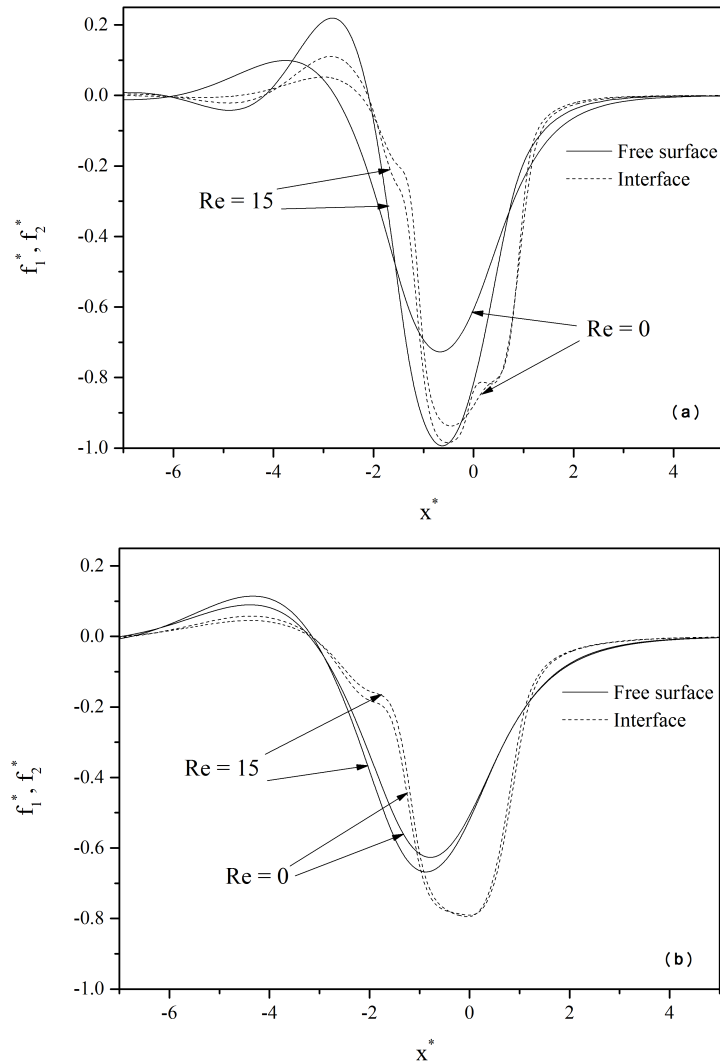


Figure 5.15: Comparison of free surface and interface disturbance in the presence and absence of inertia for flow over trench topography of  $|s_0| = 0.2$ ,  $l_t = 1.5$  when  $\theta = 10^\circ$  for (a)  $\mu = 5.0$  and (b)  $\mu = 0.5$ .

Figure 5.14 presents profiles of the free surface and interface disturbance for flow over step-down and trench topography when  $Re = 15$  for different values of  $\mu_2$ . For flow over a trench, increasing  $\mu_2$  from 0.5 to 5.0 leads to a noticeable increase in  $h_{ridge}$  and free surface depression depth of 93% and 49%, respectively, compared to 10% and 16% for non-inertial flow. A comparison between the flow with and without inertia at  $\mu_2 = 0.5$  and 5 is shown in Figure 5.15 in terms of the free surface and interface profiles for flow over trench topography when  $\rho_2 = 1.0$  and  $h_{10} = 0.5$ . The figure reveals that the influence of inertia is more remarkable at high  $\mu_2$  values.

Finally, 5.16 shows the interface profile obtained for different values of lower layer thickness,  $h_{10}$ , when  $\rho_2 = \mu_2 = 1$  together with the common free surface as changing  $h_{10}$  does not impact on its shape when the two liquids are the same. When  $h_{10}$  is small an interface profile similar to the free surface profile for single-layer flow over wide trench characterised by capillary ridge and capillary trough separated by a flat interface is observed. The two features start to merge together as  $h_{10}$  is increased with the ridge eventually pushed below the flat inlet interface and a new broader ridge is formed leading to the well known free surface shape for flow over a trench, consisting of a capillary ridge before the trench and depression afterwards.

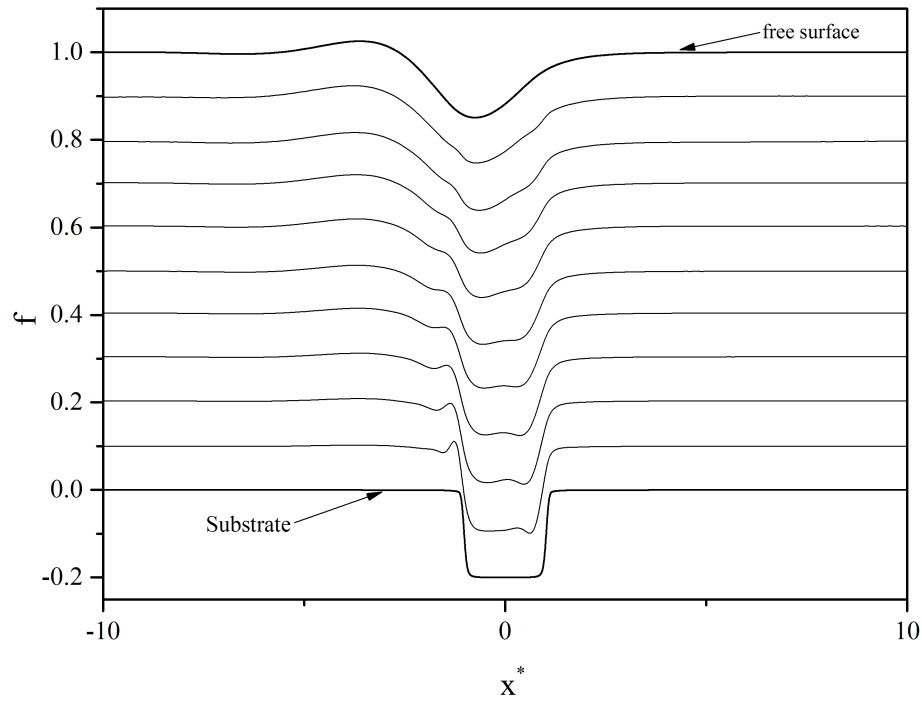


Figure 5.16: Evolution of the liquid-liquid interface profile for flow over trench topography for the single-layer equivalent flow when  $\theta = 10^\circ$  and  $Re = 15$ .

## 5.2 Three-dimensional flow over trench topography

In this section the bilayer DAF, written for three-dimensional flow, as in Section 3.1 of Chapter 3, is used to predict inertial flow over a localised trench topography. Note, this is not intended to comprise a complete and systematic investigation but as proof that the same can be achieved.

The definition of topography given by equation (2.136) has to be redefined to account for the additional dimension. The appropriate expression defining a two-dimensional rectangular trench, is thus given by:

$$s(x^*, y^*) = \frac{s_0}{4 \tan^{-1} \frac{l_t}{2\delta} \tan^{-1} \frac{w_t}{2\delta}} \left[ \begin{aligned} & \left[ \tan^{-1} \left( \frac{x^* + l_t/2}{\delta} \right) - \tan^{-1} \left( \frac{x^* - l_t/2}{\delta} \right) \right] \\ & \left[ \tan^{-1} \left( \frac{y^* + w_t/2}{\delta} \right) - \tan^{-1} \left( \frac{y^* - w_t/2}{\delta} \right) \right] \end{aligned} \right], \quad (5.2)$$

where the coordinate system  $(x^*, y^*)$  has its origin at the centre of the topography,  $(x^*, y^*) = (x - x_t, y - y_t)$ .

Solutions are generated on a square solution domain with  $l = w = 50$ , which is large enough to ensure fully developed flow both upstream and downstream. A grid hierarchy of five grid levels was used to generate the results with 65(1025) grid points, in each direction, on the coarsest(finest) mesh.

Figure 5.17 shows a complete three-dimensional visualization of the free surface disturbance generated for flow over a square trench topography having  $l_t = w_t = 1.54$  and  $|s_0| = 0.25$ , when  $\rho_2 = \mu_2 = 1$  and  $Re = 0$  - that is, the two layers are comprised of the same liquid and the system behaves as if a single fluid layer. The free surface disturbance consists of a horseshoe-shaped bow-wave in the vicinity

of the topography, instead of the single capillary ridge characterising flow over a spanwise two-dimensional trench. The free surface then exhibits a deep depression over the trench and finally a downstream surge emerges which does not have an equivalent in the two-dimensional case.

The above free surface features were noted and described by Decré and Baret (2003) in their experimental investigation but they did not provide an explanation for the existence of a downstream surge. An explanation based on the flow rate entering and leaving the trench was provided subsequently by Gaskell *et al.* (2004). Because the trench is finite in length and width, fluid enters the trench in three directions: the streamwise direction over the upstream wall and the spanwise directions over the two side walls due to transverse pressure gradients resulting from the spanwise curvature of the free surface. The liquid then leaves the trench in the streamwise direction over the downstream wall only and the downstream surge forms to allow the fluid to exit the trench across a shorter width than that across which it entered. In the two-dimensional flow case, fluid enters and exits the trench over the same width and therefore there is no mechanism for a downstream surge. Figure 5.18 shows the corresponding disturbance experienced by the liquid-liquid interface.

Figure 5.19 illustrates the streamwise free surface profile at  $y^* = 0$  for the above flow configuration, revealing that the present result agrees very well with that of Gaskell *et al.* (2004) for single-layer thin film flow.

Figures 5.20 and 5.21 show the free surface and liquid-liquid interface disturbance generated for flow over a square trench with  $l_t = w_t = 1.42$  and  $|s_0| = 0.197$  when  $Re = 5$ . The corresponding streamwise free surface profile at  $y^* = 0$  is shown in Figure 5.22 together with its single-layer equivalent by Veremieiev *et al.* (2010). The two profiles are in excellent agreement.

Topography aspect ratio,  $A_t = w_t/l_t$ , is another parameter which appears in three-

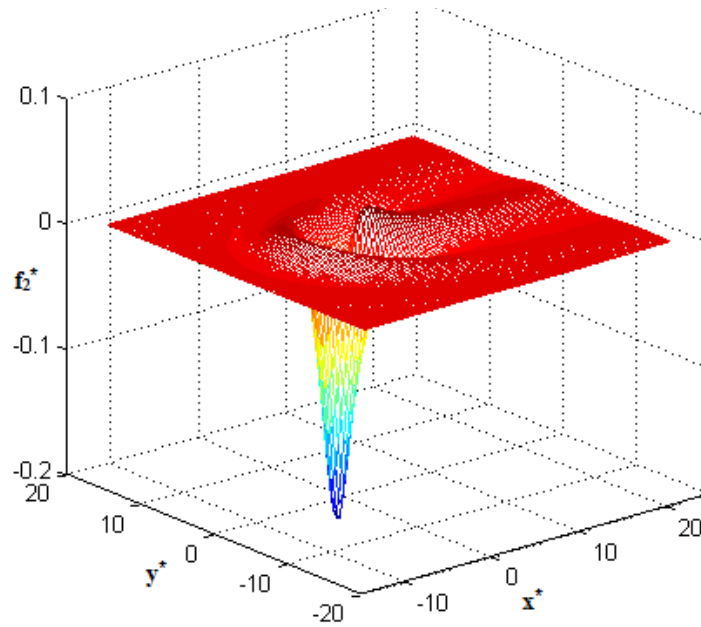


Figure 5.17: Free-surface disturbance for flow over trench topography,  $\theta = 30^\circ$ ,  $l_t = w_t = 1.54$ ,  $|s_0| = 0.25$ ,  $\text{Re}=0$ .

dimensional flow over localised topography and can affect the final free surface shape, Gaskell *et al.* (2004). Figure 5.23 shows three-dimensional visualisations of the free surface for flow over a localised trench for the more general case when the two liquids are different,  $\rho_2 = \mu_2 = 0.5$ , demonstrating the influence of changing  $A_t$  on the free surface disturbance generated. Increasing  $A_t$  from 1 to 5 widens the bow wave and increases its height while also increasing the depth of the free surface depression over the trench.

Increasing  $A_t$  to 10 causes the downstream surge to bifurcate such that two separate smaller surges appear; the depth of free surface depression and the height of the upstream capillary ridge do not exhibit considerable change. When  $A_t = 15$  the two newly formed downstream surges are pushed away from each other towards the sides with the free surface in the central area separating them becoming almost flat and the upstream capillary ridge less curved; showing that the flow near to the centreline  $y^* = 0$  approximates closely the two-dimensional case. The above

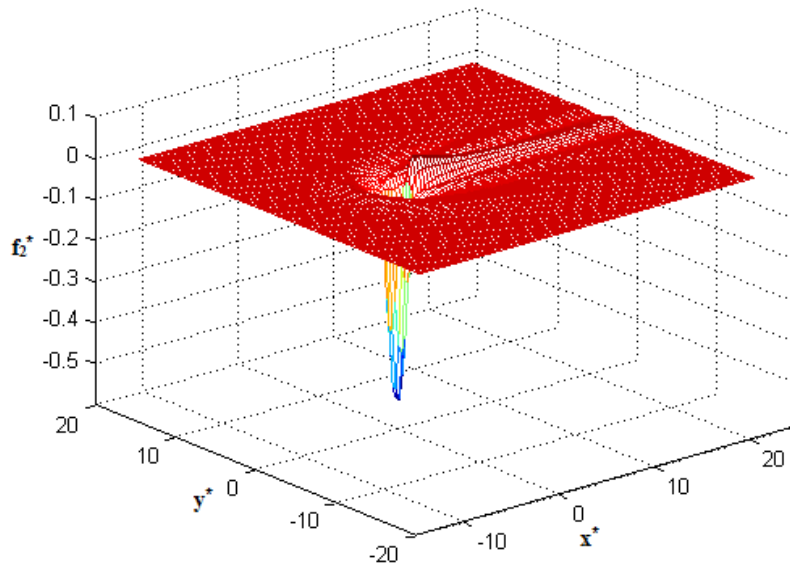


Figure 5.18: Liquid-liquid interface for flow over trench topography,  $\theta = 30^\circ$ ,  $l_t = w_t = 1.54$ ,  $|s_0| = 0.25$ ,  $Re=0$ .

mentioned behaviour of the free surface is clarified by inspection the streamwise interface profile at the centreline of the topography as shown in Figure 5.24 together with the spanwise profile at  $x^* = 0$ .

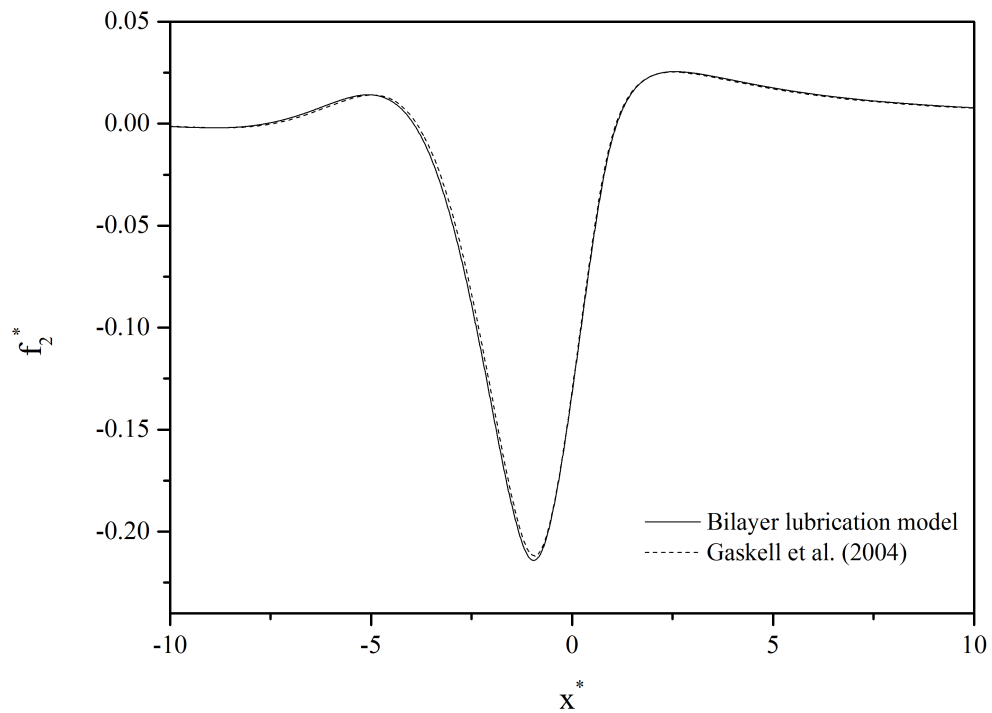


Figure 5.19: Comparison of predicted streamwise free-surface profile at  $y^* = 0$ ,  $Re = 0$ , with the lubrication approximation result of Gaskell *et al.* (2004) for flow over a trench of  $l_t = w_t = 1.54$ ,  $|s_0| = 0.25$  when  $\theta = 30^\circ$ .

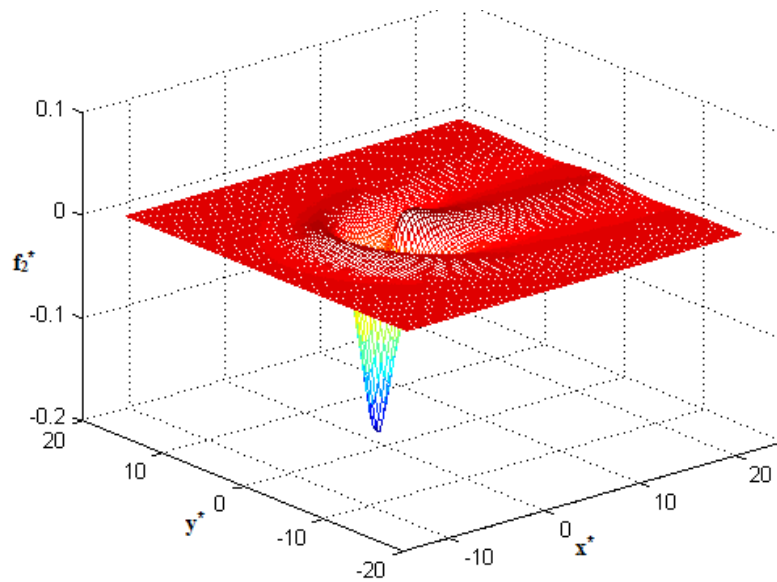


Figure 5.20: Free-surface disturbance for flow over trench topography,  $Re = 5$ ,  $\theta = 30^\circ$ ,  $l_t = w_t = 1.42$ ,  $|s_0| = 0.197$ ,  $\rho_2 = \mu_2 = 1$ .

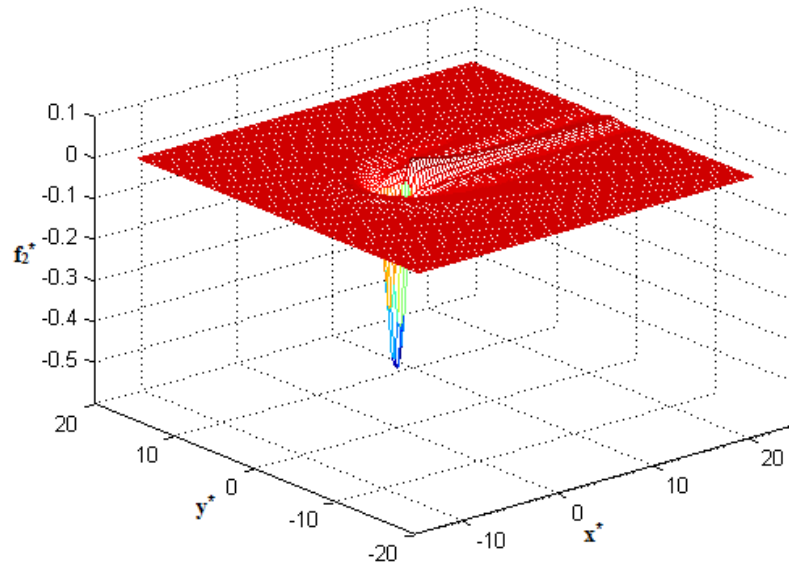


Figure 5.21: Liquid-liquid interface disturbance for flow over trench topography,  $Re = 5$ ,  $\theta = 30^\circ$ ,  $l_t = w_t = 1.42$ ,  $|s_0| = 0.197$ ,  $\rho_2 = \mu_2 = 1$ .

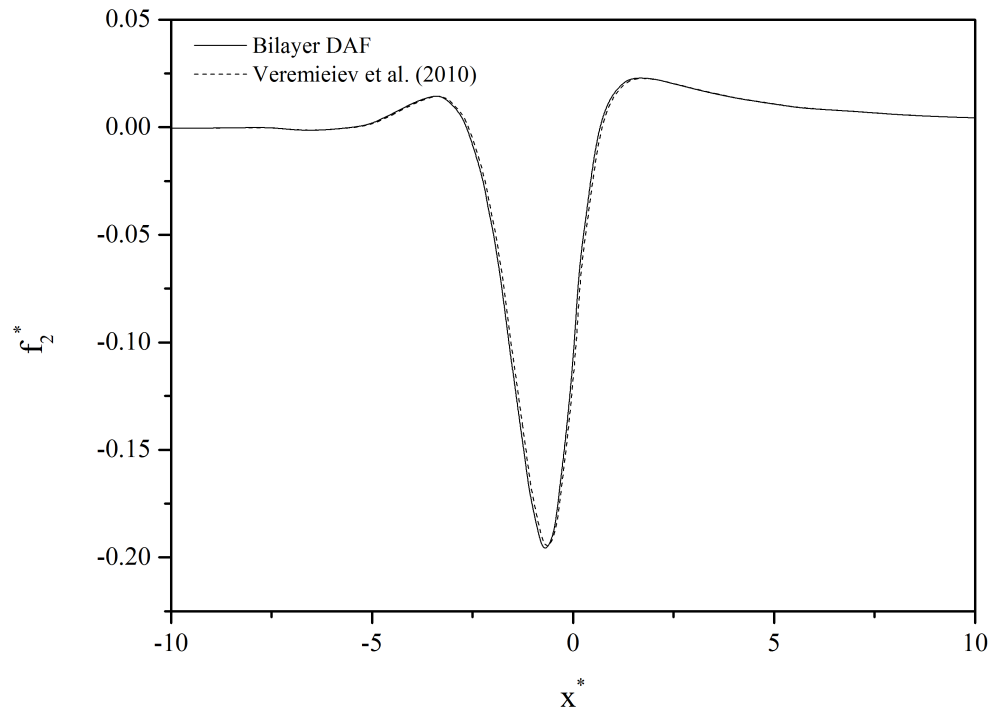


Figure 5.22: Comparison of predicted streamwise free-surface profile for the flow shown in Figure 5.20 with the results of Veremieiev *et al.* (2010) at  $y^* = 0$  for the.

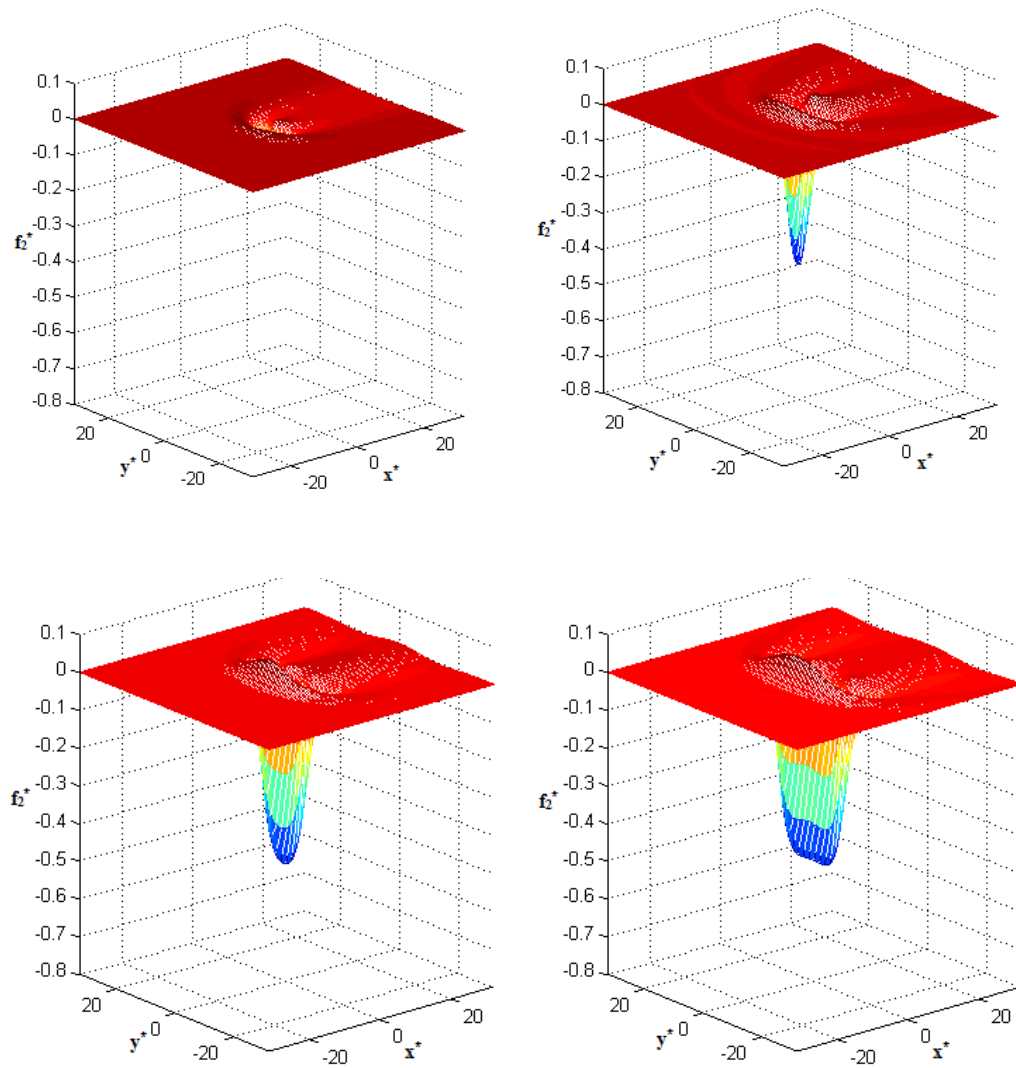


Figure 5.23: Three-dimensional plot for free surface disturbance generated by flow over trench topography, when  $\rho_2 = \mu_2 = 0.5$  and  $\theta = 10^\circ$  and  $l_t = 1.5$  when: (a)  $A_t=1$ ; (b)  $A_t=5$ ; (c)  $A_t=10$ ; (d)  $A_t=15$ .

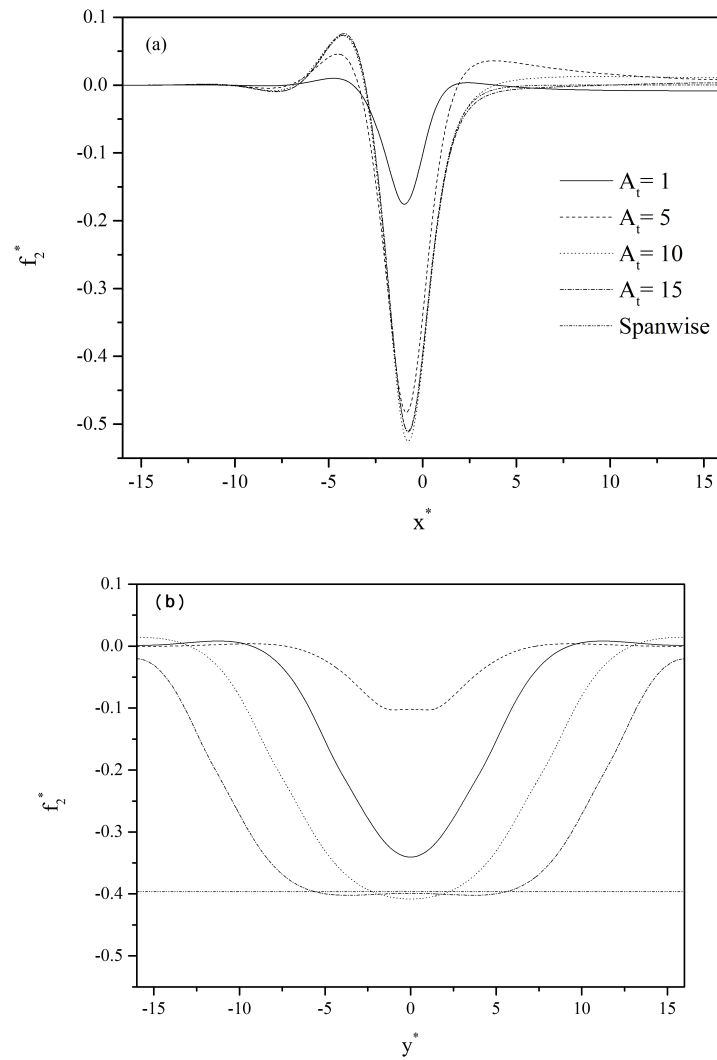


Figure 5.24: Effect of topography aspect ratio on (a) streamwise free-surface profiles  $y^* = 0$ , and (b) spanwise free-surface profiles along  $x^* = 0$  for the flow configurations shown in Figure 5.23 For comparison, the profiles for flow over the corresponding one-dimensional spanwise trench are also given when  $\rho_2 = \mu_2 = 0.5$

## Chapter 6

# Free-surface non-Newtonian Bilayer thin film flow

### Contents

---

<b>6.1</b>	<b>Introduction</b>	<b>164</b>
<b>6.2</b>	<b>Models for non-Newtonian liquids</b>	<b>164</b>
<b>6.3</b>	<b>Depth-averaged formulation for bilayer power-law thin film flow</b>	<b>169</b>
6.3.1	Bilayer Non-Newtonian flow with negligible inertia	173
6.3.2	Single-layer equivalent non-Newtonian inertial flow	175
<b>6.4</b>	<b>Method of solution</b>	<b>178</b>
6.4.1	Discretisation of the LUB equations	178
6.4.2	Discretisation of the DAF equations	180
<b>6.6</b>	<b>Results and discussion</b>	<b>182</b>

---

## 6.1 Introduction

This chapter reports an initial investigation to introduce non-Newtonian fluid behaviour into bilayer thin film flow problems for which an appropriate set of governing model equations based on the DAF of the governing Navier-Stokes equations for a generalised fluid is developed. First, however a discussion is provided of non-Newtonian fluid behaviour in general and the models that have been developed to capture the same.

## 6.2 Models for non-Newtonian liquids

Fluids are classified according to their response to shearing stress as Newtonian or non-Newtonian fluids. In Newtonian fluids the plot of shear stress,  $\tau_{xy}$  against the shear rate,  $\dot{\gamma}_{xy}$  is linear and passes through the origin. The slope of this so called flow curve is the Newtonian viscosity which is independent of  $\tau$  and  $\dot{\gamma}$  and depends only on the fluid material and its temperature and pressure. For non-Newtonian fluids the flow curve is not linear or does not pass through the origin so that the viscosity is not constant at given temperature and pressure but depends on the shear rate and in some cases on the shear rate history, Irgens (2014).

Non-Newtonian fluids are classified as: generalized Newtonian fluids in which viscosity is a function of the shear rate but is independent on the shear rate history,  $\tau_{xy} = f(\dot{\gamma}_{xy})$ ; viscoelastic fluids which exhibit characteristics of both elastic materials and viscous fluids and show partial elastic recovery when deformed; and time-dependant non-Newtonian fluids, the viscosity of which is a function of shear rate and duration of stress.

Generalised Newtonian fluids may be categorised according to the function relat-

ing shear stress to shear rate as: shear-thinning or pseudoplastic (which is the most common), viscoplastic and shear-thickening or dilatant. The later is less common in practical applications and very few reliable data for which are available in the literature, Chhabra and Richardson (2011). The apparent viscosity of a shear-thinning fluid decreases with increasing shear rate while that of shear-thickening one increases with increasing shear rate. Viscoplastic fluids are characterised by the presence of a yield stress which must be exceeded before deformation occurs. Viscoplastic fluids are classified as Bingham plastic fluids if the flow curve is linear and yield-pseudoplastic fluids when the flow curve is non-linear. Figure 6.1 shows the different curves represent each of these categories of time-independent non-Newtonian fluids.

Time-dependent non-Newtonian fluid behaviour, on the other hand, may be subdivided into: thixotropic if the apparent viscosity decreases with time when it is sheared at a constant rate; and rheopexy (or negative thixotropic) if the apparent viscosity increases with time of shearing, Wilkinson (1960).

Several models, some of them completely empirical, have been proposed to describe the behaviour of time-independent non-Newtonian fluids. The Bingham plastic model, the Herschel-Bulkley model and the Casson fluid model are used to describe viscoplastic behaviour while for pseudoplastic and diliant fluids, the most common are the power-law, Carreau and Ellis fluid models, Bird (1976):

(i) The power-law or Ostwald de Waele model is suitable for both shear-thinning and shear-thickening fluids and assumes a power law relation between shear stress and shear rate, namely:

$$\tau_{xy} = K\dot{\gamma}_{xy}^n, \quad (6.1)$$

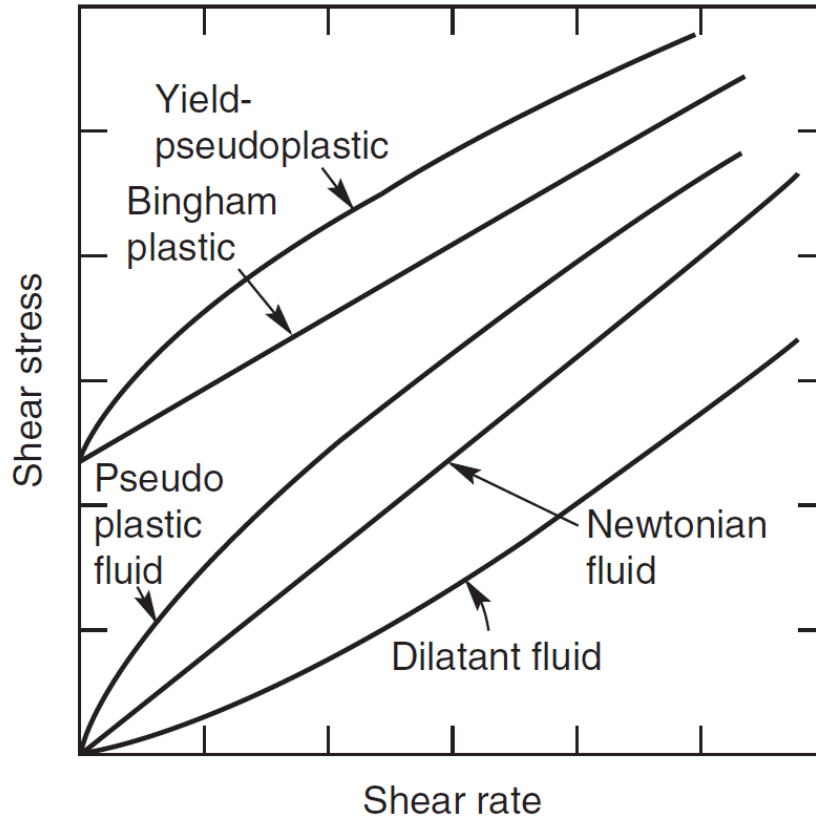


Figure 6.1: Types of time-independent non-Newtonian fluid behaviour, Chhabra and Richardson (2011)

where  $K$  and  $n$  are fluid consistency coefficient and the power law index, respectively. The power-law model is very common and widely used for modelling non-Newtonian fluids.

(ii) The Ellis fluid model is used to represent the non-Newtonian behaviour of a fluid if the power-law model fails to predict viscosities at very low shear rates. The viscosity is calculated as:

$$\hat{\mu} = \frac{\hat{\mu}_0}{1 + (\tau_{xy}/\tau_{xy1/2})^{\alpha-1}}, \quad (6.2)$$

where  $\mu_0$  is the viscosity at zero shear stress and  $\tau_{xy1/2}$  is an adjustable parameter. The index  $\alpha$  is a measure of the non-Newtonian behaviour.

(iii) The Carreau model is used when there are significant deviations from the power-law model at very high and very low shear rates as it takes account of the limiting values of viscosities  $\mu_0$  and  $\mu_\infty$ . Based on molecular network considerations, Carreau (1972) put forward the following viscosity model which incorporates both limiting viscosities:

$$\frac{\mu - \mu_\infty}{\mu_0 - \mu_\infty} = \left[ 1 + (\lambda \dot{\gamma}_{xy})^2 \right]^{\frac{n-1}{2}} \quad (6.3)$$

Although the majority of the published literature on the subject of thin film flow assume Newtonian behaviour, some studies have considered non-Newtonian behaviours either in free-surface or channel flow. Weinstein (1990) investigated the effect of shear-thinning rheology on the wave growth and stability of multilayer thin film flow down an inclined surface using the Carreau model. In order to assess the effect of the shear-thinning behaviour, the author compared his non-Newtonian results with the two limiting Newtonian cases based on the minimum and maximum viscosities attained in the shear-thinning layer. Waves on free the surface growth behaviour was found to be similar to that for a Newtonian system with a viscosity equal to the average of varying viscosity of the non-Newtonian one, while interfacial waves are significantly affected by local viscosities.

Balmforth *et al.* (2003) explored the linear and non-linear interfacial instabilities of bilayer flow down an inclined substrate of non-Newtonian power-law fluids based on the long-wave approximation. Moreover, Miladinova *et al.* (2004) investigated numerically the thin film flow of a power-law fluid down an inclined plate. It was found that the free surface evolution is similar to Newtonian flow but the shape and amplitude are significantly influenced by non-Newtonian behaviour and the maximum wave amplitude for shear-thinning flow is larger than that for a Newtonian liquid, while for a shear-thickening fluid it is smaller than that for a Newtonian one.

Myers (2005) compared power-law, Ellis and Carreau models for describing the non-Newtonian behaviour of flow down inclined substrate or in a channel in the framework of lubrication theory. The study indicates that the Ellis model produced results similar to those of the Carreau model but that power-law model led to very inaccurate results for both free-surface and channel flows. Rousset *et al.* (2007) studied the temporal stability of the non-Newtonian flow of Carreau fluid flow down a flat inclined substrate using the long-wave approximation. Their results show that waves travel faster in a shear-thinning fluid than in a Newtonian fluid. The critical Reynolds number threshold for inertial stability was found, as in Newtonian fluids, to be proportional to the cotangent of the inclination angle with the proportionality factor decreasing when the non-Newtonian becomes stronger.

More recently, Millet *et al.* (2013) studied the influence of shear-thinning properties on the stability of bilayer Carreau fluids taking into account the effects of density and viscosity stratification. They found that if the upper layer is more viscous, the stability properties is almost not influenced by the change of the shear-thinning properties in this upper layer. In the other situations, the shear-thinning properties have an influence on interface and free surface the instabilities.

Below, the power-law model, which has seen the most practical and extensive use, is employed to describe non-Newtonian behaviour in bilayer gravity-driven flow. The current study, being exploratory only, is limited to pseudoplastic (shear-thinning) and dilatant (shear-thickening) fluids.

### 6.3 Depth-averaged formulation for bilayer power-law thin film flow

The non-Newtonian behaviour is implemented using the power-law model given by equation(6.1). The viscosity is calculated from:

$$\hat{\mu}_i = K_i \dot{\gamma}^{n_i-1}, \quad (6.4)$$

where  $K_i$  and  $n_i$  are the consistency coefficient and the flow behaviour index or the power-law exponent respectively. The former (with units of  $Pa s^{n_i}$ ) is a measure of the consistency of the liquid, the higher the value of  $K_i$  the more viscous the liquid, while the latter is a measure of the degree of non-Newtonian behaviour of the liquid, having shear-thinning behaviour when  $n_i < 1$  and shear-thickening behaviour for  $n_i > 1$ . The flow is governed by the momentum conservation and the continuity equations

$$\hat{\rho}_i \left( \frac{\partial \underline{U}_i}{\partial T} + \underline{U}_i \cdot \nabla \underline{U}_i \right) = -\nabla P_i + \nabla \cdot \underline{\underline{T}}_i + \hat{\rho}_i \underline{\underline{G}}, \quad (6.5)$$

$$\nabla \cdot \underline{\underline{U}}_i = 0, \quad (6.6)$$

where  $\underline{U}_i$  and  $\underline{\underline{G}}$  are the velocity and gravity vectors respectively,  $\underline{\underline{T}}_i$  is the viscous stress tensor,  $P_i$  is the pressure, and  $\hat{\rho}_i$  is the density.  $i = 1, 2$  for the lower and upper layer respectively.

Following Ahmed *et al.* (2013), the governing equations are non-dimensionalised

using the their scaling:

$$(x, z) = \left( \frac{X}{L_0}, \frac{Z}{H_0} \right), \quad (u_i, w_i) = \left( \frac{U_i}{U_0}, \frac{W_i}{\epsilon U_0} \right), \quad p_i = \frac{P_i}{P_0} \quad (6.7)$$

$$\text{where } P_0 = \frac{\hat{\sigma}_1 \epsilon}{L_0}, \quad U_0 = \frac{L_0}{T_0}, \quad T_0 = \left( \frac{L_0 K_1}{\hat{\sigma}_1 \epsilon^{n_1+2}} \right)^{1/n_1} \quad \text{and} \quad \epsilon = \frac{H_0}{L_0}$$

Applying these scalings and neglecting terms of order  $\epsilon^2$  or higher, the governing equations, (6.5) and (6.6) for two-dimensional flow becomes:

$$\epsilon Re_i \left( \frac{\partial u_i}{\partial t} + u_i \frac{\partial u_i}{\partial x} + w_i \frac{\partial u_i}{\partial z} \right) = -A_i \left( \frac{\partial p_i}{\partial x} - \frac{\rho_i Bo \sin \theta}{\epsilon} \right) + \frac{\partial}{\partial z} \left( \frac{\partial u_i}{\partial z} \right)^{n_i}, \quad (6.8)$$

$$\frac{\partial p_i}{\partial z} + \rho_i Bo \cos \theta = 0, \quad (6.9)$$

$$\frac{\partial u_i}{\partial x} + \frac{\partial w_i}{\partial z} = 0, \quad (6.10)$$

where  $Bo = \frac{\hat{\rho}_1 g L_0^2}{\hat{\sigma}_1}$  and  $A_i = \left( \frac{\epsilon^3 \hat{\sigma}_1}{H_0 K_1} \right)^{1-\frac{n_i}{n_1}} \frac{K_1}{K_i}$ . The Reynolds number for non-Newtonian fluid is defined as:

$$Re_i = \frac{\hat{\rho}_i U_0^{2-n_i} H_0^{n_i}}{K_i}. \quad (6.11)$$

Following the same argument as for the Newtonian bilayer film case in Chapter 2, the corresponding boundary conditions are:

At inlet:

$$h_1|_{x=0} = h_{10}, \quad h_2|_{x=0} = 1 - h_{10}, \quad (6.12)$$

no-slip at liquid-solid and liquid-liquid interfaces:

$$\mathbf{u}_1|_{z=f_0} = 0, \quad u_1|_{z=f_1} = u_2|_{z=f_1}, \quad (6.13)$$

At the liquid-liquid interface and free surface, the kinematic boundary

conditions are:

$$\begin{aligned}\frac{\partial f_1}{\partial t} + u_1|_{z=f_1} \frac{\partial f_1}{\partial x} - w_1|_{z=f_1} &= 0, \\ \frac{\partial f_2}{\partial t} + u_2|_{z=f_2} \frac{\partial f_2}{\partial x} + -w_2|_{z=f_2} &= 0,\end{aligned}\tag{6.14}$$

Normal and tangential stresses balance at the free-surface and liquid-liquid

interface:

$$\left( \frac{\partial u_1}{\partial z} \Big|_{z=f_1} \right)^{n_1} = \frac{1}{A_2} \left( \frac{\partial u_2}{\partial z} \Big|_{z=f_1} \right)^{n_2},\tag{6.15}$$

$$\begin{aligned}\frac{\partial u_2}{\partial z} \Big|_{z=f_2} &= 0, \\ (p_1 - p_2) |_{z=f_1} &= -\sigma_{int} \frac{\partial^2 f_1}{\partial x^2}, \\ p_2|_{z=f_2} - p_A &= -\sigma_2 \frac{\partial^2 f_2}{\partial x^2}.\end{aligned}\tag{6.16}$$

Integrating equation (6.9) with respect to  $z$  and applying boundary condition (6.16) yields the following pressure equations:

$$p_1 = Bo \cos \theta (f_1 - z + \rho_2(f_2 - f_1)) - \sigma_{in} \nabla^2 f_1 - \sigma_2 \nabla^2 f_2,\tag{6.17}$$

$$p_2 = \rho_2 Bo \cos \theta (f_2 - z) - \sigma_2 \nabla^2 f_2.\tag{6.18}$$

Integrating the continuity equation (6.10) using Leibniz's rule and applying boundary conditions (6.13) and (6.14) as shown in Chapter 2, leads to the following depth-averaged equation for the conservation of mass:

$$\frac{\partial h_i}{\partial t} + \frac{\partial (h_i \bar{u}_i)}{\partial x} = 0.\tag{6.19}$$

The depth-averaged form of the  $z$ -momentum equation is derived, as in Chapter 2, by integrating (6.8) with respect to  $z$  and making use of Leibniz's rule and the

kinetic boundary condition (6.14). This results in the following DAF equation:

$$\begin{aligned} \varepsilon Re_i \left[ \frac{\partial \bar{u}_i}{\partial t} + \bar{u}_i \frac{\partial \bar{u}_i}{\partial x} + \frac{1}{h_i} \frac{\partial}{\partial x} \int_{f_{i-1}}^{f_i} (\bar{u}_i - u_i)^2 dz \right] \\ = -A_i \left( \frac{\partial p_i}{\partial x} - \frac{\rho_i Bo \sin \theta}{\varepsilon} \right) + \frac{1}{h_i} \left( \frac{\partial u_i}{\partial z} \right)^{n_i} \Big|_{z=f_i} - \frac{1}{h_i} \left( \frac{\partial u_i}{\partial z} \right)^{n_i} \Big|_{z=f_{i-1}}. \end{aligned} \quad (6.20)$$

To evaluate the friction and dispersion terms in equation (6.20),  $\int_{f_{i-1}}^{f_i} (\bar{u}_i - u_i)^2 dz$  and  $\left( \frac{\partial u_i}{\partial z} \right)^{n_i}$ , respectively, knowledge of the velocity profile is required. As shown in Chapter 2 the DAF assumes a self similar quadratic velocity profiles across the layers when the liquid is Newtonian. Proceeding in a similar way for power-law liquids and putting  $Re = 0$ , the right-hand side in equation (6.8) vanishes resulting in:

$$\frac{\partial}{\partial z} \left( \frac{\partial u_i}{\partial z} \right)^{n_i} = A_i \left( \frac{\partial p_i}{\partial x} - \frac{\rho_i Bo \sin \theta}{\varepsilon} \right) = \alpha_i. \quad (6.21)$$

Integrating equation (6.21) twice with respect to  $z$  and applying boundary conditions yields the following velocity profiles:

$$u_1 = -\frac{(-\alpha_1)^{\lambda_1}}{\lambda_1 + 1} \left[ \left( f_1 - z + \frac{\alpha_2}{A_2 \alpha_1} h_2 \right)^{\lambda_1 + 1} - \left( h_1 + \frac{\alpha_2}{A_2 \alpha_1} h_2 \right)^{\lambda_1 + 1} \right], \quad (6.22)$$

$$\begin{aligned} u_2 = -\frac{(-\alpha_2)^{\lambda_2}}{\lambda_2 + 1} \left[ (f_2 - z)^{\lambda_2 + 1} - h_2^{\lambda_2 + 1} \right] - \frac{(-\alpha_1)^{\lambda_1}}{\lambda_1 + 1} \left[ \left( \frac{\alpha_2}{A_2 \alpha_1} h_2 \right)^{\lambda_1 + 1} \right. \\ \left. - \left( h_1 + \frac{\alpha_2}{A_2 \alpha_1} h_2 \right)^{\lambda_1 + 1} \right], \end{aligned} \quad (6.23)$$

where  $\lambda_i = \frac{1}{n_i}$ .

The interface velocity is given by:

$$u_{int} = -\frac{(-\alpha_1)^{\lambda_1}}{\lambda_1 + 1} \left[ \left( \frac{\alpha_2}{A_2 \alpha_1} h_2 \right)^{\lambda_1+1} - \left( h_1 + \frac{\alpha_2}{A_2 \alpha_1} h_2 \right)^{\lambda_1+1} \right], \quad (6.24)$$

and the average velocity for each layer is derived as:

$$\bar{u}_1 = -\frac{(-\alpha_1)^{\lambda_1}}{\lambda_1 + 1} \left[ \frac{-\left( \frac{\alpha_2}{A_2 \alpha_1} h_2 \right)^{\lambda_1+2} + \left( h_1 + \frac{\alpha_2}{A_2 \alpha_1} h_2 \right)^{\lambda_1+2}}{h_1(\lambda_1 + 2)} - \left( h_1 + \frac{\alpha_2}{A_2 \alpha_1} h_2 \right)^{\lambda_1+1} \right], \quad (6.25)$$

$$\bar{u}_2 = \frac{(-\alpha_2)^{\lambda_2}}{\lambda_2 + 2} \left( h_2^{\lambda_2+1} \right) - \frac{(-\alpha_1)^{\lambda_1}}{\lambda_1 + 1} \left[ \left( \frac{\alpha_2}{A_2 \alpha_1} h_2 \right)^{\lambda_1+1} - \left( h_1 + \frac{\alpha_2}{A_2 \alpha_1} h_2 \right)^{\lambda_1+1} \right]. \quad (6.26)$$

What is required now is to express the velocity profiles in terms of their average velocities to obtain the friction and dispersion terms as functions of the same. For bilayer Newtonian flow this is achieved by introducing the velocity of the liquid-liquid interface,  $u_{int}$ , and thus the pressure gradient terms are eliminated. However, this task is not achievable for the non-Newtonian case without some further simplifications, due to the non-linear dependence of  $u_i$  on  $\alpha_i$ . Accordingly the attention is focused on two simplifications of the above formulation: (i) bilayer flow with negligible inertia; (ii) flow for non-negligible inertia but when both fluids have the same properties, the problem being thus equivalent to a single non-Newtonian liquid.

### 6.3.1 Bilayer Non-Newtonian flow with negligible inertia

The DAF reduces to the lubrication approximation when  $Re$  is  $O(\varepsilon)$ , the evolution equation of which is derived by substituting the average velocities from equations

(6.25) and (6.26) into the mass conservation equation (6.19), resulting in:

$$\frac{\partial h_1}{\partial t} + \frac{\partial q_1}{\partial x} = 0, \quad (6.27)$$

$$\frac{\partial h_2}{\partial t} + \frac{\partial q_2}{\partial x} = 0, \quad (6.28)$$

where

$$q_1 = -\frac{(-\alpha_1)^{\lambda_1}}{\lambda_1 + 1} \left[ \frac{\left(h_1 + \frac{\alpha_2}{A_2\alpha_1}h_2\right)^{\lambda_1+2} - \left(\frac{\alpha_2}{A_2\alpha_1}h_2\right)^{\lambda_1+2}}{\lambda_1 + 2} - \left(h_1 + \frac{\alpha_2}{A_2\alpha_1}h_2\right)^{\lambda_1+1} h_1 \right], \quad (6.29)$$

$$q_2 = -\frac{(-\alpha_2)^{\lambda_2}}{\lambda_2 + 2} \left(h_2^{\lambda_2+2}\right) - \frac{(-\alpha_1)^{\lambda_1} h_2}{\lambda_1 + 1} \left[ \left(\frac{\alpha_2}{A_2\alpha_1}h_2\right)^{\lambda_1+1} - \left(h_1 + \frac{\alpha_2}{A_2\alpha_1}h_2\right)^{\lambda_1+1} \right] \quad (6.30)$$

These equations present a significant challenge compared to their Newtonian equivalent. The problem is that for certain values of  $\lambda_i$  and if  $(-\alpha_i)$ ,  $\left(h_1 + \frac{\alpha_2}{A_2\alpha_1}h_2\right)$  or  $\left(\frac{\alpha_2}{A_2\alpha_1}h_2\right)$  are negative, this may result in complex-valued terms. Several authors, see for example Perazzo and Gratton (2003) and Wang *et al.* (2007), have discussed this problem and the signum function proposed to overcome it. Employing this approach yields the following evolution equations:

$$q_1 = \frac{\text{sign}(\alpha_1) |\alpha_1|^{\lambda_1}}{\lambda_1 + 1} \left[ -\text{sign}\left(h_1 + \frac{\alpha_2}{A_2\alpha_1}h_2\right) \left| h_1 + \frac{\alpha_2}{A_2\alpha_1}h_2 \right|^{\lambda_1+1} h_1 + \frac{\text{sign}\left(h_1 + \frac{\alpha_2}{A_2\alpha_1}h_2\right) \left| h_1 + \frac{\alpha_2}{A_2\alpha_1}h_2 \right|^{\lambda_1+2} - \text{sign}\left(\frac{\alpha_2}{A_2\alpha_1}h_2\right) \left| \frac{\alpha_2}{A_2\alpha_1}h_2 \right|^{\lambda_1+2}}{\lambda_1 + 2} \right] \quad (6.31)$$

$$q_2 = \frac{\text{sign}(\alpha_2) |\alpha_2|^{\lambda_2}}{\lambda_2 + 2} (h_2^{\lambda_2+2}) - \frac{\text{sign}(\alpha_1) |\alpha_1|^{\lambda_1} h_2}{\lambda_1 + 1} \left[ \text{sign}\left(\frac{\alpha_2}{A_2 \alpha_1} h_2\right) \left| \frac{\alpha_2}{A_2 \alpha_1} h_2 \right|^{\lambda_1+1} - \text{sign}\left(h_1 + \frac{\alpha_2}{A_2 \alpha_1} h_2\right) \left| h_1 + \frac{\alpha_2}{A_2 \alpha_1} h_2 \right|^{\lambda_1+1} \right] \quad (6.32)$$

where

$$\text{sign}(x) = \begin{cases} -1, & \text{if } x < 0 \\ 0, & x = 0 \\ 1, & \text{if } x > 0 \end{cases}$$

Equations (6.31) and (6.32) in conjunction with equations (6.17) and (6.18) constitute the full set of governing equations for free-surface bilayer non-Newtonian flow for a power-law liquid at small Reynolds number.

### 6.3.2 Single-layer equivalent non-Newtonian inertial flow

It is possible to explore the influence of inertia on free-surface thin film flow using the DAF if both liquid have the same properties.

The pressure equations (6.17) and (6.18) reduces to a single equation ( with the subscript denoting the subsequent layer dropped since the flow reduces to single-layer case) given by:

$$p = Bo \cos \theta (f - z) - \nabla^2 f, \quad (6.33)$$

and the depth-averaged equation for the conservation of mass is:

$$\frac{\partial h}{\partial t} + \frac{\partial (h\bar{u})}{\partial x} = 0. \quad (6.34)$$

The lubrication equations (6.22) and (6.23) similarly reduce to a simpler form:

$$u = -\frac{(-\alpha)^\lambda}{\lambda + 1} \left[ (f - z)^{\lambda+1} - h^{\lambda+1} \right], \quad (6.35)$$

which can be averaged across the film thickness as:

$$\bar{u} = \frac{1}{h} \int_s^{h+s} -\frac{(-\alpha)^\lambda}{\lambda + 1} \left[ (f - z)^{\lambda+1} - h^{\lambda+1} \right] \partial z, \quad (6.36)$$

resulting in the average velocity:

$$\bar{u} = \frac{(-\alpha)^\lambda}{\lambda + 2} h^{\lambda+1}. \quad (6.37)$$

The velocity profile is now written in terms of  $\bar{u}$  as:

$$u = \frac{\lambda + 2}{\lambda + 1} \frac{\bar{u}}{h^{\lambda+1}} \left[ h^{\lambda+1} - (f - z)^{\lambda+1} \right], \quad (6.38)$$

or:

$$u = \frac{\lambda + 2}{\lambda + 1} \bar{u} \left[ 1 - (1 - \xi)^{\lambda+1} \right], \quad (6.39)$$

Equation (6.39) is used to obtain the friction term as:

$$\left. \frac{\partial u}{\partial z} \right|_{z=f_0} = \frac{1}{h} \left. \frac{\partial u}{\partial \xi} \right|_{\xi=0} = (\lambda + 2) \frac{\bar{u}}{h}, \quad (6.40)$$

and the dispersion term:

$$\begin{aligned} \int_{f_0}^f (u - \bar{u})^2 \partial z &= h \int_0^1 (u^2 - 2u\bar{u} + \bar{u}^2) \partial \xi = -h(\bar{u})^2 + h \int_0^1 u^2 \partial \xi \\ &= -h\bar{u}^2 + h \left( \frac{\lambda + 2}{\lambda + 1} \right)^2 \bar{u}^2 \int_0^1 [1 - 2(1 - \xi)^{\lambda+1} + (1 - \xi)^{2\lambda+2}] \partial \xi, \end{aligned} \quad (6.41)$$

or:

$$\int_{f_0}^f (u - \bar{u})^2 \partial z = \frac{h\bar{u}^2}{2\lambda + 3}. \quad (6.42)$$

The DAF of momentum equation (6.20) becomes:

$$\varepsilon Re \left[ \frac{\partial \bar{u}}{\partial t} + \bar{u} \frac{\partial \bar{u}}{\partial x} + \frac{1}{h} \frac{\partial}{\partial x} \left( \frac{h\bar{u}^2}{2\lambda + 3} \right) \right] = - \left( \frac{\partial p}{\partial x} - \frac{Bo \sin \theta}{\varepsilon} \right) + (\lambda + 2)^n \frac{\bar{u}^n}{h^{n+1}} \quad (6.43)$$

or

$$\begin{aligned} \varepsilon Re \left[ \frac{\partial \bar{u}}{\partial t} + \bar{u} \frac{\partial \bar{u}}{\partial x} + \frac{1}{(2\lambda + 3)h} \left( h\bar{u} \frac{\partial \bar{u}}{\partial x} + \bar{u} \frac{\partial (h\bar{u})}{\partial x} \right) \right] &= - \left( \frac{\partial p}{\partial x} - \frac{Bo \sin \theta}{\varepsilon} \right) \\ &+ (\lambda + 2)^n \frac{\bar{u}^n}{h^{n+1}}, \end{aligned} \quad (6.44)$$

substituting  $\frac{\partial (h\bar{u})}{\partial x} = -\frac{\partial h}{\partial t}$  from the mass conservation equation, yields:

$$\varepsilon Re \left[ \frac{\partial \bar{u}}{\partial t} - \frac{1}{(2\lambda + 3)h} \bar{u} \frac{\partial h}{\partial t} + \frac{(2\lambda + 4)}{(2\lambda + 3)} \bar{u} \frac{\partial \bar{u}}{\partial x} \right] = - \left( \frac{\partial p}{\partial x} - \frac{Bo \sin \theta}{\varepsilon} \right) + (\lambda + 2)^n \frac{\bar{u}^n}{h^{n+1}}, \quad (6.45)$$

## 6.4 Method of solution

### 6.4.1 Discretisation of the LUB equations

Equations (6.17), (6.18) and (6.27), (6.28) are solved on a uniform computational domain,  $x \in [0, l]$  using the multigrid approach described in Chapter 3. The solution domain is subdivided using a collocated mesh arrangement of nodes with increments of  $\Delta x$ . The corresponding coupled second-order accurate discretisation scheme for  $h_i$  and  $p_i$  is written as:

$$\begin{aligned} \frac{\partial h_{1I}}{\partial t} + \frac{q_{1I+1/2} - q_{1I-1/2}}{\Delta x} &= 0, \\ \frac{\partial h_{2I}}{\partial t} + \frac{q_{2I+1/2} - q_{2I-1/2}}{\Delta x} &= 0, \end{aligned} \quad (6.46)$$

$$\begin{aligned} p_{1I} = -\sigma_{int} \left( \frac{f_{1I+1} + f_{1I-1} - 2f_{1I}}{\Delta x^2} \right) - \sigma_2 \left( \frac{f_{2I+1} + f_{2I-1} - 2f_{2I}}{\Delta x^2} \right) \\ + Bo (f_{1I} + \rho_2 (f_{2I} - f_{1I})) \cos \theta, \end{aligned} \quad (6.47)$$

$$p_{2I} = -\sigma_2 \left( \frac{f_{2I+1} + f_{2I-1} - 2f_{2I}}{\Delta x^2} \right) + Bo f_{2I} \cos \theta. \quad (6.48)$$

It is convenient to write the discretised equation in the following compact form:

$$\left. \frac{\partial h_i}{\partial t} \right|_I + \mathcal{M}_I^{h_i}(h_1, h_2, p_1, p_2) = 0, \quad (6.49)$$

$$p_i|_I + \mathcal{M}_I^{p_i}(h_1, h_2) = 0. \quad (6.50)$$

As with the DAF model, Chapter 3, an automatic adaptive time-stepping scheme is

implemented into the solution strategy to optimise time step selection. The time-stepping procedure adopted uses the local truncation error estimates (LTE) obtained from the difference between a predictor stage and the current solution stage. Fully explicit second order time discretisation of equation (6.49) yields the following expression for the predicted values of  $h_{i_{pr}}$  and  $p_{i_{pr}}$ , Veremieiev *et al.* (2010):

$$h_{i_{pr}}|_I^{n+1} = \gamma^2 h_I^{n-1} + (1 - \gamma^2) h_I^n - \Delta t^{n+1} (1 + \gamma) \mathcal{M}_I^{h_i}(h_1^n, h_2^n, p_1^n, p_2^n) \quad (6.51)$$

$$p_{i_{pr}}|_I^{n+1} + \mathcal{M}_I^{p_i}(h_1^n, h_2^n) = 0, \quad (6.52)$$

where the superscript  $n$  denotes a value at the end of the  $n$ th time step  $t = t^n$  and  $\gamma = \frac{\Delta t^{n+1}}{\Delta t^n}$  is the ratio of successive time steps.

Adaptive time-stepping, Chapter 2, is performed by keeping the LTE for  $h_{2_{pr}}$  within a pre-set tolerance to allow the size of time step to be increased in a controlled manner. An implicit and unconditionally stable Crank-Nicolson scheme, see Gaskell *et al.* (2004) and Veremieiev (2011), is used to march the solution forward in time:

$$h_{i_I}^{n+1} + \frac{\Delta t^{n+1}}{2} \mathcal{M}_I^{h_i}(h_1^{n+1}, h_2^{n+1}, p_1^{n+1}, p_2^{n+1}) = h_{i_I}^n - \frac{\Delta t^{n+1}}{2} \mathcal{M}_I^{h_i}(h_1^n, h_2^n, p_1^n, p_2^n), \quad (6.53)$$

$$p_{i_I}^{n+1} + \mathcal{M}_I^{p_i}(h_1^{n+1}, h_2^{n+1}) = 0. \quad (6.54)$$

As with the discretised DAF, Chapter 3, it is convenient to write the discrete LUB equations (6.53) and (6.54) by introducing a global time-dependant nonlinear operator, right-hand side function (defined by the solution on the previous time step) and solution vectors respectively:

$$\mathcal{N} \mathbf{u}^{n+1} = \mathbf{f} \mathbf{u}^n, \quad (6.55)$$

where:

$$\mathcal{N} = \begin{pmatrix} \mathcal{N}_I^{h_1} \\ \mathcal{N}_I^{h_2} \\ \mathcal{N}_I^{p_1} \\ \mathcal{N}_I^{p_2} \end{pmatrix}, \quad \mathbf{f} = \begin{pmatrix} \mathbf{f}_I^{h_1} \\ \mathbf{f}_I^{h_2} \\ 0 \\ 0 \end{pmatrix}, \quad \mathbf{u}^n = \begin{pmatrix} h_{1I}^n \\ h_{2I}^n \\ p_{1I}^n \\ p_{2I}^n \end{pmatrix}. \quad (6.56)$$

## 6.4.2 Discretisation of the DAF equations

As for DAF for the free-surface Newtonian flow, equations (6.33), (6.34) and (6.45) are solved for,  $\bar{u}$ ,  $h$  and  $p$ , on a computational domain,  $x \in [0, l]$  by the multigrid approach using staggered mesh arrangement. The corresponding coupled second-order accurate discrete equations can be written, omitting for convenience the over-bar denoting velocity averaging, as:

$$\varepsilon Re \left( \frac{\partial \bar{u}}{\partial t} - \frac{1}{2\lambda + 3} \frac{\bar{u}}{h} \frac{\partial h}{\partial t} + \frac{2\lambda + 4}{2\lambda + 3} \mathcal{F}(u) \right)_{I+\frac{1}{2}} + \frac{p_{I+1} - p_I}{\Delta x} - \frac{Bo \sin \theta}{\varepsilon} - f_{r_{I+\frac{1}{2}}} = 0 \quad (6.57)$$

$$\left. \frac{\partial h_i}{\partial t} \right|_I + \frac{h_{i_{I+\frac{1}{2}}} u_{i_{I+\frac{1}{2}}} - h_{i_{I-\frac{1}{2}}} u_{i_{I-\frac{1}{2}}}}{\Delta x} = 0 \quad (6.58)$$

$$p_I = - \left( \frac{f_{I+1} + f_{I-1} - 2f_I}{\Delta x^2} \right) + Bo \cos \theta f_I \cot \theta \quad (6.59)$$

The friction term is calculated from:

$$f_{r_{I+\frac{1}{2}}} = (\lambda + 2)^n \frac{u_{I+\frac{1}{2}}^n}{0.5 (h_I^{n+1} + h_{I+1}^{n+1})}, \quad (6.60)$$

The operator  $\mathcal{F}$  in equation (6.57) is discretised using central differencing as:

$$\mathcal{F}(u)|_{I+\frac{1}{2}} = u_{I+\frac{1}{2}} \left( \frac{u_{I+\frac{3}{2}} - u_{I-\frac{1}{2}}}{2\Delta x} \right), \quad (6.61)$$

Dirichlet boundary conditions are assigned as exact values at the boundary points, whereas Neumann boundary conditions are implemented by employing ghost nodes at the edge of the computational domain.

To simplify the description of the calculation procedure presented below, it is convenient to separate the leading temporal  $u_i$ ,  $v_i$ ,  $h_i$  and  $p_i$  terms from the discretised u-momentum, v-momentum, continuity and pressure operators and to express them as functions  $\mathcal{M}_{I+\frac{1}{2}}^u$ ,  $\mathcal{M}_I^h$  and  $\mathcal{M}_I^p$ , thus equations (6.57) to (6.59) and can be written as:

$$\varepsilon Re \left. \frac{\partial u}{\partial t} \right|_{I+\frac{1}{2}} + \mathcal{M}_{I+\frac{1}{2}}^u(u, h, p) = 0 \quad (6.62)$$

$$\left. \frac{\partial h}{\partial t} \right|_I + \mathcal{M}_I^h(u, h, p) = 0 \quad (6.63)$$

$$p|_I + \mathcal{M}_I^p(h) = 0 \quad (6.64)$$

The term  $\left. \frac{\partial h}{\partial t} \right|_I$  in the function  $\mathcal{M}^u$  of equation (6.62) is substituted from equation (6.63) at the appropriate mesh location.

The adaptive time stepping method, described earlier, is used and the implicit  $\beta$ -method employed to advance the solution in time:

$$u_{I+1/2}^{n+1} + \beta \Delta t^{n+1} \mathcal{M}_{I+1/2}^u(h^{n+1}, u^{n+1}) = u_{I+1/2}^n - (1 - \beta) \Delta t^{n+1} \mathcal{M}_{I+1/2}^u(h^n, u^n), \quad (6.65)$$

$$h_I^{n+1} + \beta \Delta t^{n+1} \mathcal{M}_I^h(u^{n+1}, h^{n+1}) = h_I^n - (1 - \beta) \Delta t^{n+1} \mathcal{M}_I^h(u^n, h^n), \quad (6.66)$$

which can be written in the form of equation (3.63) but with:

$$\mathcal{N} = \begin{pmatrix} \mathcal{N}_{I+1/2}^u \\ \mathcal{N}_I^h \\ \mathcal{N}_I^p \end{pmatrix}, \quad \mathbf{f} = \begin{pmatrix} \mathbf{f}_{I+1/2}^u \\ \mathbf{f}_I^h \\ 0 \end{pmatrix}, \quad \mathbf{u}^n = \begin{pmatrix} u_{I+1/2}^n \\ h_I^n \\ p_I^n \end{pmatrix}. \quad (6.67)$$

## 6.6 Results and discussion

This section presents the results of a preliminary rather than comprehensive investigation for free-surface bilayer thin film flow down an inclined substrate under the effect of gravity for non-Newtonian liquids. The discrete equations for both the LUB model and DAF, derived above, are solved for two-dimensional flow using the multigrid method, as described in Chapter 3 for the DAF and in Appendix D for the and LUB model; the details concerning the solution domain and grid arrangements are the same as for their Newtonian counterparts. Comparisons are made against Newtonian flow predictions and between the results of the LUB model and the DAF for non-Newtonian flow.

Taking into account that the scaling for the non-Newtonian flow problem is different from the Newtonian flow case and in order to make direct comparison, the flow parameters are selected to produce equivalent flow cases. To compare to a Newtonian flow with  $\varepsilon = 0.1$ ,  $Ca = 1 \times 10^{-3}$  and  $\theta = 10^\circ$ , the constant  $Bo$  in the non-Newtonian flow equations must take the value  $Bo = 1.1517$ .

Figure 6.2 shows a comparison between the free-surface disturbance obtained with the LUB model for bilayer non-Newtonian flow, when  $n_1 = n_2 = 1.0$ , and those for Newtonian fluid over trench topography with  $l_t = 1.5$ ,  $|s_0| = 0.2$ . The comparison reveals that the two profiles are exactly the same which indicates that the non-

Newtonian LUB model reduces to the Newtonian one when  $n = 1$ .

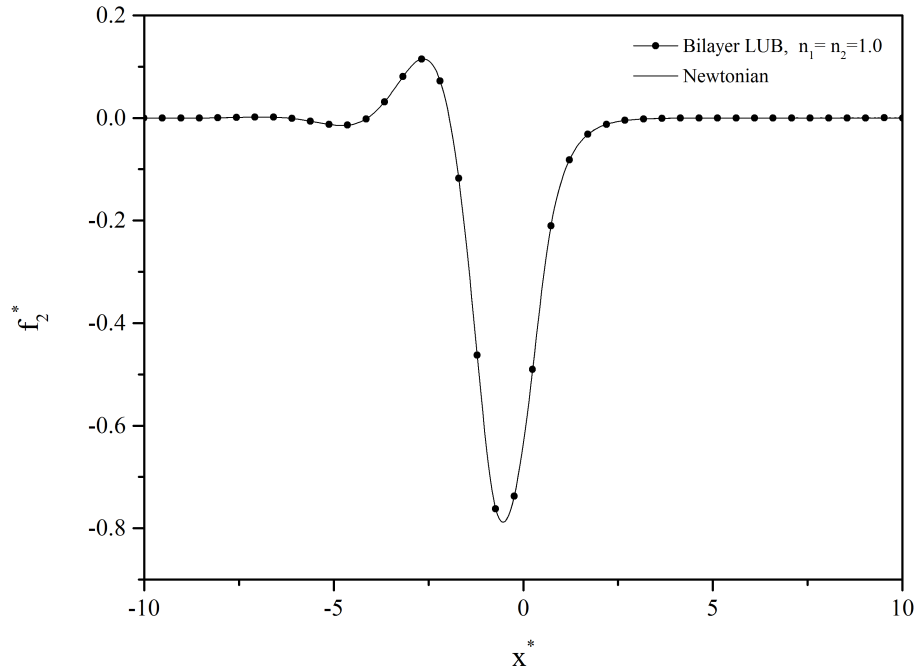


Figure 6.2: Comparison of the free-surface disturbance obtained using the LUB model for bilayer non-Newtonian flow,  $n_1 = n_2 = 1.0$ , to that of Newtonian fluid over trench topography with  $l_t = 1.5$ ,  $|s_0| = 0.2$ ;  $\theta = 10^\circ$ ,  $Re=0$ .

The influence of changing the upper layer power-law index,  $n_2$ , while keeping  $n_1 = 0.9$  is illustrated in Figure 6.3. It shows that increasing  $n_2$  from 0.7 to 1.1 significantly affects the free-surface disturbance: the free-surface depression deepens while the capillary ridge becomes more focused and its amplitude is increased. Figure 6.4 shows the opposite case, when  $n_2 = 0.9$  and  $n_1$  changes in value from 0.7 to 1.1. It is obvious from the figure that increasing  $n_1$  decreases the depth of free-surface depression and affects the capillary ridge only slightly. The free-surface disturbance for the four  $n_1 - n_2$  combinations are presented in Figure 6.5 and their corresponding liquid-liquid interface in Figure 6.6.

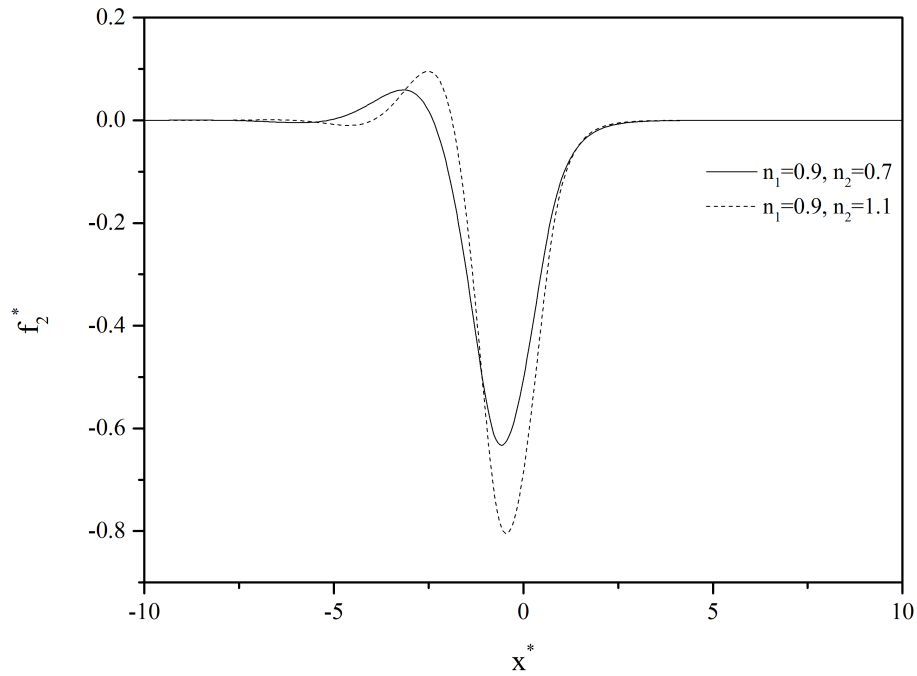


Figure 6.3: Effect of changing the upper liquid layer index,  $n_2$  for bilayer flow over trench topography; with  $l_t = 1.5$ ,  $|s_0| = 0.2$ ,  $\theta = 10^\circ$ ,  $\text{Re}=0$ .

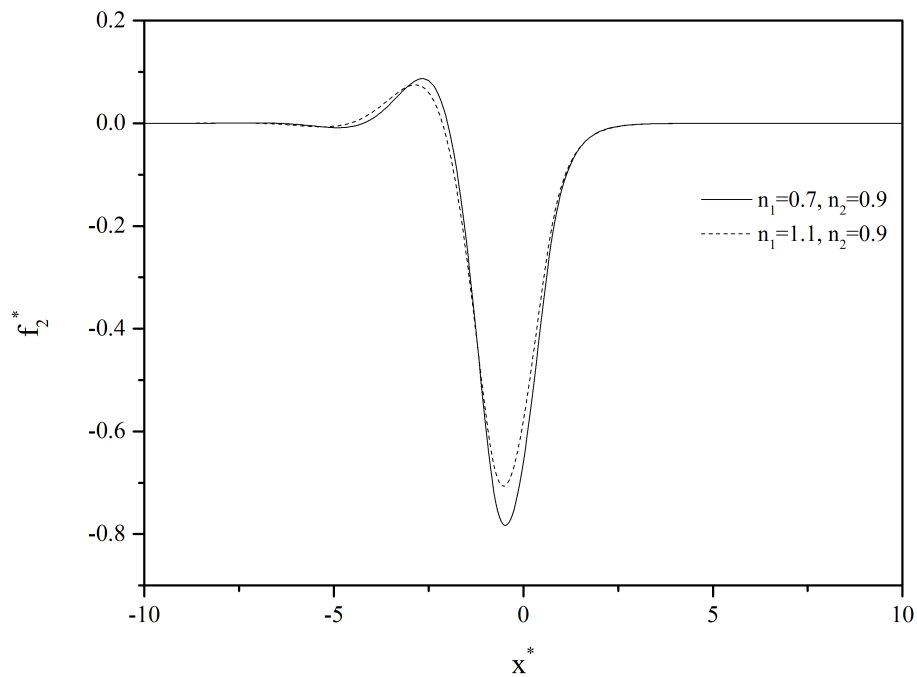


Figure 6.4: Effect of changing the lower liquid layer index,  $n_1$  for bilayer flow over trench topography; with  $l_t = 1.5$ ,  $|s_0| = 0.2$ ,  $\theta = 10^\circ$ ,  $\text{Re}=0$ .

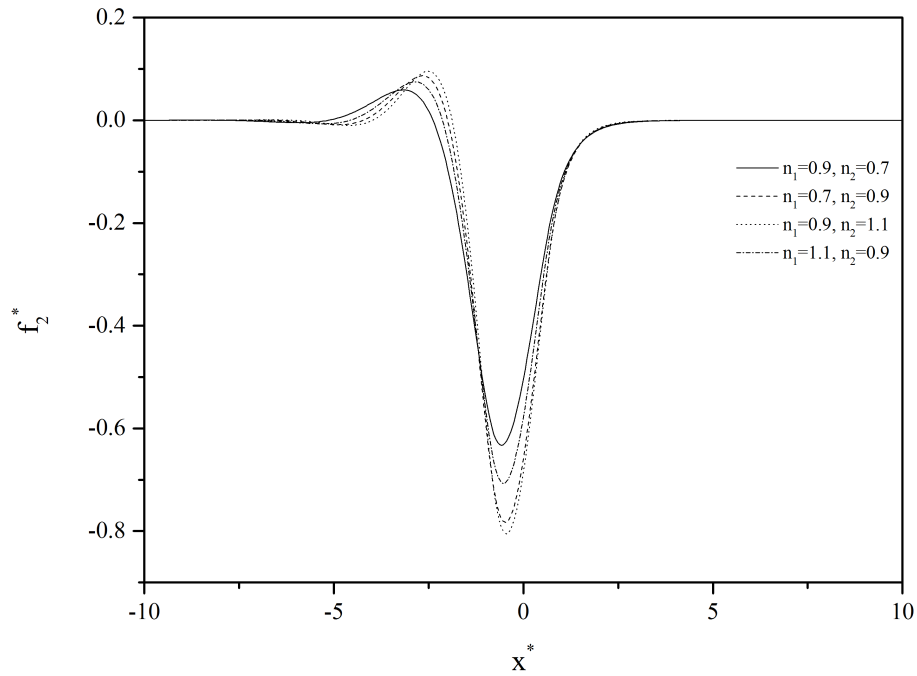


Figure 6.5: Free-surface disturbance generated for different  $n_1 - n_2$  combinations for flow over trench topography; with  $l_t = 1.5$ ,  $|s_0| = 0.2$ ,  $\theta = 10^\circ$ ,  $\text{Re}=0$ .

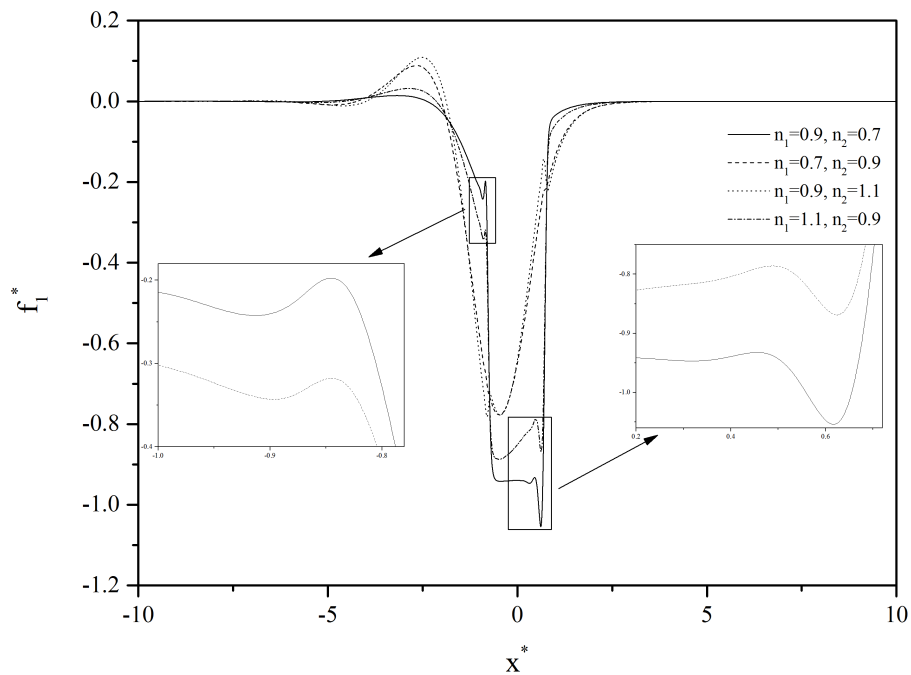


Figure 6.6: Liquid-liquid interface disturbance for different  $n_1 - n_2$  combinations for flow over trench topography; with  $l_t = 1.5$ ,  $|s_0| = 0.2$ ,  $\theta = 10^\circ$ ,  $\text{Re}=0$ .

Figure 6.7 presents a comparison between the free-surface disturbance predictions provided by the two non-Newtonian models: the DAF when  $n = 0.8$ ,  $Re = 0$  and the LUB model when  $n_1 = n_2 = 0.8$ , for flow over the same trench topography. The results show that the two profiles are in excellent agreement. The same is shown in Figure 6.8 for  $n = 1.2$ .

The effect of changing the power-law index,  $n$ , when  $Re = 10$  is shown in Figure 6.9. Increasing  $n$  from 0.8 to 1.4 increases the depth of free surface depression and marginally increases the capillary ridge height. Increasing  $Re$  influences the flow by amplifying the capillary ridge and deepening the free-surface depression above the trench as shown in Figure 6.10 for  $n = 0.8$  and Figure 6.11 for  $n = 1.2$ .

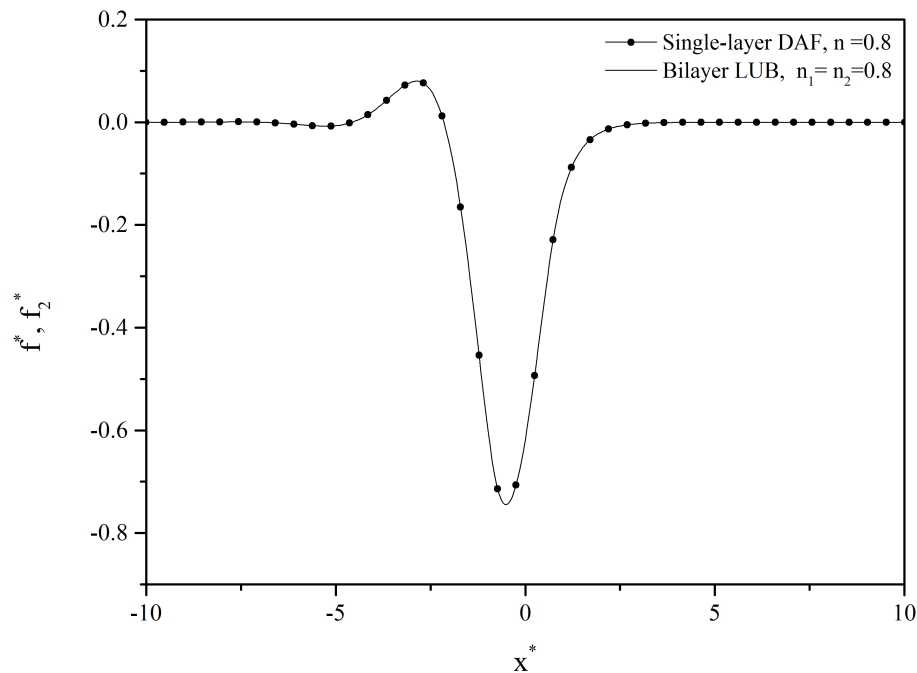


Figure 6.7: Comparison of the free-surface disturbance obtained using the LUB model and the DAF for flow of a power-law fluid,  $n = 0.8$ , over trench topography with  $l_t = 1.5$ ,  $|s_0| = 0.2$ ;  $\theta = 10^\circ$ ,  $Re=0$ .

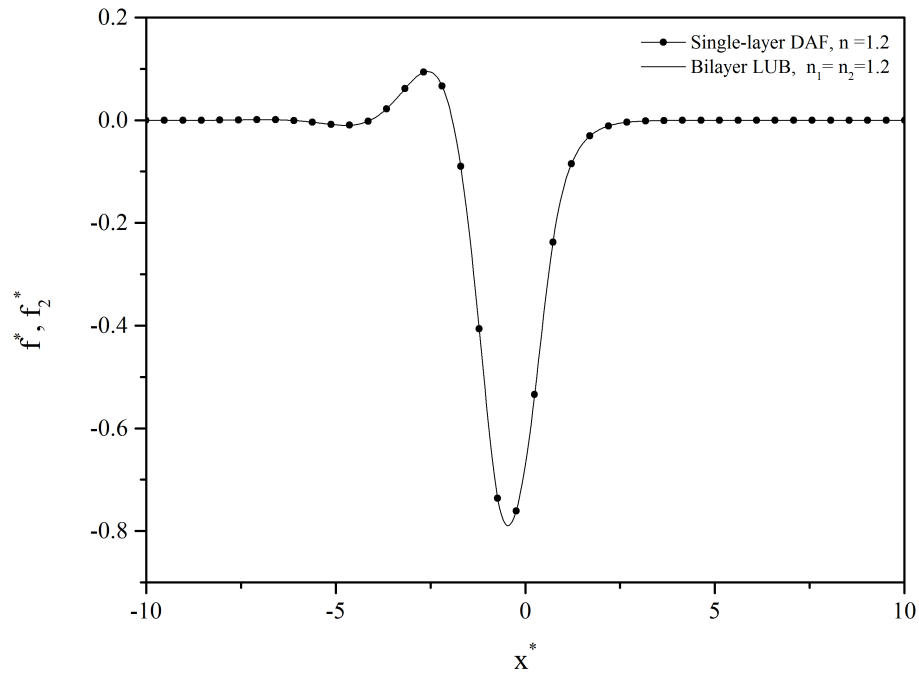


Figure 6.8: Comparison of the free-surface disturbance obtained using the LUB model and the DAF for flow of a power-law fluid,  $n = 1.2$ , over trench topography with  $l_t = 1.5$ ,  $|s_0| = 0.2$ ;  $\theta = 10^\circ$ ,  $Re=0$ .

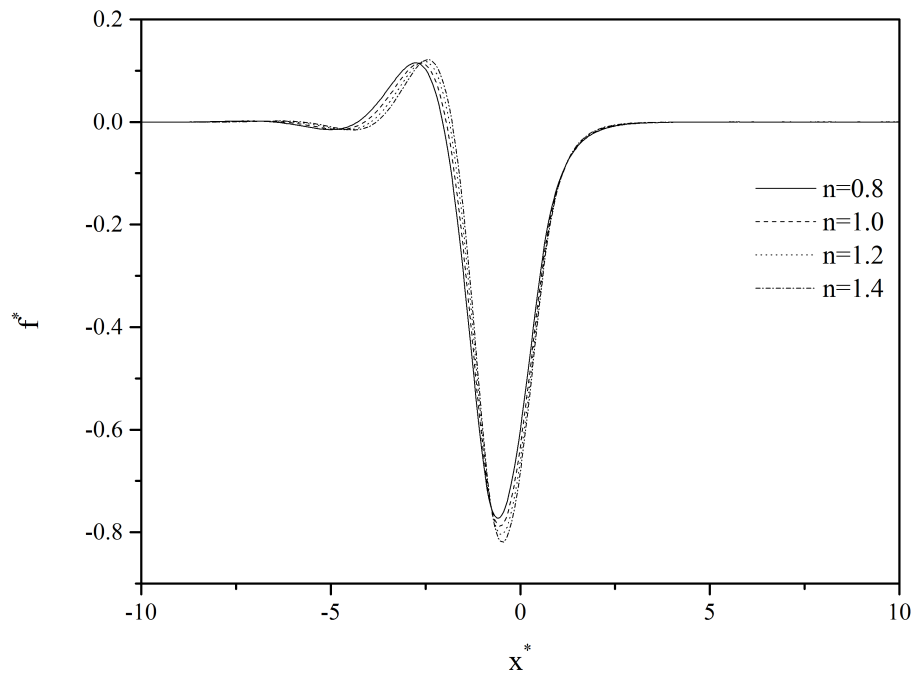


Figure 6.9: Effect of power-law index on the free-surface disturbance for flow over trench topography with  $l_t = 1.5$ ,  $|s_0| = 0.2$ ;  $\theta = 10^\circ$  and  $Re = 10$ .

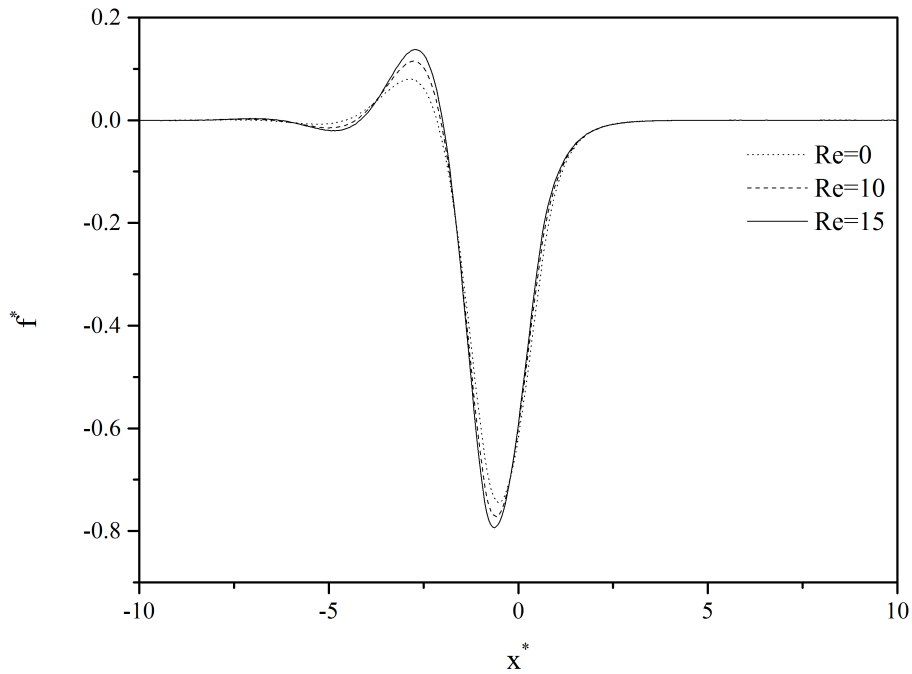


Figure 6.10: Effect of Reynolds number on the free-surface disturbance for flow of a power-law fluid,  $n = 0.9$ , over trench topography  $l_t = 1.5$ ,  $|s_0| = 0.2$ ;  $\theta = 10^\circ$ .

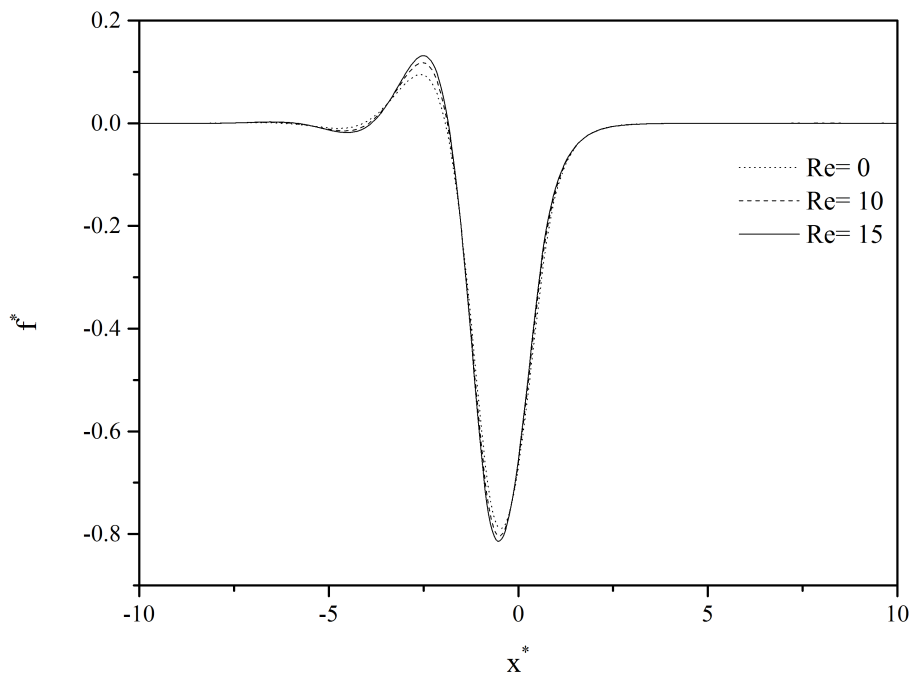


Figure 6.11: Effect of Reynolds number on free-surface disturbance for flow of a power-law fluid,  $n = 1.1$ , over trench topography with  $l_t = 1.5$ ,  $|s_0| = 0.2$ ;  $\theta = 10^\circ$ .

# Chapter 7

## Conclusion and suggestion for future work

### Contents

---

7.1	Conclusions . . . . .	190
7.2	Suggestions for future work . . . . .	194

---

## 7.1 Conclusions

The work presented in this thesis provides an important contribution to the field of thin film flow over topography by addressing a hitherto, more-or-less, ignored class of problems: ones involving bilayers comprised of immiscible liquids, separated by a distinct liquid-liquid interface. Two such problems form the basis of the investigation: confined flow through a channel and gravity-driven film flow down an inclined surface which exhibits the added complication of possessing a free-surface, the shape of which is not known *a priori*. The latter investigation is completely novel. In particular:

1. It is shown that such problems can be modelled effectively by application of the long-wave approximation, and the different equations sets generated solved, numerically, using an appropriate, efficient and accurate multigrid methodology to yield predictions of the flow behaviour in the form of the free-surface and liquid-liquid interface disturbances experienced.
2. Flow over different topography types is considered and, where possible, compared with existing and complementary results in the literature. The effect of inertia is explored and in the case of film flow, the fluid flow models are refined to embody non-Newtonian behaviour in the form of a Power Law model.

It is shown that the long-wave approximation enables the order of Navier-Stokes and continuity equations governing the problems of interest to be reduced, thus making them more amenable to solution; the important gross features of the flow can be explored at the expense of being unable to capture information about the internal flow structure, such the presence of eddies. The two different reduced equa-

tion sets derived and utilised - one based on the application of lubrication theory, the other on depth averaging - have a rigorous and comprehensive mathematical underpinning; in common with other authors the two equation sets are referred to as the LUB model and DAF, respectively. The former equation set assumes the Reynolds number,  $Re$ , to be zero and hence the flow inertialess; the latter is not compromised by this restriction but does require the assumption of a self-similar quadratic velocity profile across each liquid layer. Both equation sets are shown to be equivalent for inertialess flow conditions.

The partial differential equation sets themselves are found to be well suited to discretisation via finite differences which, in turn, are amenable to fast, accurate and efficient solution using a multigrid methodology and error-controlled automatic time-stepping. The DAF is solved using a staggered mesh arrangement for the unknowns while for the LUB model a collocated mesh suffices. The issue of mesh independence is addressed as is the consistency and equivalence of the LUB model and the DAF (when  $Re = 0$ ). The latter was demonstrated, before proceeding to a systematic study of the two problems of interest, by comparing the results obtained for bilayer flow in a channel containing a step-down feature and film flow over a trench-like topography; it is found, despite the different mesh arrangements employed, that the results are indistinguishable. The validity of the modelling and numerical approaches, used to generate the remainder of the results reported in the thesis, was further established by investigating the zero  $Re$  channel flow problem considered by Lenz and Kumar (2007). In all case, for the same flow properties and topography types, the results obtained are found to be in excellent agreement.

Having established the above, a detailed numerical investigation of the channel flow problem featuring step-up/down and trench topography was carried out and involved varying the step height/depth, the fluid properties of the upper layer, the

liquid-liquid interface height and the Reynolds number. The same was considered by Zhou and Kumar (2012), who cast it as a unsteady problem, but with limited success in that they were unable to solve for the case of a step-up, which they attributed to the solver they employed. In order to confirm this or otherwise, a method of solution similar to the one used by them was employed to solve the steady-state version of the DAF equation set. No such difficulty in obtaining solutions for the case of a step-up was experienced indicating that the inability of Zhou and Kumar (2012) to achieve the same arguably stems from a different source.

For flow over step-down, it is found that the height of the capillary ridge formed upstream of the topography shows a maximum with respect to step depth. This behaviour is different from the case of single layer flow and is attributed to the build-up of pressure in the upper layer. It was also found that for flow over step-down topography with a high step depth, increasing inertia can lead to suppression of the capillary ridge. Density ratio and inlet interface height influence the shape of interface; for example, increasing the density ratio suppresses the capillary ridge and pushes down the entire interface in the narrower part of the channel. Other means of driving the flow were considered, showing the same trends and behaviour to the results discussed above.

For the case of bilayer free surface film flow, first of all an assessment of the predictions generated is made by comparing the results obtained for the single-layer-equivalent limit, i.e. the bilayer behaving as a single layer, with the corresponding experimental data of Decré and Baret (2003) and existing numerical solutions via the LUB model, Gaskell *et al.* (2004) and DAF, Veremieiev *et al.* (2010). In all cases, the comparisons reveal excellent agreement. The DAF is subsequently used in a systematic sense to explore parameter space, in a similar way to the channel flow problem, both with and without inertia present. The presence of inertia is

found to widen and increase the amplitude of free surface and liquid-liquid interface disturbances. Lowering the density of the upper layer has a strong influence in the case of flow over a trench topography by producing a notable decrease in the free-surface depression, but less so in terms of the effect on the capillary trough/ridge for flow over step-up/down topography, respectively, or for the capillary ridge for flow over a trench. For all three types of topography, changing the liquid-liquid interface height leads to a similar effect; however, changing the upper layer viscosity has a similar amplifying effect on both the free surface depression and the capillary ridge for flow over a trench topography.

Consideration of the three-dimensional bilayer thin film flow problem for the case of flow over a localised square trench topography, reveals that the predicted free-surface disturbance agrees well with existing experimental and theoretical results from the literature; in that it is characterised by a horseshoe-shaped bow-wave with comet-tail features, together with a downstream surge that has no equivalent in two-dimensional flow over spanwise topography. The effect of the aspect ratio of the trench topography on the free-surface disturbance that is formed, when inertia is taken into account, is explored. It is noted that increasing the trench aspect ratio leads to a broadening of the upstream capillary ridge and an eventual bifurcation of the downstream surge to form two separate smaller surges; when the aspect ratio is sufficiently large the mid-plane streamwise free-surface profile is found to approach its spanwise equivalent. Unfortunately, there was insufficient time available to carry out a more extensive investigation but at least the proof of concept has been established.

An initial investigation to introduce non-Newtonian fluid behaviour into bilayer thin film flow was carried out, by adopting the Power-Law model to describe the non-Newtonian behaviour for the particular case of flow over a trench topography.

It was found that a complete and solvable equation set corresponding to the DAF could not be derived, unless additional simplifications were implemented. Two such simplifications were invoked to get around this obstacle: (i) by considering the LUB model limit; (ii) by considering just one layer when inertia is present - which for the DAF is equivalent to both liquids having the same properties. For the first of these, the results show that an increase in the power law index of the upper liquid layer leads to an amplification of the free-surface disturbance, while increasing the power law index for the lower liquid layer has the reverse effect but with less significance. For the second simplification addressed, the usual inertia effect of amplifying the capillary ridge and depression is observed for both shear thickening and thinning liquids; keeping the Reynolds number fixed reveals that increasing the power index, from shear thinning to shear thickening, results in a downstream shift in the capillary ridge with a corresponding increase in the depth of the free-surface depression.

## **7.2 Suggestions for future work**

The methodology and investigations reported in this thesis offer considerable scope for extending the work along a number of different and complimentary avenues, especially in relation to bilayer free surface flows. These are outlined below.

The bilayer LUB model and DAF for free-surface film flow could be extended to cover the more general and often encountered problem of multilayer film flow. How this can be done is illustrated in Appendix E, for the case of a three-dimensional LUB model and the general problem of N-layers. Such expressions based on the DAF can be derived similarly. In addition, when deriving model equation sets based on the DAF of the Navier-Stokes and Continuity equations it could well prove

worthwhile to explore the use of weighted averaging rather than the standard averaging employed in the present work. The reason why this might prove to be the case is that the weighted residual approach has been shown to lead to improved results in the context of determining the inertial stability limit for single layer film flow, see Ruyer-Quil and Manneville (2000, 2002 ).

As to the various equation sets provided in the thesis and the future ones as alluded to above, the efficiency of the multigrid method used to solve them could be improved further by introducing, in addition, error controlled automatic mesh refinement/de-refinement, which has been shown to be very effective at reducing calculation times in the case of the LUB model applied to single layer three-dimensional film flow, Lee *et al.* (2007); alternatively, a parallel computing approach could be adopted in such cases, Lee *et al.* (2009a). The equation set underpinning the DAF for bilayer three-dimensional free-surface flow would arguably benefit considerably from adopting either approach, as such solutions obtained using the existing solver require considerably great CPU times compared to their two-dimensional flow counterparts.

The preliminary investigation of bilayer thin flow for non-Newton liquids presented in Chapter 6 could be actively pursued from a number of aspects: first, the derivation of a three-dimensional version of the LUB model and DAF for Power-Law fluids; second, the consideration of other existing models to capture non-Newtonian behaviour. In pursuing both of these avenues of research an equal effort will have to go into resolving the obstacle associated with expressing the velocity profile within the layers in an appropriate and convenient form and the numerical methods required to solve them. A fall back position, if this were not achievable, would be to rely solely on the LUB model ( $Re = 0$ ) which does not suffer the same drawbacks. It would similarly be informative to introduce non-Newtonian behaviour into the

channel flow problem.

The free-surface bilayer film flow investigations carried out in the present work involving DAFs of the Navier-Stokes and Continuity equations could be supplemented with additional averaged transport and other equations, plus attendant boundary conditions, to include and investigate other physical effects such as evaporation, surfactants, thermal gradients, etc. and what the consequences might be if the surface containing topography were porous and/or flexible. An obvious and initial straightforward task would be to investigate the influence of other topographical shapes to those considered in the thesis and if the improvements made to the solver discussed above are made this would open the door to the investigation of flow over multiple and complex-shaped topographies, Lee *et al.* (2009a) and Gaskell *et al.* (2010).

At the time of writing, unlike for single layer free-surface film flows, there is no explicit inertial stability criteria base on the Reynolds number currently available for the case of bilayer free-surface thin film flow. Attempts could be fruitfully directed towards deriving such an expression in order to understand more clearly the influence of different flow parameters on the stability of bilayer films and to identify the instability modes that occur under different flow conditions.

Last but not least, the lack of experimental data for bilayer film and channel flow over topography represents a very worthwhile research opportunity in its own right, as a means of providing benchmark results for comparison with and the validation of theoretical investigations of the sort reported in this thesis.

## Appendix A

# Derivation of lubrication equations (LUB) for 3D free-surface flow

We begin by extending the derivation of the long-wave approximation for two-dimensional flow presented in Chapter 2 to three dimensions. The flow of bilayer thin film down a substrate inclined at angle  $\theta$  to the horizontal is governed by the Navier-Stokes and continuity equations, which in Cartesian coordinates are given by:

$$\hat{\rho}_i \left( \frac{\partial U_i}{\partial T} + U_i \frac{\partial U_i}{\partial X} + V_i \frac{\partial U_i}{\partial Y} + W_i \frac{\partial U_i}{\partial Z} \right) = -\frac{\partial P_i}{\partial X} + \hat{\mu}_i \left( \frac{\partial^2 U_i}{\partial X^2} + \frac{\partial^2 U_i}{\partial Y^2} + \frac{\partial^2 U_i}{\partial Z^2} \right) + \hat{\rho}_i g \sin \theta, \quad (\text{A.1})$$

$$\hat{\rho}_i \left( \frac{\partial V_i}{\partial T} + U_i \frac{\partial V_i}{\partial X} + V_i \frac{\partial V_i}{\partial Y} + W_i \frac{\partial V_i}{\partial Z} \right) = -\frac{\partial P_i}{\partial Y} + \hat{\mu}_i \left( \frac{\partial^2 V_i}{\partial X^2} + \frac{\partial^2 V_i}{\partial Y^2} + \frac{\partial^2 V_i}{\partial Z^2} \right), \quad (\text{A.2})$$

$$\hat{\rho}_i \left( \frac{\partial W_i}{\partial T} + U_i \frac{\partial W_i}{\partial X} + V_i \frac{\partial W_i}{\partial Y} + W_i \frac{\partial W_i}{\partial Z} \right) = -\frac{\partial P_i}{\partial Z} + \hat{\mu}_i \left( \frac{\partial^2 W_i}{\partial X^2} + \frac{\partial^2 W_i}{\partial Y^2} + \frac{\partial^2 W_i}{\partial Z^2} \right) - \hat{\rho}_i g \cos \theta, \quad (\text{A.3})$$

and

$$\frac{\partial U_i}{\partial X} + \frac{\partial V_i}{\partial Y} + \frac{\partial W_i}{\partial Z} = 0. \quad (\text{A.4})$$

The associated boundary conditions are

$$\text{at the substrate} \quad U_1 = 0, \quad V_1 = 0, \quad (\text{A.5})$$

$$\text{at the liquid-liquid interface} \quad U_1 = U_2, \quad V_1 = V_2, \quad (\text{A.6})$$

$$-(P_1 - P_2)|_{Z=F_1} + ((T_1 - T_2)|_{Z=F_1} \cdot n_1) \cdot n_1 = \hat{\sigma}_{int} K_1 \quad (\text{A.7})$$

$$((T_1 - T_2)|_{Z=F_1} \cdot n_1) \cdot t_1 = 0, \quad (\text{A.8})$$

$$\text{at the free surface} \quad (\text{A.9})$$

$$-P_2|_{Z=F_2} + (T_2|_{Z=F_2} \cdot n_2) \cdot n_2 = \hat{\sigma}_2 K_2, \quad (\text{A.10})$$

$$(T_2|_{Z=F_2} \cdot n_2) \cdot t_2 = 0. \quad (\text{A.11})$$

Converting into dimensionless form using the scaling presented in Chapter 2 to-

gether with  $y = \frac{Y}{L_0}$  and  $v = \frac{V}{U_0}$  yields:

$$\begin{aligned} \frac{\varepsilon \hat{\rho}_i U_0^2}{H_0} \left( \frac{\partial u_i}{\partial t} + u_i \frac{\partial u_i}{\partial x} + v_i \frac{\partial u_i}{\partial y} + w_i \frac{\partial u_i}{\partial z} \right) &= -\frac{\varepsilon P_0}{H_0} \frac{\partial p_i}{\partial x} + \\ \frac{\hat{\mu}_i U_0}{H_0^2} \left( \varepsilon^2 \frac{\partial^2 u_i}{\partial x^2} + \varepsilon^2 \frac{\partial^2 u_i}{\partial y^2} + \frac{\partial^2 u_i}{\partial z^2} \right) &+ \hat{\rho}_i g \sin \theta, \end{aligned} \quad (\text{A.12})$$

$$\begin{aligned} \frac{\varepsilon \hat{\rho}_i U_0^2}{H_0} \left( \frac{\partial v_i}{\partial t} + u_i \frac{\partial v_i}{\partial x} + v_i \frac{\partial v_i}{\partial y} + w_i \frac{\partial v_i}{\partial z} \right) &= -\frac{\varepsilon P_0}{H_0} \frac{\partial p_i}{\partial y} + \\ \frac{\hat{\mu}_i U_0}{H_0^2} \left( \varepsilon^2 \frac{\partial^2 v_i}{\partial x^2} + \varepsilon^2 \frac{\partial^2 v_i}{\partial y^2} + \frac{\partial^2 v_i}{\partial z^2} \right), & \end{aligned} \quad (\text{A.13})$$

$$\begin{aligned} \frac{\varepsilon^3 \hat{\rho}_i U_0^2}{H_0} \left( \frac{\partial w_i}{\partial t} + u_i \frac{\partial w_i}{\partial x} + v_i \frac{\partial w_i}{\partial y} + w_i \frac{\partial w_i}{\partial z} \right) = -\frac{\varepsilon P_0}{H_0} \frac{\partial p_i}{\partial z} + \\ \frac{\hat{\mu}_i U_0}{H_0^2} \left( \varepsilon^4 \frac{\partial^2 w_i}{\partial x^2} + \varepsilon^4 \frac{\partial^2 w_i}{\partial y^2} + \varepsilon^2 \frac{\partial^2 u_i}{\partial z^2} \right) - \hat{\rho}_i g \varepsilon \cos \theta, \end{aligned} \quad (\text{A.14})$$

and

$$\frac{U_o}{L_o} \frac{\partial u_i}{\partial x} + \frac{U_o}{L_o} \frac{\partial v_i}{\partial y} + \frac{\varepsilon U_o}{H_o} \frac{\partial w_i}{\partial z} = 0, \quad (\text{A.15})$$

where  $\varepsilon = \frac{H_0}{L_0}$ .

Dividing both sides of equations (A.12) to (A.14) by  $\frac{\hat{\mu}_1 U_0}{H_0^2}$  results in :

$$\begin{aligned} \varepsilon \rho_i Re \left( \frac{\partial u_i}{\partial t} + u_i \frac{\partial u_i}{\partial x} + v_i \frac{\partial u_i}{\partial y} + w_i \frac{\partial u_i}{\partial z} \right) = - \left( \frac{P_0}{\varepsilon H_0} \frac{\partial p_i}{\partial x} - \right. \\ \left. \rho_i \frac{\hat{\rho}_1 g H_0^2}{\hat{\mu}_1 U_0} \sin \theta \right) + \mu_i \left( \varepsilon^2 \frac{\partial^2 u_i}{\partial x^2} + \varepsilon^2 \frac{\partial^2 u_i}{\partial y^2} + \frac{\partial^2 u_i}{\partial z^2} \right), \end{aligned} \quad (\text{A.16})$$

$$\begin{aligned} \varepsilon \rho_i Re \left( \frac{\partial v_i}{\partial t} + u_i \frac{\partial v_i}{\partial x} + v_i \frac{\partial v_i}{\partial y} + w_i \frac{\partial v_i}{\partial z} \right) = - \frac{P_0}{\varepsilon H_0} \frac{\partial p_i}{\partial y} + \\ \mu_i \left( \varepsilon^2 \frac{\partial^2 v_i}{\partial x^2} + \varepsilon^2 \frac{\partial^2 v_i}{\partial y^2} + \frac{\partial^2 v_i}{\partial z^2} \right), \end{aligned} \quad (\text{A.17})$$

$$\begin{aligned} \varepsilon^3 \rho_i Re \left( \frac{\partial w_i}{\partial t} + u_i \frac{\partial w_i}{\partial x} + v_i \frac{\partial w_i}{\partial y} + w_i \frac{\partial w_i}{\partial z} \right) = - \left( \frac{P_0}{\varepsilon H_0} \frac{\partial p_i}{\partial z} + \right. \\ \left. \rho_i \varepsilon \frac{\hat{\rho}_1 g H_0^2}{\hat{\mu}_1 U_0} \cos \theta \right) + \mu_i \left( \varepsilon^4 \frac{\partial^2 w_i}{\partial x^2} + \varepsilon^4 \frac{\partial^2 w_i}{\partial y^2} + \varepsilon^2 \frac{\partial^2 u_i}{\partial z^2} \right), \end{aligned} \quad (\text{A.18})$$

and

$$\frac{U_o}{L_o} \left( \frac{\partial u_i}{\partial x} + \frac{\partial v_i}{\partial y} + \frac{\partial w_i}{\partial z} \right) = 0. \quad (\text{A.19})$$

Omitting terms of  $O(\varepsilon^2)$  gives:

$$\varepsilon \rho_i Re \left( \frac{\partial u_i}{\partial t} + u_i \frac{\partial u_i}{\partial x} + v_i \frac{\partial u_i}{\partial y} + w_i \frac{\partial u_i}{\partial z} \right) = - \left( \frac{\partial p_i}{\partial x} - \rho_i B \sin \theta \right) + \mu_i \frac{\partial^2 u_i}{\partial z^2}, \quad (\text{A.20})$$

$$\varepsilon \rho_i Re \left( \frac{\partial v_i}{\partial t} + u_i \frac{\partial v_i}{\partial x} + v_i \frac{\partial v_i}{\partial y} + w_i \frac{\partial v_i}{\partial z} \right) = - \frac{\partial p_i}{\partial y} + \mu_i \frac{\partial^2 v_i}{\partial z^2}, \quad (\text{A.21})$$

$$\frac{\partial p_i}{\partial z} + \rho_i B \varepsilon \cos \theta = 0, \quad (\text{A.22})$$

$$\frac{\partial u_i}{\partial x} + \frac{\partial v_i}{\partial y} + \frac{\partial w_i}{\partial z} = 0. \quad (\text{A.23})$$

The lubrication approximation is based on the assumption that  $Re \approx O(\varepsilon)$ . Applying this assumption leads to the right hand sides of equations (A.20) to (A.21) vanishing; the resulting governing equations after substituting the value of  $B$  as defined in Chapter 2 are:

$$\mu_i \frac{\partial^2 u_i}{\partial z^2} = \left( \frac{\partial p_i}{\partial x} - \frac{2\rho_i}{C} \right), \quad (\text{A.24})$$

$$\mu_i \frac{\partial^2 v_i}{\partial z^2} = \frac{\partial p_i}{\partial y}, \quad (\text{A.25})$$

$$\frac{\partial p_i}{\partial z} + 2\rho_i \varepsilon \cot \theta = 0, \quad (\text{A.26})$$

$$\frac{\partial u_i}{\partial x} + \frac{\partial v_i}{\partial y} + \frac{\partial w_i}{\partial z} = 0, \quad (\text{A.27})$$

while the boundary conditions become:

$$z = f_0 \quad u_1 = 0 \quad v_1 = 0, \quad (\text{A.28})$$

$$z = f_1 \quad u_1 = u_2 \quad v_1 = v_2, \quad (\text{A.29})$$

$$\mu_1 \frac{\partial u_1}{\partial z} = \mu_2 \frac{\partial u_2}{\partial z} \quad \mu_1 \frac{\partial v_1}{\partial z} = \mu_2 \frac{\partial v_2}{\partial z}, \quad (\text{A.30})$$

$$p_1 - p_2 = -\frac{\varepsilon^3}{Ca} \sigma_{int} \nabla^2 f_1, \quad (\text{A.31})$$

$$z = f_2 \quad \frac{\partial u_2}{\partial z} = 0 \quad \frac{\partial v_2}{\partial z} = 0, \quad (\text{A.32})$$

$$p_2 = -\frac{\varepsilon^3}{Ca} \sigma_2 \nabla^2 f_2. \quad (\text{A.33})$$

Integrating equation (A.26) with respect to  $z$  for layer  $i$  from  $z$  to  $f_i$ , and applying boundary conditions (A.31) and (A.33) yields the following pressure equations as derived in Chapter 2:

$$p_1 = -\frac{\varepsilon^3}{Ca} (\sigma_{int} \nabla^2 f_1 + \sigma_2 \nabla^2 f_2) + \frac{2\varepsilon}{C} [\rho_1 f_1 + \rho_2 (f_2 - f_1)] \cot \theta, \quad (\text{A.34})$$

$$p_2 = -\frac{\varepsilon^3}{Ca} \sigma_2 \nabla^2 f_2 + \frac{2\rho_2 \varepsilon}{C} f_2 \cot \theta, \quad (\text{A.35})$$

Integrating equation (A.24) twice with respect to  $z$  and applying boundary conditions (A.28), (A.30) and (A.32) enables the velocity profiles for both layers to be obtained:

$$\int_z^{f_1} \frac{\partial^2 u_1}{\partial z^2} dz = \frac{\partial u_1}{\partial z} \Big|_{z=f_1} - \frac{\partial u_1}{\partial z} = \frac{1}{\mu_1} \left( \frac{\partial p_1}{\partial x} - \frac{2\rho_1}{C} \right) (f_1 - z), \quad (\text{A.36})$$

that is

$$\begin{aligned}\frac{\partial u_1}{\partial z} &= \frac{\partial u_1}{\partial z}\Big|_{z=f_1} - \frac{1}{\mu_1} \left( \frac{\partial p_1}{\partial x} - \frac{2\rho_1}{C} \right) (f_1 - z) \\ &= \frac{\mu_2}{\mu_1} \frac{\partial u_2}{\partial z}\Big|_{z=f_1} - \frac{1}{\mu_1} \left( \frac{\partial p_1}{\partial x} - \frac{2\rho_1}{C} \right) (f_1 - z),\end{aligned}\tag{A.37}$$

with

$$\begin{aligned}\int_{f_0}^z \frac{\partial u_1}{\partial z} dz &= u_1 - u_1|_{f_0} = u_1 \\ &= \frac{\mu_2}{\mu_1} \frac{\partial u_2}{\partial z}\Big|_{z=f_1} (z - f_0) - \frac{1}{\mu_1} \left( \frac{\partial p_1}{\partial x} - \frac{2\rho_1}{C} \right) \left( f_1 (z - f_0) - \frac{z^2 - f_0^2}{2} \right),\end{aligned}\tag{A.38}$$

and

$$\int_z^{f_2} \frac{\partial^2 u_2}{\partial z^2} dz = \frac{\partial u_2}{\partial z}\Big|_{z=f_2} - \frac{\partial u_2}{\partial z} = -\frac{\partial u_2}{\partial z} = \frac{1}{\mu_2} \left( \frac{\partial p_2}{\partial x} - \frac{2\rho_2}{C} \right) (f_2 - z),\tag{A.39}$$

$$\int_{f_1}^z \frac{\partial u_2}{\partial z} dz = u_2 - u_2|_{f_1} = -\frac{1}{\mu_2} \left( \frac{\partial p_2}{\partial x} - \frac{2\rho_2}{C} \right) \left( f_2 (z - f_1) - \frac{z^2 - f_1^2}{2} \right),\tag{A.40}$$

such that

$$u_2 = u_2|_{f_1} - \frac{1}{\mu_2} \left( \frac{\partial p_2}{\partial x} - \frac{2\rho_2}{C} \right) \left( f_2 (z - f_1) - \frac{z^2 - f_1^2}{2} \right),\tag{A.41}$$

with

$$\frac{\partial u_2}{\partial z}\Big|_{z=f_1} = -\frac{1}{\mu_2} \left( \frac{\partial p_2}{\partial x} - \frac{2\rho_2}{C} \right) (f_2 - f_1),\tag{A.42}$$

and thus

$$u_1 = -\frac{1}{\mu_1} \left( \frac{\partial p_2}{\partial x} - \frac{2\rho_2}{C} \right) (f_2 - f_1) (z - f_0) - \frac{1}{\mu_1} \left( \frac{\partial p_1}{\partial x} - \frac{2\rho_1}{C} \right) \left( f_1 (z - f_0) - \frac{z^2 - f_0^2}{2} \right), \quad (\text{A.43})$$

$$u_2 = -\frac{1}{\mu_1} \left( \frac{\partial p_2}{\partial x} - \frac{2\rho_2}{C} \right) (f_2 - f_1) (f_1 - f_0) - \frac{1}{\mu_1} \left( \frac{\partial p_1}{\partial x} - \frac{2\rho_1}{C} \right) \left( f_1 (f_1 - f_0) - \frac{f_1^2 - f_0^2}{2} \right) - \frac{1}{\mu_2} \left( \frac{\partial p_2}{\partial x} - \frac{2\rho_2}{C} \right) \left( f_2 (z - f_1) - \frac{z^2 - f_1^2}{2} \right). \quad (\text{A.44})$$

Substituting the expressions for  $f_0$ ,  $f_1$  and  $f_2$  in (A.44), we find that:

$$u_1 = -\frac{1}{\mu_1} \left( \frac{\partial p_2}{\partial x} - \frac{2\rho_2}{C} \right) h_2 (z - s) - \frac{1}{\mu_1} \left( \frac{\partial p_1}{\partial x} - \frac{2\rho_1}{C} \right) (z - s) \left( h_1 - \frac{z - s}{2} \right) \quad (\text{A.45})$$

and

$$u_2 = -\frac{1}{\mu_1} \left( \frac{\partial p_2}{\partial x} - \frac{2\rho_2}{C} \right) h_2 h_1 - \frac{1}{\mu_1} \left( \frac{\partial p_1}{\partial x} - \frac{2\rho_1}{C} \right) \frac{h_1^2}{2} - \frac{1}{\mu_2} \left( \frac{\partial p_2}{\partial x} - \frac{2\rho_2}{C} \right) (z - h_1 - s) \left( h_2 - \frac{z - h_1 - s}{2} \right). \quad (\text{A.46})$$

The liquid-liquid interface velocity,  $u_{int}$  is derived by substituting  $z = h_1 + s$  in the above expression, leading to:

$$u_{int} = -\frac{1}{\mu_1} \left( \frac{\partial p_2}{\partial x} - \frac{2\rho_2}{C} \right) h_2 h_1 - \frac{1}{\mu_1} \left( \frac{\partial p_1}{\partial x} - \frac{2\rho_1}{C} \right) \frac{h_1^2}{2}, \quad (\text{A.47})$$

which allows  $u_1$  and  $u_2$  to be written in terms of the interface velocity as follows:

$$u_1 = u_{int} \frac{z - s}{h_1} - \frac{1}{\mu_1} \left( \frac{\partial p_1}{\partial x} - \frac{2\rho_1}{C} \right) (z - s) \left( \frac{h_1}{2} - \frac{z - s}{2} \right), \quad (\text{A.48})$$

$$u_2 = u_{int} - \frac{1}{\mu_2} \left( \frac{\partial p_2}{\partial x} - \frac{2\rho_2}{C} \right) (z - h_1 - s) \left( h_2 - \frac{z - h_1 - s}{2} \right). \quad (\text{A.49})$$

The averaged components of velocity are derived by averaging the right-hand-sides of (A.48) and (A.49), namely:

$$\bar{u}_i = \frac{1}{h_i} \int_{f_{i-1}}^{f_i} u_i dz. \quad (\text{A.50})$$

Therefore,

$$\bar{u}_1 = \frac{u_{int}}{2} - \frac{1}{\mu_1} \left( \frac{\partial p_1}{\partial x} - \frac{2\rho_1}{C} \right) \frac{h_1^2}{12}, \quad (\text{A.51})$$

$$\bar{u}_2 = u_{int} - \frac{1}{\mu_2} \left( \frac{\partial p_2}{\partial x} - \frac{2\rho_2}{C} \right) \frac{h_2^2}{3}, \quad (\text{A.52})$$

and from equations (A.47), (A.51) and (A.52) the following expression for the interface velocity is obtained:

$$u_{int} = \frac{6\bar{u}_1 h_2 + 3\frac{\mu_2}{\mu_1} \bar{u}_2 h_1}{4h_2 + 3\frac{\mu_2}{\mu_1} h_1}. \quad (\text{A.53})$$

Similarly the two spanwise velocities can be found by integrating equation (A.25) twice and applying the relevant boundary conditions, giving:

$$v_1 = -\frac{1}{\mu_1} \frac{\partial p_2}{\partial y} h_2 (z - s) - \frac{1}{\mu_1} \frac{\partial p_1}{\partial y} (z - s) \left( h_1 - \frac{z - s}{2} \right), \quad (\text{A.54})$$

$$v_2 = -\frac{1}{\mu_1} \frac{\partial p_2}{\partial y} h_2 h_1 - \frac{1}{\mu_1} \frac{\partial p_1}{\partial y} \frac{h_1^2}{2} - \frac{1}{\mu_2} \frac{\partial p_2}{\partial y} (z - h_1 - s) \left( h_2 - \frac{z - h_1 - s}{2} \right), \quad (\text{A.55})$$

The interface velocity is given by:

$$v_{in} = -\frac{1}{\mu_1} \frac{\partial p_2}{\partial y} h_2 h_1 - \frac{1}{\mu_1} \frac{\partial p_1}{\partial y} \frac{h_1^2}{2}, \quad (\text{A.56})$$

and  $v_1$  and  $v_2$  in terms of the interface velocity are:

$$v_1 = v_{in} \frac{z - s}{h_1} - \frac{1}{\mu_1} \frac{\partial p_1}{\partial y} (z - s) \left( \frac{h_1}{2} - \frac{z - s}{2} \right), \quad (\text{A.57})$$

$$v_2 = v_{in} - \frac{1}{\mu_2} \frac{\partial p_2}{\partial y} (z - h_1 - s) \left( h_2 - \frac{z - h_1 - s}{2} \right). \quad (\text{A.58})$$

The average spanwise components of velocity are calculated from:

$$\bar{v}_i = \frac{1}{h_i} \int_{f_{i-1}}^{f_i} v_i dz. \quad (\text{A.59})$$

Therefore:

$$\bar{v}_1 = \frac{v_{in}}{2} - \frac{1}{\mu_1} \frac{\partial p_1}{\partial y} \frac{h_1^2}{12}, \quad (\text{A.60})$$

$$\bar{v}_2 = v_{in} - \frac{1}{\mu_2} \frac{\partial p_2}{\partial y} \frac{h_2^2}{3}, \quad (\text{A.61})$$

with the interface velocity is given by:

$$v_{in} = \frac{6\bar{v}_1 h_2 + 3\frac{\mu_2}{\mu_1}\bar{v}_2 h_1}{4h_2 + 3\frac{\mu_2}{\mu_1}h_1}. \quad (\text{A.62})$$

The kinematic boundary condition is:

$$\frac{\partial h_i}{\partial t} + \nabla q_i = 0, \quad (\text{A.63})$$

where  $q_i$  is the flow rate through layer  $i$  and can be calculated from

$$q_i = \int_{f_{i-1}}^{f_i} (u_i, v_i)^T dz, \quad (\text{A.64})$$

where:

$$\int_{f_0}^{f_1} u_1 dz = \int_s^{h_1+s} \left( -\frac{1}{\mu_1} \left( \frac{\partial p_2}{\partial x} - \frac{2\rho_2}{C} \right) h_2 (z-s) - \frac{1}{\mu_1} \left( \frac{\partial p_1}{\partial x} - \frac{2\rho_1}{C} \right) (z-s) \left( h_1 - \frac{z-s}{2} \right) \right) dz, \quad (\text{A.65})$$

namely:

$$\int_{f_0}^{f_1} u_1 dz = -\frac{1}{\mu_1} \left( \frac{\partial p_2}{\partial x} - \frac{2\rho_2}{C} \right) \frac{h_2 h_1^2}{2} - \frac{1}{\mu_1} \left( \frac{\partial p_1}{\partial x} - \frac{2\rho_1}{C} \right) \frac{h_1^3}{3}. \quad (\text{A.66})$$

Similarly

$$\int_{f_0}^{f_1} v_1 dz = -\frac{1}{\mu_1} \frac{\partial p_2}{\partial y} \frac{h_2 h_1^2}{2} - \frac{1}{\mu_1} \frac{\partial p_1}{\partial y} \frac{h_1^3}{3}, \quad (\text{A.67})$$

and for the upper layer:

$$\int_{f_1}^{f_2} u_2 dz = -\frac{1}{\mu_1} \left( \frac{\partial p_2}{\partial x} - \frac{2\rho_2}{C} \right) h_2^2 h_1 - \frac{1}{\mu_1} \left( \frac{\partial p_1}{\partial x} - \frac{2\rho_1}{C} \right) \frac{h_1^2 h_2}{2} - \frac{1}{\mu_2} \left( \frac{\partial p_2}{\partial x} - \frac{2\rho_2}{C} \right) \frac{h_2^3}{3}. \quad (\text{A.68})$$

In a similar way:

$$\int_{f_1}^{f_2} v_2 dz = -\frac{1}{\mu_1} \frac{\partial p_2}{\partial y} h_2^2 h_1 - \frac{1}{\mu_1} \frac{\partial p_1}{\partial y} \frac{h_1^2 h_2}{2} - \frac{1}{\mu_2} \frac{\partial p_2}{\partial y} \frac{h_2^3}{3}, \quad (\text{A.69})$$

and substituting the expressions for  $q_i$ , equation (A.64), into equation (A.63) gives:

$$\begin{aligned} \frac{\partial h_1}{\partial t} - \frac{\partial}{\partial x} \left[ \frac{h_1^3}{3\mu_1} \left( \frac{\partial p_1}{\partial x} - \frac{2\rho_1}{C} \right) + \frac{h_1^2 h_2}{2\mu_1} \left( \frac{\partial p_2}{\partial x} - \frac{2\rho_2}{C} \right) \right] \\ - \frac{\partial}{\partial y} \left[ \frac{h_1^3}{3\mu_1} \left( \frac{\partial p_1}{\partial y} \right) + \frac{h_1^2 h_2}{2\mu_1} \left( \frac{\partial p_2}{\partial y} \right) \right] = 0, \end{aligned} \quad (\text{A.70})$$

and

$$\begin{aligned} \frac{\partial h_2}{\partial t} - \frac{\partial}{\partial x} \left[ \frac{h_1^2 h_2}{2\mu_1} \left( \frac{\partial p_1}{\partial x} - \frac{2\rho_1}{C} \right) + \left( \frac{h_1 h_2^2}{\mu_1} + \frac{h_2^3}{3\mu_2} \right) \left( \frac{\partial p_2}{\partial x} - \frac{2\rho_2}{C} \right) \right] \\ - \frac{\partial}{\partial y} \left[ \frac{h_1^2 h_2}{2\mu_1} \left( \frac{\partial p_1}{\partial y} \right) + \left( \frac{h_1 h_2^2}{\mu_1} + \frac{h_2^3}{3\mu_2} \right) \left( \frac{\partial p_2}{\partial y} \right) \right] = 0. \end{aligned} \quad (\text{A.71})$$

Equations (A.34), (A.35), (A.70) and (A.71) represent the governing equations for the lubrication model. The problem is closed in terms of the following boundary conditions:

$$h_1|_{x=0} = h_{10}, \quad h_2|_{x=0} = 1 - h_{10}, \quad (\text{A.72})$$

$$\left. \frac{\partial h_i}{\partial x} \right|_{x=l} = \left. \frac{\partial h_i}{\partial y} \right|_{y=0,w} = 0, \quad (\text{A.73})$$

$$\left. \frac{\partial p_i}{\partial x} \right|_{x=0,l} = \left. \frac{\partial p_i}{\partial y} \right|_{y=0,w} = 0, \quad (\text{A.74})$$

where  $w$  is the width of the substrate.

## Appendix B

# Derivation of lubrication equations (LUB) for 2D bilayer channel flow

After applying the lubrication approximation to the governing Navier-Stokes and continuity equations in dimensionless form reduces them to:

$$\frac{\partial^2 u_i}{\partial z^2} = \frac{1}{\mu_i} \left( \frac{\partial p_i}{\partial x} - \rho_i B \sin \theta \right), \quad (\text{B.1})$$

$$\frac{\partial p_i}{\partial z} + \rho_i B \varepsilon \cos \theta = 0, \quad (\text{B.2})$$

$$\frac{\partial u_i}{\partial x} + \frac{\partial w_i}{\partial z} = 0, \quad (\text{B.3})$$

with corresponding boundary conditions:

$$z = f_0 \quad u_1 = 0 \quad , \quad (\text{B.4})$$

$$z = f_1 \quad u_1 = u_2 \quad , \quad (\text{B.5})$$

$$\mu_1 \frac{\partial u_1}{\partial z} = \mu_2 \frac{\partial u_2}{\partial z} \quad , \quad (\text{B.6})$$

$$p_2 - p_1 = \sigma_{int} \frac{\varepsilon^3}{Ca} \nabla^2 f_1 \quad , \quad (\text{B.7})$$

$$z = f_2 = 1 \quad u_2 = u_t. \quad (\text{B.8})$$

Integrating equation (B.2) with respect to  $z$  for layer  $i$  from  $z$  to  $f_1$  yields:

$$p_1|_{f_1} - p_1 = -\rho_1 B \varepsilon \cos \theta (f_1 - z), \quad (\text{B.9})$$

$$p_2|_{f_1} - p_2 = -\rho_2 B \varepsilon \cos \theta (f_1 - z), \quad (\text{B.10})$$

and subtracting (B.10) from (B.9) gives:

$$p_2 - p_1 = (p_2 - p_1)|_{f_1} + B \varepsilon \cos \theta (\rho_2 - \rho_1) (h_1 + s). \quad (\text{B.11})$$

Applying the pressure boundary conditions and omitting the  $z$  term then yields:

$$p_2 - p_1 = \sigma_{int} \frac{\varepsilon^3}{Ca} \nabla^2 (h_1 + s) + B \varepsilon \cos \theta (\rho_2 - \rho_1) (h_1 + s). \quad (\text{B.12})$$

To derive the velocity profiles, equation (B.1) is integrated twice with respect to  $z$  and the boundary conditions applied, namely:

$$\int_z^{f_1} \frac{\partial^2 u_1}{\partial z^2} dz = \frac{\partial u_1}{\partial z} \Big|_{z=f_1} - \frac{\partial u_1}{\partial z} = \frac{1}{\mu_1} \left( \frac{\partial p_1}{\partial x} - \rho_1 B \sin \theta \right) (f_1 - z). \quad (\text{B.13})$$

with

$$\begin{aligned} \frac{\partial u_1}{\partial z} &= \frac{\partial u_1}{\partial z} \Big|_{z=f_1} - \frac{1}{\mu_1} \left( \frac{\partial p_1}{\partial x} - \rho_1 B \sin \theta \right) (f_1 - z) \\ &= \frac{\mu_2}{\mu_1} \frac{\partial u_2}{\partial z} \Big|_{z=f_1} - \frac{1}{\mu_1} \left( \frac{\partial p_1}{\partial x} - \rho_1 B \sin \theta \right) (f_1 - z), \end{aligned}$$

leading to

$$\begin{aligned} \int_{f_0}^z \frac{\partial u_1}{\partial z} dz &= u_1 - u_1|_{f_0} = u_1 \\ &= \frac{\mu_2}{\mu_1} \frac{\partial u_2}{\partial z} \Big|_{z=f_1} (z - f_0) - \frac{1}{\mu_1} \left( \frac{\partial p_1}{\partial x} - \rho_1 B \sin \theta \right) \left( f_1 (z - f_0) - \frac{z^2 - f_0^2}{2} \right), \end{aligned}$$

$$\int_{f_1}^z \frac{\partial^2 u_2}{\partial z^2} dz = \frac{\partial u_2}{\partial z} - \frac{\partial u_2}{\partial z} \Big|_{z=f_1} = \frac{1}{\mu_2} \left( \frac{\partial p_2}{\partial x} - \rho_2 B \sin \theta \right) (z - f_1),$$

$$\begin{aligned} \int_z^{f_2} \frac{\partial u_2}{\partial z} dz &= u_2 \Big|_{f_2} - u_2 = u_t - u_2 \\ &= \frac{\partial u_2}{\partial z} \Big|_{z=f_1} (f_2 - z) + \frac{1}{\mu_2} \left( \frac{\partial p_2}{\partial x} - \rho_2 B \sin \theta \right) \left( \frac{f_2^2 - z^2}{2} - f_1(f_2 - z) \right); \end{aligned}$$

$$u_2 = u_t - \frac{\partial u_2}{\partial z} \Big|_{z=f_1} (f_2 - z) - \frac{1}{\mu_2} \left( \frac{\partial p_2}{\partial x} - \rho_2 B \sin \theta \right) \left( \frac{f_2^2 - z^2}{2} - f_1(f_2 - z) \right) \quad (\text{B.14})$$

and applying the boundary conditions yields:

$$\begin{aligned} \frac{\mu_2}{\mu_1} \frac{\partial u_2}{\partial z} \Big|_{z=f_1} (f_1 - f_0) - \frac{1}{\mu_1} \left( \frac{\partial p_1}{\partial x} - \rho_1 B \sin \theta \right) \left( f_1 (f_1 - f_0) - \frac{f_1^2 - f_0^2}{2} \right) &= \\ u_t - \frac{\partial u_2}{\partial z} \Big|_{z=f_1} (f_2 - f_1) - \frac{1}{\mu_2} \left( \frac{\partial p_2}{\partial x} - \rho_2 B \sin \theta \right) \left( \frac{f_2^2 - f_1^2}{2} - f_1(f_2 - f_1) \right), & \end{aligned} \quad (\text{B.15})$$

$$\frac{\partial u_2}{\partial z} \Big|_{z=f_1} = \frac{u_t - \frac{1}{\mu_2} \left( \frac{\partial p_2}{\partial x} - \rho_2 B \sin \theta \right) \frac{h_2^2}{2} + \frac{1}{\mu_1} \left( \frac{\partial p_1}{\partial x} - \rho_1 B \sin \theta \right) \frac{h_1^2}{2}}{\frac{\mu_2}{\mu_1} h_1 + h_2}, \quad (\text{B.16})$$

and therefore:

$$\begin{aligned}
u_1 = & \frac{1}{\mu_1} \left( \frac{\partial p_1}{\partial x} - \rho_1 B \sin \theta \right) \left( \frac{z^2 - f_0^2}{2} - f_1(z - f_0) + \frac{\frac{\mu_2}{\mu_1} \frac{h_1^2}{2}}{\frac{\mu_2}{\mu_1} h_1 + h_2} (z - f_0) \right) \\
& - \frac{1}{\mu_2} \left( \frac{\partial p_2}{\partial x} - \rho_2 B \sin \theta \right) \frac{\frac{\mu_2}{\mu_1} \frac{h_2^2}{2}}{\frac{\mu_2}{\mu_1} h_1 + h_2} (z - f_0) + \frac{\frac{\mu_2}{\mu_1} u_t}{\frac{\mu_2}{\mu_1} h_1 + h_2} (z - f_0),
\end{aligned} \tag{B.17}$$

$$\begin{aligned}
u_2 = & \frac{1}{\mu_2} \left( \frac{\partial p_2}{\partial x} - \rho_2 B \sin \theta \right) \left[ \frac{z^2 - f_2^2}{2} - \left( f_1 + \frac{h_2^2}{2 \left( \frac{\mu_2}{\mu_1} h_1 + h_2 \right)} \right) (z - f_2) \right] + \\
& \frac{1}{\mu_1} \left( \frac{\partial p_1}{\partial x} - \rho_1 B \sin \theta \right) \frac{h_1^2 (z - f_2)}{2 \left( \frac{\mu_2}{\mu_1} h_1 + h_2 \right)} + u_t \left( 1 + \frac{z - f_2}{\frac{\mu_2}{\mu_1} h_1 + h_2} \right).
\end{aligned} \tag{B.18}$$

Substituting  $f_0 = s$ ,  $f_1 = h_1 + s$  and  $f_2 = 1.0$  in the above expression yields:

$$\begin{aligned}
u_1 = & \frac{1}{\mu_1} \left( \frac{\partial p_1}{\partial x} - \rho_1 B \sin \theta \right) \left( \frac{z^2 - s^2}{2} - (h_1 + s)(z - s) + \frac{\frac{\mu_2}{\mu_1} \frac{h_1^2}{2}}{\frac{\mu_2}{\mu_1} h_1 + h_2} (z - s) \right) \\
& - \frac{1}{\mu_2} \left( \frac{\partial p_2}{\partial x} - \rho_2 B \sin \theta \right) \frac{\frac{\mu_2}{\mu_1} \frac{h_2^2}{2}}{\frac{\mu_2}{\mu_1} h_1 + h_2} (z - s) + \frac{\frac{\mu_2}{\mu_1} u_t}{\frac{\mu_2}{\mu_1} h_1 + h_2} (z - s),
\end{aligned} \tag{B.19}$$

$$\begin{aligned}
u_2 = & \frac{1}{\mu_2} \left( \frac{\partial p_2}{\partial x} - \rho_2 B \sin \theta \right) \left[ \frac{z^2 - 1}{2} - \left( h_1 + s + \frac{h_2^2}{2 \left( \frac{\mu_2}{\mu_1} h_1 + h_2 \right)} \right) (z - 1) \right] + \\
& \frac{1}{\mu_1} \left( \frac{\partial p_1}{\partial x} - \rho_1 B \sin \theta \right) \frac{h_1^2 (z - 1)}{2 \left( \frac{\mu_2}{\mu_1} h_1 + h_2 \right)} + u_t \left( 1 + \frac{z - 1}{\frac{\mu_2}{\mu_1} h_1 + h_2} \right);
\end{aligned} \tag{B.20}$$

the interface velocity,  $u_{int}$  is given by:

$$u_{int} = -\frac{1}{\mu_1} \left( \frac{\partial p_1}{\partial x} - \rho_1 B \sin \theta \right) \left( \frac{\frac{h_1^2 h_2}{2}}{\frac{\mu_2}{\mu_1} h_1 + h_2} \right) - \frac{1}{\mu_2} \left( \frac{\partial p_2}{\partial x} - \rho_2 B \sin \theta \right) \left( \frac{\frac{\mu_2}{\mu_1} \frac{h_2^2}{2}}{\frac{\mu_2}{\mu_1} h_1 + h_2} \right) + \frac{\mu_2}{\mu_1} u_t \quad (\text{B.21})$$

$u_1$  and  $u_2$  can then be written in terms of the interface velocity as follows:

$$u_1 = u_{int} \frac{z-s}{h_1} - \frac{1}{\mu_1} \left( \frac{\partial p_1}{\partial x} - \rho_1 B \sin \theta \right) (z-s) \left( \frac{h_1}{2} - \frac{z-s}{2} \right), \quad (\text{B.22})$$

$$u_2 = u_{int} + (u_t - u_{int}) \frac{z-h_1-s}{h_2} - \frac{1}{\mu_2} \left( \frac{\partial p_2}{\partial x} - \rho_2 B \sin \theta \right) (z-h_1-s) \left( \frac{h_2}{2} - \frac{z-h_1-s}{2} \right), \quad (\text{B.23})$$

and the average velocities are:

$$\bar{u}_1 = \frac{u_{int}}{2} - \frac{1}{\mu_1} \left( \frac{\partial p_1}{\partial x} - \rho_1 B \sin \theta \right) \frac{h_1^2}{12}, \quad (\text{B.24})$$

$$\bar{u}_2 = \frac{u_t + u_{int}}{2} - \frac{1}{\mu_2} \left( \frac{\partial p_2}{\partial x} - \rho_2 B \sin \theta \right) \frac{h_2^2}{12}. \quad (\text{B.25})$$

The interface velocity can be written in terms of the average velocities and the layers

thickness as:

$$u_{int} = \frac{3 \bar{u}_1 h_2 + \frac{\mu_2}{\mu_1} (\bar{u}_2 - \frac{u_t}{3}) h_1}{h_2 + \frac{\mu_2}{\mu_1} h_1}. \quad (\text{B.26})$$

The flow rate of each fluid is calculated from:

$$q_i = \int_{f_i}^{f_{i+1}} u_i dz, \quad (\text{B.27})$$

with

$$\begin{aligned} q_1 = \int_s^{h_1+s} & \left[ \frac{1}{\mu_1} \left( \frac{\partial p_1}{\partial x} - \rho_1 B \sin \theta \right) \left( \frac{z^2 - s^2}{2} - (h_1 + s)(z - s) + \frac{\frac{\mu_2}{\mu_1} \frac{h_1^2}{2}}{\frac{\mu_2}{\mu_1} h_1 + h_2} (z - s) \right) \right. \\ & \left. - \frac{1}{\mu_2} \left( \frac{\partial p_2}{\partial x} - \rho_2 B \sin \theta \right) \frac{\frac{\mu_2}{\mu_1} \frac{h_2^2}{2}}{\frac{\mu_2}{\mu_1} h_1 + h_2} (z - s) + \frac{\frac{\mu_2}{\mu_1} u_t}{\frac{\mu_2}{\mu_1} h_1 + h_2} (z - s) \right] dz, \end{aligned} \quad (\text{B.28})$$

that is:

$$\begin{aligned} q_1 = & -\frac{h_1^3}{12} \left( 1 + \frac{3h_2}{\frac{\mu_2}{\mu_1} h_1 + h_2} \right) \frac{1}{\mu_1} \left( \frac{\partial p_1}{\partial x} - \rho_1 B \sin \theta \right) \\ & - \frac{\mu_2}{\mu_1} \frac{h_1^2 h_2^2}{4 \left( \frac{\mu_2}{\mu_1} h_1 + h_2 \right)} \frac{1}{\mu_2} \left( \frac{\partial p_2}{\partial x} - \rho_2 B \sin \theta \right) + \frac{\mu_2}{\mu_1} \frac{h_1^2}{2 \left( \frac{\mu_2}{\mu_1} h_1 + h_2 \right)} u_t. \end{aligned} \quad (\text{B.29})$$

and:

$$\begin{aligned} q_2 = \int_{h_1+s}^1 & \left[ \frac{1}{\mu_2} \left( \frac{\partial p_2}{\partial x} - \rho_2 B \sin \theta \right) \left[ \frac{z^2 - 1}{2} - \left( h_1 + s + \frac{h_2^2}{2 \left( \frac{\mu_2}{\mu_1} h_1 + h_2 \right)} \right) (z - 1) \right] \right. \\ & \left. + \frac{1}{\mu_1} \left( \frac{\partial p_1}{\partial x} - \rho_1 B \sin \theta \right) \frac{h_1^2 (z - 1)}{2 \left( \frac{\mu_2}{\mu_1} h_1 + h_2 \right)} + u_t \left( 1 + \frac{z - 1}{\frac{\mu_2}{\mu_1} h_1 + h_2} \right) \right] dz. \end{aligned} \quad (\text{B.30})$$

that is:

$$q_2 = -\frac{h_1^2 h_2^2}{4\left(\frac{\mu_2}{\mu_1} h_1 + h_2\right)} \frac{1}{\mu_1} \left(\frac{\partial p_1}{\partial x} - \rho_1 B \sin \theta\right) - \frac{h_2^3}{12} \left(1 + \frac{\mu_2}{\mu_1} \frac{3h_1}{\frac{\mu_2}{\mu_1} h_1 + h_2}\right) \frac{1}{\mu_2} \left(\frac{\partial p_2}{\partial x} - \rho_2 B \sin \theta\right) + \frac{h_2}{2} \left(1 + \frac{\frac{\mu_2}{\mu_1} h_1}{\frac{\mu_2}{\mu_1} h_1 + h_2}\right) u_t, \quad (\text{B.31})$$

where  $u_t \neq 0$  implies a translating upper wall for Configuration 1, Figure 1.2 and hence a shear driven component of the flow.

Now let :

$$q_1 = f_{11} \left(\frac{\partial p_1}{\partial x} - \rho_1 B \sin \theta\right) + f_{21} \left(\frac{\partial p_2}{\partial x} - \rho_2 B \sin \theta\right) + f_{31}, \quad (\text{B.32})$$

$$q_2 = f_{12} \left(\frac{\partial p_1}{\partial x} - \rho_1 B \sin \theta\right) + f_{22} \left(\frac{\partial p_2}{\partial x} - \rho_2 B \sin \theta\right) + f_{32}, \quad (\text{B.33})$$

where:

$$f_{11} = -\frac{h_1^3}{12\mu_1} \left(1 + \frac{3h_2}{\frac{\mu_2}{\mu_1} h_1 + h_2}\right), \quad (\text{B.34})$$

$$f_{21} = -\frac{h_1^2 h_2^2}{4\mu_1 \left(\frac{\mu_2}{\mu_1} h_1 + h_2\right)}, \quad (\text{B.35})$$

$$f_{31} = \frac{\mu_2}{\mu_1} \frac{h_1^2}{2 \left(\frac{\mu_2}{\mu_1} h_1 + h_2\right)} u_t, \quad (\text{B.36})$$

$$f_{12} = -\frac{h_1^2 h_2^2}{4\mu_1 \left( \frac{\mu_2}{\mu_1} h_1 + h_2 \right)}, \quad (\text{B.37})$$

$$f_{22} = -\frac{h_2^3}{12\mu_2} \left( 1 + \frac{\mu_2}{\mu_1} \frac{3h_1}{\frac{\mu_2}{\mu_1} h_1 + h_2} \right), \quad (\text{B.38})$$

$$f_{32} = \frac{h_2}{2} \left( 1 + \frac{\frac{\mu_2}{\mu_1} h_1}{\frac{\mu_2}{\mu_1} h_1 + h_2} \right) u_t. \quad (\text{B.39})$$

The flow rates in the undisturbed flow are calculated as:

$$Q_1 = -\left( \frac{h_{10}^3}{12\mu_1} + \frac{(1-h_{10})h_{10}^2}{4\mu_1 \left( \frac{\mu_2}{\mu_1} h_{10} + 1 - h_{10} \right)} \right) \frac{\Delta p}{\Delta l} + \left( \frac{\rho_1 h_{10}^3}{12\mu_1} + \frac{h_{10}^2 (1-h_{10})(\rho_1 h_{10} + \rho_2 (1-h_{10}))}{4\mu_1 \left( \frac{\mu_2}{\mu_1} h_{10} + 1 - h_{10} \right)} \right) B \sin \theta + \frac{\mu_2}{\mu_1} \frac{h_{10}^2}{2 \left( \frac{\mu_2}{\mu_1} h_{10} + 1 - h_{10} \right)} u_t, \quad (\text{B.40})$$

and

$$Q_2 = -\left( \frac{(1-h_{10})^3}{12\mu_2} + \frac{(1-h_{10})^2 h_{10}}{4\mu_1 \left( \frac{\mu_2}{\mu_1} h_{10} + 1 - h_{10} \right)} \right) \frac{\Delta p}{\Delta l} + \left( \frac{\rho_2 (1-h_{10})^3}{12\mu_2} + \frac{h_{10} (1-h_{10})^2 (\rho_1 h_{10} + \rho_2 (1-h_{10}))}{4\mu_1 \left( \frac{\mu_2}{\mu_1} h_{10} + 1 - h_{10} \right)} \right) B \sin \theta + \frac{1-h_{10}}{2} \left( 1 + \frac{\frac{\mu_2}{\mu_1} h_{10}}{\frac{\mu_2}{\mu_1} h_{10} + 1 - h_{10}} \right) u_t, \quad (\text{B.41})$$

where  $\frac{\Delta p}{l}$  is the imposed pressure gradient and  $h_0$  is the undisturbed interfacial height.

Integrating the continuity equation (B.3) and using the Leibniz's rule yields:

$$\int_{f_{i-1}}^{f_i} \left( \frac{\partial u_i}{\partial x} + \frac{\partial w_i}{\partial z} \right) dz = \frac{\partial}{\partial x} \left( \int_{f_{i-1}}^{f_i} u_i dz \right) - u_i|_{z=f_i} \frac{\partial f_i}{\partial x} + u_i|_{z=f_{i-1}} \frac{\partial f_{i-1}}{\partial x} + w_i|_{z=f_i} - w_i|_{z=f_{i-1}} = 0,$$

and results in the following form of the mass conservation equation:

$$\frac{\partial h_1}{\partial t} + \frac{\partial q_1}{\partial x} = 0, \quad (\text{B.42})$$

$$\frac{\partial h_2}{\partial t} + \frac{\partial q_2}{\partial x} = 0. \quad (\text{B.43})$$

Summing the above expressions yield

$$\frac{\partial(h_1 + h_2)}{\partial t} + \frac{\partial(q_1 + q_2)}{\partial x} = 0 \quad (\text{B.44})$$

with  $\frac{\partial(h_1 + h_2)}{\partial t} = 0$  because the channel is rigid; integrating equation (B.44) then yields:

$$q_1 + q_2 = Q_1 + Q_2 = Q_{total}. \quad (\text{B.45})$$

The full set of governing equations to solve in order to obtain  $h_1$ ,  $p_1$  and  $p_2$  are then:

$$\frac{\partial h_1}{\partial t} + \frac{\partial}{\partial x} \left[ f_{11} \left( \frac{\partial p_1}{\partial x} - \rho_1 B \sin \theta \right) + f_{21} \left( \frac{\partial p_2}{\partial x} - \rho_2 B \sin \theta \right) + f_{31} \right] = 0, \quad (\text{B.46})$$

$$p_2 - p_1 = \sigma_{int} \frac{\varepsilon^3}{Ca} \nabla^2 (h_1 + s) + B \varepsilon \cos \theta (\rho_2 - \rho_1) (h_1 + s), \quad (\text{B.47})$$

$$\begin{aligned} & \left( h_2 + \frac{\mu_2 h_1 (h_1 + h_2)}{\mu_1 \frac{\mu_2}{\mu_1} h_1 + h_2} \right) \frac{u_t}{2} - \frac{h_1^2}{4\mu_1} \left( \frac{h_1}{3} + \frac{h_2 (h_1 + h_2)}{\frac{\mu_2}{\mu_1} h_1 + h_2} \right) \left( \frac{\partial p_1}{\partial x} - \rho_1 B \sin \theta \right) \\ & - \frac{h_2^2}{4\mu_1} \left( \frac{\mu_2 h_2}{\mu_1 3} + \frac{h_1 (h_1 + h_2)}{\frac{\mu_2}{\mu_1} h_1 + h_2} \right) \left( \frac{\partial p_2}{\partial x} - \rho_2 B \sin \theta \right) = Q_{total}, \end{aligned} \quad (\text{B.48})$$

with  $h_2$  determined from:

$$h_2 = 1 - h_1 - s. \quad (\text{B.49})$$

The problem is closed in terms of the following boundary conditions:

$$h_1|_{x=0} = h_{10}, \quad (\text{B.50})$$

$$\left. \frac{\partial h_1}{\partial x} \right|_{x=l} = 0, \quad (\text{B.51})$$

$$\left. \frac{\partial p_1}{\partial x} \right|_{x=0,l} = \left. \frac{\partial p_2}{\partial x} \right|_{x=0,l} = 0. \quad (\text{B.52})$$

In the steady state case, mass conservation in each layer dictates that:

$$Q_1 = f_{11} \left( \frac{\partial p_1}{\partial x} - \rho_1 B \sin \theta \right) + f_{21} \left( \frac{\partial p_2}{\partial x} - \rho_2 B \sin \theta \right) + f_{31}, \quad (\text{B.53})$$

$$Q_2 = f_{12} \left( \frac{\partial p_1}{\partial x} - \rho_1 B \sin \theta \right) + f_{22} \left( \frac{\partial p_2}{\partial x} - \rho_2 B \sin \theta \right) + f_{32}; \quad (\text{B.54})$$

the axial pressure derivatives contained therein can be calculated from (B.53) and (B.54) as:

$$\frac{\partial p_1}{\partial x} = \frac{f_{22}(Q_1 - f_{31}) - f_{21}(Q_2 - f_{32})}{f_{22}f_{11} - f_{21}f_{12}} + \rho_1 B \sin \theta, \quad (\text{B.55})$$

$$\frac{\partial p_2}{\partial x} = \frac{f_{12}(Q_1 - f_{31}) - f_{11}(Q_2 - f_{32})}{f_{12}f_{21} - f_{11}f_{22}} - + + \rho_2 B \sin \theta. \quad (\text{B.56})$$

Differentiating the pressure equation (B.47) with respect to  $x$  yields:

$$\frac{\partial p_2}{\partial x} - \frac{\partial p_1}{\partial x} = \sigma_{int} \frac{\varepsilon^3}{Ca} \nabla^3 (h_1 + s) + B\varepsilon \cos \theta (\rho_2 - \rho_1) \frac{\partial (h_1 + s)}{\partial x}, \quad (\text{B.57})$$

and substituting for (B.55) and (B.56) into the above expression leads to the following governing equation for  $h_1$ :

$$\begin{aligned} \sigma_{int} \frac{\varepsilon^3}{Ca} \nabla^3 (h_1 + s) = & \frac{f_{12} + f_{22}}{f_{12}f_{21} - f_{11}f_{22}} (Q_1 - f_{31}) - \frac{f_{11} + f_{21}}{f_{12}f_{21} - f_{11}f_{22}} (Q_2 - f_{32}) \\ & + (\rho_2 - \rho_1)B \left( \sin \theta - \varepsilon \cos \theta \frac{\partial (h_1 + s)}{\partial x} \right), \end{aligned} \quad (\text{B.58})$$

the attendant boundary conditions being:

$$h_1|_{x=0} = h_{10}, \quad \frac{\partial h_1}{\partial x} \Big|_{x=0,l} = 0, \quad \frac{\partial^3 h_1}{\partial x^3} \Big|_{x=0,l} = 0 \quad (\text{B.59})$$

## Appendix C

# Derivation of the depth averaged form (DAF) for channel flow

The averaged form of the continuity equation derived in Appendix B can be written in terms of the depth averaged velocities,  $\bar{u}_i$  as:

$$\frac{\partial h_1}{\partial t} + \frac{\partial(h_1\bar{u}_1)}{\partial x} = 0, \quad (\text{C.1})$$

$$\frac{\partial h_2}{\partial t} + \frac{\partial(h_2\bar{u}_2)}{\partial x} = 0; \quad (\text{C.2})$$

in which case the global mass balance equation becomes:

$$h_1\bar{u}_1 + h_2\bar{u}_2 = Q_{total}. \quad (\text{C.3})$$

To obtain the depth average form of the u-momentum equation it is integrated with respect to  $z$  from  $f_{i-1}$  to  $f_i$ :

$$\rho_i \varepsilon Re \int_{f_{i-1}}^{f_i} \left[ \frac{\partial u_i}{\partial t} + u_i \frac{\partial u_i}{\partial x} + w_i \frac{\partial u_i}{\partial z} \right] dz = \int_{f_{i-1}}^{f_i} \left( -\frac{\partial p_i}{\partial x} + \rho_i B \sin \theta + \mu_i \frac{\partial^2 u_i}{\partial z^2} \right) dz; \quad (\text{C.4})$$

the

$$\text{RHS} = \left( -\frac{\partial p_i}{\partial x} + \rho_i B \sin \theta \right) h_i + \mu_i \left( \frac{\partial u_i}{\partial z} \Big|_{f_i} - \frac{\partial u_i}{\partial z} \Big|_{f_{i-1}} \right), \quad (\text{C.5})$$

and the

$$\text{LHS} = \rho_i \varepsilon Re \int_{f_{i-1}}^{f_i} \left[ \frac{\partial u_i}{\partial t} + u_i \frac{\partial u_i}{\partial x} + w_i \frac{\partial u_i}{\partial z} \right] dz = \rho_i \varepsilon Re \int_{f_{i-1}}^{f_i} \left[ \frac{\partial u_i}{\partial t} + \frac{\partial u_i^2}{\partial x} + \frac{\partial u_i w_i}{\partial z} \right] dz, \quad (\text{C.6})$$

because  $\frac{\partial u_i}{\partial x} + \frac{\partial w_i}{\partial z} = 0$  and the use of Leibniz's rule which leads to:

$$\begin{aligned} \text{LHS} &= \rho_i \varepsilon Re \left[ \frac{\partial}{\partial t} \int_{f_{i-1}}^{f_i} u_i dz + \frac{\partial}{\partial x} \int_{f_{i-1}}^{f_i} u_i^2 dz + \left( \frac{\partial f_{i-1}}{\partial t} u_i \Big|_{f_{i-1}} + \right. \right. \\ &\quad \left. \left. \frac{\partial f_{i-1}}{\partial x} u_i^2 \Big|_{f_{i-1}} - (u_i w_i) \Big|_{f_{i-1}} \right) - \left( \frac{\partial f_i}{\partial t} u_i \Big|_{f_i} + \frac{\partial f_i}{\partial x} u_i^2 \Big|_{f_i} - (u_i w_i) \Big|_{f_i} \right) \right] \\ &= \rho_i \varepsilon Re \left( \frac{\partial}{\partial t} \int_{f_{i-1}}^{f_i} u_i dz + \frac{\partial}{\partial x} \int_{f_{i-1}}^{f_i} u_i^2 dz \right), \end{aligned} \quad (\text{C.7})$$

where

$$\frac{\partial f_i}{\partial t} + \frac{\partial f_i}{\partial x} u_i \Big|_{f_i} - w_i \Big|_{f_i} = 0, \quad (\text{C.8})$$

and thus

$$\begin{aligned} \text{LHS} &= \rho_i \varepsilon Re \left[ \frac{\partial}{\partial t} (h_i \bar{u}_i) + \frac{\partial}{\partial x} \int_{f_{i-1}}^{f_i} \bar{u}_i^2 dz + \frac{\partial}{\partial x} \int_{f_{i-1}}^{f_i} (\bar{u}_i - u_i)^2 dz \right] \\ &= \rho_i \varepsilon Re \left[ \frac{\partial}{\partial t} (h_i \bar{u}_i) + \frac{\partial}{\partial x} (h_i \bar{u}_i^2) + \frac{\partial}{\partial x} \int_{f_{i-1}}^{f_i} (\bar{u}_i - u_i)^2 dz \right]. \end{aligned} \quad (\text{C.9})$$

Substituting for for (C.5) and (C.9) in (C.4) gives:

$$\begin{aligned} & \rho_i \varepsilon Re \left[ \frac{\partial}{\partial t} (h_i \bar{u}_i) + \frac{\partial}{\partial x} (h_i \bar{u}_i^2) + \frac{\partial}{\partial x} \int_{f_{i-1}}^{f_i} (\bar{u}_i - u_i)^2 dz \right] \\ & = \left( -\frac{\partial p_i}{\partial x} + \rho_i B \sin \theta \right) h_i + \mu_i \left( \frac{\partial u_i}{\partial z} \Big|_{f_i} - \frac{\partial u_i}{\partial z} \Big|_{f_{i-1}} \right). \end{aligned} \quad (\text{C.10})$$

Equation (B.47), (B.49), (C.1), (C.3) and (C.10) represent the set of equations to be solved in order to obtain the liquid-liquid interface position. The problem is closed in terms of the specified inflow conditions and imposing fully developed flow both far upstream and downstream, these are:

$$h_1|_{x=0} = h_{10}, \quad \frac{\partial h_1}{\partial x} \Big|_{x=l} = 0, \quad (\text{C.11})$$

$$\begin{aligned} \bar{u}_1|_{x=0} = & - \left( \frac{h_{10}^2}{12\mu_1} + \frac{(1-h_{10})h_{10}}{4\mu_1 \left( \frac{\mu_2}{\mu_1} h_{10} + 1 - h_{10} \right)} \right) \frac{\Delta p}{\Delta l} + \left( \frac{\rho_1 h_{10}^2}{12\mu_1} + \right. \\ & \left. \frac{h_{10}(1-h_{10})(\rho_1 h_{10} + \rho_2(1-h_{10}))}{4\mu_1 \left( \frac{\mu_2}{\mu_1} h_{10} + 1 - h_{10} \right)} \right) B \sin \theta + \frac{\mu_2}{\mu_1} \frac{h_{10}}{2 \left( \frac{\mu_2}{\mu_1} h_{10} + 1 - h_{10} \right)} u_t, \end{aligned} \quad (\text{C.12})$$

$$\begin{aligned} \bar{u}_1|_{x=0} = & - \left( \frac{(1-h_{10})^2}{12\mu_2} + \frac{(1-h_{10})h_{10}}{4\mu_1 \left( \frac{\mu_2}{\mu_1} h_{10} + 1 - h_{10} \right)} \right) \frac{\Delta p}{\Delta l} + \left( \frac{\rho_2(1-h_{10})^2}{12\mu_2} + \right. \\ & \left. \frac{h_{10}(1-h_{10})(\rho_1 h_{10} + \rho_2(1-h_{10}))}{4\mu_1 \left( \frac{\mu_2}{\mu_1} h_{10} + 1 - h_{10} \right)} \right) B \sin \theta + \frac{1}{2} \left( 1 + \frac{\frac{\mu_2}{\mu_1} h_{10}}{\frac{\mu_2}{\mu_1} h_{10} + 1 - h_{10}} \right) u_t, \end{aligned} \quad (\text{C.13})$$

$$\frac{\partial \bar{u}_i}{\partial x} \Big|_{x=l} = \frac{\partial p_1}{\partial x} \Big|_{x=l} = \frac{\partial p_2}{\partial x} \Big|_{x=l} = 0. \quad (\text{C.14})$$

To determine the dispersion term,  $\int_{f_{i-1}}^{f_i} (\bar{u}_i - u_i)^2 dz$ , and the friction term,  $\frac{\partial u_i}{\partial z} \Big|_{f_i}$ , a self-similar quadratic velocity profile is assumed. This assumption results in the

velocity profiles for channel flow having the form:

$$u_1 = 3 (u_{int} - 2\bar{u}_1) \xi_1^2 + 2 (3\bar{u}_1 - u_{int}) \xi_1, \quad (\text{C.15})$$

and

$$u_2 = 3 (u_{int} + u_t - 2\bar{u}_2) \xi_2^2 + 2 (3\bar{u}_2 - u_{int} - u_t) \xi_2 + u_t, \quad (\text{C.16})$$

where  $\xi_1 = \frac{z-s}{h_1}$  and  $\xi_2 = \frac{1-z}{h_2}$  and  $u_{int}$ , the velocity of the interface is given by:

$$u_{int} = \frac{3\bar{u}_1 h_2 + \frac{\mu_2}{\mu_1} \bar{u}_2 h_1}{2} - \frac{1}{2} \frac{\frac{\mu_2}{\mu_1} h_1}{h_2 + \frac{\mu_2}{\mu_1} h_1} u_t. \quad (\text{C.17})$$

Using the above velocity profiles the friction terms can be written as:

$$\mu_1 \left( \left. \frac{\partial u_1}{\partial z} \right|_{f_1} - \left. \frac{\partial u_1}{\partial z} \right|_{f_0} \right) = 6\mu_1 \frac{u_{int} - 2\bar{u}_1}{h_1}, \quad (\text{C.18})$$

$$\mu_2 \left( \left. \frac{\partial u_2}{\partial z} \right|_{f_2} - \left. \frac{\partial u_2}{\partial z} \right|_{f_1} \right) = 6\mu_2 \frac{u_{int} + u_t - 2\bar{u}_2}{h_2}, \quad (\text{C.19})$$

and the dispersion terms derived as follows:

$$u_1 = 3 (u_{int} - 2\bar{u}_1) \xi_1^2 + 2 (3\bar{u}_1 - u_{int}) \xi_1 = a_1 \xi_1^2 + b_1 \xi_1, \quad (\text{C.20})$$

$$u_1^2 = a_1^2 \xi_1^4 + b_1^2 \xi_1^2 + 2a_1 b_1 \xi_1^3, \quad (\text{C.21})$$

$$u_2 = 3(u_{int} + u_t - 2\bar{u}_2)\xi_2^2 + 2(3\bar{u}_2 - u_{int} - u_t)\xi_2 + u_t = a_2\xi_2^2 + b_2\xi_2 + u_t. \quad (\text{C.22})$$

The dispersion term for the lower layer is

$$\int_{f_0}^{f_1} (\bar{u}_1 - u_1)^2 dz = \int_{f_0}^{f_1} (\bar{u}_1^2 - 2\bar{u}_1 u_1 + u_1^2) dz = \int_{f_0}^{f_1} u_1^2 dz - h_1 \bar{u}_1^2, \quad (\text{C.23})$$

and

$$\begin{aligned} \int_{f_0}^{f_1} u_1^2 dz &= h_1 \int_0^1 u_1^2 d\xi_1 = h_1 \left[ a_1^2 \frac{\xi_1^5}{5} + b_1^2 \frac{\xi_1^3}{3} + 2a_1 b_1 \frac{\xi_1^4}{4} \right]_0^1 \\ &= h_1 \left[ \frac{a_1^2}{5} + \frac{b_1^2}{3} + \frac{2a_1 b_1}{4} \right] \\ &= h_1 \left( \frac{2}{15} u_{int}^2 - \frac{1}{5} \bar{u}_1 u_{int} + \frac{6}{5} \bar{u}_1^2 \right); \end{aligned} \quad (\text{C.24})$$

similarly, the dispersion term for the upper layer is

$$\begin{aligned} \int_{f_1}^{f_2} u_2^2 dz &= h_2 \int_1^0 u_2^2 d\xi_2 = h_2 \left[ a_2^2 \frac{\xi_2^5}{5} + b_2^2 \frac{\xi_2^3}{3} + 2a_2 b_2 \frac{\xi_2^4}{4} + 2a_2 u_t \frac{\xi_2^3}{3} + 2b_2 u_t \frac{\xi_2^2}{2} + u_t^2 \xi_2 \right]_1^0 \\ &= -h_2 \left[ \frac{a_2^2}{5} + \frac{b_2^2}{3} + \frac{2a_2 b_2}{4} + \frac{2a_2 u_t}{3} + \frac{2b_2 u_t}{2} + u_t^2 \right]_1^0 \\ &= h_2 \left( \frac{2}{15} u_{int}^2 - \frac{1}{5} \bar{u}_2 u_{int} + \frac{6}{5} \bar{u}_2^2 + \frac{2}{15} u_t^2 - \frac{1}{15} u_t u_{int} - \frac{1}{5} \bar{u}_2 u_t \right), \end{aligned} \quad (\text{C.25})$$

and

$$\int_{f_0}^{f_1} (\bar{u}_1 - u_1)^2 dz = \frac{2}{15} h_1 u_{int}^2 - \frac{1}{5} h_1 \bar{u}_1 u_{int} + \frac{1}{5} h_1 \bar{u}_1^2 \quad (\text{C.26})$$

$$\int_{f_1}^{f_2} (\bar{u}_2 - u_2)^2 dz = \frac{2}{15} h_2 u_{int}^2 - \frac{1}{5} h_2 \bar{u}_2 u_{int} + \frac{1}{5} h_2 \bar{u}_2^2 + \frac{2}{15} h_2 u_t^2 - \frac{1}{15} h_2 u_t u_{int} - \frac{1}{5} h_2 \bar{u}_2 u_t. \quad (C.27)$$

The DAF for the lower layer becomes:

$$\begin{aligned} \rho_1 \varepsilon Re \left[ \frac{\partial}{\partial t} (h_1 \bar{u}_1) + \frac{\partial}{\partial x} \left( \frac{6}{5} h_1 \bar{u}_1^2 + \frac{2}{15} h_1 u_{int}^2 - \frac{1}{5} h_1 \bar{u}_1 u_{int} \right) \right] \\ = \left( -\frac{\partial p_1}{\partial x} + \rho_1 B \sin \theta \right) h_1 + 6\mu_1 \frac{u_{int} - 2\bar{u}_1}{h_1}, \end{aligned} \quad (C.28)$$

which can be simplified to:

$$\begin{aligned} \rho_1 \varepsilon Re \left[ \frac{\partial \bar{u}_1}{\partial t} - \frac{\bar{u}_1}{5h_1} \frac{\partial h_1}{\partial t} + \frac{6}{5} \bar{u}_1 \frac{\partial \bar{u}_1}{\partial x} + \frac{2}{15h_1} \frac{\partial (h_1 u_{int}^2)}{\partial x} \right. \\ \left. - \frac{1}{5h_1} \frac{\partial (h_1 \bar{u}_1 u_{int})}{\partial x} \right] = -\frac{\partial p_1}{\partial x} + \rho_1 B \sin \theta + 6\mu_1 \frac{u_{int} - 2\bar{u}_1}{h_1^2}, \end{aligned} \quad (C.29)$$

similarly, the DAF for the upper layer is:

$$\begin{aligned} \rho_2 \varepsilon Re \left[ \frac{\partial \bar{u}_2}{\partial t} - \frac{\bar{u}_2}{5h_2} \frac{\partial h_2}{\partial t} + \frac{6}{5} \bar{u}_2 \frac{\partial \bar{u}_2}{\partial x} + \frac{1}{15h_2} \frac{\partial (h_2 (2u_{int}^2 - u_{int} u_t))}{\partial x} + \frac{2}{15h_2} \frac{\partial (u_t^2 h_2)}{\partial x} \right. \\ \left. - \frac{1}{5h_2} \frac{\partial (h_2 (\bar{u}_2 u_{int} - \bar{u}_2 u_t))}{\partial x} \right] = -\frac{\partial p_2}{\partial x} + \rho_2 B \sin \theta + 6\mu_2 \frac{u_{int} - 2\bar{u}_2 + u_t}{h_2^2}. \end{aligned} \quad (C.30)$$

The above DAFs can be written as:

$$\rho_1 \varepsilon Re N_1 = -\frac{\partial p_1}{\partial x} + \rho_1 B \sin \theta + 6\mu_1 \frac{u_{int} - 2\bar{u}_1}{h_1^2}, \quad (C.31)$$

$$\rho_2 \varepsilon Re N_2 = -\frac{\partial p_2}{\partial x} + \rho_2 B \sin \theta + 6\mu_2 \frac{u_{int} - 2\bar{u}_2 + u_t}{h_2^2}, \quad (C.32)$$

which upon subtracting equation (C.31) from (C.32) gives:

$$\varepsilon Re (\rho_2 N_2 - \rho_1 N_1) = \frac{\partial p_1}{\partial x} - \frac{\partial p_2}{\partial x} + (\rho_2 - \rho_1) B \sin \theta + 6\mu_2 \frac{u_{int} - 2\bar{u}_2 + u_t}{h_2^2} - 6\mu_1 \frac{u_{int} - 2\bar{u}_1}{h_1^2}, \quad (C.33)$$

with the pressure gradient difference,  $\frac{\partial p_1}{\partial x} - \frac{\partial p_2}{\partial x}$  obtained by differentiating equation (B.12) with respect to  $x$ . Equation (C.33) accordingly becomes:

$$\varepsilon Re (\rho_2 N_2 - \rho_1 N_1) = -\sigma_{int} \frac{\varepsilon^3}{Ca} \frac{\partial^3 f}{\partial x^3} + (\rho_2 - \rho_1) B \left( \sin \theta - \varepsilon \cos \theta \frac{\partial (h_1 + s)}{\partial x} \right) + f_{r2} - f_{r1}, \quad (C.34)$$

where

$$N_i = \frac{\partial \bar{u}_i}{\partial t} - \frac{\bar{u}_i}{5h_i} \frac{\partial h_i}{\partial t} + \frac{6}{5} \bar{u}_i \frac{\partial \bar{u}_i}{\partial x} + \frac{1}{h_i} \frac{\partial (h_i \phi_i)}{\partial x}, \quad (C.35)$$

and

$$\begin{aligned} \phi_1 &= \frac{2}{15} u_i n i n^2 - \frac{1}{5} \bar{u}_1 u_{int}, & \phi_2 &= \frac{2}{15} u_{int}^2 - \frac{1}{5} \bar{u}_2 u_{int} + \frac{2}{15} u_t^2 - \frac{1}{5} \bar{u}_2 u_t - \frac{1}{15} u_{int} u_t, \\ f_{r1} &= 6\mu_1 \frac{u_{int} - 2\bar{u}_1}{h_1^2}, & f_{r2} &= 6\mu_2 \frac{u_{int} - 2\bar{u}_2 + u_t}{h_2^2}. \end{aligned} \quad (C.36)$$

Equations (C.1) and (C.34) can be solved for  $h_1$  and  $\bar{u}_1$  with  $h_2$  and  $\bar{u}_2$  are obtained

from:

$$h_2 = 1 - h_1 - s, \quad \text{and} \quad \bar{u}_2 = \frac{1 - \bar{u}_1 h_1}{h_2}. \quad (\text{C.37})$$

If the flow is steady then the flow rate through each layer is constant and hence only equation (C.34) needs to be solved for  $h_1$ .

The LUB model is based on the long-wave approximation. It differs from the DAF in that it assumes the Reynolds number to be small enough so that  $\varepsilon Re$  is negligible. The DAF should reduce to the LUB one if  $\varepsilon Re$  is set to zero. Applying this to equations (C.31) and (C.32) gives:

$$-\frac{\partial p_1}{\partial x} + \rho_1 B \sin \theta + 6\mu_1 \frac{u_{int} - 2\bar{u}_1}{h_1^2} = 0, \quad (\text{C.38})$$

$$-\frac{\partial p_2}{\partial x} + \rho_2 B \sin \theta + 6\mu_2 \frac{u_{int} - 2\bar{u}_2 + u_t}{h_2^2} = 0, \quad (\text{C.39})$$

which can be solved by substituting for the interface velocity from (C.17) to yield the following following expression for the average velocities:

$$\begin{aligned} \bar{u}_1 = & -\frac{h_1^2}{12} \left( 1 + \frac{3h_2}{\frac{\mu_2}{\mu_1} h_1 + h_2} \right) \frac{1}{\mu_1} \left( \frac{\partial p_1}{\partial x} - \rho_1 B \sin \theta \right) \\ & - \frac{\mu_2}{\mu_1} \frac{h_1 h_2^2}{4 \left( \frac{\mu_2}{\mu_1} h_1 + h_2 \right)} \frac{1}{\mu_2} \left( \frac{\partial p_2}{\partial x} - \rho_2 B \sin \theta \right) + \frac{\mu_2}{\mu_1} \frac{h_1}{2 \left( \frac{\mu_2}{\mu_1} h_1 + h_2 \right)} u_t, \end{aligned} \quad (\text{C.40})$$

$$\begin{aligned} \bar{u}_2 = & -\frac{h_1^2 h_2}{4 \left( \frac{\mu_2}{\mu_1} h_1 + h_2 \right)} \frac{1}{\mu_1} \left( \frac{\partial p_1}{\partial x} - \rho_1 B \sin \theta \right) - \frac{h_2^2}{12} \left( 1 + \frac{\mu_2}{\mu_1} \frac{3h_1}{\frac{\mu_2}{\mu_1} h_1 + h_2} \right) \\ & \frac{1}{\mu_2} \left( \frac{\partial p_2}{\partial x} - \rho_2 B \sin \theta \right) + \frac{1}{2} \left( 1 + \frac{\frac{\mu_2}{\mu_1} h_1}{\frac{\mu_2}{\mu_1} h_1 + h_2} \right) u_t. \end{aligned} \quad (\text{C.41})$$

Substituting for these average velocities into equation (C.1) and (C.2) results in the following evolution equations:

$$\begin{aligned} \frac{\partial h_1}{\partial t} - \frac{\partial}{\partial x} \left[ \frac{h_1^3}{12} \left( 1 + \frac{3h_2}{\frac{\mu_2}{\mu_1} h_1 + h_2} \right) \frac{1}{\mu_1} \left( \frac{\partial p_1}{\partial x} - \rho_1 B \sin \theta \right) \right. \\ \left. + \frac{\mu_2}{\mu_1} \frac{h_1^2 h_2^2}{4 \left( \frac{\mu_2}{\mu_1} h_1 + h_2 \right)} \frac{1}{\mu_2} \left( \frac{\partial p_2}{\partial x} - \rho_2 B \sin \theta \right) - \frac{\mu_2}{\mu_1} \frac{h_1^2}{2 \left( \frac{\mu_2}{\mu_1} h_1 + h_2 \right)} u_t \right] = 0, \end{aligned} \quad (\text{C.42})$$

$$\begin{aligned} \frac{\partial h_2}{\partial t} - \frac{\partial}{\partial x} \left[ \frac{h_1^2 h_2^2}{4 \left( \frac{\mu_2}{\mu_1} h_1 + h_2 \right)} \frac{1}{\mu_1} \left( \frac{\partial p_1}{\partial x} - \rho_1 B \sin \theta \right) + \frac{h_2^3}{12} \left( 1 + \frac{\mu_2}{\mu_1} \frac{3h_1}{\frac{\mu_2}{\mu_1} h_1 + h_2} \right) \right. \\ \left. \frac{1}{\mu_2} \left( \frac{\partial p_2}{\partial x} - \rho_2 B \sin \theta \right) - \frac{h_2}{2} \left( 1 + \frac{\frac{\mu_2}{\mu_1} h_1}{\frac{\mu_2}{\mu_1} h_1 + h_2} \right) u_t \right] = 0, \end{aligned} \quad (\text{C.43})$$

or in compact form:

$$\frac{\partial h_i}{\partial t} - \frac{\partial}{\partial x} \left[ f_{1i} \left( \frac{\partial p_1}{\partial x} - \rho_1 B \sin \theta \right) + f_{2i} \left( \frac{\partial p_2}{\partial x} - \rho_2 B \sin \theta \right) + f_{3i} \right]. \quad (\text{C.44})$$

If the flow is steady, equation (C.34) reduces to:

$$\begin{aligned} \frac{\varepsilon^3}{Ca} \nabla^3 (h_1 + s) = & \frac{f_{12} + f_{22}}{f_{12} f_{21} - f_{11} f_{22}} (Q_1 - f_{31}) - \frac{f_{11} + f_{21}}{f_{12} f_{21} - f_{11} f_{22}} (Q_2 - f_{32}) \\ & + (\rho_2 - \rho_1) B \left( \sin \theta - \varepsilon \cos \theta \frac{\partial (h_1 + s)}{\partial x} \right), \end{aligned} \quad (\text{C.45})$$

where:

$$f_{11} = -\frac{h_1^3}{12\mu_1} \left( 1 + \frac{3h_2}{\frac{\mu_2}{\mu_1}h_1 + h_2} \right), \quad (\text{C.46})$$

$$f_{21} = -\frac{h_1^2 h_2^2}{4\mu_1 \left( \frac{\mu_2}{\mu_1}h_1 + h_2 \right)}, \quad (\text{C.47})$$

$$f_{31} = \frac{\mu_2}{\mu_1} \frac{h_1^2}{2 \left( \frac{\mu_2}{\mu_1}h_1 + h_2 \right)} u_t, \quad (\text{C.48})$$

$$f_{12} = -\frac{h_1^2 h_2^2}{4\mu_1 \left( \frac{\mu_2}{\mu_1}h_1 + h_2 \right)}, \quad (\text{C.49})$$

$$f_{22} = -\frac{h_2^3}{12\mu_2} \left( 1 + \frac{\mu_2}{\mu_1} \frac{3h_1}{\frac{\mu_2}{\mu_1}h_1 + h_2} \right), \quad (\text{C.50})$$

$$f_{32} = \frac{h_2}{2} \left( 1 + \frac{\frac{\mu_2}{\mu_1}h_1}{\frac{\mu_2}{\mu_1}h_1 + h_2} \right) u_t, \quad (\text{C.51})$$

which are identical to the LUB derived in Appendix B.

## Appendix D

# Discretisation of the LUB equations

### D.1 Free-surface bilayer flow

The full set of governing equations for the LUB model for three-dimensional free-surface flow, as derived in Appendix A, is:

$$\begin{aligned} \frac{\partial h_1}{\partial t} - \frac{\partial}{\partial x} \left[ \frac{h_1^3}{3\mu_1} \left( \frac{\partial p_1}{\partial x} - \frac{2\rho_1}{C} \right) + \frac{h_1^2 h_2}{2\mu_1} \left( \frac{\partial p_2}{\partial x} - \frac{2\rho_2}{C} \right) \right] \\ - \frac{\partial}{\partial y} \left[ \frac{h_1^3}{3\mu_1} \left( \frac{\partial p_1}{\partial y} \right) + \frac{h_1^2 h_2}{2\mu_1} \left( \frac{\partial p_2}{\partial y} \right) \right] = 0, \end{aligned} \quad (\text{D.1})$$

$$\begin{aligned} \frac{\partial h_2}{\partial t} - \frac{\partial}{\partial x} \left[ \frac{h_1^2 h_2}{2\mu_1} \left( \frac{\partial p_1}{\partial x} - \frac{2\rho_2}{C} \right) + \left( \frac{h_1 h_2^2}{\mu_1} + \frac{h_2^3}{3\mu_2} \right) \left( \frac{\partial p_2}{\partial x} - \frac{2\rho_2}{C} \right) \right] \\ - \frac{\partial}{\partial y} \left[ \frac{h_1^2 h_2}{2\mu_1} \left( \frac{\partial p_1}{\partial y} \right) + \left( \frac{h_1 h_2^2}{\mu_1} + \frac{h_2^3}{3\mu_2} \right) \left( \frac{\partial p_2}{\partial y} \right) \right] = 0, \end{aligned} \quad (\text{D.2})$$

$$p_1 = -\frac{\varepsilon^3}{Ca} (\sigma_{int} \nabla^2 f_1 + \sigma_2 \nabla^2 f_2) + \frac{2\varepsilon}{C} [\rho_1 f_1 + \rho_2 (f_2 - f_1)] \cot \theta, \quad (\text{D.3})$$

$$p_2 = -\frac{\varepsilon^3}{Ca} \sigma_2 \nabla^2 f_2 + \frac{2\rho_2 \varepsilon}{C} f_2 \cot \theta, \quad (\text{D.4})$$

and the boundary conditions are:

$$h_1|_{x=0} = h_{10}, \quad h_2|_{x=0} = 1 - h_{10}, \quad (\text{D.5})$$

$$\left. \frac{\partial h_i}{\partial x} \right|_{x=l} = \left. \frac{\partial h_i}{\partial y} \right|_{y=0,w} = 0, \quad (\text{D.6})$$

$$\left. \frac{\partial p_i}{\partial x} \right|_{x=0,l} = \left. \frac{\partial p_i}{\partial y} \right|_{y=0,w} = 0. \quad (\text{D.7})$$

### D.1.1 Spatial discretisation

Equations (D.1) to (D.4) are solved, subject to boundary conditions (D.5) to (D.7), on a rectangular computational domain,  $(x, y) \in [0, l] \times [0, w]$  using the multigrid approach described in Chapter 3. The solution domain is subdivided using a regular mesh arrangement of nodes with increments of  $\Delta x$  and  $\Delta y$  in the x- and the y-directions, respectively. The unknown variables, lower layer thickness,  $h_1$ , lower layer pressure,  $p_1$ , top layer thickness,  $h_2$ , and top layer pressure,  $p_2$  are located at grid nodes (I, J). Following Zhornitskaya and Bertozzi (2000), Kondic and Diez (2001), Gaskell et al. (2004b), Lee et al. (2007) and Veremieiev(2011) the corresponding coupled second-order accurate discretisation scheme for  $h_i$  and  $p_i$  can be written as:

$$\begin{aligned}
\frac{\partial h_{1I,J}}{\partial t} = & \frac{1}{3\mu_1} \left( \frac{h_{1I+1/2,J}^3 (p_{1I+1,J} - p_{1I,J}) - h_{1I-1/2,J}^3 (p_{1I,J} - p_{1I-1,J})}{\Delta x^2} \right) \\
& + \frac{1}{2\mu_2} \left( \frac{h_{1I+1/2,J}^2 h_{2I+1/2,J} (p_{2I+1,J} - p_{2I,J}) - h_{1I-1/2,J}^2 h_{2I-1/2,J} (p_{2I,J} - p_{2I-1,J})}{\Delta x^2} \right) \\
& + \frac{1}{3\mu_1} \left( \frac{h_{1I,J+1/2}^3 (p_{1I,J+1} - p_{1I,J}) - h_{1I,J-1/2}^3 (p_{1I,J} - p_{1I,J-1})}{\Delta y^2} \right) \\
& + \frac{1}{2\mu_2} \left( \frac{h_{1I,J+1/2}^2 h_{2I,J+1/2} (p_{2I,J+1} - p_{2I,J}) - h_{1I,J-1/2}^2 h_{2I,J-1/2} (p_{2I,J} - p_{2I,J-1})}{\Delta y^2} \right) \\
& - \frac{2\rho_1}{3\mu_1 C} \left( \frac{h_{1I+1/2,J}^3 - h_{1I-1/2,J}^3}{\Delta x} \right) - \frac{\rho_2}{\mu_2 C} \left( \frac{h_{1I+1/2,J}^2 h_{2I+1/2,J} - h_{1I-1/2,J}^2 h_{2I-1/2,J}}{\Delta x} \right),
\end{aligned} \tag{D.8}$$

$$\begin{aligned}
\frac{\partial h_{2I,J}}{\partial t} = & \frac{1}{2\mu_1} \left( \frac{h_{1I+1/2,J}^2 h_{2I+1/2,J} (p_{1I+1,J} - p_{1I,J}) - h_{1I-1/2,J}^2 h_{2I-1/2,J} (p_{1I,J} - p_{1I-1,J})}{\Delta x^2} \right) \\
& + \left( \frac{\left( \frac{h_{1I+1/2,J} h_{2I+1/2,J}^2}{\mu_1} + \frac{h_{2I+1/2,J}^3}{3\mu_2} \right) (p_{2I+1,J} - p_{2I,J}) - \left( \frac{h_{1I-1/2,J} h_{2I-1/2,J}^2}{\mu_1} + \frac{h_{2I-1/2,J}^3}{3\mu_2} \right) (p_{2I,J} - p_{2I-1,J})}{\Delta x^2} \right) \\
& + \frac{1}{2\mu_1} \left( \frac{h_{1I,J+1/2}^2 h_{2I,J+1/2} (p_{1I,J+1} - p_{1I,J}) - h_{1I,J-1/2}^2 h_{2I,J-1/2} (p_{1I,J} - p_{1I,J-1})}{\Delta y^2} \right) \\
& + \left( \frac{\left( \frac{h_{1I,J+1/2} h_{2I,J+1/2}^2}{\mu_1} + \frac{h_{2I,J+1/2}^3}{3\mu_2} \right) (p_{2I,J+1} - p_{2I,J}) - \left( \frac{h_{1I,J-1/2} h_{2I,J-1/2}^2}{\mu_1} + \frac{h_{2I,J-1/2}^3}{3\mu_2} \right) (p_{2I,J} - p_{2I,J-1})}{\Delta y^2} \right) \\
& - \frac{\rho_1}{\mu_1 C} \left( \frac{h_{1I+1/2,J}^2 h_{2I+1/2,J} - h_{1I-1/2,J}^2 h_{2I-1/2,J}}{\Delta x} \right) - \frac{2\rho_2}{\mu_1 C} \left( \frac{h_{1I+1/2,J} h_{2I+1/2,J}^2 - h_{1I-1/2,J} h_{2I-1/2,J}^2}{\Delta x} \right) \\
& - \frac{2\rho_2}{3\mu_2 C} \left( \frac{h_{2I+1/2,J}^3 - h_{2I-1/2,J}^3}{\Delta x} \right), \tag{D.9}
\end{aligned}$$

$$\begin{aligned}
p_{1I,J} = & -\frac{\varepsilon^3}{Ca} \sigma_{int} \left( \frac{f_{1I+1,J} + f_{1I-1,J} - 2f_{1I,J}}{\Delta x^2} + \frac{f_{1I,J+1} + f_{1I,J-1} - 2f_{1I,J}}{\Delta y^2} \right) \\
& - \frac{\varepsilon^3}{Ca} \sigma_2 \left( \frac{f_{2I+1,J} + f_{2I-1,J} - 2f_{2I,J}}{\Delta x^2} + \frac{f_{2I,J+1} + f_{2I,J-1} - 2f_{2I,J}}{\Delta y^2} \right) \tag{D.10} \\
& + \frac{2\varepsilon}{C} (\rho_1 f_{1I,J} + \rho_2 (f_{2I,J} - f_{1I,J})) \cot \theta,
\end{aligned}$$

$$\begin{aligned}
p_{2I,J} = & -\frac{\varepsilon^3}{Ca} \sigma_2 \left( \frac{f_{2I+1,J} + f_{2I-1,J} - 2f_{2I,J}}{\Delta x^2} + \frac{f_{2I,J+1} + f_{2I,J-1} - 2f_{2I,J}}{\Delta y^2} \right), \tag{D.11} \\
& + \frac{2\rho_2 \varepsilon}{C} f_{2I,J} \cot \theta
\end{aligned}$$

where the inter-nodes terms, sometimes referred to as prefactors, are computed

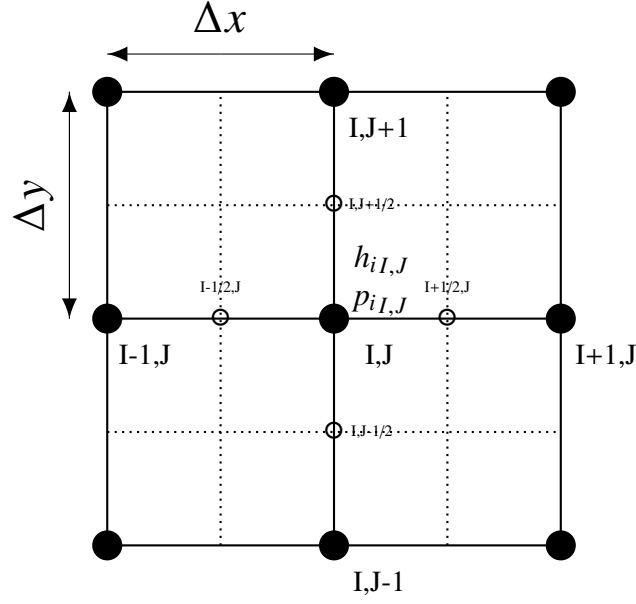


Figure D.1: Collocated mesh arrangement of variables for the LUB model.

using linear interpolation between the neighbouring nodes:

$$\begin{aligned}
 h_{iI\pm 1/2,J}^3 &= \frac{1}{2} (h_{iI,J}^3 + h_{iI\pm 1,J}^3), & h_{iI,J\pm 1/2}^3 &= \frac{1}{2} (h_{iI,J}^3 + h_{iI,J\pm 1}^3), \\
 h_{1I\pm 1/2,J}^2 h_{2I\pm 1/2,J} &= \frac{1}{2} (h_{1I,J}^2 h_{2I,J} + h_{1I\pm 1,J}^2 h_{2I\pm 1,J}), \\
 h_{1I,J\pm 1/2}^2 h_{2I,J\pm 1/2} &= \frac{1}{2} (h_{1I,J}^2 h_{2I,J} + h_{1I,J\pm 1}^2 h_{2I,J\pm 1}) & (D.12) \\
 h_{1I\pm 1/2,J} h_{2I\pm 1/2,J}^2 &= \frac{1}{2} (h_{1I,J} h_{2I,J}^2 + h_{1I\pm 1,J} h_{2I\pm 1,J}^2), \\
 h_{1I,J\pm 1/2} h_{2I,J\pm 1/2}^2 &= \frac{1}{2} (h_{1I,J} h_{2I,J}^2 + h_{1I,J\pm 1} h_{2I,J\pm 1}^2).
 \end{aligned}$$

Dirichlet boundary conditions are assigned as exact values at the boundary nodes, whereas Neumann boundary conditions are implemented by employing ghost nodes at the edge of the solution domain, namely:

$$h_{11,J} = h_{10}, \quad h_{21,J} = 1 - h_{10}, \quad (D.13)$$

$$h_{in_x+1,J} - h_{in_x-1,J} = 0, \quad h_{iI,2} - h_{iI,0} = 0, \quad h_{iI,n_y+1} - h_{iI,n_y-1} = 0, \quad (D.14)$$

$$p_{i2,J} - p_{i0,J} = 0, \quad p_{in_x+1,J} - p_{in_x-1,J} = 0, \quad (D.15)$$

$$p_{iI,2} - p_{iI,0} = 0, \quad p_{iI,n_y+1} - p_{iI,n_y-1} = 0, \quad (\text{D.16})$$

where  $n_x$  and  $n_y$  are the number of grid points in the  $x$  and the  $y$  directions, respectively. In order to simplify the description of the calculation procedure and to avoid writing lengthy expression, it is better to write the discretised equation in the following compact form:

$$\left. \frac{\partial h_i}{\partial t} \right|_{I,J} + \mathcal{M}_{I,J}^{h_i}(h_1, h_2, p_1, p_2) = 0, \quad (\text{D.17})$$

$$p_i|_{I,J} + \mathcal{M}_{I,J}^{p_i}(h_1, h_2) = 0. \quad (\text{D.18})$$

The locations where the independent variables  $(h_i, p_i)$  are stored are shown in Figure D.1.

## D.1.2 Temporal discretisation

As with the DAF, Chapter 3, an automatic adaptive time-stepping scheme is implemented into the solution strategy to optimise time step selection in order to reduce the computational resource requirements. The time-stepping procedure adopted uses the local truncation error estimates (LTE) obtained from the difference between a predictor stage and the current solution stage. Fully explicit second order time discretisation of equation (D.17) yields the following expression for the predicted values of  $h_{i\text{pr}}$  and  $p_{i\text{pr}}$ , Veremieiev *et al.* (2010):

$$h_{i\text{pr}}|_{I,J}^{n+1} = \gamma^2 h_{I,J}^{n-1} + (1 - \gamma^2) h_{I,J}^n - \Delta t^{n+1} (1 + \gamma) \mathcal{M}_{I,J}^{h_i}(h_1^n, h_2^n, p_1^n, p_2^n) \quad (\text{D.19})$$

$$p_{i\text{pr}}|_{I,J}^{n+1} + \mathcal{M}_{I,J}^{p_i}(h_1^n, h_2^n) = 0, \quad (\text{D.20})$$

where the superscript  $n$  denotes a value at the end of the  $n$ th time step  $t = t^n$  and  $\gamma = \frac{\Delta t^{n+1}}{\Delta t^n}$  is the ratio of successive time steps.

Adaptive time-stepping is performed by keeping the LTE for  $h_{2pr}$  within a pre-set tolerance to allow the size of time step to be increased in a controlled manner. A Taylor series expansion of equation (D.19) yields the following expression for the LTE for  $h_{2pr}$  in the predictor stage:

$$(LTE)_{pr}|_{I,j} = \frac{\Delta t^{n+1} \Delta t^n (1 + \gamma)}{6} \left. \frac{\partial^3 h_2}{\partial t^3} \right|_{I+\frac{1}{2},J}^{t^p}, \quad (D.21)$$

with the third-order time derivative term evaluated at time  $t^p \in (t^n, t^{n+1})$ . In the present work, an implicit and unconditionally stable Crank-Nicolson scheme, see Gaskell *et al.* (2004) and Veremieiev (2011), is used to march the solution forward in time:

$$h_{i,I,J}^{n+1} + \frac{\Delta t^{n+1}}{2} \mathcal{M}_{I,J}^{h_i}(h_1^{n+1}, h_2^{n+1}, p_1^{n+1}, p_2^{n+1}) = h_{i,I,J}^n - \frac{\Delta t^{n+1}}{2} \mathcal{M}_{I,J}^{h_i}(h_1^n, h_2^n, p_1^n, p_2^n), \quad (D.22)$$

$$p_{i,I,J}^{n+1} + \mathcal{M}_{I,J}^{p_i}(h_1^{n+1}, h_2^{n+1}) = 0. \quad (D.23)$$

The LTE for  $h$  at the solution stage,  $(LTE)_{sol}$ , is similarly given by a Taylor series expansion of equation (D.22):

$$(LTE)_{sol}|_{I,J} = -\frac{(\Delta t^{n+1})^3}{12} \left. \frac{\partial^3 h_2}{\partial t^3} \right|_{I,J}^{t^s}, \quad t^s \in (t^n, t^{n+1}). \quad (D.24)$$

As described in Chapra and Canale (2002), the assumption that the third-order derivative term varies only slightly over a time step makes it possible to estimate

the LTE as:

$$(LTE)_{I,J} = \frac{h_{2I,J}^{n+1} - h_{2prI,J}^{n+1}}{1 + 2(1 + \gamma)/\gamma}. \quad (D.25)$$

Following Dormand (1996), an estimate of the overall truncation error is obtained by finding the Euclidean norm of the above expression,  $\|LTE\|$ , which is used to specify the next time step  $\Delta t^{n+2}$  from:

$$\Delta t^{n+2} = 0.9 \Delta t^{n+1} \left( \frac{TOL}{\|LTE\|} \right)^{1/3}, \quad (D.26)$$

if  $\|LTE\| < TOL$ . The iteration is restarted with half the current time step if  $\|LTE\| > TOL$ , where TOL is a prescribed tolerance.

As with the DAF discretisation, Chapter 3, it is convenient to write the discrete LUB equations (D.22) and (D.23) by introducing a global time-dependant nonlinear operator, right-hand side function (defined by the solution on the previous time step) and solution vectors respectively:

$$\mathcal{N} \mathbf{u}^{n+1} = \mathbf{f} \mathbf{u}^n, \quad (D.27)$$

where:

$$\mathcal{N} = \begin{pmatrix} \mathcal{N}_{I,J}^{h_1} \\ \mathcal{N}_{I,J}^{h_2} \\ \mathcal{N}_{I,J}^{p_1} \\ \mathcal{N}_{I,J}^{p_2} \end{pmatrix}, \quad \mathbf{f} = \begin{pmatrix} \mathbf{f}_{I,J}^{h_1} \\ \mathbf{f}_{I,J}^{h_2} \\ 0 \\ 0 \end{pmatrix}, \quad \mathbf{u}^n = \begin{pmatrix} h_{1I,J}^n \\ h_{2I,J}^n \\ p_{1I,J}^n \\ p_{2I,J}^n \end{pmatrix}. \quad (D.28)$$

## D.2 Channel flow

For the two-dimensional channel flow problem two solution strategies can be employed, a direct solver and a multigrid solver-as described in Chapter 3. The first is based on solving the steady state equation,

$$\frac{\varepsilon^3}{Ca} \frac{\partial^3 (h_1 + s)}{\partial x^3} = \frac{f_{21} + f_{22}}{f_{21}f_{12} - f_{11}f_{22}} (Q_1 - f_{13}) - \frac{f_{11} + f_{12}}{f_{21}f_{12} - f_{11}f_{22}} (Q_2 - f_{23}) + (\rho_2 - \rho_1)B \left( \sin \theta - \varepsilon \cos \theta \frac{\partial (h_1 + s)}{\partial x} \right), \quad (D.29)$$

subject to the boundary conditions:

$$h_1|_{x=0} = h_{10}, \quad \left. \frac{\partial h_1}{\partial x} \right|_{x=0,l} = 0, \quad \left. \frac{\partial^3 h_1}{\partial x^3} \right|_{x=0,l} = 0 \quad (D.30)$$

using the MA42 subroutine (a successor of MA32) from the Harwell Subroutine Library (HSL). Equation (D.29) is solved for the only unknown  $h_1$ . The discretised form of equation (D.29) is obtained using second-order-accurate central differences:

$$\frac{\varepsilon^3 \sigma \text{int}}{Ca} \left( \frac{h_{1I+2} - 2h_{1I+1} + 2h_{1I-1} - h_{1I-2}}{2\Delta x^3} + \frac{s_{I+2} - 2s_{I+1} + 2s_{I-1} - s_{I-2}}{2\Delta x^3} \right) = \left( \frac{f_{21} + f_{22}}{f_{21}f_{12} - f_{11}f_{22}} (Q_1 - f_{13}) \right)_I - \left( \frac{f_{11} + f_{12}}{f_{21}f_{12} - f_{11}f_{22}} (Q_2 - f_{23}) \right)_I + (\rho_2 - \rho_1)B \left( \sin \theta - \varepsilon \cos \theta \frac{h_{1I+1} - h_{1I-1} + s_{I+1} - s_{I-1}}{2\Delta x} \right). \quad (D.31)$$

The solution domain  $x \in [0, l]$  is subdivided using a uniformly structured mesh with increment  $\Delta x$ . Dirichlet boundary conditions are assigned at boundary nodes,  $I = 1, n_x$ , while the Neumann boundary condition is implemented using ghost nodes

at the each end of the computational domain. Because the problem involves third order boundary conditions, two ghost nodes are required at each end of the solution domain,  $I = -1, 0, n_x + 1$  and  $n_x + 2$ . Thus the boundary conditions become:

$$h_{1I=1} = h_{10}, \quad (\text{D.32})$$

$$h_{1I=2} - h_{1I=0} = 0, \quad (\text{D.33})$$

$$h_{1I=n_x+1} - h_{1I=n_x-1} = 0 \quad (\text{D.34})$$

$$h_{1I=3} - 2h_{1I=2} + 2h_{1I=0} - h_{1I=-1} = 0. \quad (\text{D.35})$$

The second method of solution employed to solve the channel flow problem is the multigrid method. The time dependant set of governing equations is discretised in space and time as for the free-surface flow problem presented in Section D.1, giving:

$$\begin{aligned} \frac{\partial h_{1I}}{\partial t} = & \frac{1}{12\mu_1} \left( \frac{\left( h_{1I+1/2}^3 + \frac{3h_{1I+1/2}^3 h_{2I+1/2}}{\frac{\mu_2}{\mu_1} h_{1I+1/2} + h_{2I+1/2}} \right) (p_{1I+1} - p_{1I}) - \left( h_{1I-1/2}^3 + \frac{3h_{1I-1/2}^3 h_{2I-1/2}}{\frac{\mu_2}{\mu_1} h_{1I-1/2} + h_{2I-1/2}} \right) (p_{1I} - p_{1I-1})}{\Delta x^2} \right) \\ & + \frac{1}{4\mu_1} \left( \frac{\left( \frac{h_{1I+1/2}^2 h_{2I+1/2}^2}{\frac{\mu_2}{\mu_1} h_{1I+1/2} + h_{2I+1/2}} \right) (p_{2I+1} - p_{2I}) - \left( \frac{h_{1I-1/2}^2 h_{2I-1/2}^2}{\frac{\mu_2}{\mu_1} h_{1I-1/2} + h_{2I-1/2}} \right) (p_{2I} - p_{2I-1})}{\Delta x^2} \right) \\ & - \frac{\rho_1 B \sin \theta}{12\mu_1 \Delta x} \left( h_{1I+1/2}^3 - h_{1I-1/2}^3 + \frac{3h_{1I+1/2}^3 h_{2I+1/2}}{\frac{\mu_2}{\mu_1} h_{1I+1/2} + h_{2I+1/2}} - \frac{3h_{1I-1/2}^3 h_{2I-1/2}}{\frac{\mu_2}{\mu_1} h_{1I-1/2} + h_{2I-1/2}} \right) \\ & - \frac{\rho_2 B \sin \theta}{4\mu_1 \Delta x} \left( \frac{3h_{1I+1/2}^3 h_{2I+1/2}}{\frac{\mu_2}{\mu_1} h_{1I+1/2} + h_{2I+1/2}} - \frac{3h_{1I-1/2}^3 h_{2I-1/2}}{\frac{\mu_2}{\mu_1} h_{1I-1/2} + h_{2I-1/2}} \right) \\ & - \frac{\mu_2 u_t}{2\mu_1 \Delta x} \left( \frac{h_{1I+1/2}^2}{\frac{\mu_2}{\mu_1} h_{1I+1/2} + h_{2I+1/2}} - \frac{h_{1I-1/2}^2}{\frac{\mu_2}{\mu_1} h_{1I-1/2} + h_{2I-1/2}} \right), \end{aligned} \quad (\text{D.36})$$

$$p_{1I} = p_{2I} - \frac{\varepsilon^3}{Ca} \frac{(h_1 + s)_{I+1} + (h_1 + s)_{I-1} - 2(h_1 + s)_I}{\Delta x^2} + B \cos \theta (\rho_1 - \rho_2) (h_1 + s)_I, \quad (\text{D.37})$$

$$\begin{aligned} & \left( h_{2I} + \frac{\mu_2}{\mu_1} \frac{h_{1I} (h_{1I} + h_{2I})}{\frac{\mu_2}{\mu_1} h_{1I} + h_{2I}} \right) \frac{u_I}{2} - \frac{h_{1I}^2}{4\mu_1} \left( \frac{h_{1I}}{3} + \frac{h_{2I} (h_{1I} + h_{2I})}{\frac{\mu_2}{\mu_1} h_{1I} + h_{2I}} \right) \left( \frac{p_{1I} - p_{1I-1}}{\Delta x} - \rho_1 B \sin \theta \right) \\ & - \frac{h_{2I}^2}{4\mu_1} \left( \frac{\mu_2}{\mu_1} \frac{h_{2I}}{3} + \frac{h_{1I} (h_{1I} + h_{2I})}{\frac{\mu_2}{\mu_1} h_{1I} + h_{2I}} \right) \left( \frac{p_{2I} - p_{2I-1}}{\Delta x} - \rho_2 B \sin \theta \right) = Q_{total} \end{aligned} \quad (\text{D.38})$$

where  $h_{2I} = 1 - (h_1 + s)_I$ .

The boundary conditions are:

$$h_{1I=1} = h_{10}, \quad (\text{D.39})$$

$$h_{1I=n_x+1} - h_{1I=n_x-1} = 0, \quad (\text{D.40})$$

$$p_{iI=2} - p_{iI=0} = 0, \quad p_{iI=n_x+1} - p_{iI=n_x-1} = 0, \quad (\text{D.41})$$

where the boundary nodes are at  $I = 1, n_x$  and the ghost nodes at  $I = 0, n_x + 1$ . It is convenient to write the above discretised equations in the following form:

$$\frac{\partial h_1}{\partial t} \Big|_I + \mathcal{M}_I^{h_1}(h_1, p_1, p_2) = 0 \quad (\text{D.42})$$

$$p_i \Big|_I + \mathcal{M}_I^{p_i}(h_1, p_1, p_2) = 0 \quad (\text{D.43})$$

Temporal discetisation is performed, similar to the free-surface case, using an implicit and unconditionally stable Crank-Nicolson scheme to advance solution in time, namely:

$$h_{1I}^{n+1} + \frac{\Delta t^{n+1}}{2} \mathcal{M}_I^{h_1}(h_1^{n+1}, p_1^{n+1}, p_2^{n+1}) = h_{1I}^n - \frac{\Delta t^{n+1}}{2} \mathcal{M}_I^{h_1}(h_1^n, p_1^n, p_2^n), \quad (\text{D.44})$$

$$p_{iI}^{n+1} + \mathcal{M}_I^{p_i}(h_1^{n+1}, p_1^{n+1}, p_2^{n+1}) = 0 \quad (\text{D.45})$$

Adaptive time-stepping as presented in Section D.1.2 is utilised by keeping the LTE for  $h_{2pr}$  within a pre-set tolerance to allow the size of time step to be increased in a controlled manner.

Equations (D.44) and (D.45) are written in the form of (D.27) but now with:

$$\mathcal{N} = \begin{pmatrix} \mathcal{N}_I^{h_1} \\ \mathcal{N}_I^{p_1} \\ \mathcal{N}_I^{p_2} \end{pmatrix}, \quad \mathbf{f} = \begin{pmatrix} \mathbf{f}_I^{h_1} \\ 0 \\ 0 \end{pmatrix}, \quad \mathbf{u}^n = \begin{pmatrix} h_1^n \\ p_1^n \\ p_2^n \end{pmatrix}, \quad (\text{D.46})$$

### D.3 Full weighting restriction and interpolation operators

The restriction operator used to transfer information from one grid level to the next coarser one used in the present work is a *full weighting* restriction. The operator equations can be written for a one dimensional collocated grid as:

$$\Lambda_I^{k-1} = \frac{1}{4}(\Lambda_{2I-1}^k + 2\Lambda_{2I}^k + \Lambda_{2I+1}^k) \quad (\text{D.47})$$

where  $\Lambda$  is the quantity to be restricted from level  $k$  to level  $k - 1$  and the subscript refers to the nodal point position.

For a two dimensional grid, the restriction operator becomes a nine-point average, namely :

$$\Lambda_{I,J}^{k-1} = \frac{1}{16}(\Lambda_{2I-1,2J-1}^k + 2\Lambda_{2I,2J-1}^k + \Lambda_{2I+1,2J-1}^k + 2\Lambda_{2I-1,2J}^k + 4\Lambda_{2I,2J}^k + 2\Lambda_{2I+1,2J}^k + \Lambda_{2I-1,2J+1}^k + 2\Lambda_{2I,2J+1}^k + \Lambda_{2I+1,2J+1}^k) \quad (\text{D.48})$$

To transfer information from the coarse grid level to the next fine level, a bilinear interpolation operator is employed which, for a one dimensional grid, is written as:

$$\begin{aligned}\Lambda_{2I}^{k+1} &= \Lambda_I^k, \\ \Lambda_{2I\pm 1}^{k+1} &= \frac{1}{2}(\Lambda_I^k + \Lambda_{I\pm 1}^k),\end{aligned}\tag{D.49}$$

and for two dimensional grid as:

$$\begin{aligned}\Lambda_{2I,2J}^{k+1} &= \Lambda_{I,J}^k, \\ \Lambda_{2I\pm 1,2J}^{k+1} &= \frac{1}{2}(\Lambda_{I,J}^k + \Lambda_{I\pm 1,J}^k), \\ \Lambda_{2I,2J\pm 1}^{k+1} &= \frac{1}{2}(\Lambda_{I,J}^k + \Lambda_{I,J\pm 1}^k), \\ \Lambda_{2I\pm 1,2J\pm 1}^{k+1} &= \frac{1}{4}(\Lambda_{I,J}^k + \Lambda_{I\pm 1,J}^k + \Lambda_{I,J\pm 1}^k + \Lambda_{I\pm 1,J\pm 1}^k).\end{aligned}\tag{D.50}$$

## Appendix E

# Lubrication equations for three-dimensional free-surface N-layer thin film flow

We begin by deriving the lubrication equations for tri-layer flow. The governing equations in dimensionless form are:

$$\frac{\partial^2 u_i}{\partial z^2} = \frac{1}{\mu_i} \left( \frac{\partial p_i}{\partial x} - \frac{2\rho_i}{C} \right), \quad (\text{E.1})$$

$$\frac{\partial^2 v_i}{\partial z^2} = \frac{1}{\mu_i} \frac{\partial p_i}{\partial y}, \quad (\text{E.2})$$

$$\frac{\partial p_i}{\partial z} + 2\rho_i \varepsilon \cot \theta = 0, \quad (\text{E.3})$$

$$\frac{\partial u_i}{\partial x} + \frac{\partial v_i}{\partial y} + \frac{\partial w_i}{\partial z} = 0, \quad (\text{E.4})$$

and the boundary conditions:

$$z = f_0 \quad u_1 = 0, \quad v_1 = 0, \quad (\text{E.5})$$

$$z = f_1 \quad u_1 = u_2, \quad v_1 = v_2, \quad (\text{E.6})$$

$$\mu_1 \frac{\partial u_1}{\partial z} = \mu_2 \frac{\partial u_2}{\partial z}, \quad \mu_1 \frac{\partial v_1}{\partial z} = \mu_2 \frac{\partial v_2}{\partial z}, \quad (\text{E.7})$$

$$p_1 - p_2 = -\frac{\varepsilon^3}{Ca} \sigma_{12} \nabla^2 f_1, \quad (\text{E.8})$$

$$z = f_2 \quad u_2 = u_3, \quad v_2 = v_3, \quad (\text{E.9})$$

$$\mu_2 \frac{\partial u_2}{\partial z} = \mu_3 \frac{\partial u_3}{\partial z}, \quad \mu_2 \frac{\partial v_2}{\partial z} = \mu_3 \frac{\partial v_3}{\partial z}, \quad (\text{E.10})$$

$$p_2 - p_3 = -\frac{\varepsilon^3}{Ca} \sigma_{23} \nabla^2 f_2, \quad (\text{E.11})$$

$$z = f_3 \quad \frac{\partial u_3}{\partial z} = 0, \quad \frac{\partial v_3}{\partial z} = 0, \quad (\text{E.12})$$

$$p_3 = -\frac{\varepsilon^3}{Ca} \sigma_3 \nabla^2 f_3. \quad (\text{E.13})$$

Integrating equation (E.3) with respect to  $z$  for layer  $i$  from  $z$  to  $f_i$  and applying boundary conditions (E.8), (E.11) and (E.13) yields the following pressure equations:

$$p_1 = -\frac{\varepsilon^3}{Ca} (\sigma_{12} \nabla^2 f_1 + \sigma_{23} \nabla^2 f_2 + \sigma_3 \nabla^2 f_3) + \frac{2\varepsilon}{C} [\rho_1 f_1 + \rho_2 (f_2 - f_1) + \rho_3 (f_3 - f_2)] \cot \theta, \quad (\text{E.14})$$

$$p_2 = -\frac{\varepsilon^3}{Ca} (\sigma_{23} \nabla^2 f_2 + \sigma_3 \nabla^2 f_3) + \frac{2\varepsilon}{C} [\rho_2 f_2 + \rho_3 (f_3 - f_2)] \cot \theta, \quad (\text{E.15})$$

$$p_3 = -\frac{\varepsilon^3}{Ca} \sigma_3 \nabla^2 f_3 + \frac{2\rho_3 \varepsilon}{C} f_3 \cot \theta. \quad (\text{E.16})$$

Integrating equation (E.1) with respect to  $z$  yields:

$$\frac{\partial u_i}{\partial z} = \frac{1}{\mu_i} \left( \frac{\partial p_i}{\partial x} - \frac{2\rho_i}{C} \right) z + C_i, \quad (\text{E.17})$$

and integrating once more gives the velocity profile as:

$$u_i = \frac{1}{\mu_i} \left( \frac{\partial p_i}{\partial x} - \frac{2\rho_i}{C} \right) \frac{z^2}{2} + C_i z + C_{ii}. \quad (\text{E.18})$$

The six constant of integration are obtained by applying the appropriate boundary

conditions, namely:

$$C_1 = -\frac{1}{\mu_1} \left( \frac{\partial p_1}{\partial x} - \frac{2\rho_1}{C} \right) (h_1 + s) - \frac{1}{\mu_1} \left( \frac{\partial p_2}{\partial x} - \frac{2\rho_2}{C} \right) h_2 - \frac{1}{\mu_1} \left( \frac{\partial p_3}{\partial x} - \frac{2\rho_3}{C} \right) h_3, \quad (\text{E.19})$$

$$C_{11} = \frac{s}{\mu_1} \left( \frac{\partial p_1}{\partial x} - \frac{2\rho_1}{C} \right) \left( h_1 + \frac{s}{2} \right) + \frac{s}{\mu_1} \left( \frac{\partial p_2}{\partial x} - \frac{2\rho_2}{C} \right) h_2 + \frac{s}{\mu_1} \left( \frac{\partial p_3}{\partial x} - \frac{2\rho_3}{C} \right) h_3, \quad (\text{E.20})$$

$$C_2 = -\frac{1}{\mu_2} \left( \frac{\partial p_2}{\partial x} - \frac{2\rho_2}{C} \right) (h_2 + h_1 + s) - \frac{1}{\mu_2} \left( \frac{\partial p_3}{\partial x} - \frac{2\rho_3}{C} \right) h_3, \quad (\text{E.21})$$

$$C_{22} = -\frac{1}{2\mu_1} \left( \frac{\partial p_1}{\partial x} - \frac{2\rho_1}{C} \right) h_1^2 + \left( \frac{\partial p_2}{\partial x} - \frac{2\rho_2}{C} \right) \left( \frac{1}{2\mu_2} (2h_2 + h_1 + s) \right. \\ \left. (h_1 + s) - \frac{1}{\mu_1} h_1 h_2 \right) + \left( \frac{\partial p_3}{\partial x} - \frac{2\rho_3}{C} \right) \left( \frac{1}{\mu_2} h_3 (h_1 + s) - \frac{1}{\mu_1} h_1 h_3 \right), \quad (\text{E.22})$$

$$C_3 = -\frac{1}{\mu_3} \left( \frac{\partial p_3}{\partial x} - \frac{2\rho_3}{C} \right) (h_3 + h_2 + h_1 + s), \quad (\text{E.23})$$

$$C_{33} = -\frac{1}{2\mu_1} \left( \frac{\partial p_1}{\partial x} - \frac{2\rho_1}{C} \right) h_1^2 - \left( \frac{\partial p_2}{\partial x} - \frac{2\rho_2}{C} \right) \left( \frac{1}{\mu_1} h_2 h_1 + \frac{1}{2\mu_2} h_2^2 \right) + \\ \left( \frac{\partial p_3}{\partial x} - \frac{2\rho_3}{C} \right) \left( \frac{(h_2 + h_1 + s)(2h_3 + h_2 + h_1 + s)}{2\mu_3} - \frac{h_1 h_3}{\mu_1} - \frac{h_2 h_3}{\mu_2} \right). \quad (\text{E.24})$$

Substituting these constants of integration into equation (E.18) yields the following expression for the velocity profiles:

$$u_1 = \frac{1}{\mu_1} \left( \frac{\partial p_1}{\partial x} - \frac{2\rho_1}{C} \right) (z - s) \left( \frac{z - s}{2} - h_1 \right) \\ - \frac{1}{\mu_1} \left( \frac{\partial p_2}{\partial x} - \frac{2\rho_2}{C} \right) h_2 (z - s) - \frac{1}{\mu_1} \left( \frac{\partial p_3}{\partial x} - \frac{2\rho_3}{C} \right) h_3 (z - s), \quad (\text{E.25})$$

$$u_2 = -\frac{1}{2\mu_1} \left( \frac{\partial p_1}{\partial x} - \frac{2\rho_1}{C} \right) h_1^2 - \frac{1}{\mu_1} \left( \frac{\partial p_2}{\partial x} - \frac{2\rho_2}{C} \right) h_1 h_2 \\ - \frac{1}{\mu_1} \left( \frac{\partial p_3}{\partial x} - \frac{2\rho_3}{C} \right) h_1 h_3 + \frac{1}{\mu_2} \left( \frac{\partial p_2}{\partial x} - \frac{2\rho_2}{C} \right) (z - h_1 - s) \left( \frac{z - h_1 - s}{2} - h_2 \right) \\ - \frac{1}{\mu_2} \left( \frac{\partial p_3}{\partial x} - \frac{2\rho_3}{C} \right) (z - h_1 - s),$$

(E.26)

$$\begin{aligned}
u_3 = & -\frac{1}{2\mu_1} \left( \frac{\partial p_1}{\partial x} - \frac{2\rho_1}{C} \right) h_1^2 - \left( \frac{\partial p_2}{\partial x} - \frac{2\rho_2}{C} \right) \left( \frac{h_1 h_2}{\mu_1} + \frac{h_2^2}{2\mu_2} \right) - \left( \frac{\partial p_3}{\partial x} - \frac{2\rho_3}{C} \right) \left( \frac{h_1 h_3}{\mu_1} + \frac{h_2 h_3}{\mu_2} \right) \\
& + \frac{1}{\mu_3} \left( \frac{\partial p_3}{\partial x} - \frac{2\rho_3}{C} \right) (z - h_2 - h_1 - s) \left( \frac{z - h_2 - h_1 - s}{2} - h_3 \right).
\end{aligned} \tag{E.27}$$

Similarly, the spanwise velocities are:

$$v_1 = \frac{1}{\mu_1} \frac{\partial p_1}{\partial y} (z - s) \left( \frac{z - s}{2} - h_1 \right) - \frac{1}{\mu_1} \frac{\partial p_2}{\partial y} h_2 (z - s) - \frac{1}{\mu_1} \frac{\partial p_3}{\partial y} h_3 (z - s), \tag{E.28}$$

$$\begin{aligned}
v_2 = & -\frac{1}{2\mu_1} \frac{\partial p_1}{\partial y} h_1^2 - \frac{1}{\mu_1} \frac{\partial p_2}{\partial y} h_1 h_2 - \frac{1}{\mu_1} \frac{\partial p_3}{\partial y} h_1 h_3 + \frac{1}{\mu_2} \frac{\partial p_2}{\partial y} (z - h_1 - s) \\
& \left( \frac{z - h_1 - s}{2} - h_2 \right) - \frac{1}{\mu_2} \frac{\partial p_3}{\partial y} (z - h_1 - s),
\end{aligned} \tag{E.29}$$

$$\begin{aligned}
v_3 = & -\frac{1}{2\mu_1} \frac{\partial p_1}{\partial y} h_1^2 - \frac{\partial p_2}{\partial y} \left( \frac{h_1 h_2}{\mu_1} + \frac{h_2^2}{2\mu_2} \right) - \frac{\partial p_3}{\partial y} \left( \frac{h_1 h_3}{\mu_1} + \frac{h_2 h_3}{\mu_2} \right) \\
& + \frac{1}{\mu_3} \frac{\partial p_3}{\partial y} (z - h_2 - h_1 - s) \left( \frac{z - h_2 - h_1 - s}{2} - h_3 \right).
\end{aligned} \tag{E.30}$$

The flow rate through each layer in the streamwise and spanwise directions,  $q_{ix}$  and  $q_{iy}$ , are calculated by integrating the relevant velocity profile over the layer thickness, leading to:

$$q_{1x} = \int_{f_0}^{f_1} u_1 dz = -\frac{h_1^2}{\mu_1} \left[ \frac{h_1}{3} \left( \frac{\partial p_1}{\partial x} - \frac{2\rho_1}{C} \right) + \frac{h_2}{2} \left( \frac{\partial p_2}{\partial x} - \frac{2\rho_2}{C} \right) + \frac{h_3}{2} \left( \frac{\partial p_3}{\partial x} - \frac{2\rho_3}{C} \right) \right], \tag{E.31}$$

$$q_{1y} = \int_{f_0}^{f_1} v_1 dz = -\frac{h_1^2}{\mu_1} \left[ \frac{h_1}{3} \frac{\partial p_1}{\partial y} + \frac{h_2}{2} \frac{\partial p_2}{\partial y} + \frac{h_3}{2} \frac{\partial p_3}{\partial y} \right], \tag{E.32}$$

$$q_{2x} = \int_{f_1}^{f_2} u_2 dz = -\frac{h_1^2 h_2}{2\mu_1} \left( \frac{\partial p_1}{\partial x} - \frac{2\rho_1}{C} \right) - \left( \frac{h_1 h_2^2}{\mu_1} + \frac{h_2^3}{3\mu_2} \right) \left( \frac{\partial p_2}{\partial x} - \frac{2\rho_2}{C} \right) - \left( \frac{h_2^2 h_3}{\mu_2} + \frac{h_1 h_2 h_3}{\mu_1} \right) \left( \frac{\partial p_3}{\partial x} - \frac{2\rho_3}{C} \right), \quad (\text{E.33})$$

$$q_{2y} = \int_{f_1}^{f_2} v_2 dz = -\frac{h_1^2 h_2}{2\mu_1} \frac{\partial p_1}{\partial y} - \left( \frac{h_1 h_2^2}{\mu_1} + \frac{h_2^3}{3\mu_2} \right) \frac{\partial p_2}{\partial y} - \left( \frac{h_2^2 h_3}{\mu_2} + \frac{h_1 h_2 h_3}{\mu_1} \right) \frac{\partial p_3}{\partial y}, \quad (\text{E.34})$$

$$q_{3x} = \int_{f_2}^{f_3} u_3 dz = -\frac{h_1^2 h_3}{2\mu_1} \left( \frac{\partial p_1}{\partial x} - \frac{2\rho_1}{C} \right) - \left( \frac{h_2^2 h_3}{2\mu_2} + \frac{h_1 h_2 h_3}{\mu_1} \right) \left( \frac{\partial p_2}{\partial x} - \frac{2\rho_2}{C} \right) - \left( \frac{h_1 h_3^2}{\mu_1} + \frac{h_2 h_3^2}{\mu_2} + \frac{h_3^3}{3\mu_3} \right) \left( \frac{\partial p_3}{\partial x} - \frac{2\rho_3}{C} \right), \quad (\text{E.35})$$

$$q_{3y} = \int_{f_2}^{f_3} v_3 dz = -\frac{h_1^2 h_3}{2\mu_1} \frac{\partial p_1}{\partial y} - \left( \frac{h_2^2 h_3}{2\mu_2} + \frac{h_1 h_2 h_3}{\mu_1} \right) \frac{\partial p_2}{\partial y} - \left( \frac{h_1 h_3^2}{\mu_1} + \frac{h_2 h_3^2}{\mu_2} + \frac{h_3^3}{3\mu_3} \right) \frac{\partial p_3}{\partial y}. \quad (\text{E.36})$$

Substituting these expressions into equation (A.63) results in the following lubrication equations:

$$\frac{\partial h_1}{\partial t} - \frac{\partial}{\partial x} \left[ \frac{h_1^3}{3\mu_1} \left( \frac{\partial p_1}{\partial x} - \frac{2\rho_1}{C} \right) + \frac{h_1^2 h_2}{2\mu_1} \left( \frac{\partial p_2}{\partial x} - \frac{2\rho_2}{C} \right) + \frac{h_1^2 h_3}{2\mu_1} \left( \frac{\partial p_3}{\partial x} - \frac{2\rho_3}{C} \right) \right] - \frac{\partial}{\partial y} \left[ \frac{h_1^3}{3\mu_1} \frac{\partial p_1}{\partial y} + \frac{h_1^2 h_2}{2\mu_1} \frac{\partial p_2}{\partial y} + \frac{h_1^2 h_3}{2\mu_1} \frac{\partial p_3}{\partial y} \right] = 0, \quad (\text{E.37})$$

$$\begin{aligned}
\frac{\partial h_2}{\partial t} - \frac{\partial}{\partial x} \left[ \frac{h_1^2 h_2}{2\mu_1} \left( \frac{\partial p_1}{\partial x} - \frac{2\rho_1}{C} \right) + \left( \frac{h_1 h_2^2}{\mu_1} + \frac{h_2^3}{3\mu_2} \right) \left( \frac{\partial p_2}{\partial x} - \frac{2\rho_2}{C} \right) \right. \\
\left. + \left( \frac{h_2^2 h_3}{\mu_2} + \frac{h_1 h_2 h_3}{\mu_1} \right) \left( \frac{\partial p_3}{\partial x} - \frac{2\rho_3}{C} \right) \right] - \frac{\partial}{\partial y} \left[ \frac{h_1^2 h_2}{2\mu_1} \frac{\partial p_1}{\partial y} \right. \\
\left. + \left( \frac{h_1 h_2^2}{\mu_1} + \frac{h_2^3}{3\mu_2} \right) \frac{\partial p_2}{\partial y} + \left( \frac{h_2^2 h_3}{\mu_2} + \frac{h_1 h_2 h_3}{\mu_1} \right) \frac{\partial p_3}{\partial y} \right] = 0,
\end{aligned} \tag{E.38}$$

$$\begin{aligned}
\frac{\partial h_3}{\partial t} - \frac{\partial}{\partial x} \left[ \frac{h_1^2 h_3}{2\mu_1} \left( \frac{\partial p_1}{\partial x} - \frac{2\rho_1}{C} \right) + \left( \frac{h_2^2 h_3}{2\mu_2} + \frac{h_1 h_2 h_3}{\mu_1} \right) \left( \frac{\partial p_2}{\partial x} - \frac{2\rho_2}{C} \right) \right. \\
\left. + \left( \frac{h_1 h_3^2}{\mu_1} + \frac{h_2 h_3^2}{\mu_2} + \frac{h_3^3}{3\mu_3} \right) \left( \frac{\partial p_3}{\partial x} - \frac{2\rho_3}{C} \right) \right] - \frac{\partial}{\partial y} \left[ \frac{h_1^2 h_3}{2\mu_1} \frac{\partial p_1}{\partial y} \right. \\
\left. + \left( \frac{h_2^2 h_3}{3\mu_2} + \frac{h_1 h_2 h_3}{\mu_1} \right) \frac{\partial p_2}{\partial y} + \left( \frac{h_1 h_3^2}{\mu_1} + \frac{h_2 h_3^2}{\mu_2} + \frac{h_3^3}{3\mu_3} \right) \frac{\partial p_3}{\partial y} \right] = 0.
\end{aligned} \tag{E.39}$$

Having derived the lubrication equations for bi-layer and tri-layer thin film flows it is possible to use these equations alongside the single layer equations available in literature, see for example Gaskell *et al.* (2004), to derive a general set of equations for N-layer thin film flow. Following the pattern of the above argument the following general set of equations that governs the flow of a N-layer thin film over an inclined substrate containing topography is given by :

$$\frac{\partial h_l}{\partial t} + \nabla q_l = 0, \tag{E.40}$$

$$p_l = \frac{2\varepsilon \cot(\theta)}{C} \left( \rho_l f_l + \sum_{j=l+1}^n \rho_j h_j \right) - \frac{\varepsilon^3}{Ca} \sum_{j=1}^n (\sigma_j \nabla^2 f_j), \tag{E.41}$$

here  $l = 1$  to  $n$  where  $n$  is the number of layers;  $h_l$  is the thickness of layer  $l$ .

The flow rates for each fluid layer are calculated from:

$$q_{lx} = - \sum_{j=1}^{l-1} \left\{ \left( \frac{1}{2} \frac{h_j^2 h_l}{\mu_j} + \sum_{i=1}^{j-1} \frac{h_i h_j h_l}{\mu_i} \right) \left( \frac{\partial p_j}{\partial x} - \frac{2\rho_j}{C} \right) \right\} - \left( \frac{1}{3} \frac{h_l^3}{\mu_l} + \sum_{i=1}^{l-1} \frac{h_i h_l^2}{\mu_i} \right) \left( \frac{\partial p_l}{\partial x} - \frac{2\rho_l}{C} \right) - \sum_{j=l+1}^n \left\{ \left( \frac{1}{2} \frac{h_l^2 h_j}{\mu_l} + \sum_{i=1}^{l-1} \frac{h_i h_j h_l}{\mu_i} \right) \left( \frac{\partial p_j}{\partial x} - \frac{2\rho_j}{C} \right) \right\}, \quad (\text{E.42})$$

and

$$q_{ly} = - \sum_{j=1}^{l-1} \left\{ \left( \frac{1}{2} \frac{h_j^2 h_l}{\mu_j} + \sum_{i=1}^{j-1} \frac{h_i h_j h_l}{\mu_i} \right) \frac{\partial p_j}{\partial y} \right\} - \left( \frac{1}{3} \frac{h_l^3}{\mu_l} + \sum_{i=1}^{l-1} \frac{h_i h_l^2}{\mu_i} \right) \frac{\partial p_l}{\partial y} - \sum_{j=l+1}^n \left\{ \left( \frac{1}{2} \frac{h_l^2 h_j}{\mu_l} + \sum_{i=1}^{l-1} \frac{h_i h_j h_l}{\mu_i} \right) \frac{\partial p_j}{\partial y} \right\}, \quad (\text{E.43})$$

where  $f_j$  is the liquid-liquid interface between layer  $j$  and layer  $j + 1$  and  $\sigma_j$  is dimensionless interracial tension between liquid  $j$  and liquid  $j + 1$ . The position of interface is calculated from :

$$f_j = \sum_{i=1}^j h_i + s, \quad (\text{E.44})$$

where  $f_n$  represents the free surface. In the above expressions  $\sum_{k=a}^b f(k) = 0$  if  $a > b$  (empty sum).

# Bibliography

- AFSAR-SIDDIQUI, A.B., LUCKHAM, P.F. AND MATAR, O.K. (2004) Dewetting behavior of aqueous cationic surfactant solutions on liquid films. *Langmuir* **20**(18), 7575–7582.
- AHMED, G., SELLIER, M., LEE, Y.C., JERMY, M. AND TAYLOR, M. (2013) Modeling the spreading and sliding of power-law droplets. *Colloids Surf. A: Physicochem. Eng. Aspects* **432**, 2–7.
- ALBA, K., KHAYAT, R.E. AND PANDHER, R.S. (2008) Steady two-layer gravity-driven thin-film flow. *Phys. Rev. E* **77**(5), 056304.
- ALBA, K., LAURE, P. AND KHAYAT, R.E. (2011) Transient two-layer thin-film flow inside a channel. *Phys. Rev. E* **84**(2), 026320.
- ALEKSEENKO, S.V., NAKORYAKOV, V.E. AND POKUSAEV, B.G. (1994) *Wave Flow of Liquid Films*. 3 edn, Begell House, New York.
- AMAUCHE, M., MEHIDI, N. AND AMATOUSSE, N. (2005) An accurate modeling of thin film flows down an incline for inertia dominated regimes. *Eur. Phys. J. B.* **24**(1), 49–70.
- AMAUCHE, M., MEHIDI, N. AND AMATOUSSE, N. (2007) Linear stability of a two-layer film flow down an inclined channel: A second-order weighted residual approach. *Phys. Fluids* **19**(8), 084106.
- ANCEY, C. (2007) Plasticity and geophysical flows: A review. *J. Non-Newton. Fluid Mech.* **142**(1-3), 4–35.
- ARGYRIADI, K., VLACHOGIANNIS, M. AND BONTOZOGLOU, V. (2006) Experimental study of inclined film flow along periodic corrugations: The effect of wall steepness. *Phys. Fluids* **18**(1), 15.
- ARGYROS, I. (2007) *Computational theory of iterative methods*. Vol. 15, Elsevier.
- BALMFORTH, N.J., CRASTER, R.V. AND TONIOLO, C. (2003) Interfacial instability in non-newtonian fluid layers. *Phys. Fluids* **15**(11), 3370–3384.
- BANDYOPADHYAY, D. AND SHARMA, A. (2008) Dewetting pathways and morphology of unstable thin liquid bilayers. *J. Phys. Chem. B* **112**(37), 11564–11572.

- BANDYOPADHYAY, D. AND SHARMA, A. (2010) Self-organized microstructures in thin bilayers on chemically patterned substrates. *J. Phys. Chem. C* **114**(5), 2237–2247.
- BARET, J.C. AND DECRÉ, M.M.J. (2000) Gravity driven flows over two-dimensional topographies: Measurement of the free surface using phase stepped interferometry. Unclassified report: NL-UR 2000/829, Philips Research.
- BAXTER, S.J., POWER, H., CLIFFE, K.A. AND HIBBERD, S. (2009) Three-dimensional thin film flow over and around an obstacle on an inclined plane. *Phys. Fluids* **21**(3), 032102.
- BAXTER, S.J., POWER, H., CLIFFE, K.A. AND HIBBERD, S. (2010) Free surface Stokes flows obstructed by multiple obstacles. *Int. J. Num. Meth. Fl.* **62**(5), 530–564.
- BENJAMIN, T.B. (1957) Wave formation in laminar flow down an inclined plane. *J. Fluid Mech.* **2**(6), 554–574.
- BENNEY, D.J. (1966) Long waves in liquid films. *J. Math. Phys.* **45**(2), 150–155.
- BERTOZZI, A.L. AND BRENNER, M.P. (1997) Linear stability and transient growth in driven contact lines. *Phys. Fluids* **9**(3), 530–539.
- BIELARZ, C. AND KALLIADASIS, S. (2003) Time-dependent free-surface thin film flows over topography. *Phys. Fluids* **15**(9), 2512–2524.
- BIRD, R.B. (1976) Useful non-newtonian models. *Annu. Rev. Fluid Mech.* **8**(1), 13–34.
- BLYTH, M.G. AND POZRIKIDIS, C. (2004) Effect of surfactant on the stability of film flow down an inclined plane. *J. Fluid Mech.* **521**, 241–250.
- BLYTH, M.G. AND POZRIKIDIS, C. (2006) Film flow down an inclined plane over a three-dimensional obstacle. *Phys. Fluids* **18**(5), 052104.
- BONTOZOGLU, V. AND SERIFI, K. (2008) Falling film flow along steep two-dimensional topography: The effect of inertia. *Int. J. Multiphas. Flow* **34**(8), 734–747.
- BRANDT, A. (1977) Multi-level adaptive solutions to boundary-value problems. *Math. compu.* **31**(138), 333–390.
- BRANDT, A. (1982) Guide to multigrid development. In: *Multigrid methods* Springer, pp. 220–312.
- BRIGGS, W.L., HENSON, V.E. AND McCORMICK, S.F. (2000) *A Multigrid Tutorial*. 2 edn, SIAM.
- CARREAU, P.J. (1972) Rheological equations from molecular network theories. *Trans. Soc. Rheology (1957-1977)* **16**(1), 99–127.

- CHANG, H.C. (1986) Traveling waves on fluid interfaces: Normal form analysis of the kuramoto-sivashinsky equation. *Phys. Fluids* **29**(10), 3142–3147.
- CHAPRA, S.C. AND CANALE, R.P. (2002) *Numerical Methods for Engineers*. 4 edn, McGraw-Hill, New York.
- CHEN, K. (1993) Wave formation in the gravity-driven low-reynolds number flow of two liquid films down an inclined plane. *Phys. Fluids A* **5**(12), 3038–3048.
- CHHABRA, R.P. AND RICHARDSON, J.F. (2011) *Non-Newtonian flow and applied rheology: engineering applications*. Butterworth-Heinemann.
- CHRISTOV, C.I., PONTES, J., WALGRAEF, D. AND VELARDE, M.G. (1997) Implicit time splitting for fourth-order parabolic equations. *Comp. Meth. Appl. Mech. Engrg.* **148**(3-4), 209–224.
- CHUNG, T.J. (2002) *Computational Fluid Dynamics*. Cambridge University Press, Cambridge.
- COWLING, N.P., GASKELL, P.H., LEE, Y.C. AND THOMPSON, H.M. (2011) Towards the efficient numerical solution of three-dimensional thin film flows on real surfaces: an evolution of finite-difference based schemes. *Proc. I. Mech. E. part C, J. Mech. Sci.* p. 0954406211399852.
- CRASTER, R.V. AND MATAR, O.K. (2009) Dynamics and stability of thin liquid films. *Rev. Mod. Phys.* **81**(3), 1131–1198.
- D’ALESSIO, S.J.D., PASCAL, J.P. AND JASMINE, H.A. (2009) Instability in gravity-driven flow over uneven surfaces. *Phys. Fluids* **21**(6), 062105.
- D’ALESSIO, S.J.D., PASCAL, J.P., JASMINE, H.A. AND OGDEN, K.A. (2010) Film flow over heated wavy inclined surfaces. *J. Fluid Mech.* **665**, 418–456.
- DANOV, K.D., PAUNOV, V.N., ALLEBORN, N., RASZILLIER, H. AND DURST, F. (1998) Stability of evaporating two-layered liquid film in the presence of surfactant—i. the equations of lubrication approximation. *Chem. Eng. Sci.* **53**(15), 2809–2822.
- DANOV, K.D., PAUNOV, V.N., STOYANOV, S.D., ALLEBORN, N., RASZILLIER, H. AND DURST, F. (1998) Stability of evaporating two-layered liquid film in the presence of surfactant—ii. linear analysis. *Chem. Eng. Sci.* **53**(15), 2823–2837.
- DASSORI, C.G., DEIBER, J.A. AND CASSANO, A.E. (1984) Slow two-phase flow through a sinusoidal channel. *Int. J. Multiphas. Flow* **10**(2), 181–193.
- DATE, A.W. (1993) Solution of navier-stokes equations on non-staggered grid *Int. J. Heat Mass Trans.* **36**(7), 1913–1922.
- DAVIS, J.M. AND TROIAN, S.M. (2005) Generalized linear stability of noninertial coating flows over topographical features. *Phys. Fluids* **17**(7).

- DAVIS, S.H. (1987) Thermocapillary instabilities. *Annu. Rev. Fluid Mech.* **19**, 403–435.
- DE SANTOS, J.M., MELLI, T.R. AND SCRIVEN, L.E. (1991) Mechanics of gas-liquid flow in packed-bed contactors. *Annu. Rev. Fluid Mech.* **23**, 233–260.
- DECRÉ, M.M.J. AND BARET, J.C. (2003) Gravity-driven flows of viscous liquids over two-dimensional topographies. *J. Fluid Mech.* **487**, 147–166.
- DORMAND, J.R. (1996) *Numerical Methods for Differential Equations Computational Approach*. CRC Press, Boca Raton.
- ERES, M.H., SCHWARTZ, L.W. AND ROY, R.V. (2000) Fingering phenomena for driven coating films. *Phys. Fluids* **12**(6), 1278–1295.
- FERNANDEZ PARENT, C., LAMMERS, J.H. AND DECRÉ, M.M.J. (1998) Flow of a gravity driven thin liquid film over one-dimensional topographies. Unclassified report: NL-UR 823/98, Philips Research.
- FOCKE, W.W. AND KNIBBE, P.G. (1986) Flow visualization in parallel-plate ducts with corrugated walls. *J. Fluid Mech.* **165**, 73–77.
- GASKELL, P.H., JIMACK, P.K., SELIER, M. AND THOMPSON, H.M. (2006) Flow of evaporating, gravity-driven thin liquid films over topography. *Phys. Fluids* **18**(1), 013601.
- GASKELL, P.H., JIMACK, P.K., SELIER, M., THOMPSON, H.M. AND WILSON, M.C.T. (2004) Gravity-driven flow of continuous thin liquid films on non-porous substrates with topography. *J. Fluid Mech.* **509**, 253–280.
- GASKELL, P.H., LEE, Y.C. AND THOMPSON, H.M. (2010) Thin film flow over and around surface topography: a general solver for the long-wave approximation and related equations. *CMES-Comp. Model. Eng. Sci.* **62**(1), 77–112.
- GATES, B.D., XU, Q., STEWART, M., RYAN, D., WILLSON, C.G. AND WHITESIDES, G.M. (2005) New approaches to nanofabrication: molding, printing, and other techniques. *Chem Rev.* **105**(4), 1171–1196.
- GLASS, C.R., WALTERS, K.F.A., GASKELL, P.H., LEE, Y.C., THOMPSON, H.M., EMERSON, D.R. AND GU, X.J. (2010) Recent advances in computational fluid dynamics relevant to the modelling of pesticide flow on leaf surfaces. *Pest Manag. Sci.* **66**(1), 2–9.
- GRAMLICH, C.M., KALLIADASIS, S., HOMSY, G.M. AND MESSER, C. (2002) Optimal leveling of flow over one-dimensional topography by Marangoni stresses. *Phys. Fluids* **14**(6), 1841–1850.
- GROTBERG, J.B. (1994) Pulmonary flow and transport phenomena. *Annu. Rev. Fluid Mech.* **26**, 529–571.

- GROTBERG, J.B. (2001) Respiratory fluid mechanics and transport processes. *Annu. Rev. Biomed. Eng.* **3**, 421–457.
- GU, F., LIU, C.J., YUAN, X.G. AND YU, G.C. (2004) CFD simulation of liquid film flow on inclined plates. *Chem. Eng. Technol.* **27**(10), 1099–1104.
- HAN, C. (2012) *Multiphase flow in polymer processing*. Elsevier.
- HARLOW, F.H., WELCH, J.E. ET AL. (1965) Numerical calculation of time-dependent viscous incompressible flow of fluid with free surface. *Phys. Fluids* **8**(12), 2182.
- HAYES, M., O'BRIEN, S.B.G. AND LAMMERS, J.H. (2000) Green's function for steady flow over a small two-dimensional topography. *Phys. Fluids* **12**(11), 2845–2858.
- HEINING, C. (2009) Influence of two- and three-dimensional topography on viscous gravity-driven film flow. PhD thesis, University of Bayreuth.
- HEINING, C. AND AKSEL, N. (2009) Bottom reconstruction in thin-film flow over topography: Steady solution and linear stability. *Phys. Fluids* **21**(8), 083605.
- HEINING, C., POLLAK, T. AND AKSEL, N. (2012) Pattern formation and mixing in three-dimensional film flow. *Phys. Fluids* **24**(4), 042102.
- HELBIG, K., NASAREK, R., GAMBARYAN-ROISMAN, T. AND STEPHAN, P. (2009) Effect of longitudinal minigrooves on flow stability and wave characteristics of falling liquid films. *J. Heat Trans.-T. ASME* **131**(1), 011601.
- HELFRICH, K.R. AND MELVILLE, W.K. (2006) Long nonlinear internal waves. *Annu. Rev. Fluid Mech.* **38**, 395–425.
- HO, W.K., TAY, A., LEE, L.L. AND SCHAPER, C.D. (2004) On control of resist film uniformity in the microlithography process. *Control Eng. Pract.* **12**(7), 881–892.
- HU, J., MILLET, S., BOTTON, V., HADID, H.B. AND HENRY, D. (2006) Inertialess temporal and spatio-temporal stability analysis of the two-layer film flow with density stratification. *Phys. Fluids* **18**(10), 104101.
- HU, J., YIN, X.Y., HADID, H.B. AND HENRY, D. (2008) Linear temporal and spatiotemporal stability analysis of two-layer falling films with density stratification. *Phys. Rev. E* **77**(2), 026302.
- IRGENS, F. (2014) *Rheology and Non-Newtonian Fluids*. Springer.
- ISRAELACHVILI, J.N. (2011) *Intermolecular and surface forces: revised third edition*. Academic press.
- JENSEN, O.E. AND GROTBERG, J.B. (1993) The spreading of heat or soluble surfactant along a thin liquid film. *Phys. Fluids A* **5**(1), 58–68.

- KALLIADASIS, S., BIELARZ, C. AND HOMSY, G.M. (2000) Steady free-surface thin film flows over topography. *Phys. Fluids* **12**(8), 1889–1898.
- KALLIADASIS, S. AND HOMSY, G.M. (2001) Stability of free-surface thin-film flows over topography. *J. Fluid Mech.* **448**, 387–410.
- KANG, H., LEE, S.-H., KIM, S. AND CHAR, K. (2003) Dewetting and layer inversion of inverted pvp/ps bilayer films. *Macromolecules* **36**(23), 8579–8583.
- KAO, T.W. (1965) Stability of two-layer viscous stratified flow down an inclined plane. *Phys. Fluids* **8**(5), 812–820.
- KAO, T.W. (1968) Role of viscosity stratification in the stability of two-layer flow down an incline. *J. Fluid Mech.* **33**(03), 561–572.
- KHAYAT, R.E. AND TIAN, G. (2009) Steady two-layer flow in narrow channels of variable width. *Phys. Rev. E* **79**(4), 046326.
- KISTLER, S.F. AND SCHWEIZER, P.M (EDS.) (1997) *Liquid Film Coating*. Chapman and Hall.
- KONNUR, R., KARGUPTA, K. AND SHARMA, A. (2000) Instability and morphology of thin liquid films on chemically heterogeneous substrates. *Phys. Rev. Lett.* **84**(5), 931.
- LEE, Y.C., THOMPSON, H.M. AND GASKELL, P.H. (2007) An efficient adaptive multi-grid algorithm for predicting thin film flow on surfaces containing localised topographic features. *Comput. Fluids* **36**(5), 838–855.
- LEE, Y.C., THOMPSON, H.M. AND GASKELL, P.H. (2009a) FILMPAR: A parallel algorithm designed for the efficient and accurate computation of thin film flow on functional surfaces containing micro-structure. *Comput. Phys. Commun.* **180**(12), 2634–2649.
- LEE, Y.C., THOMPSON, H.M. AND GASKELL, P.H. (2009b) Thin film flow over flexible membranes containing surface texturing: bio-inspired solutions. *Proc. I. Mech. E. part J, J. Eng. Tribol.* **223**(J3), 337–345.
- LEE, Y.C., THOMPSON, H.M. AND GASKELL, P.H. (2011) Dynamics of thin film flow on flexible substrate. *Chem. Eng. Process.: Process Intens.* **50**(5), 525–530.
- LEENAARS, A.F.M., HUETHORST, J.A.M. AND VAN OEKEL, J.J. (1990) Marangoni drying: a new extremely clean drying process. *Langmuir* **6**(11), 1701–1703.
- LENZ, R.D. AND KUMAR, S. (2007) Steady two-layer flow in a topographically patterned channel. *Phys. Fluids* **19**, 102103.
- LIN, S.P. (1974) Finite amplitude side-band stability of a viscous film. *J. Fluid Mech.* **63**(3), 417–429.

- LIU, J. AND GOLLUB, J.P. (1993) Onset of spatially chaotic waves on flowing films. *Phys. Rev. Lett.* **70**(15), 2289–2292.
- LIU, J. AND GOLLUB, J.P. (1994) Solitary wave dynamics of film flows. *Phys. Fluids* **6**(5), 1702–1712.
- LIU, J., PAUL, J.D. AND GOLLUB, J.P. (1993) Measurements of the primary instabilities of film flows. *J. Fluid Mech.* **250**, 69–101.
- LOEWENHERZ, D.S. AND LAWRENCE, C.J. (1989) The effect of viscosity stratification on the stability of a free surface flow at low reynolds number. *Phys. Fluids A* **1**(10), 1686–1693.
- LUCEA, M., DECREÉ, M.M.J. AND LAMMERS, J.H. (1999) Flow of a gravity driven thin liquid film over one-dimensional topographies: A detailed comparison of theory and experiments. Unclassified report: NL-UR 823/98, Philips Research.
- LUO, H. AND POZRIKIDIS, C. (2006) Effect of inertia on film flow over oblique and three-dimensional corrugations. *Phys. Fluids* **18**(12), 078107.
- LUO, H. AND POZRIKIDIS, C. (2007) Gravity-driven film flow down an inclined wall with three-dimensional corrugations. *Acta Mech.* **188**(3-4), 209–225.
- MALAMATARIS, N.A. AND BONTOZOGLOU, V. (1999) Computer aided analysis of viscous film flow along an inclined wavy wall. *J. Comput. Phys.* **154**(2), 372–392.
- MALAMATARIS, N.A., VLACHOGIANNIS, M. AND BONTOZOGLOU, V. (2002) Solitary waves on inclined films: Flow structure and binary interactions. *Phys. Fluids* **14**(3), 1082–1094.
- MARRA, J. AND HUETHORST, J.A.M. (1991) Physical principles of marangoni drying. *Langmuir* **7**(11), 2748–2755.
- MATAR, O.K., CRASTER, R.V. AND KUMAR, S. (2007) Falling films on flexible inclines. *Phys. Rev. E* **76**(5).
- MATAR, O.K., LAWRENCE, C.J. AND SISOEV, G.M. (2007) Interfacial dynamics in pressure-driven two-layer laminar channel flow with high viscosity ratios. *Phys. Rev. E* **75**(5), 056314.
- MAZOUCHI, A. AND HOMSY, G.M. (2001) Free surface Stokes flow over topography. *Phys. Fluids* **13**(10), 2751–2761.
- MELAAEN, M.C. (1992) Calculation of fluid flows with staggered and nonstaggered curvilinear nonorthogonal grids—a comparison *Num. Heat Trans. B* **21**(1), 21–39.
- MESSÉ, S. AND DECREÉ, M.M.J. (1997) Experimental study of a gravity driven water film flowing down inclined plates with different patterns. Unclassified report: NL-UR 030/97, Philips Research.

- MILADINOVA, S., LEBON, G. AND TOSHEV, E. (2004) Thin-film flow of a power-law liquid falling down an inclined plate. *J. non-Newton. fluid mech.* **122**(1), 69–78.
- MILLET, S., BOTTON, V., HADID, H.B., HENRY, DA. AND ROUSSET, F. (2013) Stability of two-layer shear-thinning film flows. *Phys. Rev. E* **88**(4), 043004.
- MYERS, T.G. (1998) Thin films with high surface tension. *Int. J. Math. Anal.* **40**(3), 441–462.
- MYERS, T.G. (2005) Application of non-newtonian models to thin film flow. *Phys. Rev. E* **72**(6), 066302.
- NAKAYA, C. (1975) Long waves on a thin fluid layer flowing down an inclined plane. *Phys. Fluids* **18**(11), 1407–1412.
- NGUYEN, L.T. AND BALAKOTAIAH, V. (2000) Modeling and experimental studies of wave evolution on free falling viscous films. *Phys. Fluids* **12**(9), 2236–2256.
- O'BRIEN, S.B.G.M. (1993) On marangoni drying: nonlinear kinematic waves in a thin film. *J. Fluid Mech.* **254**, 649–670.
- ORON, A., DAVIS, S.H. AND BANKOFF, S.G. (1997) Long-scale evolution of thin liquid films. *Rev. Mod. Phys.* **69**(3), 931–980.
- PANDHER, R.S. AND KHAYAT, R.E. (2011) Transient two-layer thin-film flow. *Int. J. Num. Meth. Fl.* **66**(5), 581–607.
- PATANKAR, S. (1980) *Numerical heat transfer and fluid flow*. CRC Press.
- PAUNOV, V.N., DANOV, K.D., ALLEBORN, N., RASZILLIER, H. AND DURST, F. (1998) Stability of evaporating two-layered liquid film in the presence of surfactant—iii. non-linear stability analysis. *Chem. Eng. Sci.* **53**(15), 2839–2857.
- PERAZZO, C.A. AND GRATTON, J. (2003) Thin film of non-newtonian fluid on an incline. *Phys. Rev. E* **67**(1), 016307.
- PERIĆ, M., KESSLER, R. AND SCHEUERER, G. (1988) Comparison of finite-volume numerical methods with staggered and collocated grids *Comput. Fluids* **16**(4), 389–403.
- PEURRUNG, L.M. AND GRAVES, D.B. (1991) Film thickness profiles over topography in spin coating. *J. Electrochem. Soc.* **138**(7), 2115–2124.
- PEURRUNG, L.M. AND GRAVES, D.B. (1993) Spin coating over topography. *IEEE Trans. Semicond. Manu.* **6**(1), 72–76.
- POTOTSKY, A., BESTEHORN, M., MERKT, D. AND THIELE, U. (2005) Morphology changes in the evolution of liquid two-layer films. *J. Chem. Phys.* **122**(22), 224711.

- POZRIKIDIS, C. (1988) The flow of a liquid film along a periodic wall. *J. Fluid Mech.* **188**, 275–300.
- POZRIKIDIS, C. (2003) Effect of surfactants on film flow down a periodic wall. *J. Fluid Mech.* **496**, 105–127.
- POZRIKIDIS, C. AND THORODDSEN, S.T. (1991) The deformation of a liquid-film flowing down an inclined plane wall over a small particle arrested on the wall. *Phys. Fluids A* **3**(11), 2546–2558.
- PRITCHARD, W.G., SCOTT, L.R. AND TAVENER, S.J. (1992) Numerical and asymptotic methods for certain viscous free-surface flows. *Philos. T. Roy. Soc. A* **340**(1656), 1–45.
- RAMASWAMY, B., CHIPPADA, S. AND JOO, S.W. (1996) A full-scale numerical study of interfacial instabilities in thin-film flows. *J. Fluid Mech.* **325**, 163–194.
- REISFELD, B. AND BANKOFF, S.G. (1990) Nonlinear stability of a heated thin liquid film with variable viscosity. *Phys. Fluids A* **2**(11), 2066–2067.
- RHIE, C.M. AND CHOW, W.L. (1983) Numerical study of the turbulent flow past an airfoil with trailing edge separation *AIAA journal* **21**(11), 1525–1532.
- ROUSSET, F., MILLET, S., BOTTON, V. AND HADID, H.B. (2007) Temporal stability of carreau fluid flow down an incline. *J. Fluid. Eng.-T. ASME* **129**(7), 913–920.
- RUCKENSTEIN, E. AND JAIN, R.K. (1974) Spontaneous rupture of thin liquid films. *J. Chem. Soc. Faraday Trans. 2: Molec. Chem. Phys.* **70**, 132–147.
- RUYER-QUIL, C. AND MANNEVILLE, P. (1998) Modeling film flows down inclined planes. *Eur. Phys. J. B.* **6**(2), 277–292.
- RUYER-QUIL, C. AND MANNEVILLE, P. (2000) Improved modeling of flows down inclined planes. *Eur. Phys. J. B.* **15**(2), 357–369.
- RUYER-QUIL, C. AND MANNEVILLE, P. (2002) Further accuracy and convergence results on the modeling of flows down inclined planes by weighted-residual approximations. *Phys. Fluids* **14**(1), 170–183.
- SAPRYKIN, S., KOOPMANS, R.J. AND KALLIADASIS, S. (2007) Free-surface thin-film flows over topography: influence of inertia and viscoelasticity. *J. Fluid Mech.* **578**, 271–293.
- SCHLICHTING, H. AND GERSTEN, K. (2000) *Boundary-layer theory*. Springer.
- SCHNEIDER, G.E. AND RAW, M.J. (1987) Control volume finite-element method for heat transfer and fluid flow using collocated variables—1. computational procedure *Num. Heat Trans. A* **11**(4), 363–390.

- SCHOLLE, M. AND AKSEL, N. (2007) A general free surface rule for Stokes flow of fluid films over obstacles. *Acta Mech.* **191**(3-4), 155–159.
- SCHOLLE, M., HAAS, A., AKSEL, N., WILSON, M.C.T., THOMPSON, H.M. AND GASKELL, P.H. (2008) Competing geometric and inertial effects on local flow structure in thick gravity-driven fluid films. *Phys. Fluids* **20**(12), 123101.
- SCHOLLE, M., RUND, A. AND AKSEL, N. (2006) Drag reduction and improvement of material transport in creeping films. *Arch. Appl. Mech.* **75**(2-3), 93–112.
- SCHOLLE, M., WIERSCHEM, A. AND AKSEL, N. (2004) Creeping films with vortices over strongly undulated bottoms. *Acta Mech.* **168**(3-4), 167–193.
- SCHWARTZ, L.W. AND ELEY, R.R. (1998) Simulation of droplet motion on low-energy and heterogeneous surfaces. *J. Colloid Interf. Sci.* **202**(1), 173–188.
- SCHWARTZ, L.W., ROY, R.V., ELEY, R.R. AND PETRASH, S. (2001) Dewetting patterns in a drying liquid film. *J. Colloid Interf. Sci.* **234**(2), 363–374.
- SCOTT, J.A. (2004) Ma42 element—a state-of-the-art frontal solver for finite-element applications. Technical report, Council for the Central Laboratory of the Research Councils.
- SCRIVEN, L.E. AND STERNLING, C.V. (1960) The marangoni effects. *Nature* **187**, 186–188.
- SELLIER, M. (2003) The numerical simulation of thin film flow over heterogeneous substrates. PhD thesis, University of Leeds.
- SELLIER, M. (2008) Substrate design or reconstruction from free surface data for thin film flows. *Phys. Fluids* **20**(6), 062106.
- SELLIER, M., LEE, Y.C., THOMPSON, H.M. AND GASKELL, P.H. (2009) Thin film flow on surfaces containing arbitrary occlusions. *Comput. Fluids* **38**(1), 171–182.
- SELLIER, M. AND PANDA, S. (2010) Beating capillarity in thin film flows. *Int. J. Num. Meth. Fl.* **63**(4), 431–448.
- SHARMA, A, KONNUR, R. AND KARGUPTA, K. (2003) Thin liquid films on chemically heterogeneous substrates: self-organization, dynamics and patterns in systems displaying a secondary minimum. *Phy. A Stat. Mech. App.* **318**(1–2), 262 – 278.
- SHEU, T.W.H. AND LIN, R.K. (2003) An incompressible navier-stokes model implemented on nonstaggered grids *Num. Heat Trans. B* **44**(3), 277–394.
- SHKADOV, V.Y. (1967) Wave flow regimes of a thin layer of viscous fluid subject to gravity. *Izv. Akad. Nauk SSSR Fluid Dynamics* **2**(1), 29–34.
- SHKADOV, V.Y. (1968) Wave-flow theory for a thin viscous liquid layer. *Izv. Akad. Nauk SSSR Fluid Dynamics* **3**(2), 12–15.

- SHYY, W., FRANCOIS, M., UDAYKUMAR, H.S., N'DRI, N. AND TRAN-SON-TAY, R. (2001) Moving boundaries in micro-scale biofluid dynamics. *Appl. Mech. Rev.* **54**(5), 405–454.
- SLADE, D. (2013) Gravity-driven thin liquid films: rivulets and flow dynamics. PhD thesis, University of Leeds.
- SLADE, D., VEREMIEIEV, S., LEE, Y.C. AND GASKELL, P.H. (2013) Gravity-driven thin film flow: The influence of topography and surface tension gradient on rivulet formation. *Chem. Eng. Process.: Process Intens.* **68**, 7–12.
- SPURK, J.H. AND AKSEL, N. (2008) *Fluid Mechanics*. Academic Press, 2 edn, Springer.
- SQUIRES, T.M. AND QUAKE, S.R. (2005) Microfluidics: Fluid physics at the nanoliter scale. *Rev. Mod. Phys.* **77**, 977–1026.
- STILLWAGON, L.E. AND LARSON, R.G. (1988) Fundamentals of topographic substrate leveling. *J. Appl. Phys.* **63**(11), 5251–5258.
- STILLWAGON, L.E. AND LARSON, R.G. (1990) Leveling of thin-films over uneven substrates during spin coating. *Phys. Fluids A* **2**(11), 1937–1944.
- STILLWAGON, L.E., LARSON, R.G. AND TAYLOR, G.N. (1987) Planarization of substrate topography by spin coating. *J. Electrochem. Soc.* **134**(8), 2030–2037.
- STOKER, J.J. (2011) *Water waves: The mathematical theory with applications*. Vol. 36, John Wiley & Sons.
- STONE, H.A., STROOCK, A.D. AND AJDARI, A. (2004) Engineering flows in small devices. *Annu. Rev. Fluid Mech.* **36**, 81–411.
- THIART, G.D. (1990) Finite difference scheme for the numerical solution of fluid flow and heat transfer problems on nonstaggered grids *Num. Heat Trans. B* **17**(1), 43–62.
- TRIFONOV, Y.Y. (1999) Viscous liquid film flows over a periodic surface. *Int. J. Multiphas. Flow* **24**(7), 1139–1161.
- TRIFONOV, Y.Y. (2004) Viscous film flow down corrugated surfaces. *J. Appl. Mech. Tech. Phys.* **45**(3), 389–400.
- TRIFONOV, Y.Y. (2007) Stability of a viscous liquid film flowing down a periodic surface. *Int. J. Multiphas. Flow* **33**, 1186–1204.
- TROTTENBERG, U., OOSTERLEE, C.W. AND SCHÜLLER, A. (2001) *Multigrid*. Academic Press.

- TSELUIKO, D., BLYTH, M.G., PAPAGEORGIOU, D.T. AND VANDEN-BROECK, J.M. (2008) Effect of an electric field on film flow down a corrugated wall at zero Reynolds number. *Phys. Fluids* **20**(4), 042103.
- TSELUIKO, D., BLYTH, M.G., PAPAGEORGIOU, D.T. AND VANDEN-BROECK, J.M. (2009) Viscous electrified film flow over step topography. *SIAM J. Appl. Math.* **70**(3), 845–865.
- VAN OSS, C.J., CHAUDHURY, M.K. AND GOOD, R.J. (1988) Interfacial lifshitz-van der waals and polar interactions in macroscopic systems. *Chem Rev.* **88**(6), 927–941.
- VEREMIEIEV, S. (2011) Gravity-driven continuous thin film flow over topography. PhD thesis, University of Leeds.
- VEREMIEIEV, S., THOMPSON, H.M., LEE, Y.C. AND GASKELL, P.H. (2010) Inertial thin film flow on planar surfaces featuring topography. *Comput. Fluids* **39**(3), 431–450.
- VEREMIEIEV, S., THOMPSON, H.M., SCHOLLE, M., LEE, Y.C. AND GASKELL, P.H. (2012) Electrified thin film flow at finite reynolds number on planar substrates featuring topography. *Int. J. Multiphas. Flow* **44**, 48–69.
- VLACHOGIANNIS, M. AND BONTOZOGLU, V. (2002) Experiments on laminar film flow along a periodic wall. *J. Fluid Mech.* **457**, 133–156.
- WALTERS, D.R. (2006) Disguising the leaf surface: the use of leaf coatings for plant disease control. *Eur. J. Plant Pathol.* **114**(3), 255–260.
- WANG, C., KRAUSCH, G. AND GEOGHEGAN, M. (2001) Dewetting at a polymer-polymer interface: film thickness dependence. *Langmuir* **17**(20), 6269–6274.
- WANG, C.Y. (1981) Liquid film flowing slowly down a wavy incline. *A.I.Ch.E. J.* **27**(2), 207–212.
- WANG, C.Y. (1984) Thin film flowing down a curved surface. *Zeitschrift Fur Angewandte Mathematik Und Physik* **35**(4), 532–544.
- WANG, C.Y. (2005) Low Reynolds number film flow down a three-dimensional bumpy surface. *J. Fluid. Eng.-T. ASME* **127**(6), 1122–1127.
- WANG, X.D., LEE, D.J., PENG, X.F. AND LAI, J.Y. (2007) Spreading dynamics and dynamic contact angle of non-newtonian fluids. *Langmuir* **23**(15), 8042–8047.
- WEBB, R.L. (1994) *Principles of Enhanced Heat Transfer*. John Wiley & Sons, The University of Michigan.
- WEIDNER, D.E., SCHWARTZ, L.W. AND ELEY, R.R. (1996) Role of surface tension gradients in correcting coating defects in corners. *J. Colloid Interf. Sci.* **179**(1), 66 – 75.

- WEINSTEIN, S.J. (1990) Wave propagation in the flow of shear-thinning fluids down an incline. *AIChE journal* **36**(12), 1873–1889.
- WIERSCHEM, A. AND AKSEL, N. (2004) Influence of inertia on eddies created in films creeping over strongly undulated substrates. *Phys. Fluids* **16**(12), 4566–4574.
- WIERSCHEM, A., SCHOLLE, M. AND AKSEL, N. (2002) Comparison of different theoretical approaches to experiments on film flow down an inclined wavy channel. *Exp. Fluids* **33**(3), 429–442.
- WIERSCHEM, A., SCHOLLE, M. AND AKSEL, N. (2003) Vortices in film flow over strongly undulated bottom profiles at low Reynolds numbers. *Phys. Fluids* **15**(2), 426–435.
- WILKINSON, W.L. (1960) *Non-Newtonian fluids: fluid mechanics, mixing and heat transfer*. Pergamon Press London.
- WILSON, S.K., DUFFY, B.R. AND DAVIS, S.H. (2001) On a slender dry patch in a liquid film draining under gravity down an inclined plane. *Eur. J. Appl. Math.* **12**, 233–252.
- YIANTSIOS, S.G. AND HIGGINS, B.G. (1988) Linear stability of plane poiseuille flow of two superposed fluids. *Phys. Fluids* **31**(11), 3225.
- YIH, C.-S. (1963) Stability of liquid flow down an inclined plane. *Phys. Fluids* **6**(3), 321–334.
- YIH, C.-S. (1967) Instability due to viscosity stratification. *J. Fluid Mech.* **27**(02), 337–352.
- ZHOU, C. AND KUMAR, S. (2012) Two-dimensional two-layer channel flow near a step. *Chem. Eng. Sci.* **81**, 38–45.